A GEOCHEMICAL STUDY OF GALLIUM, GERMANIUM AND INDIUM, IN SULFIDE MINERALISATION OF THE KOMBAT, TSUMEB AND KHUSIB SPRINGS DEPOSITS, OTAVI MOUNTAIN LAND, NAMIBIA

A DISSERTATION SUBMITTED IN FULFILLMENT OF THE REQUIREMENTS FOR THE DEGREE OF

DOCTOR OF PHILOSOPHY IN SCIENCE
(GEOLOGY)

OF

UNIVERSITY OF NAMIBIA

BY

ESTER SHALIMBA

200627155

OCTOBER 2024

MAIN SUPERVISOR: DR. ANSGAR WANKE (UNIVERSITY OF NAMIBIA)
CO-SUPERVISOR: Dr. STEPHANIE LOHMEIER (TECHNICAL UNIVERSITY OF CLAUSTHAL)

Abstract

Carbonate-hosted base metal deposits are known to contain significant contents of critical metals such as Ga, Ge, and In. These metals occur mainly as inclusions or incorporated within the crystal lattice of the main sulfide minerals while they form rarely discrete minerals. The aim of this Doctor of Philosophy (PhD) study is to determine the geochemical characteristics of the critical raw metals that are associated with the sulfide mineralisation of the base metal deposits of the Otavi Mountain Land, with the emphasis on the Tsumeb, Kombat and Khusib Springs deposits. Tsumeb mine is an over the decades exploited breccia-pipe like polymetallic deposit, hosted by Neoproterozoic dolomite and limestones in the Otavi Group of the Damara Orogenic Belt. Exploitation took place between 1897 and 1996, with a production of about 30 Mt of ore, yielding 1.7 Mt Cu, 2.8 Mt Pb, 0.9 Mt Zn, and 80 t Ge. Mineralisation at this deposit consists of tennantite and sphalerite as the most abundant ore minerals, associated with galena, pyrite, bornite, chalcocite, digenite, and minor enargite, renierite, germanite, chalcopyrite, and traces of various arsenates. Kombat deposit, which is a stratabound, syntectonic Cu-Pb (Ag) sulfide deposit, is hosted in the dolomite of the Hüttenberg Formation, Otavi Group. Mining of the Kombat deposit is currently ongoing, with a total endowment of approximately 13.6 Mt, of which 12 Mt has been exploited until 2008. The ore mineralisation of the Kombat deposit is quite variable comprising massive, disseminated, veinlet-controlled, and brecciated mineralisation styles with abundant bornite, chalcopyrite, galena, covellite, and chalcocite set into quartz-calcite gangue. Khusib Springs deposit is a high-grade Cu-Pb-Zn deposit which is classified as a “Tsumeb-type deposit”, hosted by Neoproterozoic dolomite, limestone and phyllites of the Maieberg Formation, Otavi Group. The main aim of this study is to show the siting of the most important minor and trace elements in the diverse sulfide mineral phases and to highlight the relationships between common trace elements and critical metals within the sulfide mineral phases. Various analytical techniques, including laser ablation inductively coupled plasma spectrometry (LA-ICP-MS), electron microprobe analysis (EPMA), inductively coupled plasma mass spectrometry (ICP-MS), and X-ray fluorescence (XRF), were employed to study the bulk

geochemistry and the siting of the trace elements, for the sole purpose of answering the above-mentioned objectives. Additionally, portable X-ray fluorescence (pXRF) technique was utilized with the aim of evaluating the possible usability of a low-cost analytical technique in exploration for base and critical elements in carbonate-hosted sulfide mineralisations. The Kombat mineralization comprises three mineral assemblages (1) bornite-chalcopyrite-covellite, (2) bornite-galena-chalcocite, and (3) bornite-chalcopyrite, set into dolomite-quartz-calcite gangue, with chalcopyrite identified as the main carrier of Ga, Ge, and In in this deposit. The profound micro-analysis of Tsumeb ore revealed the presence of both Ga and Ge, associated with trace elements (Ag, As, Cd, Co, Cu, Fe, Ga, Ge, In, Ni, Pb, Sb, Zn), in the different sulfides. The most significant carriers of Ge are renierite (av. 8.21 wt.%) and enargite (0.78 wt.%), while Ga is mainly incorporated into renierite (av. 0.12 wt.%) and sphalerite (av. 0.11 wt%). Trace element abundance in sphalerite is characterized by elevated Cd, Ge, and Ga, suggestive of low formation temperatures, which corroborates with earlier research on the formation of Tsumeb ore. Reconnaissance Zn isotope data (-0.19 to 0.14‰) delineate Tsumeb ore as typical Zn-rich massive sulfide ore, with Zn isotope values overlapping with those of the Irish MVT deposits (-0.17 to 1.33‰), while Cu isotopes are comparable to isotopic data of hypogene mineralisation. In Khusib Springs ore, tennantite (Fe, Zn, Ag, Sb) and chalcopyrite (Cu, Pb, Ag) are the most important carriers of trace elements while all other sulfides are characterized by a surprisingly low trace element content. In contrast, Khusib Springs massive ore reveals a wealth of Ag-bearing minerals of the pearceite-polybasite mineral group. Modern portable tools are successfully applied for the analyses of selected elements in various fields. Portable XRF can be used as well for the analyses of selected elements (Cu, Fe, Mn, Pb, Zn) in Kombat-type ore, while these instruments fail for the analyses of elements like Ag, Sr, and, in particular, for the analyses of the target elements Ga, Ge, and In. Therefore, this study gives a detailed overview about the relationship between critical elements Ga, Ge, and In and associated elements in sulfide ores in the carbonate-hosted base metal deposits of the Otavi Mountain Land, while showing at the same time the limitations when access to modern analytical technologies is limited.

Keywords: Gallium, Germanium, Indium, Otavi Mountain Land, trace elements, sulfide mineralisation, Kombat deposit, Khusib Springs deposit, Tsumeb deposit

Preface

The thesis summarises the study at the department of Geoscience, Faculty of Agriculture and Natural Science, University of Namibia. This thesis forms up part of the Low-cost surveys for high-technology metals: Applying field portable instruments under quasi-realistic conditions in Subsaharan Africa (LoCoSu) project, which was a collaborative project between Rheinisch-Westfälische Technische Hochschule (RWTH), Aachen University, Germany, Geoscience department, University of Namibia, Geological Survey of Namibia and University of Zambia, which was funded by the BMBF, Germany. The thesis discusses Three aspects all related to the exploration of the critical raw material in the sulphide carbonate hosted deposit of the Otavi Mountain Land, focusing on:

1) Portable XRF as a possible tool for the exploration of the carbonate hosted polymettalic deposit of the Kombat deposit. (Chapter 4)
2) Petrography of the ore minerals of Kombat, Tsumeb and Khusib Springs deposits. (Chapter 5, 6, and 7)
3) Trace element in sulfide mineralisation of Kombat, Tsumeb and Khusib Springs deposit. (Chapter 5, 6, and 7)

Conference presentation and Posters

- **Shalimba, E.,** Lohmeier, S., 2023. Trace element characteristics of the sulfide mineralization of the Tsumeb deposit, Otavi Mountain Land, Namibia. CAG29 conference, Windhoek Namibia. **(Oral presentation)**
- **Shalimba, E.,** Lohmeier, S., Wanke, A., 2021. Ore mineralogy and textural, characteristic of Cu-Pb-Zn-Ag Tsumeb deposit, Namibia. Annual Research

Conference on Agriculture, Engineering and Natural Science,2021. **(Virtual presentation)**

- **Shalimba, E.,** Lohmeier, S., Wanke, A., 2020. Using portable X-ray fluorescence in the exploration of carbonate-hosted sulphide mineralization (Otavi Mountain Land, Namibia). AIMS conference, 2020, Aachen, Germany, J. Conf. Abstr. No. 022.
- **Shalimba, E.,** Lohmeier, S., Wanke, A., 2020. Trace element concentrations in the Kombat deposit of Otavi Mountain Land, Namibia. AIMS conference, 2020, Aachen, Germany, J. Conf. Abstr. No. 023.
- **Shalimba, E.,** Wanke, Sindern S (2019) Indium and Gallium in Cu Pb (Ag) sulphide deposits of the Otavi Mountain Land, Namibia; a LA ICP MS. SGA conference, 2019, Gasglow, Scot land). **(Poster Presentation)**
- **Shalimba, E.,** Wanke, A (2018), Application of pXRF to exploration for Ga, Ge and In associated with sulphide deposits of the Otavi Mountainland, Namibia. RFG conference, 2018, Vancover Canada. **(Poster presentation)**

Acknowledgements

A special thanks are due to my Supervisors, Dr S Lohmeier, her unwaverly support, patient and contribution was the great driving force behind finishing this study. This PhD would not have been possible without her support, especially in the moments I wanted to give up, she believed in me more than I believed in myself. In her I found a mentor and a friend at the same time, so thank you. Dr A Wanke, for granting me the opportunity to start this journey, for the support and scientific contribution. This project was funded by BMBF (DLR and DAAD) through the LoCoSu project (grant number 01DG16011), through the leadership of Prof Bernd Lottermoser, this opportunity is highly appreciated. I would like to thank TU Clausthal University, BGR Hannover, Geological Survey of Namibia, Ministry of Mines and Energy, RWTH Aachen University, Geochemistry division, Czech Geological Survey, Husab Energy PTY (LTD), Kombat mine (Trigon metals), for allowing me to either collect samples at their premises, sample preparation and analyses at little to no cost at all, Thank you. University of Namibia for granting me the opportunity to pursue this dream and allowing me to take time off now and then to concentrate on my study.

I would like to thank my colleagues from the Department of Geoscience, for the unwavering support, you have taken on my workload at times with no complains at all and for allowing me to pick your brains from time to time. I would also like to thank my family and friends for the support, this study was done during some of the darkest moments of my life, but you made sure that I had a shoulder to lean on and the words of encouragement were the cherry on the cake that allowed me to operate smoothly.

Dedication

To my little Twayambekwa, thank you being patient with mummy during this period. I don’t remember how many times I left you behind for days, even years just in pursuit of this, but you took it gracefully like the real G that you are. Thank you, my baby, I LOVE YOU.

Declaration

I, Ester Shalimba, hereby declare that this study is my own work and is a true reflection of my research, and that this work, or any part thereof has not been submitted for a degree at any other institution. No part of this thesis/dissertation may be reproduced, stored in any retrieval system, or transmitted in any form, or by means (e.g., electronic, mechanical, photocopying, recording or otherwise) without the prior permission of the author, or The University of Namibia.

I, Ester Shalimba, grant The University of Namibia the right to reproduce this thesis in whole or in part, in any manner or format, which The University of Namibia may deem fit.

Student name: Ester Shalimba Signature: October 2024

Table of Content

List of Tables

List of Figures

List of Appendix

1. Introduction

1.1 Background of the study

Using the definition of the United States Geological Survey (USGS), critical raw materials are those that are vital to economic growth, particularly in terms of technological advancement, and have significant supply risks (Fortier et al., 2018). Economic importance and supply risks are the two parameters frequently used to determine how critical the raw materials are (Graedel et al., 2011). Gallium (Ga), germanium (Ge) and indium (In) are critical for a variety of high technology applications, such as semiconductors, robotics, 3D drone printings, flat panel displays, ICT, solar power arrays, wide angle camera lenses as well as pharmaceutical products (Paradis, 2015; Shanks et al., 2017, Bobba et al., 2020). These elements are all trace elements with a corresponding low crustal abundance, but they can occur in elevated concentrations in a variety of geological materials such as coal, epithermal deposits and sulfide ore deposits (Höll et al., 2007; Frenzel et al., 2014; Sahlström et al., 2017; Benites et al., 2021).

There is still a great potential for Ga, Ge and In in the carbonate rocks in the Otavi Mountain Land (OML), which are the host rocks of some of the largest base metal deposits worldwide (Melcher et al., 2006). The OML is situated at the transition between the Northern Zone and the Northern Platform of the Neoproterozoic Damara Belt and hosts various polymetallic deposits which carried trace amounts of critical raw metals (Melcher et al., 2006; Kamona and Günzel, 2007). The province has clusters of various sulfide mineralization that are linked to two mineralization episodes (Pirajno and Jourbert, 1993).

Exploration for base metals has been highly cyclical in recent decades, but resurgence of global exploration targeted on these deposits will likely result in increased Ga, Ge, and In reserves (Paradis, 2015). This research aims to employ various multidisciplinary geochemical techniques coupled with a profound petrographic study, to investigate the association of selected critical metals with the sulfide mineralization of the carbonate hosted base metal deposit of the OML. This research focuses on the distribution and geochemical concentration of Ga, Ge and In in Tsumeb, Kombat and Khusib Spring deposits, which are all hosted in the carbonate rocks of the OML.

1.2 Problem Statement

The OML province has clusters of various ore deposits that are linked to at least two mineralization episodes, with several genetic models proposed (Pirajno and Joubert, 1993; Chetty and Frimmel, 2000; Kamona and Günzel, 2007). The genesis of the mineralization in the province remains controversial despite the several genetic models that have been proposed, owing to the intricacy of the deposits. Additionally, the geochemical concentration of Ga, Ge, and In and their relation to the base metal sulfide mineralization of the OML is poorly constrained. Therefore, a trace element characterization of the sulfide ore minerals will provide variable information that will contribute to the understanding of the deposits, in hindsight the genesis.

1.3 Objectives of the study

This research aims to provide an insight into the geochemical characteristics of the critical raw materials Ga, Ge, and In, as well as other trace elements associated with the sulfide mineralization of the Tsumeb, Kombat and Khusib Spring deposits of the OML.

Understanding the geochemical characteristics of the trace elements in these deposits' aids in the better understanding of the genesis of the ore mineralization of the different deposits in the province. These points are achieved by looking at the following four objectives:

a) Determine the distribution and concentration of Ga, Ge and In in Tsumeb, Kombat, and Khusib Spring deposits.
b) Determine the relationship between the base metal mineralisation and Ga, Ge, and In, in Tsumeb, Kombat and Khusib Spring deposits.
c) Identifying indicator minerals and base metal elements, which can be used as proxies or indicator elements/minerals for Ga, Ge, and In in Tsumeb, Kombat and Khusib Spring deposits.
d) Assess whether pXRF can serve as an acceptable low-cost exploration technique for exploring for Ga, Ge, and In associated with sulphide base metal ores.

1.4 Significance of the study

Understanding the distribution of the critical raw metals such as Ga, Ge, and In in the sulfide mineralisation and their relation to the base metal within the deposits of the OML has a great potential to expand exploration and subsequently mining in the province in future. This study provides a viable data set that supports the development of exploration of the base metal deposits hosted in the carbonate units of the OML.

1.5 Limitation of the study

Recovery of core materials and access to some deposits requires seeking permission from the companies that have exploration or mining rights to the sites of interest. Limitation of access to various geochemical facilities has proven to be of great challenge during this

study. Consequently, some of the wanted trace element data are still not available. Unfortunately, the corona pandemic and the current ongoing conflicts had great influence on the study as analytical facilities in Africa, Canada and Europe closed and had to cope later with sample delay for months. Moreover, sample shipment was challenging or even not possible for months during corona times. Therefore, some of the investigations of this study have to rely on the available trace element data at time, as some wanted LA-ICP-MS trace element data (Chinese Academy of Science, Bejing, China) and age data on carbonate gangue (Karlsruhe Institute of Technology, Karlsruhe, Germany) are still pending and thus have to remain for ongoing research.

1.6 Delimitation of the study

The study focuses on the sulfide mineralization of Tsumeb, Kombat and Khusib Springs deposit within the OML, mainly focusing on the petrography and geochemical components.

1.7 Research Methods

1.7.1 Research Design

The foundation of this study included field work, sample collection, detailed mineralogical and geochemical analyses, detailed petrographic studies, and data interpretation. The methodology for this research is summarized in subsection 1.7.2 below, and the detailed methodology used to acquire data are described in detail in the respective chapters.

Three prepared manuscripts and six (extended) abstracts related to poster and oral presentations on international conferences (RFG Vancouver, Canada, 2018; SGA,

Glasgow, 2019; AIMS, Aachen, 2020 (2x); Unam Faculty of Science annual conference, Windhoek, 2021; CAG29, Windhoek, 2023) came out so far from this study. The manuscripts are still under review. Some of the chapters are enlarged versions of the conference abstracts.

1.7.2 Procedure

The key objectives outlined in section 1.3 are achieved using the following key procedures:

a) Field work

This research is based on at least three phases of sample collection; the first phase involved field work that took place in February 2018. For this field trip a total of 30 samples were collected from outcrops and heap dumps at the Kombat mine, for petrography and geochemical study. Main purpose of the trip was to collect geological data and representative samples of the mineralization of the Kombat deposit. Additional samples of the Kombat mineralization were collected in February 2021 for further geochemical investigations. The second phase involves the sample collection of the Tsumeb deposit, whereby 40 samples were collected in February 2021. These samples were collected from the historical collection by Schneiderhohn housed at the Ministry of Mines and Energy, Geological Survey of Namibia (GSN), Windhoek, Namibia. The Tsumeb deposit at the Tsumeb mine has been mined out, making collection of samples from outcrops not possible anymore. Additionally, investigation of the Tsumeb mineralization was conducted on polished blocks obtained from the collection housed at Bundesanstalt für Geowissenschaften und Rohstoffe/Federal Institute for Geosciences and Natural

Resources (BGR), Hannover, Germany. In November 2022, phase three was completed, whereby approximately forty samples of the Khusib Springs mineralization and the host rock were taken from heap dumps, drill cores, and outcrops for petrography and geochemical analysis of the deposit.

b) Laboratory work

Laboratory work conducted for this research includes petrography, bulk-rock geochemistry, mineral phases geochemistry and preliminary zinc (Zn) and copper (Cu) isotope analysis. Preliminary as additional data are still pending. This was done to fulfil the objectives outlined in section 1.3 above:

- For petrography studies, polished sections and double-polished thin sections were prepared at the Geochemistry division of the GSN and the Technical University of Clausthal (TUC). Those sections were carefully studied for the textural characterization of the ore, for ore paragenesis and ore phase relationships using transmitted and reflected light microscopes at the University of Namibia, TUC, BGR, and RWTH Aachen University.
- For geochemistry studies, a total of 120 representative samples of the mineralized lithologies and host rocks were analysed for major and trace elements using inductively coupled plasma mass spectrometry (ICP-MS), X-ray fluorescence (XRF) and portable XRF (pXRF). These analyses were done at four different institutions: 1) Central Analytical Facility (CAF), Stellenbosch, South Africa, 2) Actlabs, Canada, through their subsidiary Actlabs Namibia, 3) SGS Bulgaria, LTD laboratory in Serbia, and 4) TUC. Data obtained from these

analyses were used for the interpretation of the geochemical data for all three deposits in the respective chapter(s).

- Selected polished sections of the Tsumeb deposit and the Khusib Springs deposit were analysed using the Electron Microprobe Analysers (EMPA) at TUC and BGR for the determination of the mineral chemistry of the respective sulfide mineral phases. For the Kombat deposit, trace elements were analysed in bornite and chalcopyrite using the LA-ICP-MS device at RWTH Aachen University.
- Representative sample powders were selected for Zn and Cu isotopes which was performed at the laboratory of the Geological Survey of the Czech Republic.

2. Geological Overview

2.1 Regional Geology

Namibian rock units' range in age from Pre-Cambrian to recent (Fig. 2-1). The oldest exposed units are dominantly Paleoproterozoic and Mesoproterozoic metamorphic complexes, although remnants of the Archean age are recognised from magnetic and gravity signature data (Corner, 2000; Becker et al., 2006). Most of the Paleoproterozoic rock units exposed in Namibia are dated between ±1.8 billion years to ±1.7 billion years (Brandt et al., 2003; Drüppel et al., 2007; Miller, 2008a; Kröner et al., 2010; Kleinhanns et al., 2013; Mapani et al., 2014). Mesoproterozoic units were formed at ~1200 to 1000 Ma, during the Namaqua orogenic event (Becker et al., 2006; Cornell, 2006). The oldest Neoproterozoic rock units are mainly granitic and syenitic intrusive rocks formed at ~920 Ma (Miller, 1983; 2008b). However, the dominant rock units of the Neoproterozoic are the units of the Damara Supergroup, consisting of different sedimentary, metamorphic, and associated intrusive rocks, with the evolution of the Damara Supergroup reported to have commenced at ~820 Ma (Clifford, 2008; Gray et al., 2008; Miller, 2008b). Late Proterozoic to Cenozoic rocks in Namibia include units of the Karoo Supergroup associated with several late Cretaceous igneous complexes (Miller, 2008c; Dauteuil et al., 2018). The youngest units are those of the Kalahari Group, which mainly consists of sediments deposited in the Owambo, Omaheke and Aranos Basins, covering the eastern and southern part of Namibia (Miller, 2008c).

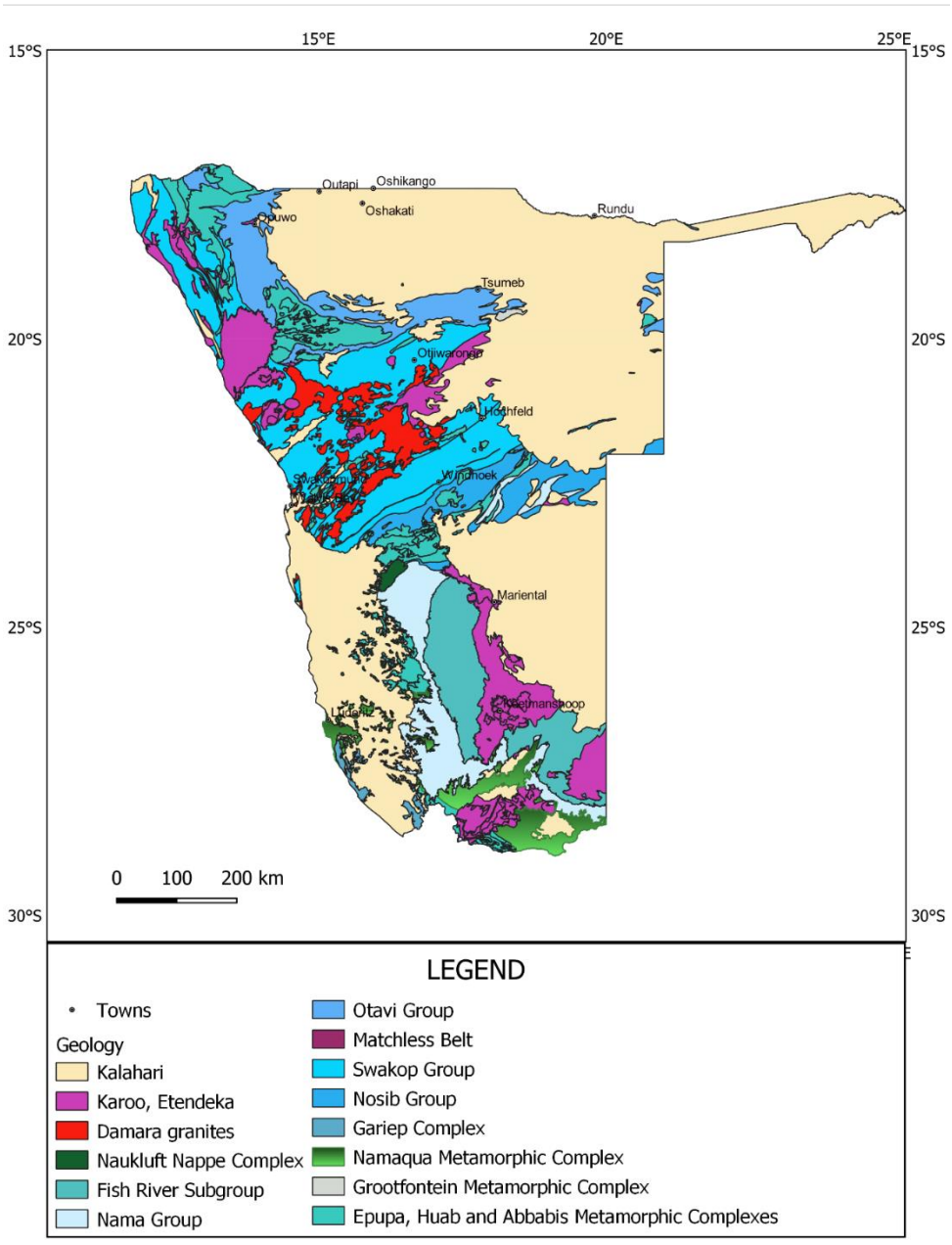

Fig. 2-1 Simplified geological map of Namibia, outlining geological units from the oldest Paleoproterozoic basement units to younger Tertiary sediments. Simplified after the 1:1,000,000 geological map sheet of Namibia from the Geological Survey of Namibia.

2.1.1 Paleoproterozoic-Mesoproterozoic Basement rock units

There are several Paleoproterozoic rock units, exposed from southern to northern Namibia, which are mainly composed of granitic and gneissic rocks (Fig. 2-1; Brandt et al., 2003; Schlüter, 2006; Miller, 2008a; Mapani et al., 2014). Paleoproterozoic units are represented by the Epupa, Huab, Grootfontein, Abbabis, Hohewarte and Kangas Metamorphic Complexes, in association with younger sedimentary and volcanic rock units (Miller, 2008a). Detailed information of the metamorphic evolution, main rock types and geochronological data of the Paleoproterozoic metamorphic complexes are discussed, for example, in Kleinhanns et al. (2013), Kröner et al. (2004; 2010), Miller (2008a) and Mapani et al. (2014). Rocks of the Mesoproterozoic Era include those of the high-grade Namaqua Metamorphic Complex located in the south and low-grade metamorphic rock units of the Sinclair Group (Fig. 2-1; Becker et al., 2006). In the following paragraphs, a very brief summary of the geology of the complexes is given.

The Epupa Metamorphic Complex (EMC) is exposed in the northwestern part of Namibia (Fig. 2-1), consisting of remnants of the southwestern margin of the Congo craton, separating the high-temperature Kaoko Belt from the Damara Orogenic Belt (Miller, 2008a; Kröner et al., 2010; Jelsma et al., 2018; Brandt et al., 2021). The complex is mainly composed of migmatites, ultrahigh-temperature granulites and granitoid orthogneisses, ranging in age from 1861±3 to 1758±3 Ma, intruded by gabbros of the Kunene Anorthosite Complex (Brandt et al., 2003; Drüppel et al., 2007; Kröner et al., 2010). Evolution of the granitoid gneisses of the Epupa Metamorphic Complex is linked to the Eburnian Orogeny during which these rocks are derived from a large batholith extending from northwest Namibia into Southern Angola (Kröner et al., 2010). Furthermore, these granitoid gneisses

are associated with the 1760 Ma Otjitanda granite rock unit, which has resulted from the migmatisation of the gneisses (Kröner et al., 2010). According to Brandt et al. (2003), the EMC is subdivided into two units, defined by the variation in metamorphic grade and separated by a E-W and NE-SW trending subvertical, ductile shear zone. These are the Orue Unit which comprises of upper-amphibolite facies ortho- and para-gneisses and the Epembe Unit which is made up of ultrahigh-temperature granulite rock units (Miller, 1983; Brandt et al., 2003; 2021).

Huab Metamorphic Complex (HMC; Fig. 2-1) covers most parts of the Kamanjab Inliers and a portion of the Welwitschia and Braklaagte Inliers on the western side of the Khorixas and on the northern edge of the Summas Mountains, respectively (Tegtmeyer and Kröner, 1985; Miller, 2008b). The complex mainly contains metasedimentary rock units which underwent a medium grade metamorphic overprint during the intrusion of mafic and felsic units (Kleinhanns et al., 2013). This complex is subdivided into two sections: the lower metasedimentary units on the southern part of the Kamanjab Inliers and the uppermost metavolcanic units in the north, ranging from 1830±17 to 1801±27 Ma (Miller, 2008a; Kleinhanns et al., 2013). The lowermost sequence mainly contains high-grade metavolcanic rocks associated with pegmatites, migmatites and structurally complex domes and basins, while the uppermost sequence is characterized by an intercalation of felsic and mafic volcanic rock units with metasediments (Kleinhanns et al., 2013). The Kamanjab inlier is correlated with the Hohewarte Metamorphic Complex, which is characterized by various gneisses that date between 1758± 10 Ma and 1061± 10 Ma (Mapani et al., 2014).

Grootfontein Metamorphic Complex (GMC; Fig. 2-1), also known as Grootfontein Inlier, is a Paleo-Mesoproterozoic complex which extends from north-northeast Namibia eastwardly into Botswana (Laukamp, 2006; Schlüter, 2006; Miller, 2008b). This complex is made up of three main units that are characterized by different lithologies: (1) a pack of well foliated gneisses, amphibolite, and metasedimentary rocks, (2) Grootfontein gabbros, and (3) Grootfontein granites that essentially intruded the gneisses (Miller, 2008b). The complex is estimated to be about 2022±15 Ma, with the age information derived from the Tsumkwe-Tarikora Massif, which is an extension of the GMC and its evolution is associated with the magmatic differentiation from dioritic to granitic in composition in a convergent tectonic setting (Hoal et al., 2000; Laukamp, 2006).

Namaqua Metamorphic Complex (NMC) is part of the ~400 km wide Mesoproterozoic Namaqua Natal Province (Fig. 2-1), which stretches from southern Namibia to the northwestern and southeastern coast of South Africa (Miller, 2008b; Bial et al., 2015). The complex is associated with the formation of the Kalahari Craton and is subdivided into four terranes, which are the Bushmanland, Kakama, Areachap and Kaaien Terraines (Thomas et al., 1994; Macey et al., 2017). The NMC consists of sedimentary successions that were subject to high-temperature, low-pressure metamorphic conditions, as well calc-silicate rocks and various types of granitoids that are intercalated with metapelites (Becker et al., 2006; Bial et al., 2015). The NMC is correlated to the highly deformed and metamorphosed units that underlie the Sinclair Sequence (Hoal, 1993). The Sinclair Group consists of low-grade to unmetamorphosed units that lie disconformably on the units of the Kumbis and Kairab Complexes (Hoal, 1993; Becker et al., 2006). The oldest rock units of this group form up part of the Kumbis and Nagatis Formations as well as the

Helmeringhausen Gabbro, which are dated at 1374±7 Ma to 1358±5 Ma, 1363±11 and 1372±12, respectively (Harris et al., 2020).

2.1.2 Neoproterozoic rock units

2.1.2.1 Damara Orogenic Belt

Hoffmann (1989) and Gray et al. (2006; 2008) describe the Damara Orogenic Belt (DOB) as a deep eroded, doubly-vergent structural, well exposed, high collisional orogenic belt that records the Western Gondwana amalgamation. The belt is part of the triple junction orogenic system, which is defined by the north trending Gariep Belt, the north-northwest trending Kaoko Belt and the east-northeast trending Damara Belt (Miller, 1983; 2008b; Gray et al., 2008; Goscombe et al., 2018). Damara Orogenic Belt formed due to the collision of the Congo-São Francisco and the Río de la Plata cratons at around 580-550 Ma, forming a suture that is on the northern side of Gondwana, followed by the collision of the Congo-São Francisco and the Río de la Plata suture with the Kalahari-Antarctic craton at approximately 530 Ma, forming a suture on the southern side of Gondwana (Prave, 1996; Gray et al., 2008). Damara Orogenic Belt experienced three notable deformation events: (1) The first deformation episode is associated with multiple phases of orogenesis and is estimated to have occurred at ~530-525 Ma; (2) at ~508 Ma the second deformation event occurred involving shortening of the Damara Belt; (3) and the last event is recorded at ~505 Ma, which is associated with the formation of the metamorphic core complex across the Central zone (Goscombe et al., 2017).

Stratigraphically, the DOB is subdivided into various groups based on the depositional environments, namely the Nosib, Swakop, Otavi, Mulden and Nama Groups, collectively

known as Damara Supergroup (SG) (Martin and Porada, 1977; Miller, 1983; 2008b). Nosib group is the oldest group, which is characterised by rift related fluviatile clastic rocks of the Etusis Formation and quartzite schists and calc-silicates of the Khan Formation (Miller, 2008b). Deposition of the Nosib Group is linked to the rifting episode of the Paleoproterozoic basement units (Porada and Behr, 1988). The estimated age of deposition of the Nosib Group is reported to be between ~861 and ~746 Ma, with the clastic units of the Etusis Formation dated at ~861 Ma, thereby representing the oldest units (Hoffmann et al., 1996; Foster et al., 2015; Nascimento et al., 2017; Goscombe et al., 2018). Swakop Group consists of deep-water facies turbidites, carbonate sequences, pelitic schist units as well as diamictites of the Chuos and Ghaub Formation (Miller, 1983). Chuos and Ghaub Formation units are evidence of the global glaciogenic events, that took place at Sturtian (~720-700 Ma) and Marinoan age (~635 Ma), respectively (Hoffmann et al., 2004; Goscombe et al., 2018). The age of deposition of the units of the Swakop Group ranges between ~720 and 570 Ma (Foster, 2015; Goscombe et al., 2018). Otavi Group rock units are deposited, mainly during a spreading event, on the northern platform and are dominated by carbonate units that are deposited on a rifted passive margin (Hoffmann and Prave, 1996). Similarly, to the Swakop Group, the Otavi Group contains rock units belonging to the glaciogenic Chuos and Ghaub Formation (Miller, 1983; 2008). Deposition of the Otavi Group is estimated to have occurred between ~750 Ma and 545 Ma (Melcher, 2003). Mulden Group is dominated by clastic molasse sediments that are estimated to be deposited between ~710 and 590 Ma (Foster et al., 2015; Basei et al., 2018). The youngest rock units of the Damara Supergroup belong to the Fish River Subgroup of the Nama Group, consisting of carbonates and siliciclastic

rocks that formed as a result of collisions between the Damara Belt and the Gariep Belt (Germs, 1983; Miller, 1983).

Furthermore, the DOB is subdivided into various tectonostratigraphic zones, that are characterised by metamorphic grade, structures, stratigraphy, and geochronology as described in Miller (1983; 2008). These zones are: 1) Southern Margin Zone, which consists of pre-Damaran basement rock, gneissic basement units, successions of the Nosib Group as well as traces of diamictites of the Chuos Formation (Miller, 1983; 2008). 2) Southern Zone, which is sandwiched by the Southern Margin Zone in the south and the Okahandja Lineament in the north, consists of passive margin successions of the Kuiseb Formation (Miller, 2008). 3) Central Zone which is subdivided into the Northern Central Zone and the Southern Central Zone, which are delineated by the Omaruru lineament. Both zones consist of syn- and post-tectonic granitic plutons, rock units of the Nosib Group and units of the lower Swakop Group (Miller, 2008; Longridge et al., 2017). The Central Zone is characterized by a northeast trending dome and a basin fold pattern as well as high-temperature low-pressure metamorphic rocks and comprises various intrusive rocks (Miller, 1983; 2008). 4) Northern Zone, which is characterised by northward vergence thrust, consists of rocks of the Nosib and Swakop Groups (Miller, 2008). 6) Northern Margin Zone overlaps with units of the Kaoko Belt, represented by the rock units of the Otavi and Mulden Group (Miller, 2008; Goscombe et al., 2018). 7) Northern Platform is mainly represented by the shallow water facies of the Otavi Group as well as low-grade metamorphosed units of the Nosib and Mulden Groups (Miller, 2008).

2.2 Local Geology

2.2.1 Otavi Mountain Land

Otavi Mountain Land (OML) province is situated at the transition between the Northern Zone and the Northern Platform of the Neoproterozoic Damara Orogen, as described in Martin and Porada (1977) and Miller (1983; 2008b). This province is composed of 1) Paleoproterozoic basement rock units of the GMC, consisting mainly of granites and gneisses; 2) Neoproterozoic rock units of the Damara SG which include clastic and metavolcanic rocks of the Nosib Group, carbonate rock units of the Otavi Group, the molasse sequence of the Mulden Group, and 3) Tertiary and Quaternary rock units of the Karoo Supergroup and Kalahari sediments, which are covering the units of the Damara SG (Fig. 2-2; Frimmel et al., 2004; Boni et al., 2007; Kamona and Günzel, 2007; Miller, 2008; Schneider et al., 2008). Rock units of the OML underwent low-grade metamorphism and are structurally characterized by north-verging recumbent folds that overprint the older east-west folds and north-trending folds (Cairncross, 1997). At least three deformation phases are recorded in the OML province as summarized in Frimmel et al. (1996), Goscombe et al. (2004), Melcher et al. (2006), and Miller (2008b). Rocks of the Nosib Group, exposed in the OML, are those of Nabis and Askevold Formations (Hoffmann et al., 1996, Kamona and Günzel, 2007; Miller, 2008b). Nabis Formation is dominated by siliciclastic rocks with minor quartzite, while the Askevold Formation consists of metavolcanic rocks, dolomite, and some siliciclastic rocks (Hoffmann et al., 1996; Kamona and Günzel, 2007; Miller, 2008; Schneider et al., 2008).

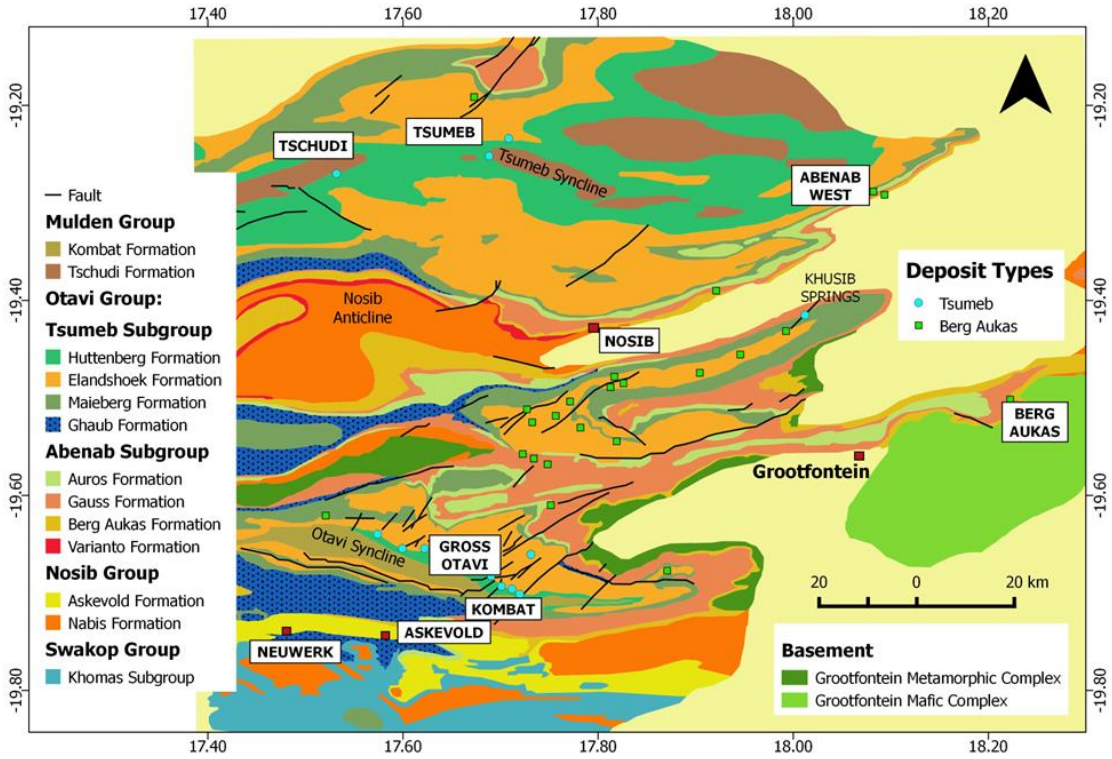

Fig. 2-2 Geological map of the Otavi Mountain Land, outlining the formations and mineral deposits in the province. Map simplified after the 1:250,000 geological sheet map from the Geological Survey of Namibia (modified after Chetty and Frimmel, 2000;Kamona and Günzel, 2007)

Otavi Group in the OML is subdivided into two subgroups, Tsumeb and Abenab Subgroups, which are further subdivided into various formations (Miller, 1983; 2008b; 2013; Hoffmann and Prave, 1996; Kamona and Günzel, 2007; Schneider et al., 2008). The Otavi Group mainly consists of carbonate platforms that are estimated to be formed between 720 and 600 Ma (Halverson et al., 2005; Hoffman, 2005; Hoffman et al., 2021). Diamictites belong to the Chuos and Ghaub Formations and are positioned at the bottom of the Abenab Subgroup and at the bottom of the Tsumeb Subgroup, respectively (Miller, 1983; 2008, 2013; Hoffmann, 1996; Frimmel et al., 2004; Boni et al., 2007; Kamona and

Günzel, 2007; Schneider et al., 2008). The Abenab Subgroup's basement is made up of the diamictite, ironstone, and pyroclastic rocks of the Chuos Formation (Hoffmann, 1994; 1996; 2004; Hoffmann and Prave, 1996; Kamona and Günzel, 2007; Miller, 2008, Schneider et al., 2008). Diamictites of the Chuos Formation are capped off by the cap carbonate units belonging to the Berg Aukas Formation (Hoffmann et al., 2004; Miller, 2008). Gauss Formation conformably lies on top of rock units of the Berg Aukas Formation and comprises massive and bedded, shallow water carbonate units and traces of stromatolites (Frimmel et al., 1996; Kamona and Günzel, 2007; Miller, 2008). Auros Formation forms up the uppermost part of the Abenab Subgroup, consisting of oolites, limestones, dolomite as well as stromatolites (Kamona and Günzel, 2007; Miller, 2008).

The basement of the Tsumeb Subgroup is made up of the Ghaub Formation, which is overlain by the Maieberg, Elandshoek and Hüttenberg Formations (Miller, 2008b). Ghaub Formation consists of diamictites, shale and graded dropstones (Hoffmann et al., 1996; Miller, 2008b), with dolomite and limestone of the Maieberg Formation forming up the cap carbonate on top of the Ghaub Formation’s glacial deposit (Miller, 2008). Both Elandshoek and Hüttenberg Formations consist of dolomite, chert, breccia, and stromatolites that are mainly known from the Hüttenberg Formation (Kamona and Günzel, 2007; Miller, 2008). Mulden Group within the OML province is sitting un- to para-conformably on the carbonate platform of the Otavi Group and consists of phyllite interbedded with lenses of dolomite, shale, sandstone, and siltstone of the Kombat Formation (Miller, 1997; Kamona and Günzel, 2007). Tschudi Formation is represented

by shale, slate, greywacke, quartzite, sandstone, and conglomerate (Kamona and Günzel, 2007; Miller, 2008, 2013; Schneider et al., 2008).

2.2.2 Otavi Group

Otavi Group, which was deposited between 750 and 545 Ma, consists of thick folded Neoproterozoic successions of carbonates exposed within the Otavi foreland fold belt, overlying the siliciclastic and local volcanic rocks of the Nosib Group (Hoffmann and Prave, 1996; Melcher, 2003). Lithostratigraphically, the group is subdivided into two subgroups, the lowermost Abenab Subgroup, and the uppermost Tsumeb Subgroup (Miller, 1983; Kamona and Gunzel, 2007). Both groups consist of diamictites of the Neoproterozoic glaciogenic event, with the Abenab Subgroup hosting the Chuos Formation while the Ghaub Formation is hosted in the younger Tsumeb Subgroup as well as shallow facies carbonate rocks (Melcher, 2003).

2.3 Mineralisation

The carbonate platform of the Otavi Group in the OML is known for the various types of mineralization it hosts (Kamona and Günzel, 2007). Pirajno and Joubert (1993) argued that there must have been at least two separate events that led to the metal concentration in the deposits of the OML. They concluded that Berg Aukas type deposits were formed by the first event, which was associated with compaction and dewatering of sediments of a northern rift, whereas Tsumeb type deposits were a result of a much later episode that was associated with devolatilization reactions during regional prograde metamorphism of the sediments in the northern rift. A number of studies and documentations ranging from scientific reports to peer-reviewed publications, have been done on the sulfide

mineralisation of the OML since the early 1900s. Various scientists have looked over the years at the complexity of the mineralogy of the Tsumeb deposit including Söhnge (1964), Lombard et al. (1986), Hughes (1987), and the most recent release by Bowell and Mocke (2019) who studied the mineralogy of the Tsumeb mine in detail. Genesis, enrichment, and alteration processes linked to the deposits in the OML have been reported in detail by Allsopp and Ferguson (1970), Kamona (1999), Chetty and Frimmel (2000), and Melcher (2003). Melcher (2003) reported on the geochemistry and mineralogy of Ge-bearing ore in the Tsumeb and Khusib Springs deposits and the difference with Ge-bearing ore at the Kombat and Berg Aukas deposits.

2.3.1 Tsumeb Deposit

Throughout the mining history of the Tsumeb orebody, approximately 30 Mt ore has been recovered, with ore grades of 10% Pb, 4.3% Cu and 3.5% Zn (Melcher, 2003). The deposit is hosted within a breccia karst pipe, filled by a mixture of feldspathic sandstone of the overlying Mulden Group and carbonates of the Hüttenberg Formation of the Otavi Group (Laukamp, 2006; Bowel and Mocke, 2019). Alteration styles in the Tsumeb deposit include calcitisation and silicification (Chetty and Frimmel, 2000). Major mineralisation consists of tennantite, galena, sphalerite, pyrite, bornite, chalcopyrite, digenite, and chalcocite with minor arsenates and other minerals (Bowell and Mocke, 2019). Several studies have been conducted on the Tsumeb mineralisation, focusing on the complexity of the mineralogy (e.g., Bowell and Mocke, 2019), the paragenesis of germanite and renierite (Sclar and Geier, 1957), and the ore genesis (e.g., Pirajno and Jourbert, 1993). Sulfur isotope investigations on galena revealed that Tsumeb ore is generated from evaporite sulfate minerals and that the high U/Pb ratios are consistent with the upper

continental crust, implying that the upper continental crust is the primary source of the metals. (Hughes, 1987; Pirajno et al., 1992; Kamona et al., 1999). Age of mineralisation for the Tsumeb deposit is estimated to be between 500 to 600 Ma, deduced from the Pb isotope data as well as from preliminary Re-Os isotopic data (Pirajno and Joubert, 1993; Melcher, 2003).

2.3.2 Kombat Deposit

The Kombat deposit, is a stratabound, syntectonic, carbonate-hosted Cu-Pb(-Ag) deposit, which sits in the Hüttenberg Formation (Deane, 1995). The deposit was mined from the early 1900s until 2007 when it was closed due to flooding and operation resume in 2023. Indicated remaining reserves comprise 12.22 Mt with average 1.94 wt% Cu, 0.70 wt% Pb and 13.67 ppm Ag (Kamona and Günzel, 2007; Trigon Metals, 2021). Rock units in the Kombat area have endured metamorphism intensity up to greenschist facies. The exposed rock units associated with the deposit include carbonate rock and phyllite (Pirajno and Joubert, 1993; Kamona and Günzel, 2007). There are at least six distinct ore bodies identified to date in the Kombat area, which are all associated with the actual Kombat deposit, having Cu-Pb-Ag and Fe-Mn mineralisations (Nghoongoloka et al., 2020).

2.3.3 Khusib Springs Deposit

Khusib Springs Deposit is a steeply plugging pipe or lens like orebody that is hosted within the limestones of the Maierberg Formation, Otavi Group (Melcher et al., 2006; Kamona and Günzel, 2007). Melcher et al. (2006) investigated the distribution of Ge in the deposit and interpreted Khusib Springs as a high-grade Cu-Ag sulfide deposit. Tennantite and enargite are the predominant ore minerals with minor chalcopyrite,

sphalerite, galena, pyrite and Ge-bearing colusite (Melcher et al., 2003; Melcher, 2003). In total approximately 300,000 tons of ore, with an average grade of 10% Cu, 1.8% Pb and 584 ppm Ag have been produced at Khusib Springs between 1995 and 2000 (Melcher et al., 2006).

3 Literature Review

3.1 Critical raw Materials/Metals

In response to the challenges surrounding the sustainable supply of natural resources, the United States (US) and the European Union (EU) embarked on research to identify alternative raw materials that can support the rapid increase of the green industrial revolution and the in hindsight global population growth (Perez et al., 2019; Gonzalez-Alvarez et al., 2021). These necessities led to the identification of several metals that are deemed essential mainly to the green industrial revolution, which are classified as critical minerals/metals. Critical metals are those metals or non-metals that are of high economic importance, that underly a high risk of supply shortage and may be difficult and rare to be extracted in their pure form (Fig. 3-1; Skirrow et al., 2013; European Commission, 2014; 2017; 2020; Perez et al., 2019; Gonzalez-Alvarez et al., 2021). This includes dispersed elements such as Ga, Ge, V, In, Tl, and Hf, and the so-called Heavy Rare Earth Elements (HREEs) as well as the Light Rare Earth Elements (LREEs) and the Platinum Group Elements (PGEs; Liu et al., 2022). Worldwide there are several known deposits from which critical raw materials are recovered either as primary mined commodity or as by-product(s), with China being the major producer of critical metals such as Ga and Ge in the world (Kastanaki and Giannis, 2022). Critical metals enrichment in carbonate-hosted base metal and sulphide ores has been investigated and documented in detail (e.g., Cook et al., 2009; Ye et al., 2011; Li et al., 2020; Liu et al., 2022; Luo et al., 2022; Niu et al., 2023).

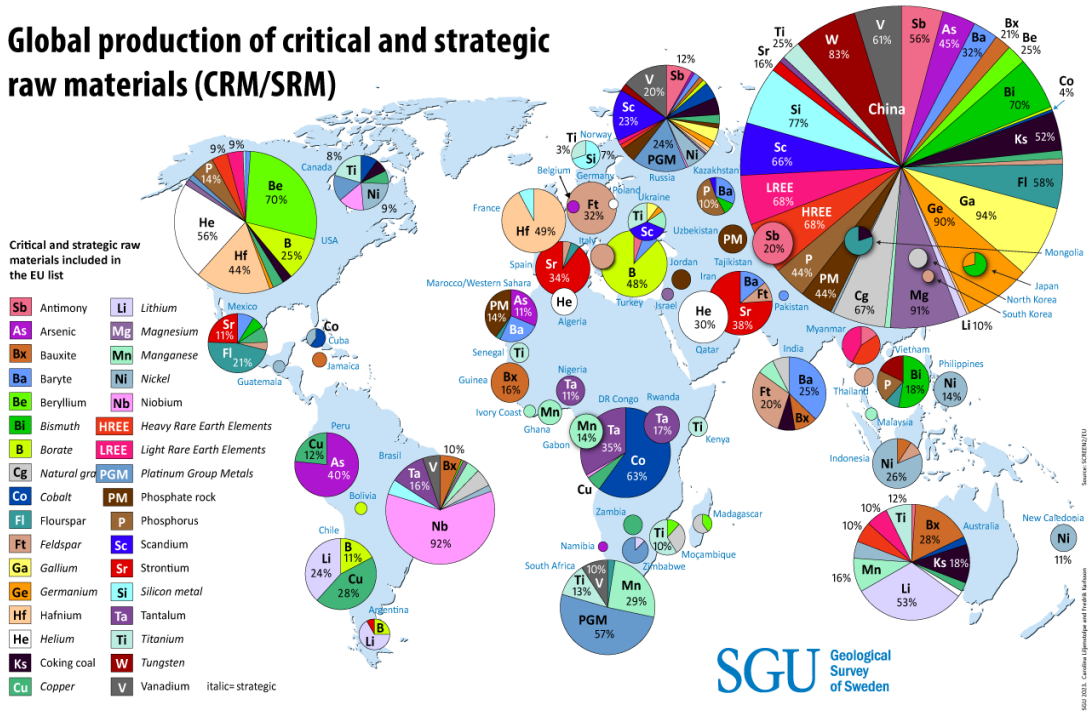

Fig. 3-1 Global distribution and production of critical raw materials. The pie chart represents the total global production of the critical metal in a specific country (SGU, 2023).

3.1.1 Gallium, Germanium, and Indium

Gallium, Ge and In are minor and trace elements in a variety of mineral deposit types, with a significant concentration in base metal deposits with the potential to reach economic viability (Höll et al., 2007; Fig. 3-2). Sphalerite is the major ore mineral of Zn, and it is known to be one of the most abundant carriers of Ga, Ge and In (Cook et al., 2009; Shanks et al., 2017; Bauer et al., 2019a; b; Cugerone et al., 2021). In general, Ga, Ge and In occur either as micro-inclusion(s) or in solid solution via single or coupled substitutions in different host minerals as described, for example, in Höll et al. (2007),

Cook et al. (2009), Pfaff et al. (2011), Belissont et al. (2014), Bauer et al. (2019 a; b), Cugerone et al. (2021), and (Luo et al., 2022).

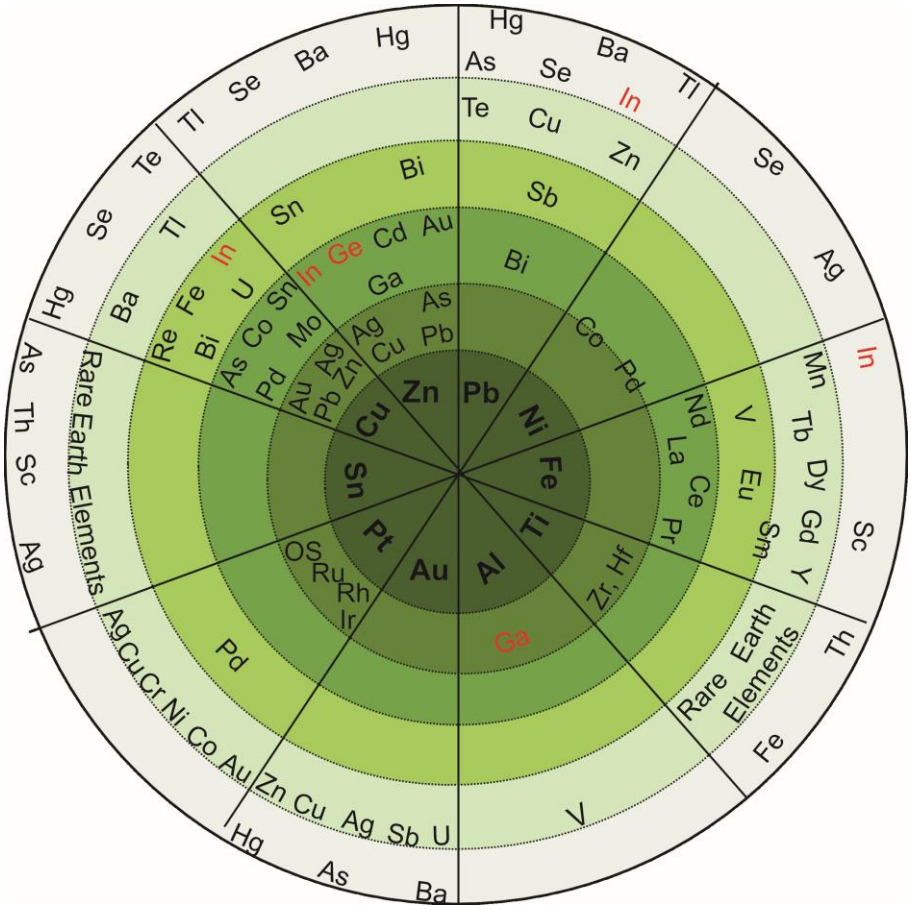

Fig. 3-2 A diagram of various elements in mineral resources, which depicts the linkage between metal associations in mineral resources. The primary metals found in most deposits are shown by the inner circle (dark green). The gradation colour is attributing to the decrease in association (modified after Reuter & Verhoef, 2004; Nassar et al., 2015).

The existence of Ge can be dated back to the 1800s, when chemists J. Newland and D. Mendeleev independently predicted its existence in 1864 and 1871, respectively, followed by the subsequent discovery by Clemens Winkler in 1886 (Shanks et al., 2017).

Germanium is considered as a critical raw material primarily because it is currently in high demand due to its use in fibre optics (Belissont et al., 2014; Frenzel et al., 2014; Shanks et al., 2017). Because of the multiple geochemical characteristics of Ge (siderophile, chalcophile, lithophile and organophile), Ge is present in trace amounts of most rocks on Earth (Bernstein, 1985). Therefore, Ge occurs in the Earth crust enriched in coal, sphalerite-rich ores, Cu-Ag-As sulphide rich ores and iron oxides, having a crustal abundance of approximately 1.4-1.6 ppm (Bernsteins, 1985; Höll et al., 2007; Frenzel et al., 2014). It is commonly found in association with several base metal (Cu)-Zn-Pb ore types, in particular Mississippi Valley Type (MVT) deposits, and coal deposits (Bernstein, 1985; Melcher et al., 2006; Frenzel et al., 2014). Bernstein (1985) and Melcher et al. (2006) suggested that As-bearing sulphides and carbonate-hosted metal sulphide deposits are one of the major sources of both Ge and Ga.

Gallium is one of the crucial elements used in green energy, as well as in manufacturing of high technology devises such as optoelectronics devices, high performance computers, transistors, and semiconductors (Foley et al., 2017). Its existence was first predicted by Dmitri Mendeleev in 1871, followed by its discovery in sphalerite by P.-E. Lecoq in 1875 (Foley et al., 2017). Gallium occurs as Ga(III) in nature, and it is a considerable trace element with a crustal abundance of 17 ppm that is commonly associated with Al-, Zn-, Pb-, Fe ores and coal, typically found in bauxite, sedimentary Zn-Pb, MVT (Zn-Pb) and clastic type Zn and Pb deposits (Gao et al., 1988; Bradley and Leach, 2003; Hu and Gao, 2008; Cook et al., 2009; Butcher and Brown, 2014; Redlinger and Eggert, 2016; Frenzel et al., 2016; Foley et al., 2017). Geochemically Ga is associated with Fe, Al, Zn, Cd, In, Ge, Si and Sn, with the first three elements being more susceptible to substitution by Ga

due to similar ionic radii (Foley et al., 2017). To date, there are several minerals discovered in which Ga has significant concentration ranging between 15wt% ≤ Ga ≥ 60 wt%, including gallite ($CuAgS_2$), gallobeudantite ($PbGa_3(AsO_4)(SO_4)(OH)_6$), sohngeite ($Ga(OH)_3$) and tsumgallite (GaO(OH) (Frimmel et al., 1996).

Indium can be used as coating in displaying devices, solar collectors, alloys, and semiconductors among others (Jorgenson and George, 2005; Shanks et al., 2017; Fontana et al., 2021). Its discovery can be dated back to 1863, when F. Reich and H.T. Ritcher found it in trace amounts in association with sphalerite, Cu- and Fe-Sn sulphides (Jorgenson and George, 2005; Shanks et al., 2017). Indium is a highly volatile chalcophile, with a crustal abundance estimated to be about 0.05-0.072 ppm (Taylor and McLennan, 1985). Indium is directly associated with deposits such as VMS, porphyry, skarns and sedimentary-hosted base metals, with the dominant In-bearing mineral in (Pb)–Zn ores and concentrates being sphalerite (Schwarz-Schampera and Herzig, 2002; Ye et al., 2011). Previous studies indicate that the highest concentration of In coincide with Zn and Cu sulphides, with In favouring roquesite, sphalerite, chalcopyrite, tennantite, cassiterite and stannite (Paradis, 2015).

3.2 Methods used

Trace element characterisation of sulfide minerals in selected ore samples for this study was carried out using Laser Ablation Inductively Coupled Plasma Mass Spectrometry (LA-ICP-MS) and Electron Probe Micro Analysis (EPMA). The various techniques used for the analyses of sample in this research, are described in detail in respective chapter. Paragraphs below gives a summary review of the technique used.

LA-ICP-MS is a technique that has been used widely over the last three decades for the determination of elemental concentration(s) in various materials (Sylvester and Jackson, 2016). In geosciences the technique is especially used in the branch of geochemistry, for trace elements and isotope characterisation as well as in fluid inclusion analysis (Chew et al., 2014; Breiter et al., 2020; Hartnady et al., 2020; Chew et al., 2021; Laurent et al., 2021; Yang et al., 2022). Wang et al. (2023), Fan et al. (2023), and Yang et al. (2022) used LA-ICP-MS to investigate textural and distribution of trace elements in various sulfide mineralisation. The technique has been used widely in the analysis of trace elements in carbonate hosted base metal sulfide deposits (Cook et al., 2009; George et al., 2015; Hu et al., 2021; Wei et al., 2021; Aldis et al., 2022; Zhang et al., 2022; Liu et al., 2023; Paradis et al., 2023). EPMA is a non-destructive technique with the capability of determining concentration of elements in solid materials at micron scale (Kearns and Wade, 2021). In ore deposit geology, EPMA has been widely used in mineral chemistry as well as elemental distribution in mineral phases (Demir et al., 2013; Sadati et al., 2016; Mishra et al., 2021; Ye et al., 2023).

Whole rock geochemistry is a fundamental concept that is used in geology to determine the geochemical properties of the natural solid materials (Göçmengil et al., 2022). The geochemical data is obtained using various techniques including Inductively Coupled Plasma-Mass Spectrometry (ICP-MS), Inductively Coupled Plasma Atomic Absorption Spectroscopy (ICP-AAS), X-Ray Florescence (XRF) and portable X-Ray Fluorescence (pXRF). ICP-MS is a well-established analytical technique with high precision that is used to determine the abundance of chemical elements in geological samples (Jenner et al., 1990). ICP-AAS is a multi-element analytical technique that is widely used in the field of

geochemistry for the quantification of element concentration in ores, rocks, and soils (Ward et al., 1969; Viets and O'Leary, 1992). XRF is widely used in geochemistry for the characterisation of major and trace elements of ores, soil, rocks and even tailings (Rollison, 2021). Various scholar has used the above-mentioned techniques to obtain geochemical dataset, that lead to the deducing of tectonic environment of the ore deposits (Hammerli et al., 2015; Duran et al., 2016; Conliffe et al., 2018; Cordeiro et al., 2018).

Portable X-Ray Fluorescence is a rapid, cost-effective technique that has been utilised in geochemical exploration over the past decade (Brand and Brand, 2014; Piercey and Devine, 2014). The instrument provides a data set that has high precision but low accuracy for certain elements, hence the technique is not widely used in large-scale mineral exploration projects (Brand and Brand, 2014; Zhou et al., 2023). The capabilities and limitation of the instrument application in geology are best described in Hall et al. (2014), Bourke and Ross (2016), Gallhofer and Lottermoser (2018), Lemière (2018), and Zhou et al. (2023).

Copper has two stable isotopes ^{63}Cu (69.17% relative abundance) and ^{64}Cu (30.83% relative abundance), and its isotopic ratio is used effectively as a tracer in various geological processes including mineral deposits (Shields, 1964; 1965; Cooke et al., 2014). The analytical techniques frequently employed in copper isotope analysis on diverse geological materials, such as ore, rock, water, and soils, include Multicollector Inductively Coupled Plasma Mass Spectrometers (MC-ICP-MS) and plasma source mass spectrometers (Zhang et al., 2020; Mathur and Zhao, 2023). Over years, researchers have utilized these approaches to trace the oxidation-redox cycle and mass transfer during mineralization, helping them to understand the genesis of the deposit (Graham et al., 2004;

Asael et al., 2007; 2009; Mathur, et al., 2012; Brzozowski et al., 2021; Lehmann, et al., 2022; Mathur and Zhao, 2023).

Zinc has five stable isotopes (^{64}Zn, ^{66}Zn, ^{67}Zn, ^{68}Zn, and ^{70}Zn), with relative abundance of 48.6%, 27.9%, 4.1%, 18.8% and 0.6% respectively, which are mainly used to decipher ore formation processes and to characterise ore deposits (Kelley et al., 2009; Bullen, 2014; Mason et al., 2015; Wilkinson et al., 2015; Moynier, 2018; Wilkinson, 2023). Additionally, Zn isotopic system has been utilized in mineral exploration of low-temperature sedimentary-hosted Zn sulfide deposits (Baumgartner et al., 2021). Similar to Cu isotopes, Zn isotopes are also measured using an MC-ICP-MS (Moynier, 2018).

4 Application of portable X-ray fluorescence for exploration of carbonate-hosted sulfide mineralisation, Otavi Mountain Land, Namibia

E. Shalimba[a]*, S. Lohmeier[b], and A. Wanke[a]

[a] Department of Geosciences, Southern Campus, Faculty of Agriculture, Engineering & Natural Sciences, University of Namibia, Keetmanshoop, 9000 Namibia,

[b]Mineral Resources, Clausthal University of Technology, Adolph-Roemer Str. 2A, 38678 Clausthal-Zellerfeld, Germany

* e-mail: eshalimba@unam.na/eshalimba@gmail.com.

Abstract

Otavi Mountain Land province forming up part of the Damara Orogenic Belt, consists of Neoproterozoic carbonate platform, which are well-known for their sedimentary-hosted polymetallic mineralized zones, including the Cu-Pb(-Ag) Kombat deposit. The ore mineralisation of the Kombat deposit occurs in a massively disseminated, veinlet-controlled, and brecciated mineralisation style and it comprises mainly of bornite, chalcopyrite, galena, covellite and chalcocite associated with quartz and calcite as gangue minerals. Mineralized zones are distinctly enriched in chalcophile elements, including Pb, Cu, As and Ag. For the analysis of such rocks, laboratory-based analytical methods including inductively coupled plasma mass spectrometry (ICP-MS) and atomic absorption spectroscopy (AAS), are well established, in contrast to onsite geochemical analytical methods. This study shows the applicability and limitations of portable X-ray fluorescence

(pXRF) in the geochemical exploration of sulfide (Ag, Cu, Fe, Mn, Pb, Zn) ores in carbonate matrix. By using additional ICP-MS/AAS data and certified reference materials, the applicability of such portable tools can be assessed for Kombat-type ores, resulting in pXRF data of excellent or very good precision for elements like Cu, Fe, Mn, Pb, and Zn (RSD ≤10%), while other elements (Ag, Sr) show poor precision. The trace element concentrations obtained by pXRF are comparable to ICP-MS results yielding a good correlation (R^2 ≥0.,85) and acceptable accuracy and precision. Portable XRF is identified as a low-cost tool that can be used successfully in the geochemical exploration for a list of elements in carbonate-hosted sulfide ores.

Keywords: Portable XRF, sulfide mineralisation, carbonate host rock, Otavi Mountain Land, Namibia

4.1 Introduction

Neoproterozoic carbonate rocks in are known to host a variety of base metal deposits that are important for the world supply of metals such as lead and zinc (Leach et al., 2010; Haest and Muchez, 2011; Xiong et al., 2019). The Otavi Mountain Land (OML) is a metallurgical province well known for its sediment-hosted ore deposits rich in base metal sufides and oxides, which are concentrated in the upper part of the Neoproterozoic Carbonate Platform of the Damara Orogenic Belt (DOB) (Miller, 1983; Melcher et al., 2006; Boni et al., 2007; Kamona and Günzel, 2007). Most of the base metal deposits including Tsumeb, Kombat, Berg Aukas, Abenab West and Khusib Spring are hosted in the sedimentary units of the Otavi Group (Melcher et al., 2006; Kamona and Günzel, 2007; Fig. 4-1-1). This chapter focuses on samples from the Kombat deposit, which is a stratabound, syntectonic Cu-Pb (Ag) sulfide deposit hosted in the dolomite of the Hüttenberg Formation (Deane, 1995). The mineralisation is mainly related to the contact between dolomite and phyllite, and its genesis is associated with a magmatic hydrothermal event (Kamona and Günzel, 2007).

Exploration and mining in the OML dates back to the 1960s. One of the greatest challenges in exploration and mining are operational costs, and the costs of sampling and sample analyses can be considerable. This chapter aims to investigate whether a low-cost technique such as portable X-ray fluorescence (pXRF) can be applied in exploration of carbonate-hosted sulphide base metal deposits. Over the past years, pXRF has been extensively and successfully used in the exploration of base metals, rare earth elements (REEs) and precious metals linked to magmatic and sedimentary rocks (Simandl et al.,

2014a; Gazley et al., 2014a; Hall et al., 2014; Quye-Sawyer et al., 2015). However, there is a distinct lack in knowledge of the applicability of this tool on low-grade hosted in carbonate rocks. Application of pXRF in geochemical exploration is recognised as a viable method which can be employed to obtain a reliable dataset during field mapping, and which assists in sample selection (Young et al., 2016). This instrument has two advantages: a) it allows direct, on-site measurements of selected elements and thus offers a dataset, that provides valuable insights in mining and exploration, leading to rapid field decisions and, b) it is cost-effective (Andrew and Barker, 2017; Lemière, 2018). However, in order to optimise results obtained by pXRF, there is a need to recalibrate the instrument using certified reference materials (CRMs) with the same matrix as the samples of interest (Simandl et al., 2014b), as it is common practice for conventional laboratory based XRF devices. Portable XRF results, when compared to known samples such as CRMs, yield a moderate to high precision but there is usually a high variation when it comes to accuracy (Piercy and Devine, 2014). Hall et al. (2014) showed that pXRF performance is different for various elements. Elements such as Cu and Pb are recorded with a very good performance, whereas performance is moderate for Cr and U, but only poor for Ag and V, and extremely poor for elements like W and Au. Limitations and capabilities of a pXRF device, as well as a quality control of the dataset obtained by pXRF are discussed in detail in Arne and Jeffress (2014), Brand and Brand (2014), Fisher et al. (2014), and Hall et al. (2014).

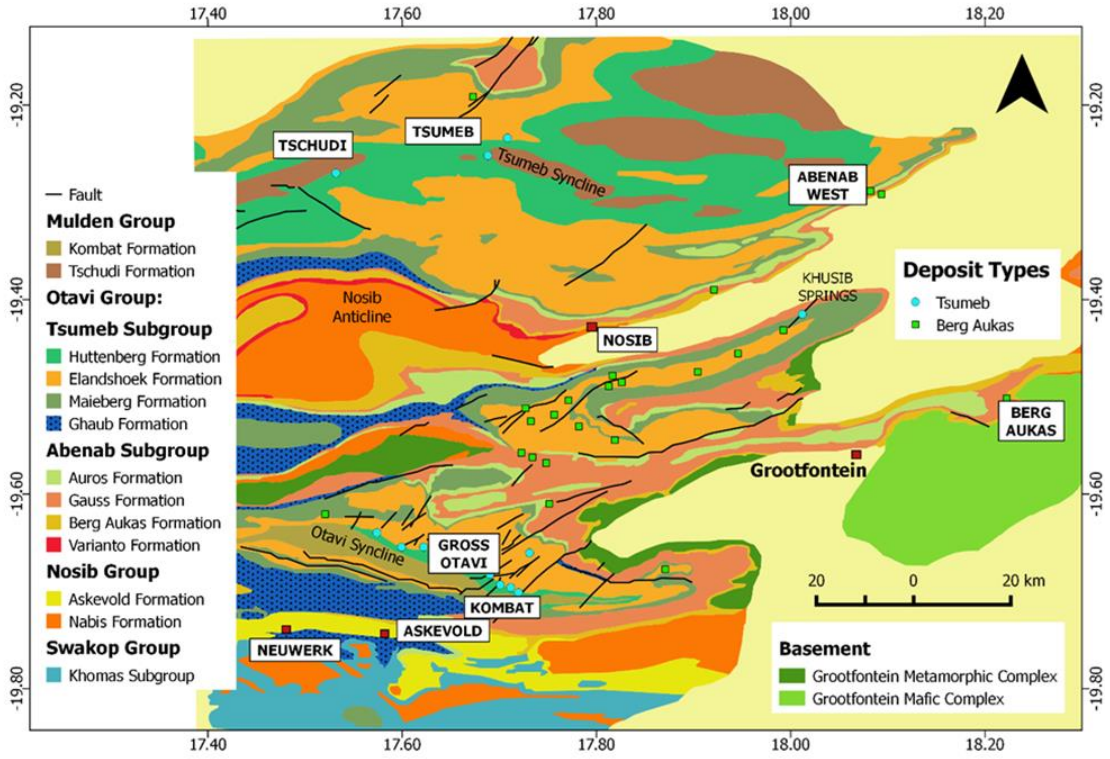

Fig. 4.1-1 Simplified regional geological map of the OML, with outlined deposits (modified after Chetty and Frimmel, 2000; Kamona and Günzel, 2007).

This chapter integrates mineralogical, petrological and bulk rock trace element geochemical analyses of the carbonate-hosted sulphide mineralisation of the Kombat deposit. The application of pXRF analysis combined with inductively coupled plasma mass spectrometry (ICP-MS) plus atomic absorption spectroscopy (AAS) for the geochemical exploration of sulfide mineralisations of Kombat deposit hosted in carbonate rocks are presented in this chapter. The results from the pXRF device and from the laboratory-based instruments are compared in order to assess the applicability and the limitations of the pXRF device for analysis of such rocks. Precision and accuracy of the pXRF instrument is assessed using pXRF results of CRMs.

4.2 Geological setting

The Neoproterozoic Damara Orogen forms part of the west Gondwana suture, which resulted from the collision of the South American Río de la Plata, Congo, and Kalahari Cratons in Southern Africa (Miller, 1983; Gray et al., 2008). In Namibia, this orogen is sub-divided into three-fold belts: the NNW-trending northern coastal Kaoko Belt, the ENE-trending inland branch DOB and the S-trending southern coastal Gariep Belt (Martin and Porada, 1977; Miller, 1983, 2008). The Damara Orogenic Belt (DOB) is a 350 km wide belt (Fig. 4-2), which formed during continuous stages of crustal thickening, rifting, spreading, subduction of continental arc, upper lithospheric thinning, and continental collision between the Kalahari and Congo Cratons, ending with the closure of the Khomas Sea (Porada, 1979; Miller, 1983; Gray et al., 2008; Goscombe et al., 2018). The DOB consists of basement inliers of Archean-Proterozoic age, early Damaran rift type sedimentary and volcanic units of the Nosib Group, Neoproterozoic deep and shallow carbonate rocks of the Otavi and Swakop Groups, and foreland basin deposits of the Mulden and Nama Groups (Miller, 1983; Gray et al., 2008; Miller, 2008b). Additionally, the belt is further subdivided into various tectonostratigraphic zones such as the here relevant Northern Zone and the Northern Platform (Fig. 4-2) that are defined by age, structure and metamorphic grade (Miller, 2008b).

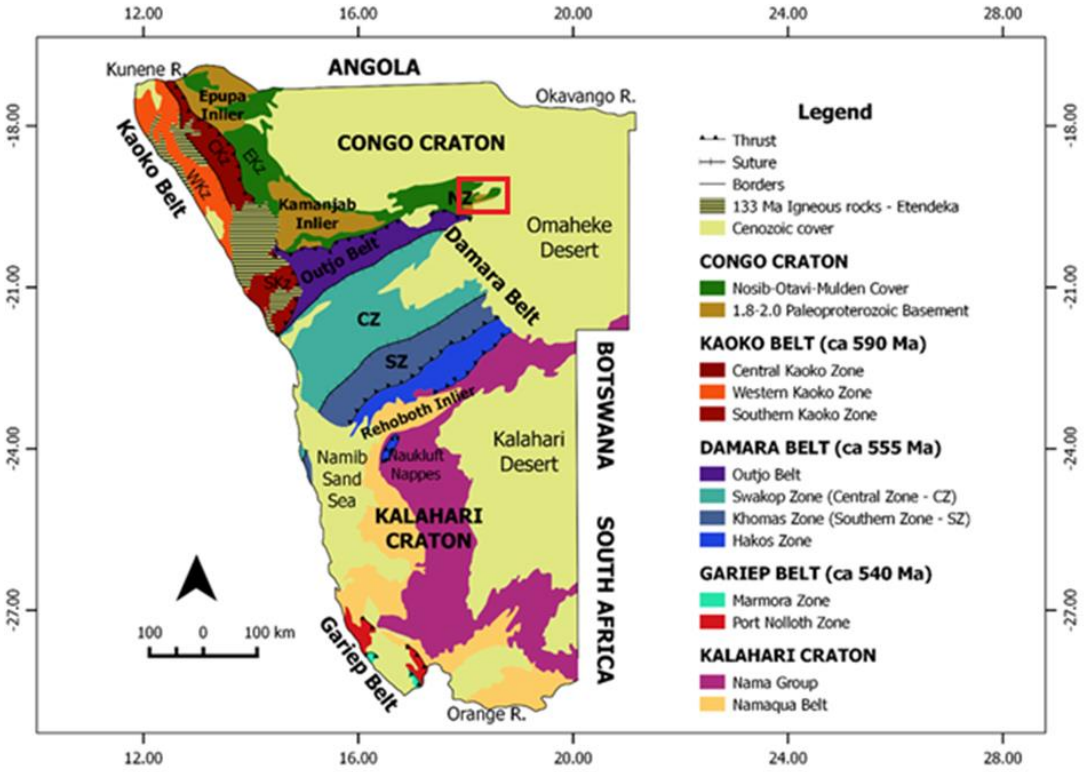

Fig. 4.2-1 DOB geological map of Namibia, showing the various tectonostratigraphic units of the Damara Orogen. The study area, the OML, is shown by the red box (modified after Hoffman, 2013).

Following the initial rifting during the sediments of the Nosib Group were deposited, the Otavi Group was deposited during the subsequent opening of the Khomas Sea (Miller, 2008b). In the Northern and Northern Platform tectonostratigraphic zones, the Otavi Group is dominated by shallow water platform successions of carbonate units that largely rest on the southern Congo Craton (Chetty and Frimmel, 2000; Hoffman, 2011). The Otavi Group carbonates is the dominant unit of the base-metal rich OML province, which covers 10,000 km^2 and is situated at the transition between the Northern Zone and the Northern Platform of the DOB where portions of the Neoproterozoic Carbonate Platform are well exposed (Pirajno and Joubert, 1993; Kamona and Günzel, 2007). This province is

associated with three Damara deformation episodes: during the first tectonic event D1 the southern part of the OML was folded and faulted (Miller, 1983). The ultimate collision of the Congo and Kalahari Cratons led to the D2 and D3 tectonic events, which are attributed to post-Damara deformation processes (Kröner, 1982; Miller, 1983; Goscombe et al., 2004; Schneider et al., 2008).

4.3 Local Geological setting

The OML unconformably overlies the Paleoproterozoic basement rocks of the Grootfontein Metamorphic Complex which is mainly composed of dolomites and calc-silicate rocks, as well as the Grootfontein Mafic Bodies which are mainly composed of anorthosites and gabbros (Miller, 1983; Kamona and Günzel, 2007; Schneider et al., 2008). This carbonate platform in the OML is known for its various clusters of epigenetic mineralisation related to two major mineralisation stages: the Tsumeb-type mineralization, which is characterised by distinct sulfide ores enriched in Ag, As, Cd, Cu, Ga, Ge, Pb, and Zn, and the Berg Aukas-type mineralization which consists of ore bodies containing Pb, Zn and V (Pirajno and Joubert, 1993; Cairncross, 1997). The Berg Aukas-type deposits are confined to the lower Abenab Subgroup (Fig. 4.3-1). They were formed during the first mineralising event that is associated with compaction and dewatering of sediments of a northern rift (Pirajno and Joubert, 1993; Cairncross, 2021). Tsumeb type deposits are mainly found in the Upper Tsumeb Subgroup and were formed as a result of a later metamorphic episode associated with devolatilization reactions during regional prograde metamorphism of the sediments in the northern rift (Pirajno and Joubert, 1993). However, despite these author's conclusions, there is still debate and controversy

surrounding the genesis of the mineralizations in the OML, and this can be attributed to the complexity of the overlapping structural features in the area.

The location of the Kombat deposit within the stratigraphy of the OML is shown on Figs. 4.1-1 and 4.3-1. This deposit is located on the northern limb of the Otavi syncline and is positioned along the contact between the phyllite of the Mulden Group and the underlying dolostones of the Otavi Group (Deane, 1995; Kamona and Günzel, 2007; Minz, 2008). The uppermost part of the Otavi Group consists of dolomite, chert and breccia of the Hüttenberg Formation, while, in the area of Kombat, the lowermost part of the Mulden Group consists of phyllite, slate, and sandstones of the Kombat Formation (Kamona and Günzel, 2007). The deposit is characterized by base metal sulfides mineralisation in fracture veins and galena-rich alteration breccias that are spatially associated with a replacement Fe-Mn oxide/silicate mineralisation (Pirajno and Joubert, 1993).

There are at least seven distinct mineralized zones identified in the Kombat deposit, which are described either as Cu-Pb-Ag Mississippi valley type (MVT) mineralization or as stratiform, syn-sedimentary Fe-Mn-type mineralizations (Deane, 1995; Nghoongoloka et al., 2020). Base metal sulfide mineralisation styles include massive and semi-massive ores to mineralized vein fractures, which are mostly hosted in the dolomites of the Hüttenberg Formation. Major ore minerals include chalcopyrite, bornite, galena, chalcocite, pyrite, and tennantite, which are associated with sedimentary breccia, calcitized dolostone and lenses of feldspathic sandstone (Deane, 1995). Minor ore minerals include malachite, sphalerite, with calcite, dolomite, and quartz as gangue. Concentration of base metals in the deposit is attributed to the conversion of anhydrite in the dolostone to calcite via the release of SO_4 to brines by incorporation of CO_2 and CH_4 from shale of the Mulden Group

(Trigon Metals, 2017). Additionally, isotope data from Deane (1995) are alluding to a magmatic and metamorphic source for the mineralising fluids. Structurally, genesis of this deposit is related to D2, which is coeval to the sedimentation of the Mulden Group (Deane, 1995). Alteration is widespread to locally pervasive and comprises a heterogeneous assemblage of calcite-quartz-sericite-pyrite-chalcopyrite and minor chlorite-hematite-pyrophyllite-kaolinite (Deane, 1995; Minz, 2008).

Era	SuperGroup	Group	Sub-Group	Formation	Lithologies	Deposits
Neoproterozoic	Damara	Mulden		Owambo	Undefined	
				Kombat	Phyllite, Shale, Sandtone, Siltstone	
				Tschudi	Shale, Greywacke, Conglomerate, Slate	
		Unconformity				
		Otavi	Tsumbeb	Hüttenberg	Dolomite, Chert, Phyllite, Shale, Stromatolite, Breccia, Oolite	Tschudi (Cu-(Ag)), Kombat (Cu-Pb-(Zn) , Tsumeb (Pb-Cu-Zn-(Ge)
				Elandshoek	Dolomite and Chert	
				Maiberg	Dolomite, Limestone	Abenab (V), Khusib springs (Cu-Pb-Zn)
				Ghaub	Tillite	
			Abenab	Auros	Dolomite, Stromatolite	Abenab West (Pb-Zn-V)
				Gauss	Dolomite, Breccia, Chert	Berg Aukas (Zn-Pb-V)
				Berg Aukas	Dolomite, Limestone, Chert	Berg Aukas (Zn-Pb-V)
				Chuos	Tillite	
		Nosib		Askevold	Tuff, Quartzite	Nosib (Cu), Askevold Cu
				Nabis	Quartzite, Sandstone, Conglomerate	
Paleoproterozoic	Grootfontein Metamorphic Complex				Granite, Gneiss, Gabbro	

Fig. 4.3-1 Stratigraphic column of the OML showing the main base-metal ore deposits in that region (modified after Kamona and Günzel, 2007).

4.4 Material and Methods

4.4.1 Sampling and petrography

Samples were taken from outcropping sites and heap dumps that consists of materials from underground mining activities, stored at the mining site. These samples are representative of the primary sulfide mineralization of the deposit. The samples were collected for the purpose of a geochemical, petrographic, and mineralogical study. Polished sections were prepared from the samples at the Geological Survey of Namibia (GSN). The sections were examined under a Leica DM 4500p polarization microscope under reflected light for mineralogic and textural properties at the Institute of Applied Mineralogy and Economic Geology at RWTH Aachen University (RWTH; Germany).

4.4.2 pXRF analysis

Rock samples were dried, crushed, and pulverised to analytical fineness, and subsequently homogenised for whole-rock geochemical analysis, using the facilities at the GSN. Sample cups were conventionally prepared at RWTH for pXRF analysis. All cups are covered with a 4.0 μm thick polypropylene film for comparability of results. Portable XRF analysis was performed at Clausthal University of Technology (Germany) using a Niton™ XL3t RFA analyser equipped with a silver anode (6 to 50 kV, 0 to max 200 μA). Both major and trace elements were analysed using the factory standard calibration mining mode with beam count time set to 100 s. For precision and accuracy of the instrument, different OREAS CRMs (OREAS 623, 134b, 932) with varying Zn and Cu contents, reasonably covering the concentration range of the sample suite, were analysed. CRMs were analysed at the beginning and after every fifth samples measurement. Certified

values of the CRMs used in this study, were compared to the obtained pXRF values for these materials, whereby standard deviations, relative standard deviations, and percentage differences were calculated and, in the following, used to evaluate the precision and the accuracy of the instrument. A full spectrum of major and trace element concentrations determined by pXRF is provided in the electronic supplementary material (Appendix 4-1a and b).

4.4.3 ICP-MS/ AAS Analysis

Standard ICP-MS/AAS analyses after near total 4 acid digestion were adapted from the same samples. Pulps of all samples were analysed for Ag (0.005), As (1.0), Ce (0.05), Cd (0.01), Co (0.1), Cr (1.0), Cu (0.5), Fe (100), Ga (0.1), In (0.02), La (0.1), Mn (5), Nb (0.1), Pb (2), and Zn (0.5) [lower detection limits, in ppm, are given in brackets] via ICP-MS at the conventional run SGS Bulgaria LTD laboratory in Serbia. Analyses of added internal standards verify ICP-MS results of good quality. Samples with elemental concentrations above the upper detection limit were re-analysed using AAS at the SGS Bulgaria LTD laboratory. All ICP-MS and AAS results of major and trace elements are shown in the electronic supplementary material (Appendix 4-2).

4.5 Results

4.5.1 Ore mineralogy

The mineralisation is hosted in a medium to coarse-grained dolomitic unit and is largely defined by the ore paragenesis of bornite, chalcopyrite, galena, covellite, and chalcocite, mainly associated with quartz and calcite (Fig. 4.5-1). Mineralisation is largely textural-

controlled, but quite variable leading to an overlap of zones of massive, disseminated, and veinlet-controlled ore mineralization style as well as brecciated mineralized zones. Petrographic ore textures include the following: skeletal (Fig. 4.5-1 a), replacement (Fig. 4.5-1 a, b, d & f), subhedral to anhedral (Fig. 4.5-1 c &d), enveloping rims (Fig. 4.5-1 e). Anhedral, brown coloured bornite is the dominant ore mineral. Bornite is overgrown by thin rims of chalcocite that are commonly associated with galena and pyrite and by fine patches of covellite (Fig. 4.5-1c, e & f). Frequently, bornite is replaced by coarse-grained chalcopyrite that forms massive disseminations (Fig. 4.5-1 f). Pyrite is dominantly medium to coarse grained, exhibiting subhedral to anhedral form and is mostly associated with chalcopyrite and galena and occasionally enclosed within anhedral galena grains (Fig. 4.5-1 b & d). Covellite is minor and probably of supergene origin. It forms at the outer rims of bornite and is mostly within the bornite-chalcopyrite occurrence. Covellite is irregular, fine-grained, showing a patchy occurrence within bornite grains, probably replacing chalcopyrite (Fig. 4.5-1f). Chalcocite is mostly associated with bornite and occurs irregularly disseminated in the calcite matrix.

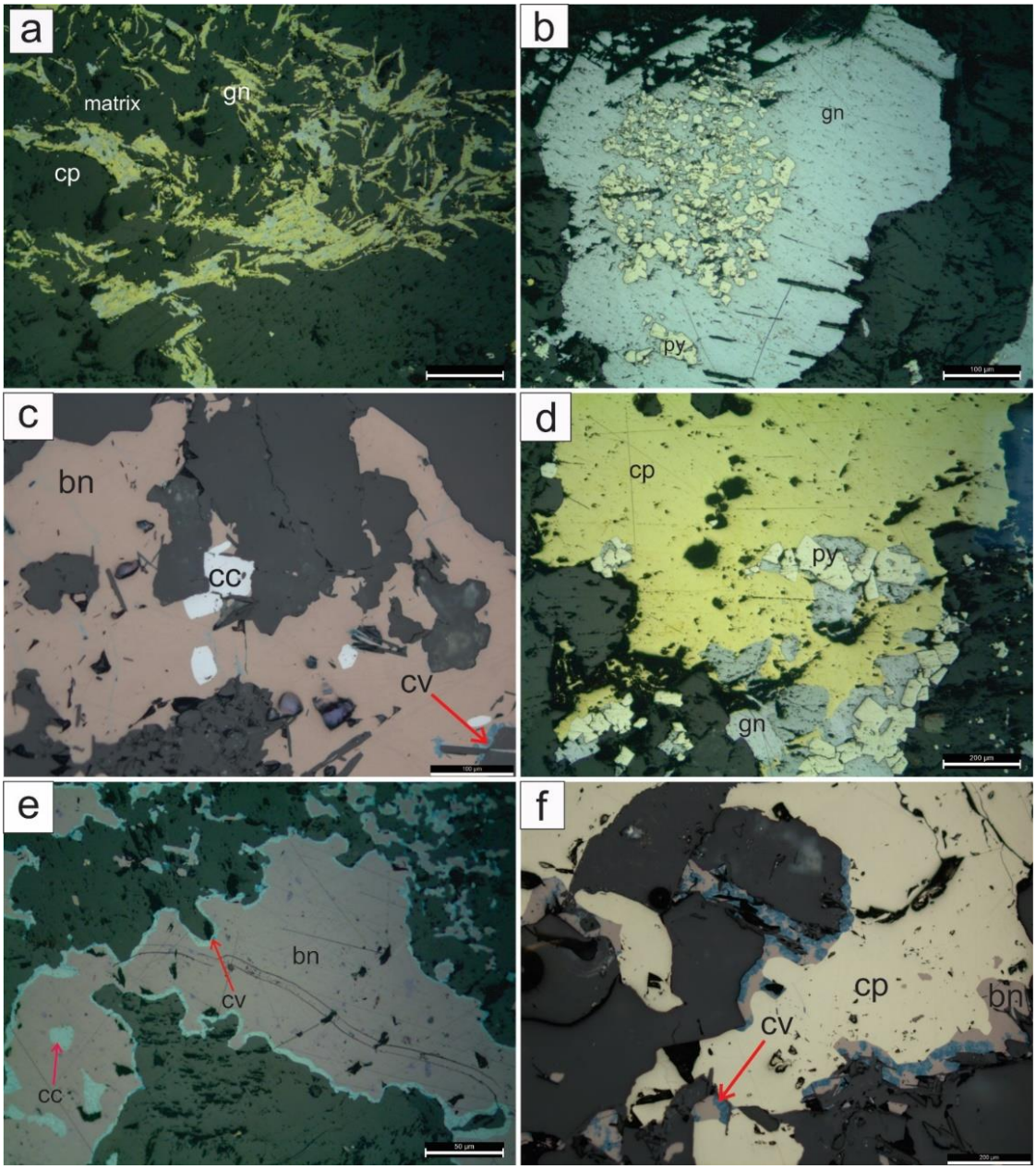

Fig. 4.5-1 Reflected light microphotographs showing microtextural features of the sufide ores at Kombat. a) Emulsion texture of massive chalcopyrite and galena embedded in the dolomitic matrix. b) Disseminated pyrite grains embedded in galena. c) Coarse bornite grains with rims of covellite and minor chalcocite. d) Coarse-grained chalcopyrite with subhedral grains of pyrite embedded within galena grains. e) Replacement of galena by chalcopyrite, with subhedral to euhedral form pyrite. f) Bornite crystals largely replaced by chalcopyrite. Abbreviation: bn-bornite; cp-chalcopyrite, cv-covellite, cc-chalcocite, gn-galena, py-pyrite.

4.5.2 ICP-MS/ASS vs pXRF

ICP-MS analyses point out quite varying element contents within the sample suite. Non-metal contents such as S and P vary between ≤0.01 and ≤2.5 wt.%. The concentrations of metalloids such as As and Sb vary between ≤0.4 and ≤1,100 ppm, of transitional metals such as Cu, Zn, Ag, Cd, Cr, Co, Nb, and Mn vary between ≤0.4 and ≥10,000 ppm, of post-transitional metals such as Pb and Ga vary between ≤0.5 and ≥10,000 ppm and of rare earth elements such as Ce and La vary between ≤1 and ≤2.5 ppm. The concentrations of Ag, Cu, Fe, Pb and Zn analysed by pXRF are all within acceptable range in comparison to ICP-MS data. There is a high positive correlation between pXRF and ICP-MS values for the abovementioned elements as depicted by the R^2 values (coefficient of correlation; R^2 ≥0.90) in Table 4.5-1. The non-metal elements have a much lower correlation, ranging between R^2 = 0.6-0.8. The analytical concentrations of Cr, Co and Nb were largely below the lower analytical detection limits of the pXRF analyser.

Table 4.5-1 Correlation coefficients applicable to pXRF data

Element	Mean Value (wt%)	Error	Error (%)	R^2
Ag	0.003	0.001	33	0.99
Cu	0.60	0.008	1.40	0.97
Fe	4.08	0.042	1.03	0.99
Pb	1.79	0.020	1.80	0.96
Zn	1.44	0.023	1.50	0.96

Element correlations were studied in all samples using ICP-MS/AAS obtained data (Table 4.5-2). A relatively strong correlation was observed between a number of elements such as; As with Cd and Zn ($R_{As/Cd}$=0.89; $R_{As/Zn}$= 0.98); Cd and Zn ($R_{Cd/Zn}$= 0.86); Ce with Ga, Tb and Yb ($R_{Ce/Ga}$=0.82, $R_{Ce/ Tb}$=0.86; $R_{Ce/Y}$=0.93); Cs with K and Rb ($R_{Cs/K}$=0.91; $R_{Cs/Rb}$=0.91); Fe with Sr, U and W ($R_{Fe/Sr}$=0.96; $R_{Fe/U}$=0.89; $R_{Fe/W}$=0.99); Ga with Tb, Y and Yb ($R_{Ga/Tb}$=0.88; $R_{Ga/Tb}$=0.87; $R_{Ga/Yb}$=0.86); La with P and Y ($R_{La/P}$=0.82; $R_{La/Y}$=0.86); Lu with Sr, Tb, Y and Yb ($R_{Lu/Sr}$=0.86; $R_{Lu/Tb}$=0.94; $R_{Lu/Y}$=0.87; $R_{Lu/Yb}$=0.98); Sr with U and W ($R_{Sr/U}$=0.91; $R_{Sr/W}$=0.97); Tb with Y and Yb ($R_{Tb/Y}$=0.95; $R_{Tb/Yb}$=0.95); U and W ($R_{U/W}$=0.91) and Y and Yb ($R_{Y/Yb}$=0.88).

Table 4.5-2 Correlation coefficient between various elements of the Kombat sulfide mineralization, all analysed by ICP-MS-AAS

	Ag	As	Cd	Ce	Co	Cr	Cs	Cu	Fe	Ga	K	La	Li	Lu	Mg	Mn	Mo	Ni	P	Pb	Rb	Sb	Sr	Tb	Tl	U	V	W	Y	Yb	Zn
Ag	1																														
As	-0.08	1																													
Cd	0.07	0.89	1																												
Ce	-0.30	-0.04	0.02	1																											
Co	-0.16	0.45	0.50	0.35	1																										
Cr	-0.30	0.21	0.12	0.08	0.06	1																									
Cs	-0.15	0.09	0.13	0.51	0.13	0.11	1																								
Cu	0.76	0.10	0.16	-0.32	-0.05	-0.20	-0.29	1																							
Fe	-0.09	-0.03	0.37	0.16	-0.13	0.02	-0.11	-0.06	1																						
Ga	-0.31	-0.08	0.01	0.82	0.31	-0.09	0.40	-0.42	0.41	1																					
K	-0.22	-0.13	-0.01	0.63	0.15	-0.02	0.91	-0.35	-0.07	0.61	1																				
La	-0.23	-0.25	-0.27	0.81	-0.07	0.17	0.28	-0.34	0.08	0.64	0.41	1																			
Li	-0.23	-0.05	0.02	0.29	-0.02	0.10	0.79	-0.30	-0.20	0.19	0.73	0.10	1																		
Lu	-0.28	-0.11	0.01	0.75	0.12	-0.03	0.27	-0.29	0.71	0.84	0.40	0.60	0.05	1																	
Mg	-0.12	-0.24	-0.26	-0.28	-0.22	-0.19	0.14	-0.28	-0.27	-0.25	0.14	-0.21	0.15	-0.38	1																
Mn	0.19	0.19	0.19	-0.20	-0.13	-0.17	-0.08	0.22	-0.19	-0.29	-0.15	-0.23	0.13	-0.23	-0.18	1															
Mo	-0.17	0.06	0.13	0.56	0.25	0.13	-0.13	-0.14	0.71	0.63	-0.05	0.43	-0.29	0.79	-0.38	-0.18	1														
Ni	-0.09	-0.15	-0.28	0.08	0.02	-0.32	0.15	-0.28	-0.77	-0.02	0.22	0.19	0.20	-0.3	0.14	0.26	-0.51	1													
P	-0.21	-0.27	-0.22	0.74	-0.08	0.00	0.67	-0.40	-0.09	0.61	0.78	0.82	0.49	0.44	0.11	-0.16	0.06	0.33	1												
Pb	-0.09	0.17	0.27	0.13	0.78	0.03	0.09	-0.12	-0.05	0.32	0.20	-0.12	-0.04	0.08	-0.12	-0.34	0.10	-0.04	-0.07	1											
Rb	-0.20	-0.01	0.09	0.59	0.25	0.04	0.91	-0.26	-0.01	0.57	0.97	0.29	0.73	0.37	0.06	-0.08	-0.02	0.08	0.67	0.26	1										
Sb	-0.12	0.64	0.55	-0.04	0.35	0.23	-0.13	0.46	0.07	-0.16	-0.2	-0.23	-0.14	-0.06	-0.31	0.07	0.08	-0.38	-0.31	0.08	-0.04	1									
Sr	-0.11	-0.11	0.03	0.30	-0.16	-0.05	-0.04	-0.19	0.96	0.58	0.05	0.23	-0.15	0.81	-0.28	-0.19	0.75	-0.60	0.06	-0.06	0.07	-0.11	1								
Tb	-0.27	-0.08	0.02	0.86	0.16	0.04	0.36	-0.34	0.54	0.88	0.49	0.75	0.08	0.94	-0.39	-0.3	0.70	-0.18	0.61	0.15	0.44	-0.13	0.67	1							
Tl	-0.15	0.32	0.42	0.62	0.80	0.01	0.34	-0.20	-0.14	0.64	0.47	0.31	0.15	0.32	-0.18	-0.11	0.36	0.18	0.33	0.67	0.50	0.13	-0.04	0.42	1						
U	-0.13	-0.11	0.10	0.26	0.01	-0.03	0.03	-0.22	0.89	0.60	0.14	0.17	-0.15	0.76	-0.25	-0.26	0.64	-0.58	0.08	0.26	0.17	-0.13	0.91	0.67	0.08	1					
V	-0.16	0.20	0.42	0.37	0.60	0.09	0.08	-0.16	0.66	0.56	0.13	0.04	-0.11	0.64	-0.30	-0.18	0.71	-0.55	-0.06	0.59	0.24	0.13	0.63	0.56	0.48	0.77	1				
W	-0.09	-0.10	0.19	0.16	-0.21	0.01	-0.08	-0.15	0.99	0.43	-0.03	0.12	-0.18	0.71	-0.21	-0.19	0.68	-0.70	-0.03	-0.08	0.00	-0.08	0.97	0.57	-0.17	0.91	0.62	1			
Y	-0.32	-0.13	-0.07	0.93	0.18	0.02	0.35	-0.36	0.34	0.87	0.50	0.86	0.12	0.87	-0.35	-0.29	0.66	0.02	0.69	0.07	0.42	-0.13	0.50	0.95	0.48	0.45	0.39	0.36	1		
Yb	-0.31	-0.13	-0.05	0.77	0.13	-0.05	0.29	-0.31	0.69	0.86	0.43	0.60	0.08	0.98	-0.34	-0.3	0.78	-0.32	0.46	0.11	0.41	-0.07	0.79	0.95	0.34	0.76	0.63	0.70	0.88	1	
Zn	-0.09	0.98	0.86	-0.10	0.38	0.21	0.05	0.20	-0.05	-0.15	-0.16	-0.29	-0.05	-0.16	-0.23	0.21	0.00	-0.17	-0.3	0.10	-0.03	0.74	-0.14	-0.14	0.24	-0.15	0.12	-0.13	-0.19	-0.18	1

4.5.3 Precision and accuracy

Assessment of sample precision and instrument precision was done according to the studies of Le Vaillant et al. (2014), Piercy and Devine (2014), and Simandl et al. (2014a). For determination of sample precision, pXRF and ICP-MS/AAS results of four samples from the OML (KC002: brecciated, sulphide-mineralised zone; KH002: chalcopyrite-rich dolomite; KEN004: coarse grained dolomite, rich in galena; and KEN002: massive, disseminated chalcopyrite and bornite), were examined. The instrument's precision was determined by analysing matrix-matched CRMs (OREAS 932, 134b, 623), with a range of concentration of elements matching the elemental concentration range of the samples. The instrument's precision of selected elements is illustrated graphically (Fig. 4.5-2) using the relative standard deviation (RSD) obtained from pXRF results of samples combined with the certified values of the CRMs. The RSD was calculated using equation 1; the accuracy was derived from the percentage difference (%diff) which was obtained using equation 2.

$$\%\mathrm{RSD} = \frac{\mathrm{SD}}{\bar{x}(\mathrm{pXRF})} * 100\% \qquad \text{[equation 1]}$$

$$\%\mathrm{d} = \frac{\bar{x}(\mathrm{pXRF}) - x(\mathrm{CV})}{x(\mathrm{CV})} * 100\% \qquad \text{[equation 2]}$$

Whereby SD is the standard deviation and $\bar{x}_{(pXRF)}$ is the mean of the respective pXRF value. The percentage difference (%diff) represents the deviation of the pXRF analysed value of a selected element ($\bar{x}_{(pXRF)}$) of a CRM from the respective certified value of the CRM (x(CV)).

Table 4.5-3 Assessment summary table of sample precision and accuracy. The table summarizes the relative standard deviations (RSD), mean pXRF values ($\bar{x}_{(pXRF)}$), the standard certified values (CRV), and the percentage differences (%diff) of the samples KEN002, KEN004, KC002 and KH002.

KEN002					
	$\bar{x}_{(pXRF)}$	CRV	SD	RSD	%diff
Ag	0.001	0.001	0.001	91.287	186
Ba	0.015	0.001	0.002	14.142	1775
Cu	0.347	0.544	0.002	0.676	-36
Fe	0.627	0.890	0.006	1.013	-30
Mn	0.565	0.618	0.009	1.530	-8.55
Pb	0.725	1.150	0.004	0.572	-37
Sr	0.016	0.003	0.001	2.830	5.33
S	0.389	2.100	0.010	2.529	-81
Zn	0.007	0.006	0.001	6.211	19
KEN 004					
Ag	186	0.001	0.001	0.001	39.123
Ba	1775	0.029	0.001	0.003	9.118
Cu	-36	2.296	2.150	0.020	0.886
Fe	-30	3.501	3.930	0.006	0.177
Mn	-8.55	0.826	0.784	0.012	1.469
Pb	-37	1.626	1.450	0.009	0.573
Sr	5.33	0.020	0.018	0.005	2.259
S	-81	2.138	4.300	0.053	2.469
Zn	19	0.046	0.038	0.002	3.606
KC002					
Ag	0.001	0.001	0.001	56	31
Ba	0.063	0.051	0.002	2.848	22
Cu	0.652	0.737	0.004	0.546	-11
Fe	0.280	0.260	0.004	1.530	7.54
Mn	0.417	0.458	0.005	1.181	-8.86
Pb	0.066	0.095	0.001	1.738	-31
Sr	0.011	0.011	0.000	0.0	3.77
S	0.072	1.300	0.002	2.095	-94
Zn	0.005	0.002	0.001	24	113
KH002					
Ag	0.001	0.001	0.001	37	97
Ba	0.009	0.002	0.002	19	462
Cu	4.662	6.910	0.028	0.600	-32
Fe	4.893	5.270	0.013	0.271	-7.15
Mn	0.523	0.488	0.006	1.107	7.19
Pb	0.003	0.002	0.001	21	53
Sr	0.014	0.013	0.001	3.149	5.97
S	2.445	3.500	0.052	2.122	-30
Zn	0.046	0.038	0.002	4.734	22

A summary of the statistical data for CRMs, including averages, standards deviations as well as relative standard deviations and percentage differences are presented in Appendix 4-3.

Using the classification criteria adopted from Piercey and Devine (2014), the instrument's precision ranges from excellent to very good for Cu, Zn, and Pb with $0.13 \leq \%RSD \leq 7.4$ (Fig. 4.5-2). Similarly, the sample results reveal that Cu, Zn, and Pb show an excellent to very good precision with the exception of one Pb value which is considered as an outlier (sample KH002; RSD ≥10%; Table 4.5-3). Accuracy is deduced from the %diff, noting that this is representative of the systematic error for each given element. Accuracy for all elements with %diff value of <10% are considered as excellent, and a value between 10% and 20% as good. All data within these ranges can be used for interpretation, while %diff values of >20% are considered to be too poor so that they cannot be used for interpretation according to Hughes and Barker, (2018). Certified reference materials yielded good accuracy for Cu, Zn, and Pb (%d ≤15), however, there is at the samte time a large variation in sample accuracy for Cu, Zn and Pb ($6 \leq \%d \geq 100$).

Iron and Mn values are of excellent to very good precision ($0.1 \leq \%RSD \leq 3.6$) for both samples and CRMs. There is a slight variation in accuracy for Fe values in both CRMs and samples, ranging from very good to poor. Manganese, in contrary to Fe, yields a better accuracy in both samples and CRMs. Both Ag and Ba have low precision and accuracy in CRMs and samples. Certified reference materials with an average concentration of Ag of 0.02 wt.% have a fairly good precision with ≤5.5%, but a relatively poor accuracy of only ≤25%.

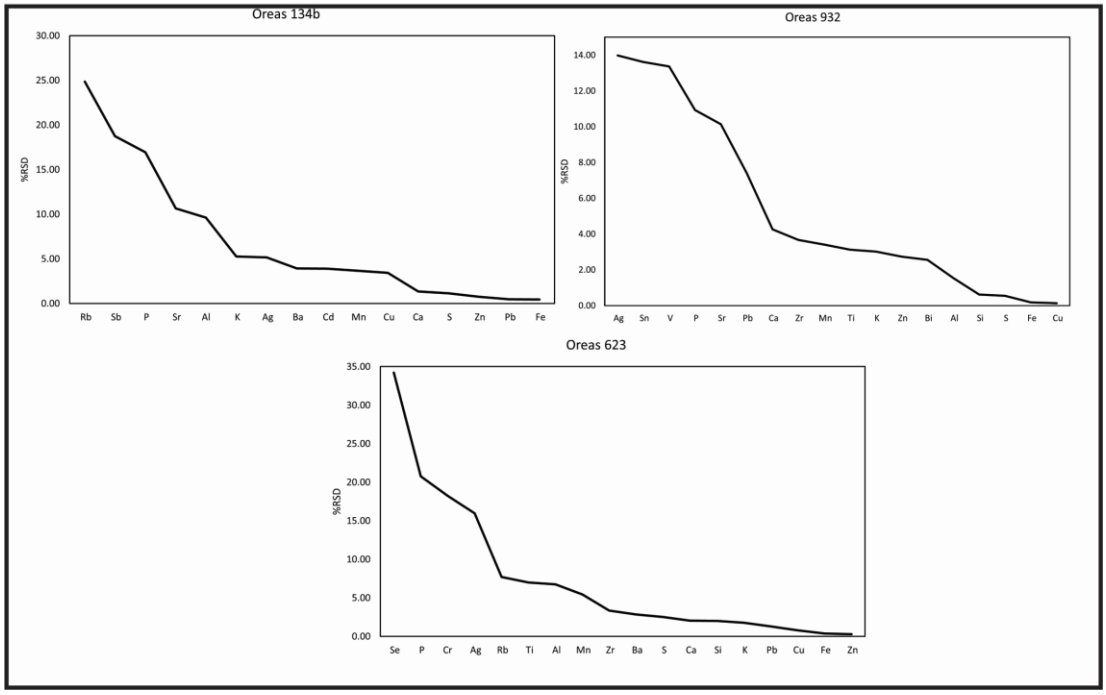

Fig. 4.5-2 . Line graphs showing the relative standard deviations (%RSD) of pXRF results and certified values of selected elements of the OREAS 37, 134b, and 932 CRMs.

4.6 Discussion

The Kombat deposit can be described as a discordant structurally controlled sulphide mineralization that forms part of the complex mineralogically, and it is classified as cupriferous Tsumeb-type deposit, as discussed in Frimmel et al. (1996), Melcher (2003), and Kamona and Günzel (2007). Chalcopyrite, bornite, pyrite, and galena are the most abundant sulfide minerals, with minor occurrence of covellite and chalcocite (Fig. 4.5-1). Chalcopyrite, bornite, pyrite, and galena are mainly fine to medium grained and subhedral. The minor minerals are either presented as intergrowths or rims surrounding the primary ore minerals of the deposit (Fig. 4.5-1).

Out of all the trace elements analysed, at least 12 of these are present in measurable concentrations and have an arithmetic mean that is above bulk continental crust (bcc) estimates (Fig. 4.6-1; data for comparison from Rudnick and Gao, 2003). There is a clear enrichment of Pb, Cu, Ag, As, Cd, S, and Sb, and a less pronounced enrichment of Mn, Mo, and P. Most major elements show a slight depletion compared to bulk continental crust or are neither enriched nor depleted. Squares reflect the arithmetic mean; arrows reflect the concentration range of each element. If elements have values below analytical detection limit (grey arrow tip) the lower element range was set to half lower detection limit. All values below analytical detection limit are considered with half detection limit. Lithophile elements such as Rb, Hf and U are significantly depleted (with mean values ranging between 0.02 and 0.70 ppm) compared to bcc, with an exception of W and Mn (mean 1.71-9.41 ppm) which are moderately enriched. Siderophiles such as Fe, Co, and Ni are largely depleted (mean 0.10-0.55 ppm); however, P shows a somewhat enrichment with a mean of 7 ppm. Most of the chalcophiles in the samples are enriched in comparison to bcc. The highest enrichment is observed in Pb, Cu, As, and Ag (mean 115-680 ppm), which are at least 100 times more than the average bcc, but Bi and Ga are depleted (mean <0.3 ppm). These elements are all associated with the bornite-chalcopyrite-galena mineral assemblage. Bowell (2014) and Bowell and Mocke (2019) described a variety of As-bearing minerals that are typical for the Tsumeb deposit and since the Kombat deposit is classified as a ‘Tsumeb-type deposit’, the enrichment of As in the Kombat deposit as shown in Fig. 4.6-1, can be correlated to various arsenic minerals of the main Tsumeb deposit.

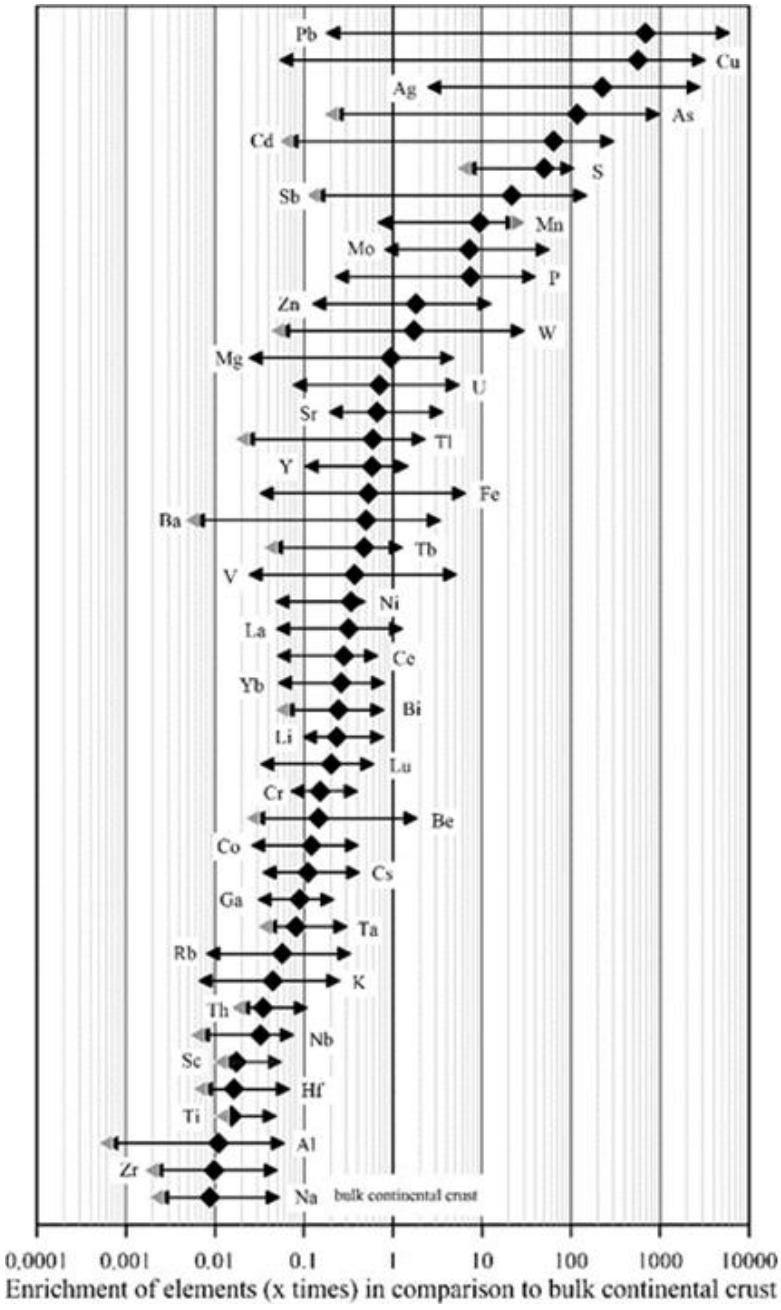

Fig. 4.6-1 Enrichment of elements of Kombat ore in comparison to bulk continental crust (data from Rudnick and Gao, 2003) based on ICP-MS data.

The evaluation of the correlation or match of pXRF results and ICP-MS results is done using the coefficient of determination (R^2; Fig. 4.6-2). There is a strong correlation

between values of samples obtained via pXRF and laboratory-driven ICP-MS/ASS values for most of the metallic elements of interest, e.g., Ag (R^2 = 0.99), Cu (R^2 = 0.97), Fe (R^2 = 0.99), Pb (R^2 = 0.96), and Zn (R^2 = 0.96). Most elements including Cu, Pb, and Zn were measured with an adequate accuracy by pXRF (%diff ≤10), based on the precision qualification from Piercey and Devine (2014). However, this is mostly applicable for samples with concentrations well above the lower detection limit of the instrument. If elements are low to very low in concentration, there seems to be an underestimation of values by pXRF. Additionally, elements such as Ag with a low concentration have the highest analytical error (Table 4.5-1).

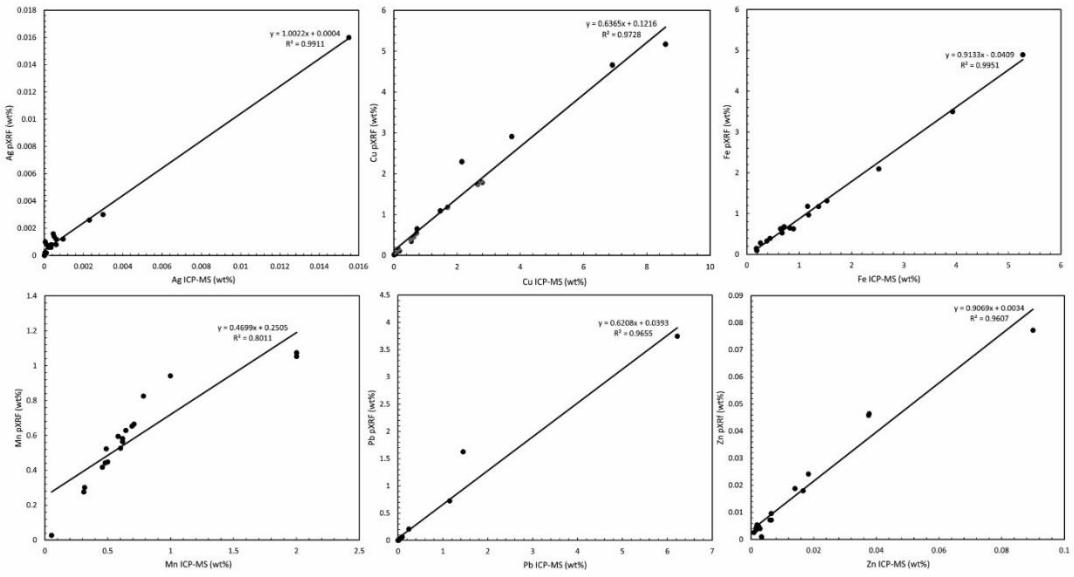

Fig. 4.6-2 Scatter plot diagrams, showing the correlation between the ICP-MS obtained results (x-axis) and pXRF results (y-axis) for all analyzed samples.

Most of the trace elements detected by ICP-MS such as Ga, Nb, Cr, V and W were not picked up by the pXRF. This is mostly because they are too low in concentration and well

below the detection limit and therefore could not be detected by the pXRF instrument. In cases when the elements cannot be detected by the instrument, either due to low concentration or factory calibration of the instrument, pathfinder elements can be used to infer the presence of those trace elements. Pathfinder elements are elements that have a positive correlation with the selected trace elements and can be analyzed by the pXRF accurately and precisely.

Based on the data from ICP-MS for the samples analysed, there hardly a positive correlation observed between the elements detectable by pXRF and the trace elements that are not detectable by pXRF. There is a positive correlation observed between Y and Yb, Y and Tb, Y and Lu, Yb, and Lu (Fig. 4.6-3); however, all the elements showing positive correlations cannot be measured using pXRF, therefore they cannot be used as pathfinders for this purpose. For that reason, it can be argued that pXRF is an effective rapid tool in geochemical exploration of the analyse of selected elements like Ag, Cu, Fe, Pb, and Zn of carbonate-hosted sulfide mineralized zones. However, there is still a need for it to be paired with other traditional geochemical analytical methods to get an overview of the whole elemental concentration spectrum.

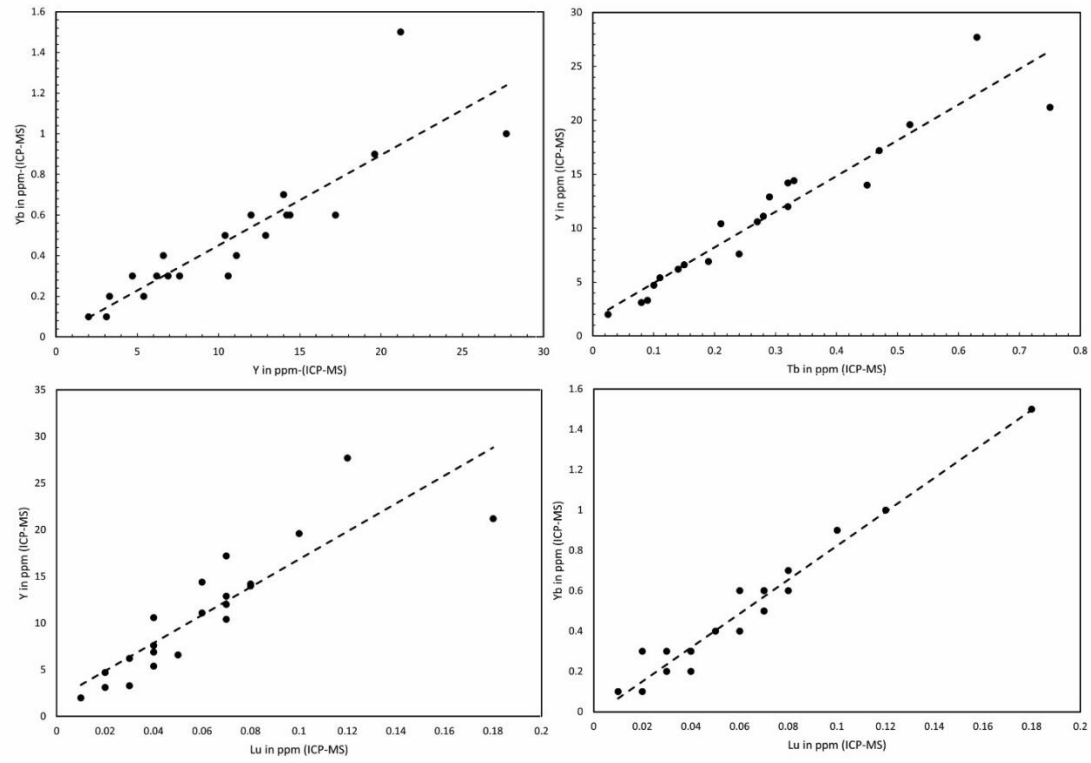

Fig. 4.6-3 Binary plots showing positive correlations between selected elements. Element concentrations are plotted in ppm. A) Y vs. Y b) Tb vs. Y, c) Lu vs. Y, d) Lu vs. Yb.

4.7 Conclusion

Portable XRF obtained results of carbonate-hosted Pb-Zn-Ag ores match adequately well with ICP-MS obtained results of the same samples. This indicates that pXRF is capable to detect the concentration of trace elements, with sufficient precision and accuracy, in carbonate-hosted sulphide mineralized zones; and can thus be used as a successful geochemical exploration tool for these types of sulphide ore deposits. However, when the metal concentration is relatively low, there is a quantitative under-estimation of trace element values by pXRF. Nevertheless, pXRF is an effective low-cost method that can be

easily used in geochemical exploration to obtain quantitative results of selected metal concentrations of sulfide mineralized zones. As Kombat sulfide ore comprises beside Cu other elements of interest as e.g. Pb, Ag, and As, exploration of similar carbonate-hosted deposits using pXRF tools might be an adequate means in projects with minor access to expensive laboratory facilities. However, pXRF is not capable of analysing Ga and other trace elements when present in low concentrations.

Acknowledgement

Many thanks to the staff of the Mineral Resources Department of Clausthal University of Technology for providing access to their pXRF instrument and to Trigon Metal for granting us permission to collect samples on site.

5 Indium and Gallium in Cu-Pb (Ag) sulfide deposits of the Otavi Mountain Land, Namibia: a LA-ICP-MS study

Ester Shalimba[a], Ansgar Wanke[a], Sven Sindern[b]

[a] Geosciences Department, University of Namibia

[b]RWTH Aachen University, Institute of Applied Mineralogy and Economic Geology

Abstract

The Kombat Cu-Pb-(Ag) deposit, hosted by the carbonate units of the Hüttenberg Formation is classified as a Tsumeb-type deposit. The deposit hosts a sulfide mineralisation that is dominated by chalcopyrite and bornite. Chalcopyrite and bornite are major sulfide minerals with crystal structures that can accommodate significant amounts of other commodities. The herein presented study focuses on the concentration of Ga and In and associated metals within chalcopyrite and bornite of the Kombat Cu-Pb-(Ag) deposit in the Otavi Mountain Land, Namibia. This chapter aims to correlate base metal element concentrations with Ga and In concentrations in the above-mentioned mineral. Insitu trace element analyses in bornite and chalcopyrite were determined by LA-ICP-MS. Both, bornite and chalcopyrite show large concentration variations for minor and trace elements (e.g. 192 ppm≥ Ag ≤ 257 ppm and 2.78 ppm ≥ Ag ≤ 3.57 ppm respectively). Gallium concentrations are present in a range greater than 1 ppm in bornite, while chalcopyrite has significantly higher concentrations of Ga (≤14 ppm). Indium concentrations are below the detection limit in bornite, and they are relatively low in chalcopyrite grains (<0.10 ppm). Element correlation plots show that high Ga concentrations correlate with low Ag concentrations in chalcopyrite and correlation

between Ag and Pb is weak in both bornite and chalcopyrite. Additionally, chalcopyrite grains with significant amounts of Ga always contain traces of In. Further studies will investigate the influence of the concentration of base metals on the distribution of the above. *This chapter is an expansion of the extended abstract that was presented at the 15th Biennial SGA meeting Glasgow, Scotland (August 27-30, 2019).*

Keywords: Kombat deposit, Indium, Gallium, LA-ICP-MS- Otavi Mountain Land

5.1 Introduction

Critical raw materials are essential for economic growth, especially in terms of technological evolution. Economic importance and supply risks are the two parameters frequently used to determine how critical the raw materials are (Graedel et al., 2011). Gallium and In are critical for a variety of high technology applications, such as in semiconductors, wide angle camera lenses as well as pharmaceutical industries (Paradis, 2015). These elements are mainly recovered as by-products of base metals from Zn and Cu deposits. The trivalent Ga is considered as a trace element with a crustal abundance of 17 ppm, which is commonly associated with aluminum ores, zinc ores, iron ores, and coal (Redlinger et al., 2015; Frenzel et al., 2016). Indium is typically associated with minerals such as Zn, Cu and Fe-Sn sulfides. It dominantly occurs as In-bearing mineral in Pb–Zn ores as well as concentrates is sphalerite (Cook et al., 2011; USGS, 2019). Indium is a highly volatile chalcophile, with a crustal abundance estimated to be at about 0.05-0.072 ppm (Taylor and McLennan, 1985). Thus far only China, Belgium, Canada, Japan, and the Republic of Congo are known for primary production of In (Shanks et al., 2017).

This chapter presents a combined mineralogical and geochemical study of bornite and chalcopyrite mineralization from the Kombat Cu-Pb(-Ag) deposit hosted in carbonate rocks of the Otavi Mountain Land, Namibia. This study aims to correlate the relations between base metal elements and Ga and In concentrations in the chalcopyrite and bornite mineral phases. Both, bornite and chalcopyrite are stable copper minerals and major source of copper metal and can be associated with other high value commodities of foreign elements (Wang, 2005).

5.2 Geological background

5.2.1 Regional Geology

The Otavi Mountain Land (OML) province is located at the transition between the Northern Zone and Northern Platform of the Neoproterozoic Damara Orogen. The Damara Orogenic Belt is best described in Martin and Porada (1977), Miller (1983, 2008b), and Pirajno and Joubert (1993) as a late Proterozoic suture zone between the Kalahari and Congo Cratons. The OML province consists of various base metal sulfide deposits, which are hosted within the sedimentary units of the Damara sequence (Kamona and Günzel, 2007). To date there are at least two mineralisation episodes that are known to be responsible for the formation of various deposits in the OML province (Pirajno and Joubert, 1993). Type one, formed by the first event, is classified as the Berg Aukas-type deposit, which was associated with the compaction and dewatering of sediments in a northern rift, and the second type is the Tsumeb-type deposits that were formed as a result of a much later episode that was associated with devolatilization reactions during regional prograde metamorphism of the sediments in this northern rift (Pirajno and Joubert, 1993).

5.2.2 Geology of the Kombat deposit

The Kombat mine comprises of the Kombat Cu-Pb-(Ag) mineralisation, which is hosted in the dolomitic units of the Otavi Group (Kamona and Günzel, 2007). This mineralisation is located at the northern limb of the Otavi valley syncline, hosted by the dolostones of the Hütternberg Formation, which consist of dolostones, oolite, breccia, chert, shale and stromatolite (Fig. 5.2-1; Kamona and Günzel, 2007; Trigon Metals Inc, 2017).

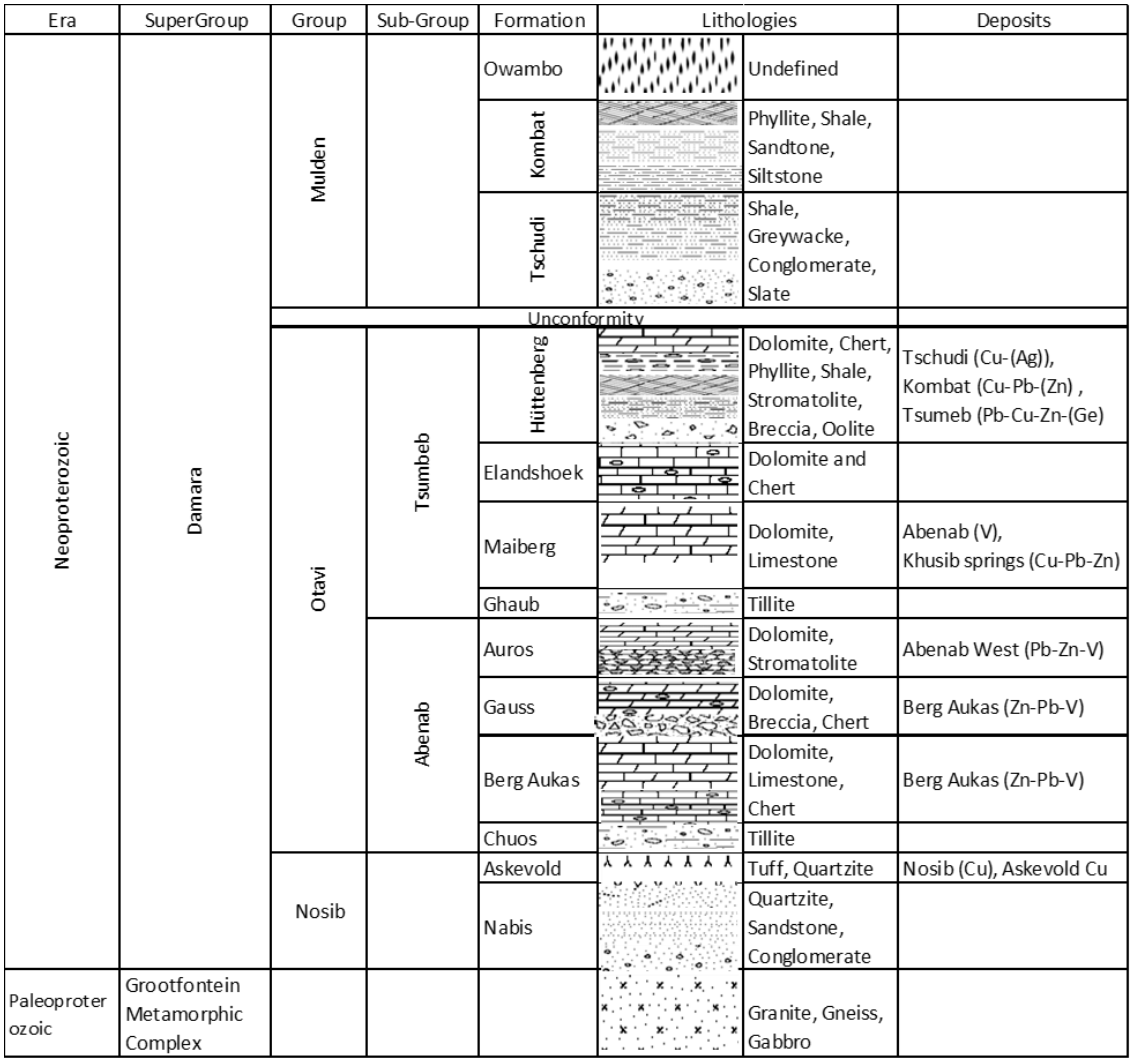

Fig. 5.2-1 Stratigraphic column of the Otavi Mountain Land, Namibia, highlighting the different groups, subgroup, formations, lithologies as well as deposits hosted within the Otavi Mountain Land province. Modified after: Kamona and Günzel, 2007).

There are at least seven mineralized zones that are associated with this deposits, Asis Ost, E900, Kombat East, Kombat Central, Kombat West, Asis West and Asis Far West (Changara, 2009; Nghoongoloka et al., 2020). They further stated that mineralisation at Kombat is categorised into two types: the Missisipi Valley type (MVT) which is characterised by Cu-Pb-Ag ±Zn and the Fe-Mn mineralisation, which is classified as a

stratiform syn-sedimentary deposit. Formation of the Kombat mineralisation is attributed to a brine hydrothermal fluid system with temperatures estimated to be at ~183°C (Nghoongoloka et al., 2020).

5.3 Methodology

Bulk ore geochemical analysis for major and trace elements concentration was conducted to characterize geochemical variability of the deposit. Thirty-one representative samples of mineralised and host rock collected from the Kombat central, Kombat hean and Kombat E900 were pulverised to 75 µm at the Geological Survey of Namibia and were sent to Central analytical Facility, Stellenbosch, and ACTSlab Canada for whole rock analysis. Epoxy mount polished sections were prepared at the Geological Survey of Namibia, from samples collected during a field exclusion at Kombat mine for petrographic study and LA-ICP-MS analyses. Petrographic analyses were done using a Leica DM 4500p transmitted and reflected light microscope at RWTH Aachen University, Germany. Laser ablation inductively coupled plasma-mass spectrometry (LA-ICP-MS) was used to measure trace element concentrations in bornite and chalcopyrite. Spot analysis of element concentrations of bornite and chalcopyrite was done on pre-selected sites based on petrographic study conducted on the samples. The LA-ICP-MS system comprises a NewWave UP193Fx (ArF-Excimer-Laser) operated at 150 µm laser beam diameter and 6 Hz repetition rate connected to a quadrupole ICP-MS system (PerkinElmer Elan DRCe). Total analysis time was 100 s, approximately 40 s on background and 60 s on signal. MASS-1 reference material was used as an external calibration standard, and sulfide stoichiometric concentrations of bornite (25.56% S) and chalcopyrite (34.94% S) were

used as internal standards. Analytical reproducibility is better than 10% for all trace elements. Full LA-ICP-MS results and bulk ore geochemistry are presented in appendix 5-1 and 5-2 respectively.

5.4 Result

5.4.1 Petrography

Petrographic examination of polished sections from the Kombat mineralisation reveals that the primary ores are massive, disseminated, and to a certain extent brecciated. There are three distinct ore assemblages observed in the samples: (1) bornite-chalcopyrite-covellite, (2) bornite-galena-chalcocite and (3) bornite-chalcopyrite (Fig. 5.4-1). The primary sulphide mineralization consists of bornite, galena, and chalcopyrite, while covellite, and chalcocite are the secondary minerals. The common gangue minerals are dolomite and calcite. The primary ore textures comprise of subhedral-anhedral grains, disseminations, intergrowths, and replacement textures. Bornite is characterized throughout by anhedral coarse-grained texture with grains size in a range up to 1 cm in diameter, and it is replaced by chalcopyrite and chalcocite in most samples (Fig. 5.4-1a-d and i). Most of the bornite grains are light orange in color, while some exhibit a light grey color.

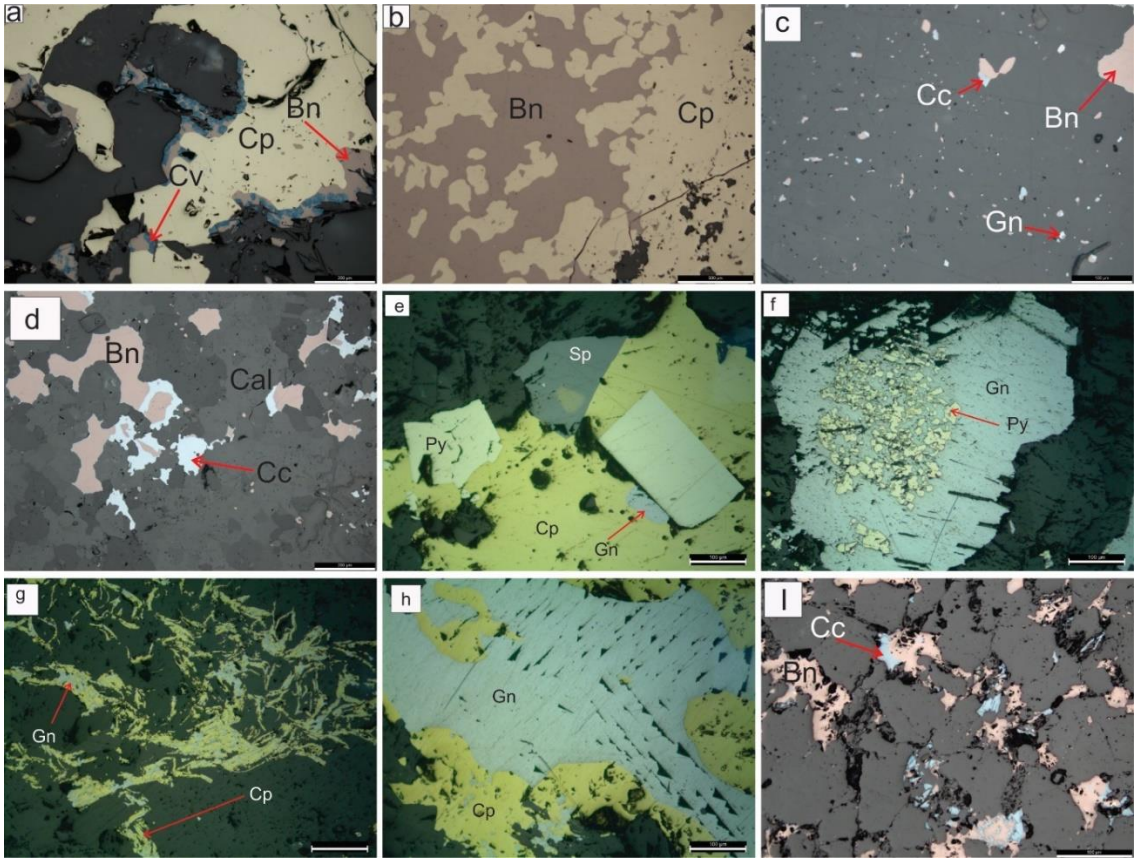

Fig. 5.4-1 Microphotography in reflected light showing ore mineralogy and textures observed. a) Bornite replaced by chalcopyrite with intergrowth of covellite; b) Bornite replaced by chalcopyrite; c) dissemination of bornite, chalcocite and galena; d) Intergrowth of bornite and chalcocite; e) subhedral pyrite grains associated with chalcopyrite, galena and sphalerite; f) replacement of pyrite by galena; g) chalcopyrite replacement by galena; h) deformation cleavage in galena that is replacing chalcopyrite; i) Bornite and chalcocite in carbonate matrix. Abbreviations: Bn-bornite, Cp= chalcopyrite, Cc=chalcocite, Cv=covellite, Cal=calcite, Sp= sphalerite; Gn=galena.

Galena is fine grained and occurs mainly as inclusions in bornite and exhibit deformation cleavage (Fig. 5.4-1 c, and h). Galena commonly replaces chalcopyrite and pyrite (Fig 5.4-1 f, g, and h). Chalcopyrite displays a replacement texture and is massively disseminated within the dolomite. Sphalerite occurs as a minor mineral, exhibiting anhedral crystal shape with inclusions of chalcopyrite (Fig. 5.4-1 e). Covellite is mainly

observed in the brecciated zone and occurs as veinlets and intergrowths in bornite that is replaced by chalcopyrite (Fig. 5.4-12 a).

5.4.2 Bulk ore geochemistry

Major oxides analysis was done on 13 samples of the Kombat deposit from the Kombat E900 pit. All sample shows a record of high CaO ranging from 29.93 wt% to 45 wt%, while MgO and Si_2O both have a wide range, with content ranging from 1.39 wt% to 21.09 wt% and 0.16 wt% to 17.38 wt% respectively. The Fe_2O_3 content is significantly low in most sample ranging between 0.24 wt% and 4.75 wt%, and this can be due to the presence of abundant pyrite in the samples, taking up most of the Fe. Other oxides such as NiO, Al_2O_3, MnO, NaO, K_2O, TiO_2, P_2O_5, Cr_2O_3, and V_2O_5 all have low content that are below 2 wt%.

Copper, Pb, and Mn are the dominant metals in the Kombat E900 pit's samples with content ranging between 0.035 wt% to 6.9 wt%, 0.0002 wt% to 8.8 wt%, and 0.054 wt% to 0.997 wt% respectively. The content of other metals such as Zn (0.0014 wt% to 0.2 wt%), Ag (0.029 ppm to 19.6 ppm), Cd (0.01 ppm to 72.9 ppm) and Ga (0.05 ppm to 3.4 ppm) are relatively low. Samples from Kombat central pit has much lower content, with Cu, Pb, Zn, Ag, Cd and Ga concentrations ranging between 0.008 wt% to 1.4 wt%, 5 ppm to 2405 ppm, 9.2 ppm to 166 ppm, 0.14 ppm to 6.1 ppm, 0.73 ppm to 11.51 ppm and 0.8 ppm to 2.9 ppm respectively. Kombat central is dominated by Cu (range: 77 ppm to 14700 ppm), Mn (range: 3092 ppm to 7091 ppm), and Pb (5 ppm to 2405 ppm). Other metals such as Ag (range: 0.14 ppm to 6.1 ppm), As (range: 1.3 ppm to 380 ppm), Cd (0.73 ppm

to 11.51 ppm), Ga (range: 0.80 ppm to 2.9 ppm), and Zn (range: 9.2 ppm to 166 ppm) are relatively low in concentration.

5.4.3 Trace element concentration in bornite and chalcopyrite.

Results obtained for trace element concentrations by LA-ICP-MS for bornite and chalcopyrite element concentrations' mean, median, max', and min are listed in Tables 5.4-1 and 5.4-2 respectively. The data obtained consists of 342 spot analyses in bornite and 184 spot analyses in chalcopyrite. Representative time-resolved LA-ICP-MS depth profiles are shown in Fig. 5.4-2 & 5.4-3.

5.4.3.1 Trace elements in Bornite

Silver, Bi, Fe, Ga, Pb and V values are well above the detection limit in most of the bornite grains analysed, whereas Cd, Sb, and W were detectable only in a few grains. Bornite exhibits significantly high Ag contents in all the samples examined (Table 5.4-1). All bornite grains contain Ag with a mean concentration ranging between 100 and 290 ppm (median 194-259 ppm; Fig. 5.4-2). There is a variation in Pb concentration, with most values typically in the range of >1 ppm, except for some bornites in KH0517 sample and KH0515 sample with values as high as ±1200 ppm, indicating a possible galena micro-inclusion in bornite. Spot P7.11 (Fig.5.4-2 b) records the highest Pb concentration (≥1200 ppm) and based on the time-resolved signal diagram it is associated with a peak of Ag and Bi, alluding to a possible galena inclusion in the bornite (Fig. 5.4-2 a & d). All samples contain measurable Ga concentrations in bornite although there is a relatively low, varying between 0.8 and 7.6 ppm (median 1.1-1.3 ppm). Vanadium concentration in bornite grains where detectable varies significantly, ranging between 2.2 ppm (KH0517) and 75 ppm

(KH0516). There are no absolute values for In in bornite. If detectable, Cd, Sb, and W are all in low concentrations in all the samples (mean 2.4 ppm, 0.3 ppm and 0.9 ppm; median 2.5 ppm, 0.3 ppm and 0.8 ppm, respectively).

Table 5.4-1 Mean concentrations for minor and trace elements in Bornite (ppm) by LA-ICP-MS.

	V	**Ga**	**Ag**	**Cd**	**Sb**	**W**	**Pb**
KH0517							
Mean	4.6	1.5	257	2.4	0.3	0.9	93
Median	3.8	1.1	259	2.5	0.3	0.8	5.9
Min	2.2	0.7	207	1.9	0.2	0.4	1.4
Max	12.	7.6	281	2.7	0.4	2.3	1270
KH0516							
Mean	13.3	1.5	242	-	-	-	1.1
Median	5.3	1.3	244		-	-	1.1
Min	2.3	0.9	213	-	-	-	0.7
Max	75	2.9	292	-	-	-	1.8
KH0515	**V**	**Ga**	**Ag**	**Cd**	**Sb**	**W**	**Pb**
Mean	-	1.3	191	-	-	-	74
Median	-	1.3	195	-	-	-	12.6
Min	-	0.8	100	-	-	-	2.6
Max	3.59	3.1	239	1.9	-	-	656

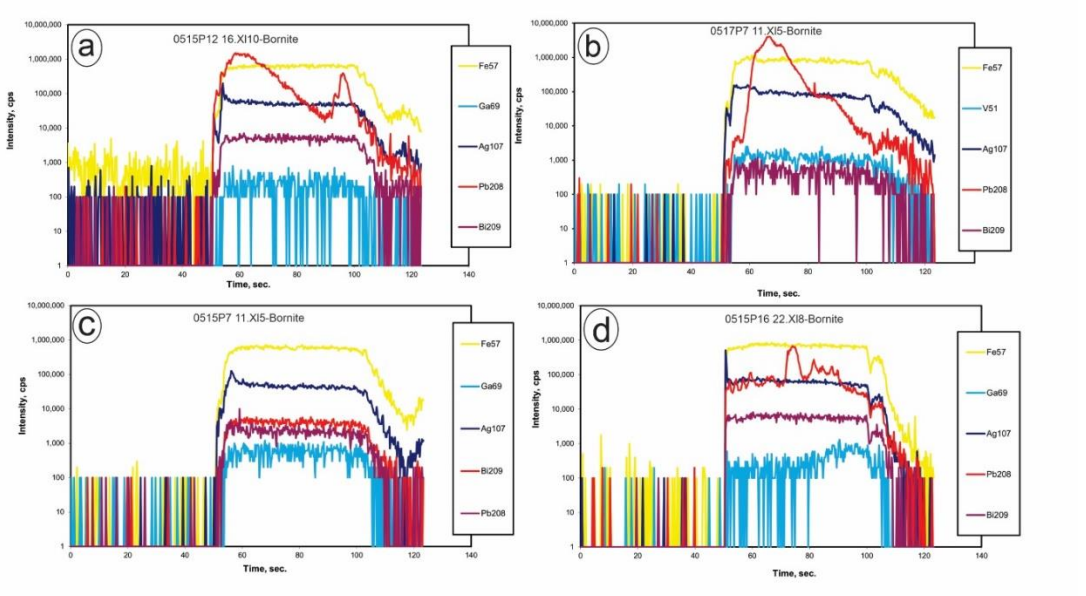

Fig. 5.4-2 Representative time-resolved LA-ICP-MS depth profiles for analysed bornite.

Pearson's matrix correlation (Table 5.4-2) indicates that there are positive correlations between Fe and Bi (0.70), and Fe and Cd (0.45), suggesting a possible incorporation of Cd and Bi in the bornite crystal lattices. Cook et al. (2011b) reported Bi inclusion in bornite via a solid solution, which resulted in micro inclusion. There is a strong positive correlation between V and Ga (0.90), suggesting that the two elements coexist and can possibly substitute in the bornite mineral lattice.

Table 5.4-2 The Pearson matrix correlation coefficient of Bornite trace element concentration. Green blocks reflect a significant link between the elements, pink blocks represent a moderate correlation, and cream blocks represent no correlation.

	V	*Fe*	*Ga*	*Ag*	*Cd*	*Sb*	*W*	*Pb*	*Bi*
V	1.00								
Fe	0.16	1.00							
Ga	0.90	0.11	1.00						
Ag	-0.05	-0.26	-0.11	1.00					
Cd	-0.60	0.15	0.28	0.31	1.00				
Sb	-0.03	0.45	0.08	0.28	1.00	1.00			
W	0.29	-0.06	-0.27	-0.11	0.42	-0.11	1.00		
Pb	-0.09	0.05	-0.09	0.08	-0.19	0.28	-0.24	1.00	
Bi	0.29	0.70	-0.02	-0.11	-0.61	0.23	0.26	-0.19	1.00

5.4.3.2 Trace elements in chalcopyrite

There is a detectable amount of Ag, V, Ga, In, Pb, and W in the chalcopyrite grains of the Kombat deposit. Elemental concentrations in chalcopyrite is summarised in Table 5.4-3. Gallium has a significantly higher concentration in chalcopyrite compared to bornite in all the samples studied. KH0517 has a high concentration of Ga (mean: 13.22 ppm) and moderate concentration of Ag and Pb (mean: 3.57 ppm; mean: 6.10 ppm, respectively). Vanadium concentration is low (mean: 1.94 ppm), while In is low in concentration with a single spot in sample KH0517. Indium is detectable in some of the chalcopyrite grains in the other two samples with relatively low concentration varying between 0.1 ppm and 0.4 ppm. Germanium is detectable in limited grains of chalcopyrite, with relative low concentrations ($\leq$ 4 ppm).

Table 5.4-3 LA-ICP-MS Mean concentrations for minor and trace elements in chalcopyrite (ppm). Owing to restrictions of the MASS1 standard, In is given as information values.

	V	Ga	Ge	Ag	In	W	Pb
KH0517							
Mean	1.9	13.2	-	3.6	-	0.9	6.1
Median	1.3	12.9		2.1	-	0.9	4.9
Min	0.8	11.6	-	0.9	-	0.5	3.3
Max	5.0	16.6	2.9	14.6	0.9	1.4	11.0
KH0516							
Mean	30.5	12.5	-	2.8	0.4	-	1.6
Median	30.6	13.2	-	2.3	0.4	-	1.6
Min	23.4	10.5	-	1.2	0.3	-	0.8
Max	37.4	13.9	-	5.1	0.4	-	2.3
KH0515							
Mean	-	14.1	3.7	3.1	0.2	-	8.5
Median	-	14.3	3.7	1.5	0.2	-	3.6
Min	-	10.8	3.6	0.5	0.1	-	0.6
Max		16.6	3.9	19.2	0.2	5.3	43.3

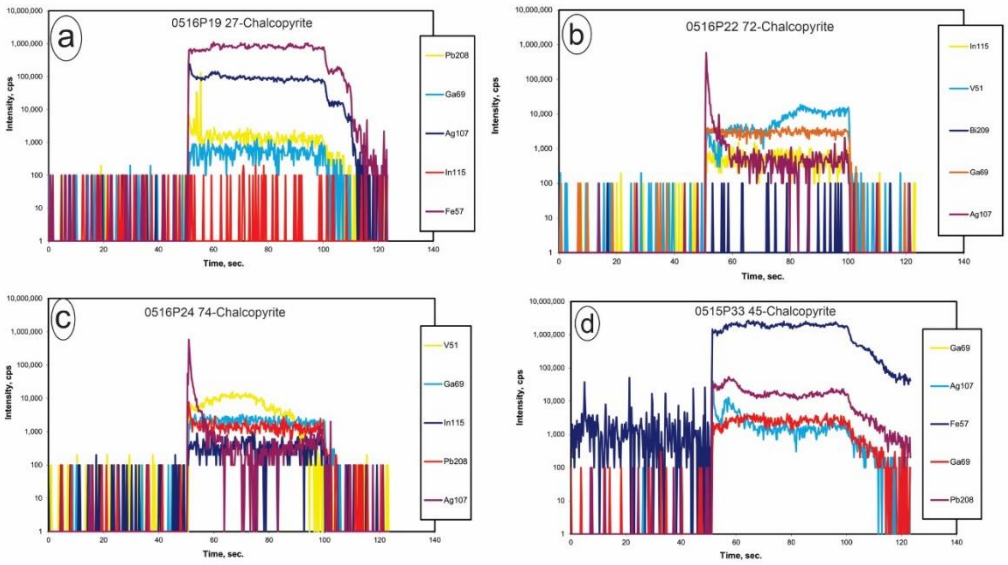

Figure 5.4-3 Representative time-resolved LA-ICP-MS depth profiles for analysed chalcopyrite.

Pearson's matrix correlation summarised in Table 5.4-4, shows that Fe and V, and Fe and In have a positive correlation, with values of 0.80 and 0.89 respectively. This suggests a possible incorporation of the mentioned elements in the chalcopyrite crystal structure. Silver and Pb (0.66) .and Pb and Sb (0.69) yield a positive corelation, suggesting possible galena micro-inclusions within the chalcopyrite grains.

Table 5.4-4 Pearson's correlation matrix for the analysed trace elements in chalcopyrite.

	V	*Fe*	*Ga*	*Ag*	*In*	*Sb*	*W*	*Pb*
V	1.00							
Fe	0.80	1.00						
Ga	-0.16	0.35	1.00					
Ag	-0.13	-0.40	-0.35	1.00				
In	0.89	0.06	-0.29	-0.02	1.00			
Sb	-0.46	0.30	0.03	0.26		1.00		
W	0.46	0.39	0.27	-0.06		-0.50	1.00	
Pb	-0.72	-0.05	-0.13	0.66	-0.17	0.69	-0.24	1.00

5.5 Discussion

The main ore minerals in the Kombat deposit are bornite, chalcopyrite, pyrite, galena, chalcocite, and sphalerite. Mineralisation is hosted within carbonate rock units, with mineralisation styles classified as massive, disseminated, and brecciated.

The incorporation of trace elements in sulfide mineralisation can occur as micro-inclusions or via stoichiometric substitution of major elements with respect to a particular mineral phase (Huston et al., 1995). Concentration of the trace elements analysed in chalcopyrite and bornite phases of the Kombat mineralisation are presented in the box and whisker plots in Figure 5. The variation in elemental concentration and lack of correlation between various trace elements in both bornite and chalcopyrite is a clear indication of micro-inclusion in both mineral phases. Bornite is considerably one of the good mineral phases that is receptive to precipitate silver (Palmer, 1915). In this study Ag is present in high concentration, appearing as a solid solution in the bornite phase. However, based on the Pearson matrix correlation, there is a lack of correlation between Ag and all the analysed trace element in bornite. Additionally, there is no apparent correlation between the other trace elements that are analysed within the bornite phases in our study (Fig.5.5-2).

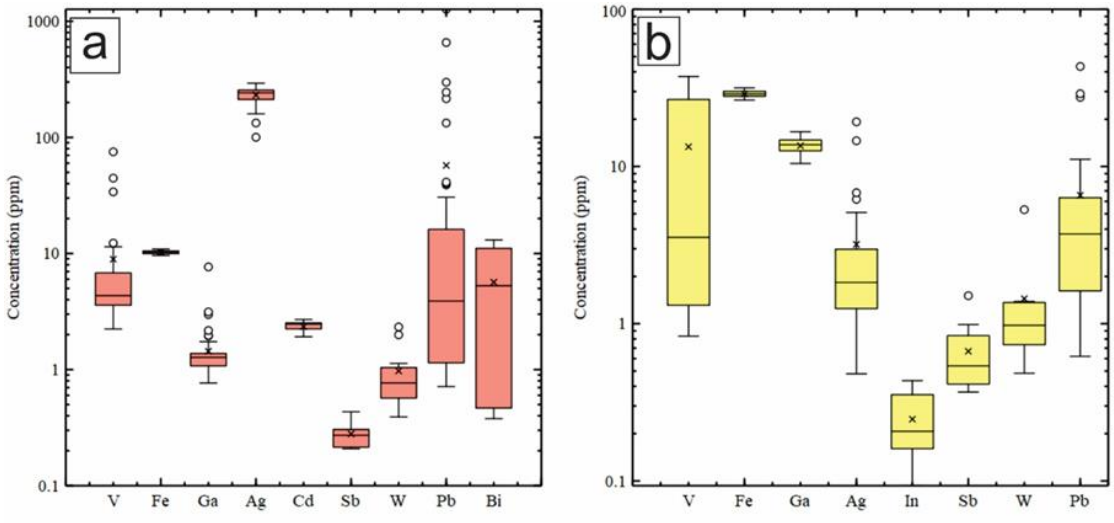

*Fig. 5.5-1 Box and Whisker diagrams representing trace element concentration in a) bornite phases, b) chalcopyrite phases of the Kombat deposit. * Fe concentration is in wt%.*

Chalcopyrite is known to be poor in hosting various trace elements especially when there is a presence of other sulphide minerals such as galena and sphalerite (Cook et al, 2011b; George et al, 2016; 2018). However, chalcopyrite is considered to be one of the main primary hosts of Ga and In in recrystallised mineralisation (George et al, 2016). In the samples analysed in this study chalcopyrite accommodates higher concentrations of Ga and In compared to bornite. Furthermore, the higher Ga concentrations in chalcopyrite correlate with In concentrations above the detection limit. Ag is more accommodated in bornite than in chalcopyrite, indicating that substitution for Ag may explain the limited accommodation of Ga in bornite. However, neither within bornite, nor within chalcopyrite a conclusive correlation of Ga with Ag was observed.

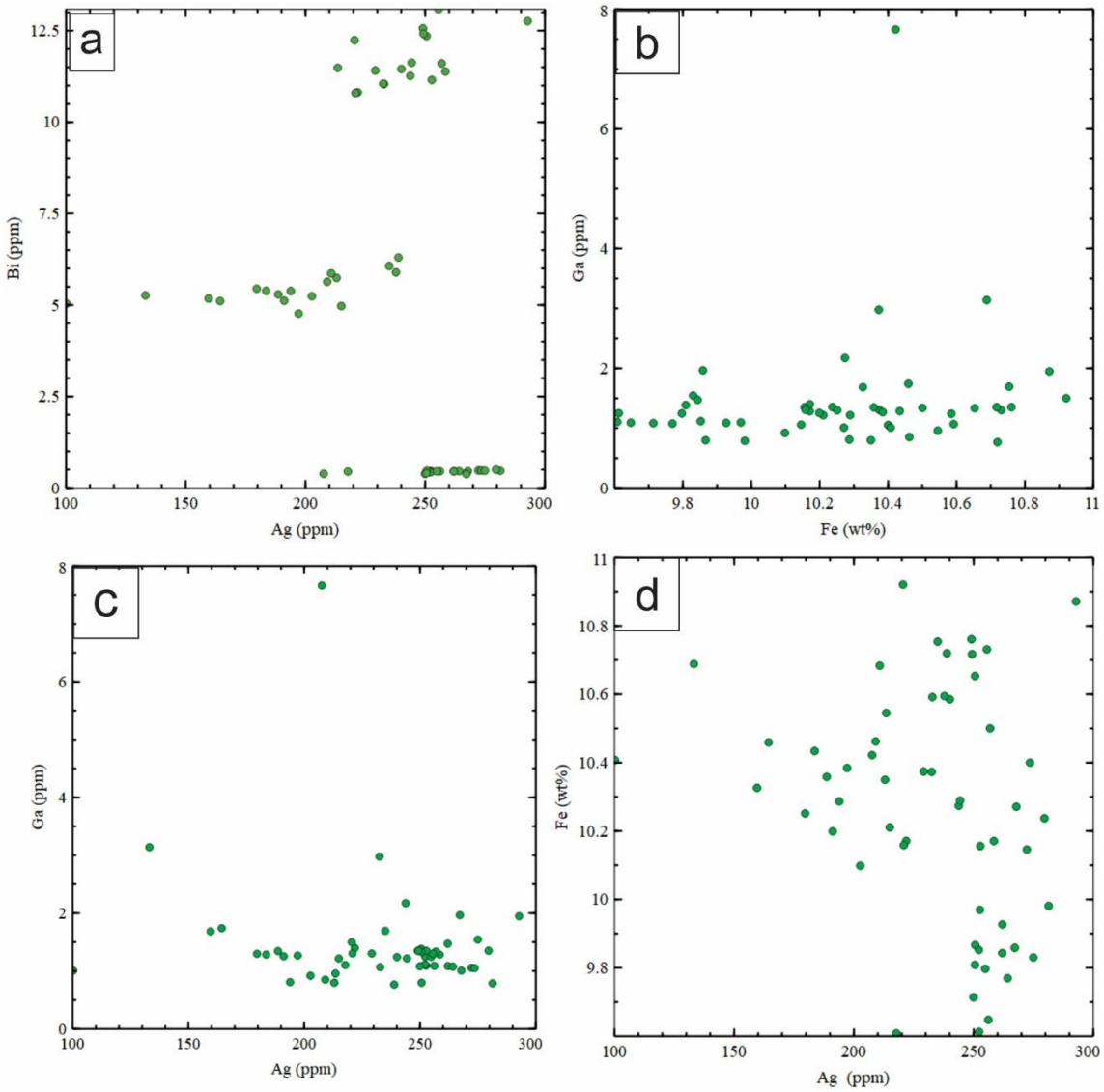

Fig. 5.5-2 Binary plots showing trace elements correlation in bornite phases a) Bi Vs Ag; b) Ga vs Fe; Ga Vs Ag; d) Fe Vs Ag.

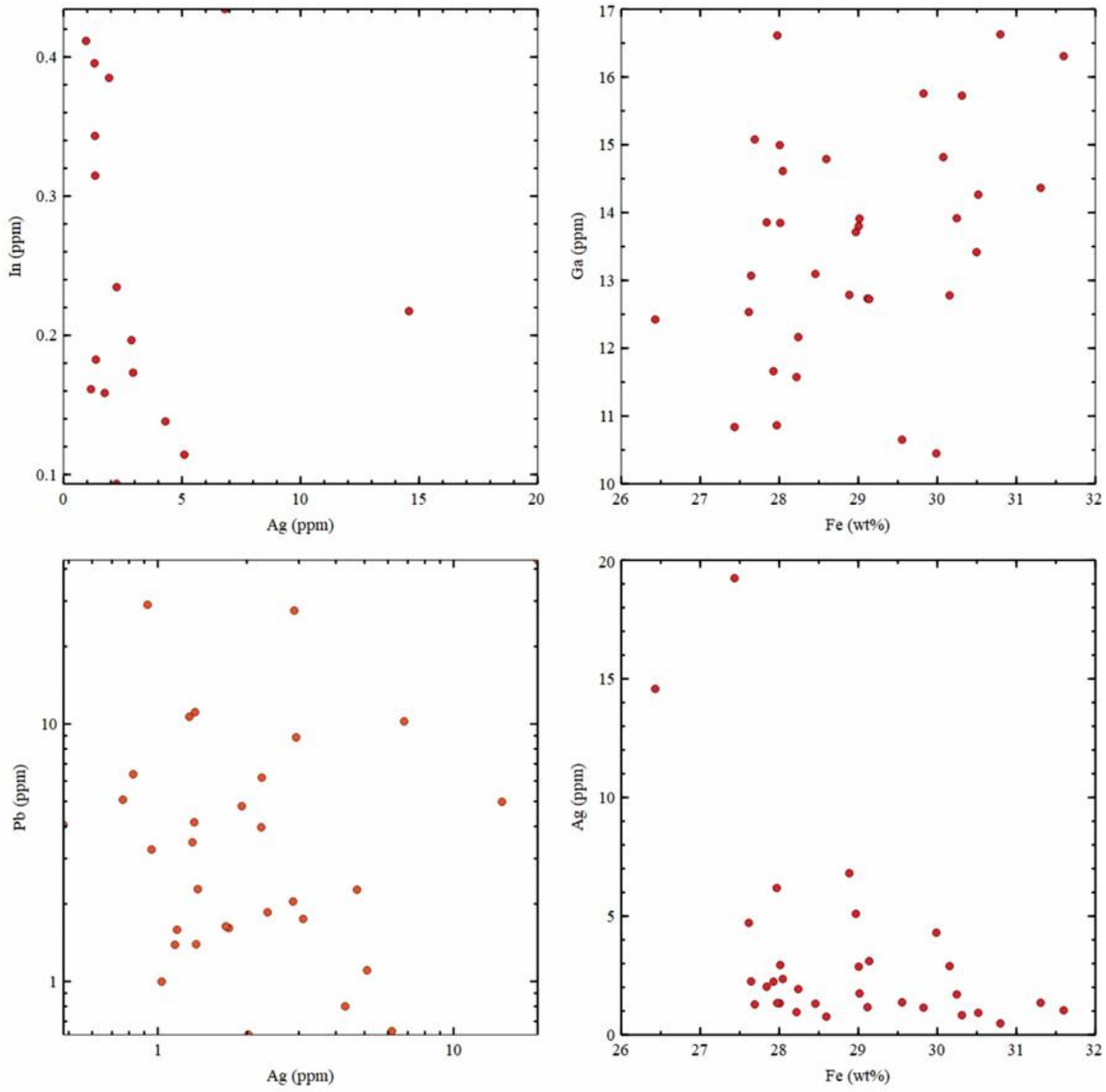

Fig. 5.5-3 Comparison of Pb-In, Ag-In, Ag-Ga and Pb-Ga by LA-ICP-MS analysis for chalcopyrite.

5.6 Conclusion

- Both bornite and chalcopyrite host a significant amount of other trace elements, with bornite enriched in Ag and chalcopyrite enriched in Ga.

- The trace elements are either in solid solution with the respective minerals phase or as micro inclusion, with the latter being the most favourable scenario as it can be deduced form the lack of apparent correlation between the elements.
- Lastly, In order to fully study the association of the selected critical metals with base metals, significantly more trace elements need to be sought after, and extension of analysis to other sulphide minerals that are present.

6 Trace element characteristics of the sulfide mineralization of the Tsumeb deposit, Otavi Mountain Land, Namibia

Ester Shalimba[1], Stephanie Lohmeier[2], Simon Goldmann[3], Jan Pašava[4], Ansgar Wanke[1],

[1]Department of Geology, University of Namibia, 340 Mandume Ndemufayo Avenue, Pioneerspark, Windhoek, Namibia; Email: eshalimba@unam.na; ansgarwanke@gmail.com

[2]Mineral Resources/ Surface Mining and International Mining, Clausthal University of Technology, Adolph-Roemer Str. 2A, 38678 Clausthal-Zellerfeld, Germany; Email: stephanie.lohmeier@tu-clausthal.de

[3] Federal Institute for Geosciences and Natural Resources / Bundesanstalt für Geowissenschaften und Rohstoffe (BGR), Stilleweg 2, 30655 Hannover, Germany; Email: simon.goldmann@bgr.de

[4]Česká geologická služba / Czech Geological Survey, 152 00 Prag 5 – Barrandov, Czeck Republic; Email: jan.pasava@geology.cz

Abstract

The polymetallic Tsumeb deposit in the Otavi Mountain Land of the Damara Belt in Namibia is well-known for its large mineralogical variety and complexity. Sulfide mineralization over a depth range of about 1500 m (mining Levels 16, 17, 18, 19, 20, 29, 30, 32, and 46) displays mineral assemblages that are typically Cu-rich (pyrite-galena-tennantite-renierite, carbonate-galena-pyrite-sphalerite, renierite-galena-chalcopyrite-chalcocite-digenite-renierite). We describe the distribution of Ga, Ge, and associated trace elements (Ag, As, Cd, Co, Cu, Fe, Ga, Ge, In, Ni, Pb, Sb, Zn) in the sulfide ore from

historical deep underground mining. Electron microprobe analysis reveals that renierite and enargite are significant carriers of Ge, with averages of 8.21 wt% and 0.78 wt%, respectively, while Ga is mainly incorporated into renierite and sphalerite (av. 0.12 wt%, 0.11 wt%). Sphalerite trace element abundance is characterized by elevated Cd, Ge, and Ga, suggestive of low formation temperatures. The bulk-ore Zn isotopic composition of the Tsumeb deposit (δ^{66}Zn = -0.0133 to 0.125‰) is within the range of typical Zn-rich massive sulfide deposits, while the range of δ^{65}Cu varies from 0.80‰ to 1.32‰, which is consistent with mineralization within a hypogene environment. *This is an extension of an abstract submitted and presented at CAG29 conference in Windhoek, September 2023. The chapter is to be submitted to the special to CAG29 special edition in Journal of African Geology.*

Keywords: Tsumeb deposit, sulfide mineralization, trace element geochemistry, copper isotopes, zinc isotopes.

6.1 Introduction

The polymetallic, carbonate-hosted, replacement-type Tsumeb deposit, with the famous De Wet shaft as main mine adit, is located directly north of the mining town of Tsumeb in Namibia's Oshikoto Region, about 435 km north of the capital city of Windhoek (Fig. 6.1-1). Mineralization at Tsumeb was first discovered by missionaries in 1857 and exploitation took place between 1897 and 1996 (Melcher, 2003; Bowell and Mocke, 2019). The mine produced about 30 Mt of ore yielding 1.7 Mt Cu, 2.8 Mt Pb, 0.9 Mt Zn, as well as 80 t Ge. The average ore grade was 10% Pb, 4.3% Cu, 3.5% Zn, 100 ppm Ag, and 50 ppm Ge (Lombaard et al., 1986). The deposit is world-renowned for its unique and complex mineralogy, comprising approximately 337 minerals for which Tsumeb is the type locality for at least 72 of these minerals (Bowell and Mocke, 2019). The mineralization is hosted in dolomite of the Neoproterozoic carbonaceous units of the Otavi Group. The main ore body is a breccia pipe filled with massive sulfide ore of locally manto-style, disseminated, and stringer type (Kamona and Günzel, 2007; Miller, 2008 b). The primary sulfidic ore underwent extensive post-depositional oxidative overprint, promoted by permeable faults, and deep surficial weathering (Bowell and Mocke, 2019). The Tsumeb deposit is famous in particular for its diverse arsenic minerals, but also for enrichment of other trace elements, such as Ge, Ga, and In which are of interest for modern (green) industry (Bowell, 2014; USGS, 2018). These critical metals in this deposit are mainly associated with the sulfide mineralization and less with the oxide mineralization (Kamona et al., 1999; Melcher, 2003; Bowel, 2014).

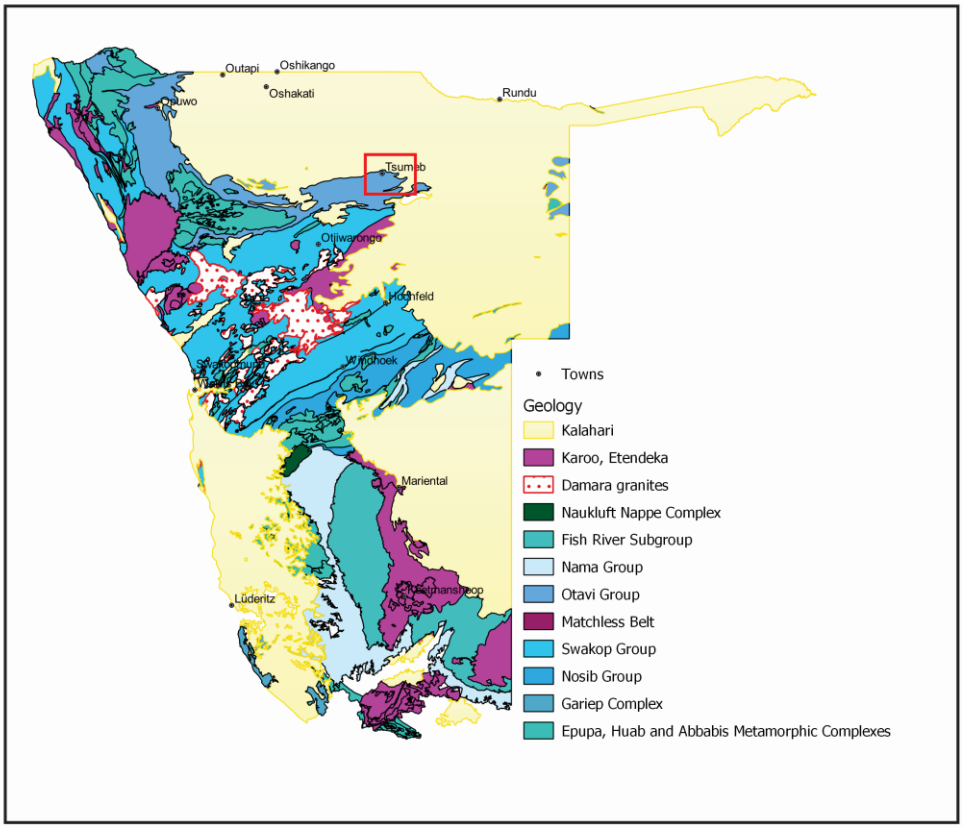

Fig. 6.1-1 Simplified geological map of Namibia showing the Mesoproterozoic to Tertiary pre-Damara, Damaran and post-Damara geological units. The location of the study area is marked by the red box.

Germanium is usually recovered only as a by-product of global mining, and there are historically only two primary Ge ore producers: Tsumeb in Namibia and Kipushi in D.R. Congo, formerly Zaire (Bernstein, 1985; Butterman and Jorgenson, 2005). Germanium in these two deposits is directly associated with the high-grade Cu zones, and forms discrete sulfide minerals, such as renierite ($(Cu,Zn)_{11}Fe_4(Ge,As)_2S_{16}$), germanite ($Cu_{13}Fe_2Ge_2S_{16}$), and briartite ($Cu_2(Fe,Zn)GeS_4$) (Frondel and Ito, 1957; Bernstein, 1985). Previous studies of the Tsumeb deposit mainly focused on the geochemistry of Ge, the paragenetic relation

of Ge in renierite and the general complexity of the mineralogy of the deposit (Frondel and Ito, 1957; Sclar and Geier, 1957). Sclar and Geier (1957) discussed the distribution of Ge in the hypogene sulfide ores, while the details of Ge geochemistry within the oxidized mineralization of the deposit are discussed in Frondel and Ito (1957).

This chapter reports on Ga and Ge and associated trace element abundance in selected sulfide minerals of the Tsumeb deposit, using electron microprobe analysis (EMPA). Additionally, first reconnaissance data on Cu and Zn isotopes are provided. The data is used to gain insight into the geochemical distribution of trace elements in the Tsumeb ore system with an outlook at the ore formation processes of this deposit.

6.2 Regional Geology

The Tsumeb Cu-Pb-Zn-Ag deposit is a breccia pipe-like structure, sitting in the upper part of the Neoproterozoic carbonate rocks of the Otavi Group within the Otavi Mountain Land (OML) of the Damara Orogenic Belt (Melcher, 2003; Kamona and Günzel, 2007; Miller, 2008b). The formation of the Damara Belt took place between 900 Ma and 460 Ma and is linked to rifting, spreading, subduction and collision of the Kalahari, Congo, and Río de la Plata Cratons (Martin and Porada, 1977; Gray et al., 2008; Miller, 2008b). The belt is subdivided into various tectonostratigraphic zones, defined by structural features, lithology, and degree of metamorphism (Miller, 2008b). The Damara Supergroup is composed of five subgroups which formed as a result of tectonic activities over a span of approximately 150 Ma (Gray et al., 2006; 2008; Miller, 2008b). The Damara sequence was initiated by rifting, with the deposition of the siliciclastic rock units of the Nosib Group, ranging in age between 757 Ma and 745 Ma (Hoffman et al., 1994; 1998; Gray et

al., 2008). This was followed by more intracontinental rifting, with crustal stretching and spreading which resulted in the deposition of carbonate and siliciclastic rocks of the Swakop Group and carbonate-shelf rock units of the Otavi Group which were deposited on a stable platform (Miller, 2008b). Both the Otavi and the Swakop Group contain glaciogenic deposits and cap-carbonate units, deposited as a result of two glacial episodes related to the Neoproterozoic "Snowball Earth" (Hoffman et al., 1998; Miller, 2008b). The molasse sequence of the overlying Mulden Group is linked to two deformation episodes of the Damara Orogen (D_1 and D_2) (Miller, 1997; 2008; Halverson et al., 2002). The youngest unit of the Damara sequence is the Nama Group consisting of Ediacaran fossil-rich carbonate rocks of the Kuibis and Schwarzrand Subgroup at the bottom, and the upper sediments of the Fish River Subgroup (Germs et al., 1986; Saylor et al., 1995; Bowyer et al., 2020).

6.3 Local Geology

The OML is a metallogenic province rich in sulfide and non-sulfide mineral occurrences, which are aligned along the transition of the Northern Zone and the Northern Platform of the Damara Orogenic Belt (Kamona and Günzel, 2007). The OML comprises two main units: (1) the Paleoproterozoic basement units of the Grootfontein Metamorphic Complex and the Grootfontein Mafic Body, and (2) the Neoproterozoic rift sedimentary rock units of the Nosib Group, carbonate platforms of the Otavi Group and low-grade metamorphic units of the Mulden Group (Fig. 6.3-1; Melcher, 2003; Kamona and Günzel, 2007; Miller, 2008b).

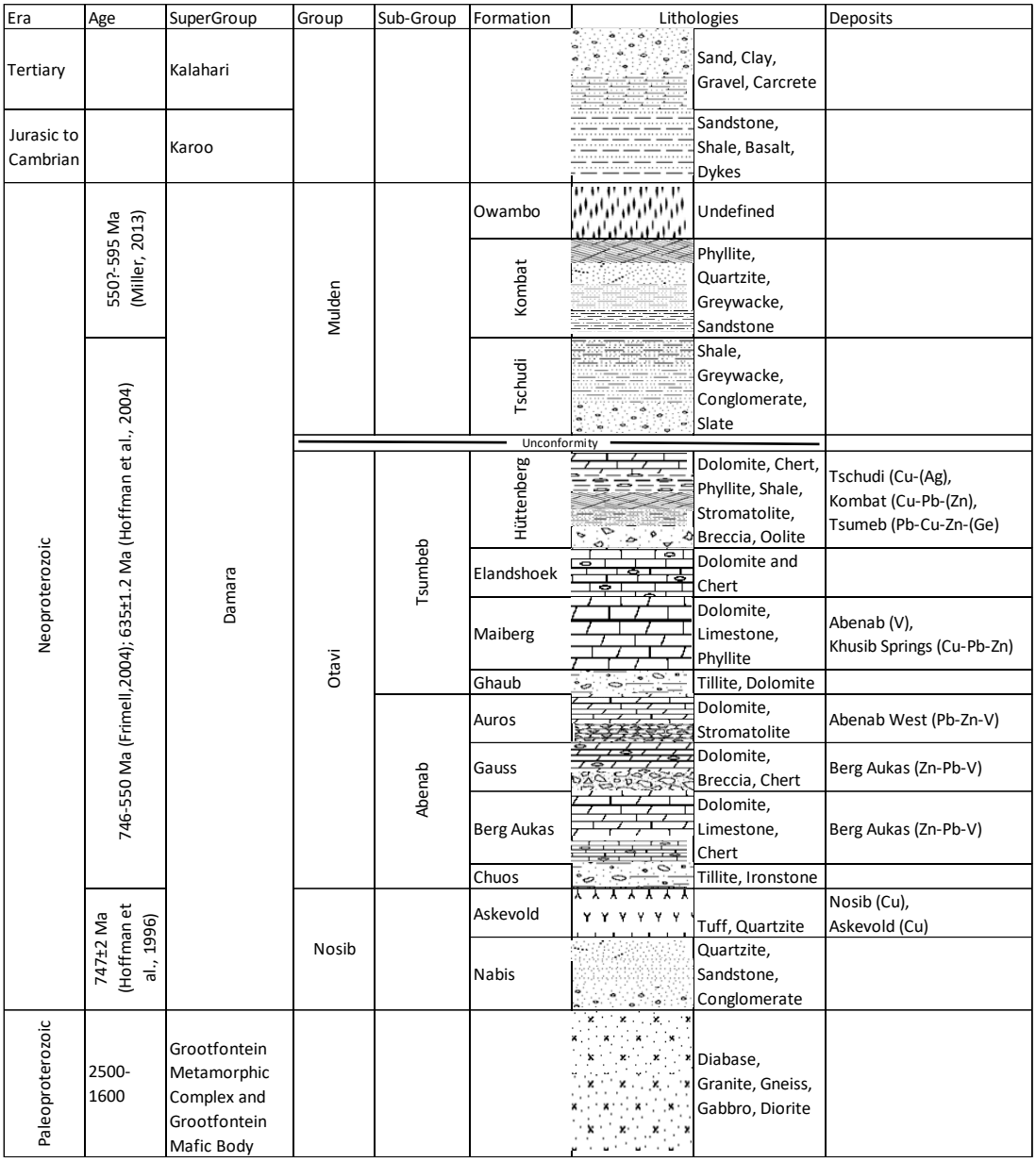

Fig. 6.3-1 Stratigraphy of the Otavi Mountain Land, highlighting the ore deposits in their respective lithostratigraphic setting (modified after Hoffman et al., 1996, 2004; Frimmel, 2004; Kamona and Günzel, 2007; Miller, 2008).

These units experienced a complex geological evolution providing favourable conditions that resulted in the formation of various kinds of deposits within the province (Melcher,

2003; Laukamp, 2006; Kamona and Günzel, 2007). The Otavi Group, hosting most of the orebodies of the OML, is carbonate dominated and is subdivided into two subgroups: the older Abenab and the younger Tsumeb Subgroup, with the Abenab Subgroup further subdivided into the Varianto, Chuos, Berg-Aukas, Gauss, Auros, and Ghaub Formations and the Tsumeb Subgroup subdivided into the Ghaub, Maieberg, Elandshoek, and Hüttenberg Formations (Melcher, 2003; Kamona and Günzel, 2007). The lowest unit, the Hüttenberg Formation mainly consists of a carbonate breccia which hosts the Tsumeb deposit, while the uppermost part is made up of dolostones which host the Kombat deposit (Kamona and Günzel, 2007).

6.4 Deposit Characteristics

The Tsumeb deposit sits in the dolomite of the Hüttenberg Formation and is characterized by structurally controlled features including folding, fracturing and shearing of ore in discordant pipes with dolomite breccia and feldspathic sandstone filling (Fig. 6.4-1; Melcher, 2003; Kamona and Günzel, 2007). Ore mineralization is largely represented by tennantite and sphalerite as the most abundant ore minerals, associated with galena, pyrite, bornite, chalcocite, digenite, and minor enargite, renierite, germanite, chalcopyrite, and traces of various arsenates and other minerals as described in Bowell et al. (2014) and Bowell and Mocke (2019). Calcite, dolomite, and quartz are the dominant gangue minerals (Bowell and Mocke, 2019).

Uranium/lead isotope data of the Tsumeb deposit indicate a high U/Pb ratio, which is alluding to an upper crustal metal source (Kamona, 1999). The $\delta^{34}S$ values of the deposit range between -18.1 and 20.5‰ suggesting the involvement of evaporitic sulfate in ore

formation (Kamona, 1999). The mineralizing fluids were likely released as a result of regional metamorphism during the second deformation episode of the Damara Belt, including syntectonic granite magmatism (Laukamp, 2006).

The ore experienced extensive oxidation of the massive peripheral sulfide ores, manto-style ore, disseminations, and stringer ores (Bowell, 2014; Bowell and Mocke, 2019). Three zones of oxidation over a vertical distance of approximately 1200 m are recognized in the mineralized pipe structure, based mainly on secondary mineral assemblages linked to supergene alteration of primary sulfides (Fig. 6.4-1; Melcher, 2003; Bowell and Mocke, 2019). The oxidation zones are a result of interaction between groundwater and the primary sulfide mineralisation (Bowell and Mocke, 2019). The first oxidation zone is between the surface and Level 12 (500 m mining depth) and represents the vadose zone, influenced by fluctuations of the water table. This zone largely consists of sulfide, carbonate minerals such as galena, tennantite, sphalerite, chalcocite, bornite, chalcopyrite, enargite, smithsonite, and wulfenite among others (Bowell and Mocke, 2019; Southwood, 2019). Bowel and Mocke (2019) further state that level 12 to 24 is characterised mainly by unaltered sulfide minerals including galena, sphalerite, tennantite and pyrite. The second oxidation zone is observed from Level 24 down to Level 34 which is characterized by minerals such as sphalerite, galena, chalcopyrite, chalcocite, smithsonite, and pyrite, associated with rare minerals such as leiteite, legrandite, reinerite, tscumicorite, stottite, stranskiite, and zincroselite (Geier and Ottemann, 1970; Cairncross, 2017). The third oxidation zone is observed from Level 42 downwards (below 1500 m mining depth) and is largely composed of diverse primary and secondary minerals as such as tennantite,

chalcopyrite, leiteite, renierite, schneiderhöhnite, and authurite among others as described in Cairncross (2017) and Bowell and Mocke (2019).

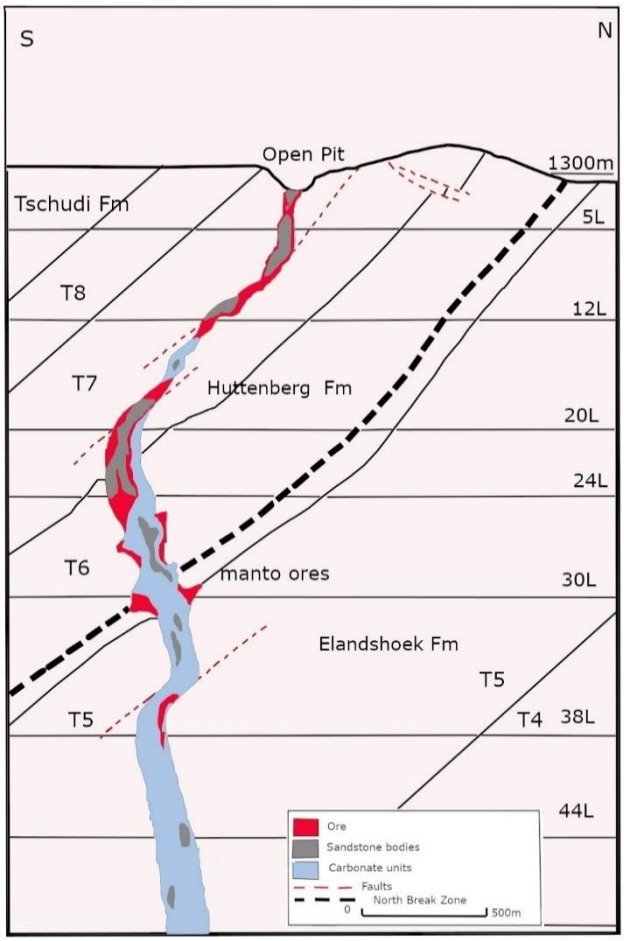

Fig. 6.4-1 Cross section showing the geological profile of the Tsumeb mine with the orebody hosted in the collapsed breccia pipe (modified after Laukamp, 2006; Bowel, 2019).

6.5 Samples and analytical methods

6.5.1 Samples and sample preparation

Forty historical samples, collected by Hans Schneiderhöhn at the then active Tsumeb mine, are investigated. These samples belong to the Tsumeb collection of the 'Museum of the Geological Survey of Namibia' in Windhoek (Fig. 6.5-1).

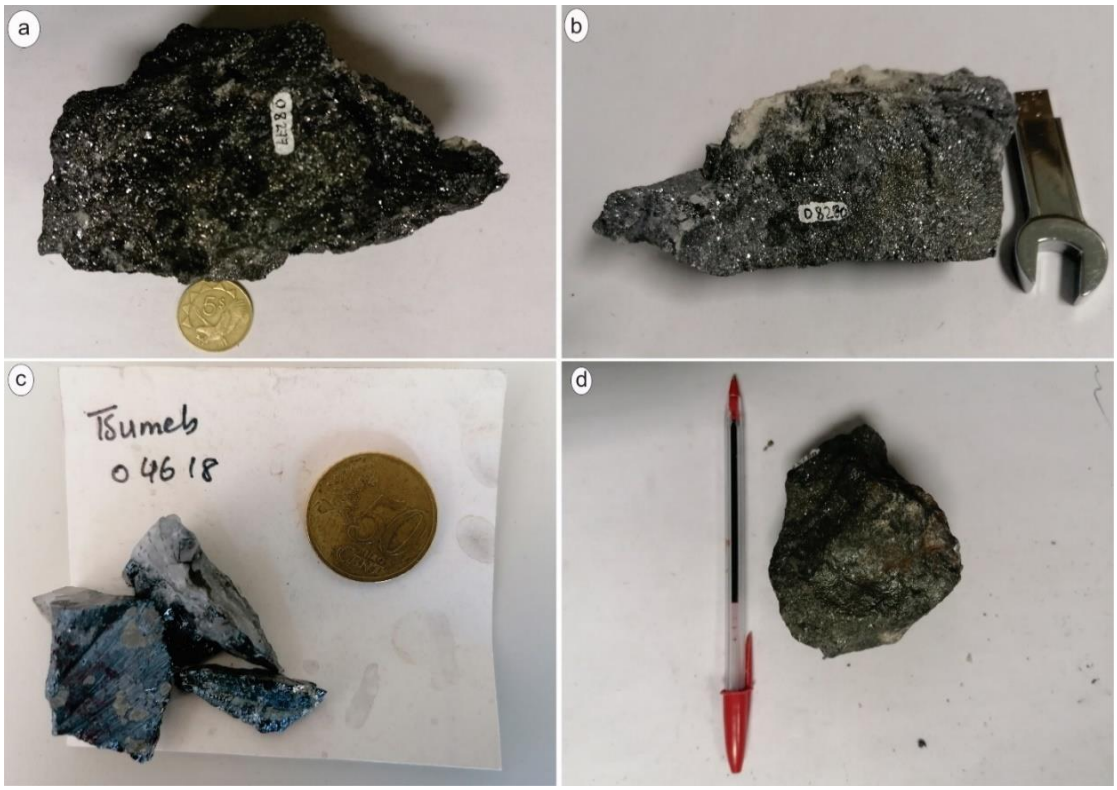

Fig. 6.5-1 Representative photographs of the samples from the historical collection of the Geological Museum at the Geological Survey of Namibia. A) Sample showing disseminated galena and sphalerite in carbonate matrix; B) sample showing quartz vein in carbonate rock with sphalerite, galena, and pyrite; C) sample with disseminated tennantite, sphalerite, and galena with clasts of pyrite; D) sample of massive chalcocite, sphalerite, galena, and tennantite in carbonate matrix.

These samples are from different mining levels and are representative of the Tsumeb sulfidic ore assemblages, the list of samples Appendix 6-1. Polished sections were prepared of all samples at Clausthal University of Technology (TUC). Ore petrography at TUC revealed tennantite, chalcopyrite, pyrite, galena, sphalerite, enargite, renierite, bornite, covellite, and digenite as the most abundant mineral phases, which were subsequently studied by electron microprobe analysis (EMP) at Bundesanstalt für Geowissenschaften und Rohstoffe (BGR) in Hannover.

6.5.2 Bulk Ore Geochemistry

Rock samples were submitted to Activation Laboratories LTD (ACTS LAB), Namibia, for sample preparation (crushing and pulverizing) while bulk rock trace element analysis was subsequently conducted by Activation Laboratories Ltd, Ontario, Canada. Trace elements were analysed by inductively coupled mass spectrometry (ICP-MS). Copper, Zn, Pb, As and Ag results were obtained using the 8-pre-oxide ICP assay method. The batch of samples was analysed including blanks, duplicates, and standards, complying with the quality control procedures of ACTS LAB. The complete analytical results are provided in Appendix 6-2.

6.5.3 EPM on sulfides

Galena, sphalerite, chalcopyrite, digenite, tennantite, and renierite were analysed for their trace element concentrations using a JEOL-JXA 8530F electron microprobe at BGR. All polished sections were carbon coated before analysis and sulfide minerals were preselected before EMP analysis (Fig. 6.5-2). All sulfides were analysed at 25 kV, 80 nA, with a 1-µm beam diameter, using the following X-ray lines, spectrometer crystals and

reference materials (in parentheses): Ag *Lα*, PETH (pure metal); As *Lα*, TAP (synthetic GaAs); Cd *Lα*, PETH (synthetic CdS); Co *Kα*, LIFL (cobaltite); Cu *Kα,* LIFL (chalcopyrite); Fe *Kα*, LIFL (pyrite); Ga *Kα*, LIFL (synthetic GaAs); Ge *Kα*, LIFL (pure metal); In *Lα*, PETH (pure metal); Ni *Kα*, LIFL (pentlandite); Pb *Mα*, PETH (galena); S *Kα*, PETH (pyrite); Sb *Lα*, PETH (stibnite); Zn *Kα*, LIFL (sphalerite). Measurement time was 10 s for Fe, Zn, Cu, S, 20 s for Co and Ni, 40 s for Pb, 50 s for Sb and Cd, 60 s for Ag and Ge, 70 s for Ga, 120 s for As, and 200 s for In. The mean atomic number (MAN) background intensity data was calibrated, and continuum absorption corrected for all elements, as described in Donovan and Tingle (1996) and Donovan et al. (2016).

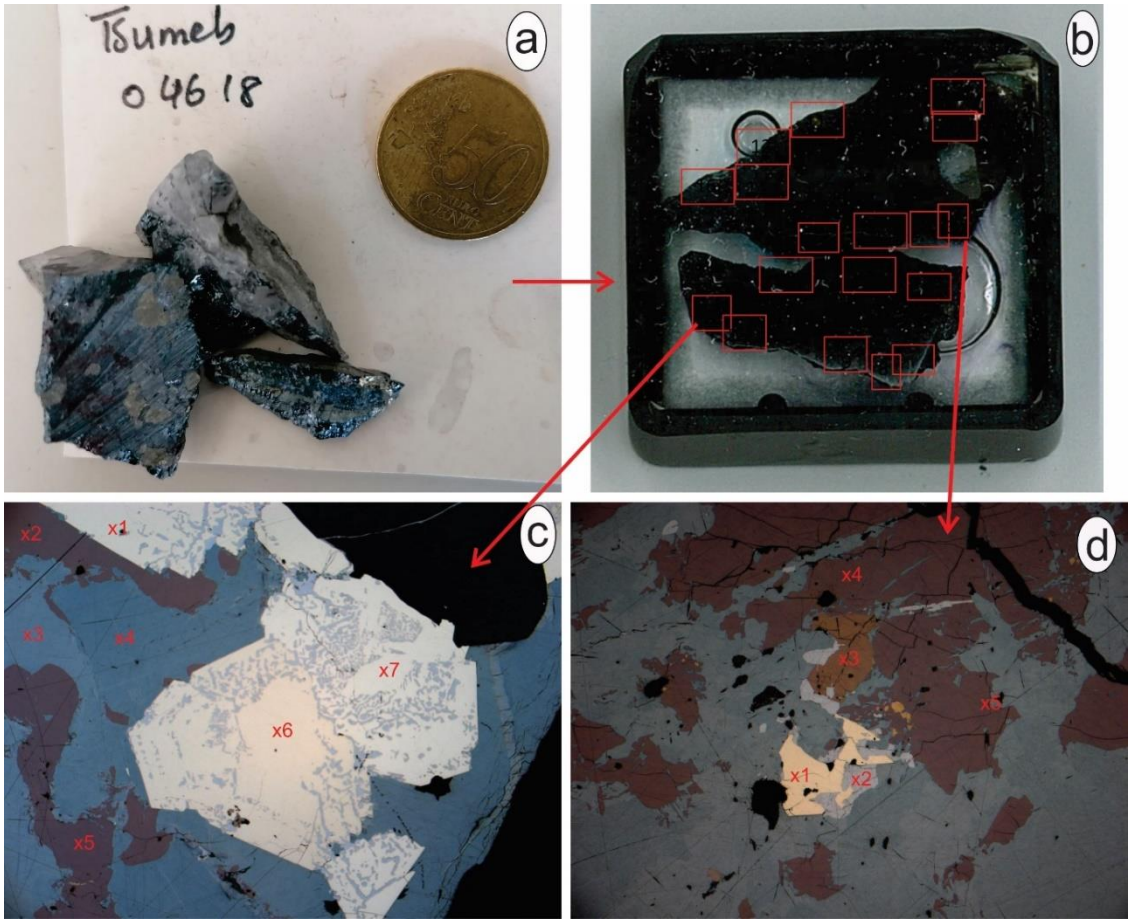

Fig. 6.5-2 Photographs showing hand specimens, polished section, and microphotographs illustrating the point selection for EMP analysis for a specific sample. A) Disseminated sulfide ore; B) polished section of the same sample with delineated points for EMP analysis; C) & D) microphotographs of the sulfide mineralization indicating points of EMP analysis.

6.5.4 Reconnaissance Cu and Zn Isotopes

Bulk Cu and Zn isotope compositions were obtained on six composite sulfide samples. Selected samples are from massive ore at levels 17 and 18, and from manto-style ore at levels 30, 32, and 34. Sample preparation, including crushing and milling, was done at TUC. The isotope measurements were performed at the Czech Geological Survey, using a Neptune (Thermo) double focusing multi-collector inductively coupled plasma mass

spectrometer (MC-ICP-MS), equipped with nine Faraday detectors. The detailed procedure for sample digestion and instrument analysis is described in Lehmann et al. (2022). Copper isotope data are reported in standard δ notation in per mil relative to standard reference material (SRM) AE633, while Zn isotope data are recorded against the NIST 683 standard as expressed by equation 6-1 and 6-2. Error for the analysis was determined from monitoring the variation of the NIST 976, with standard varying at ±0.16 ‰, and since all measurements fall within this error margin, it is assumed for all sample.

$$\delta^{65}Cu = [(^{65}Cu/^{63}\ Cu)_{sample} / (^{65}Cu/^{63}Cu)_{AE633} - 1] \times 1000 \quad \text{Equation 6-1}$$

$$\delta^{66}Zn = [(^{66}Zn/^{64}Zn)_{sample} / (^{66}Zn/^{64}Zn)_{NIST863} - 1] \times 1000 \quad \text{Equation 6-2}$$

6.6 Results

6.6.1 Mineralogy and ore texture

The principal sulfide minerals tennantite, galena, sphalerite, bornite, enargite, renierite, covellite, pyrite, and chalcopyrite can be traced in the samples studied (Figs 6.6-1, 6.6-2), with at least three main sulfides present at every mine level in the ore assemblage.

Galena is the most abundant sulfide mineral, and is closely associated with pyrite, tennantite, and sphalerite, thereby frequently surrounding sphalerite. Four different growth habits were identified for galena, with anhedral grains exhibiting a polycrystalline texture (Fig. 6.6-1 a), massive and irregular grains having triangular cleavage pits of different sizes (Fig. 6.6-1 b), galena replacement textures with pyrite (Fig. 6.6-1 c), and anhedral galena grains enclosed in sphalerite that are not affected by any deformation stage (Fig. 6.6-1 d). There are at least three deformation episodes reflected by deformed galena grains, defined by cleavage pits (Fig. 6.6-1 b).

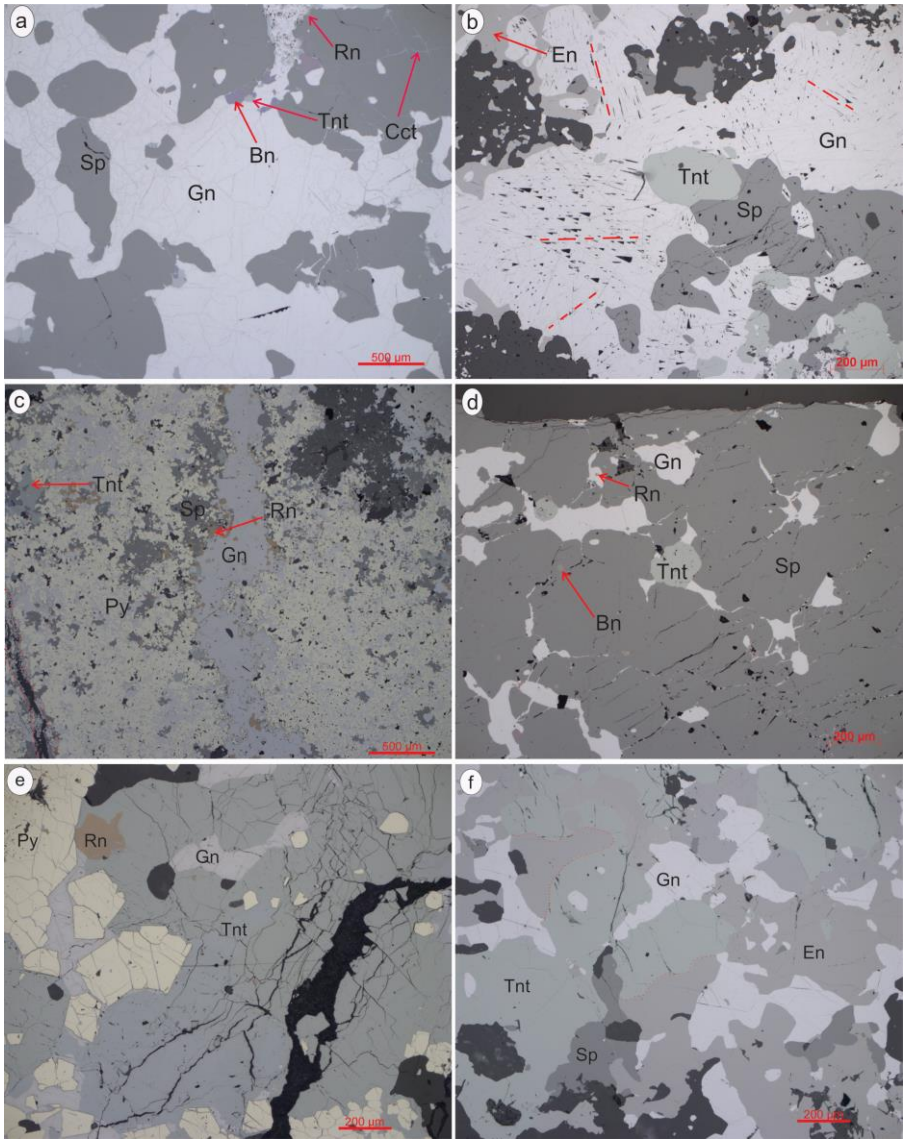

Fig. 6.6-1 Photomicrographs showing different galena mineral assemblages and textures from the Tsumeb deposit. a) Assemblage of sphalerite and polycrystalline galena. Sphalerite with microfractures filled by chalcocite and micro-inclusions of renierite. Bornite replaces tennantite; b) Assemblage of massive galena with deformation cleavage pits, sphalerite, tennantite, and minor enargite. At least three deformation episodes are reflected in the galena crystals (deformation indicated by the red dashed lines in galena); c) Galena replaced by pyrite with minor sphalerite and renierite; d) fractured massive sphalerite associated with tennantite, enclosing galena and disseminated inclusions of bornite. Fractures are filled with host matrix. Renierite occurs as inclusion in galena e) assemblage of tennantite and pyrite with minor galena and renierite. Fracture is filled with gangue minerals; f) enargite replacement of tennantite with microfractures filled with gangue minerals in tennantite. Abbreviations: Bn-bornite, En-enargite, Gn-galena, Py-pyrite, Rn-renierite, Sp-sphalerite, Tnt-tennantite,

Tennantite is the second most abundant sulfide mineral phase. The medium- to coarse-grained (approximately 50 to ≥ 500 μm) tennantite crystals are characterized by a striking greenish color. They are associated with galena, pyrite, sphalerite, and enargite (Fig. 6.6-1 a-f) and are locally replaced by enargite (Fig. 6.6-1 f). At places, tennantite is truncated by fractures filled with gangue minerals (Fig. 6.6-1 e).

Sphalerite is generally semi-massive to massive and occurs dominantly in association with tennantite, galena, and pyrite (Fig. 6.6-1 a-d). Occasionally, sphalerite is replaced either by tennantite, and chalcocite (Figs 6.6-1 a, b), or occurs as vein infill with gangue minerals and rare covellite (not shown).

Pyrite in Tsumeb shows two distinct morphologies, which includes the coarse grained subhedral pyrite categorised as pyrite-1 and the fine-grained pyrite, which is categorised as pyrite-2. Pyrite occurs in massive, semi-massive, and disseminated mineralization styles (Fig. 6.6-2 a-d), often associated with galena and sphalerite. Pyrite-1 grains have dominantly subhedral shape (Fig. 6.6-2 a), but anhedral and euhedral grains with inclusions of galena and rare renierite are also present (not shown). Texturally, pyrite-1 exhibits sometimes a pseudomorphic replacement texture, which is defined by galena after pyrite (Fig. 6.6-2 b), can occur as cataclastic grains replaced by galena, and as fracture infill with chalcocite (not shown).

Renierite is typically observed in two forms, as minor greyish-purplish crystals that are associated with chalcocite, sphalerite, chalcopyrite, and galena (Fig. 6.6-2 d) and as abundant brown, orange renierite, which is associated with fractured pyrite-1, tennantite, galena, and sphalerite (Fig. 6.6-2 g, h).

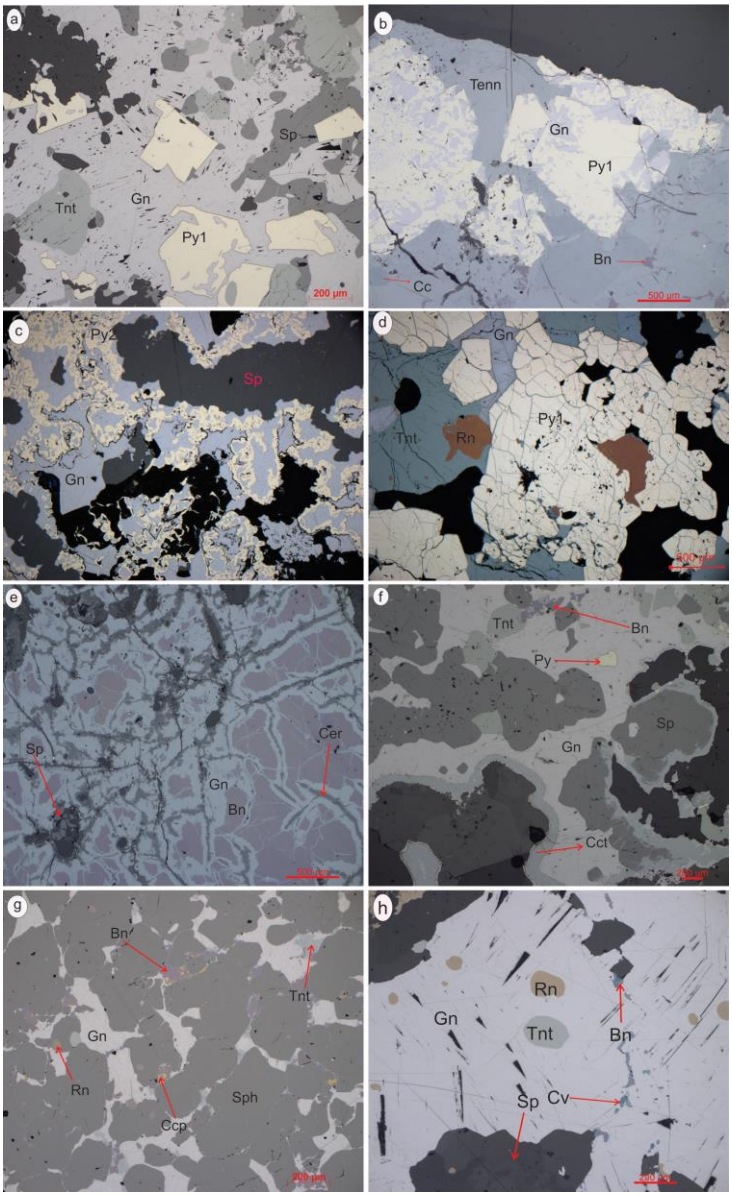

Fig. 6.6-2 Photomicrographs showing textural features of Tsumeb sulfidic ore. A) Subhedral to euhedral pyrite-1 crystals and tennantite in galena and sphalerite; B & C) pseudomorphic replacement of pyrite by galena, with chalcocite and borninte inclusions in tennantite; D) coarse-grained pyrite-1 with microfractures filled by tennantite, associated with renierite that replacing tennantite. Tennantite has fractures that are filled by matrix; E) replacement of bornite by galena, with carbonate matrix infill along fractures; F) chalcocite rims surrounding sphalerite, in an assemblage with pyrite, galena and bornite; G) massive sphalerite with inclusions of renierite, associated with tennantite and bornite with exsolution of chalcopyrite; H) massive galena with deformation cleavage pits and inclusions of reinierite, tennantite, bornite, and covellite. Abbreviations: Bn-bornite, Cer- cerusite, Cct- chalcocite, Ccp-chalcopyrite, Cv-covellite, En-enargite, Gn-galena, Py-pyrite, Sp-sphalerite, Tnt-tennantite.

Chalcopyrite is distinctly less abundant than sphalerite, galena, and pyrite, and occurs mostly as small inclusions in bornite (Fig. 6.6-2 g). In addition, chalcopyrite is locally part of a chalcopyrite-sphalerite-galena-renierite-chalcocite assemblage (Fig. 6.6-2 g). Bornite is associated with sphalerite, galena, tennantite, chalcocite and occasionally renierite in disseminated and massive mineralization styles (Figs 6.6-2 a, d; 6.6-2 b, f-h). Locally, bornite is replaced by galena, that is associated with fractures that are filled with cerussite (Fig. 6.6-2 e). Digenite, chalcocite, and covellite (Fig. 6.6-2 h) are only minor constituents in the ore. Covellite occurs as a replacement of sphalerite and bornite, and is directly associated with brittle deformed pyrite, renierite, bornite, sphalerite, and galena.

6.6.2 Bulk Ore geochemistry

A correlation matrix was generated using bulk ore Geochemical data, in order to determine the correlations between Ga, Ge and In with other elements which is summarised in Table 6.6-1. The highest correlation coefficient is observed between Mo and Co (r = 0.99), Nb and V (r = 0.99), Ba and V (r =0.98), Ba and Nb (r =0.95), Sb and Se (r = 0.95), Ga and Sb (r = 0.97), Ga and Se (r = 0.97), As and Ga (r =0.90), Mo and W (r= 0.90), Co and Tl (r = 0.89), Co and Ni (r = 0.88), Cu and Ag (r = 0.88), As and Sb (r =0.87), As and W (r = 0.87), Cr and Nb (r =0.86), Cr and V (r = 0.85), Cd and Zn (r = 0.84), and Ga and W (r = 0.82).

Table 6.6-1 correlation matrix between selected elements from the Tsumeb ore. Green colour scheme is assigned to 1 (positive correlation), yellow is assigned to 0 (no correlation), and red is assigned to -1 (negative correlation).

	Ag	*As*	*Ba*	*Bi*	*Cd*	*Co*	*Cr*	*Cu*	*Fe*	*Ga*	*Ge*	*In*	*Mo*	*Mn*	*Nb*	*Ni*	*Pb*	*Sb*	*Se*	*Tl*	*W*	*V*	*Zn*
Ag	1.00																						
As	-0.27	1.00																					
Ba	-0.16	-0.32	1.00																				
Bi	0.06	-0.24	0.00	1.00																			
Cd	-0.15	-0.13	-0.34	0.21	1.00																		
Co	0.08	-0.02	-0.17	0.40	0.47	1.00																	
Cr	0.12	-0.33	0.82	0.00	-0.20	-0.30	1.00																
Cu	0.88	0.15	-0.29	-0.21	-0.33	-0.15	0.04	1.00															
Fe	0.11	-0.04	-0.10	-0.20	0.26	-0.16	0.00	0.18	1.00														
Ga	-0.21	0.90	-0.34	-0.34	-0.07	0.18	-0.34	0.17	0.04	1.00													
Ge	-0.32	0.65	-0.29	-0.44	0.08	-0.12	-0.27	0.05	0.60	0.76	1.00												
In	-0.07	0.45	-0.18	0.06	0.26	0.79	-0.22	-0.03	-0.23	0.68	0.27	1.00											
Mo	0.12	-0.03	-0.18	0.50	0.45	0.99	-0.27	-0.13	-0.23	0.13	-0.20	0.76	1.00										
Mn	-0.31	-0.54	0.19	0.30	0.16	-0.03	0.14	-0.51	0.05	-0.48	-0.23	-0.27	-0.05	1.00									
Nb	-0.05	-0.25	0.95	-0.12	-0.26	-0.08	0.86	-0.14	-0.02	-0.20	-0.18	-0.01	-0.11	0.16	1.00								
Ni	-0.07	0.28	-0.20	0.24	0.51	0.88	-0.40	-0.17	0.04	0.37	0.14	0.73	0.83	-0.14	-0.11	1.00							
Pb	-0.18	0.67	-0.38	0.21	0.29	0.32	-0.38	-0.04	-0.31	0.58	0.23	0.54	0.34	-0.55	-0.37	0.45	1.00						
Sb	-0.24	0.87	-0.43	-0.21	0.08	0.32	-0.48	0.09	0.10	0.97	0.77	0.73	0.27	-0.44	-0.31	0.51	0.64	1.00					
Se	-0.05	0.84	-0.39	-0.23	-0.12	0.32	-0.39	0.28	-0.04	0.97	0.64	0.76	0.29	-0.51	-0.24	0.43	0.56	0.95	1.00				
Tl	0.05	-0.16	0.24	0.50	0.39	0.89	0.11	-0.24	-0.23	-0.01	-0.30	0.67	0.90	0.00	0.29	0.74	0.24	0.09	0.10	1.00			
W	-0.19	0.87	-0.25	-0.42	-0.27	-0.03	-0.40	0.20	0.13	0.82	0.65	0.33	-0.09	-0.42	-0.17	0.34	0.37	0.78	0.76	-0.22	1.00		
V	-0.10	-0.29	0.98	-0.01	-0.27	-0.08	0.85	-0.22	-0.07	-0.26	-0.24	-0.06	-0.10	0.20	0.99	-0.11	-0.35	-0.36	-0.31	0.32	-0.21	1.00	
Zn	-0.24	-0.10	-0.33	-0.08	0.84	0.10	-0.20	-0.29	0.59	0.01	0.43	0.01	0.03	0.19	-0.26	0.20	0.12	0.12	-0.12	-0.02	-0.17	-0.28	1.00

6.6.3 Trace elements in sulfide mineralization

A total of 48 EMP spot analyses was performed on enargite, sphalerite, renierite, chalcopyrite, pyrite, galena, and covellite grains. Trace element contents vary significantly from mineral to mineral; they are summarized in Table 6.6-2 and illustrated in Fig. 6.6-3. Calculation of average, median and standard deviation was done with the assumption that concentration was zero for spot analyses below the analytical detection limit (LOD).

<u>Renierite</u>

Renierite has from 38.7 to 49.9 wt% Cu (av. 44.2 wt%), 5.07 to 12.7 wt% Ge (av. 8.21 wt%), and 1.39 to 4.84 wt% As (av. 2.72 wt%). Iron and Zn concentrations are erratic, ranging between 4.31 wt% and 13.9 wt% (av. 12.1 wt%), and 0.12 wt% and 9.34 wt% (av. 2.04 wt%), respectively. There are traces of Ag, Cd, Sb, and Pb in some grains,

however, they are relatively low with values ≤0.5 wt% (av. ≤0.05 wt%). Only two out of 38 spots had detectable concentrations of Co, with 0.004 and 0.005 wt%.

Sphalerite

Zinc concentrations range from 63.4 to 66.6 wt%, with an average of 65.2 wt%. Sphalerite is known to be one of few sulfide minerals having a great potential to host Ge and Ga (Frenzel et al., 2016). Concentrations of Ga in sphalerite range from 0.014 to 0.58 wt% (av. 0.11 wt%); however, no Ge was detected in any of the sphalerite grains analysed. A few grains have measurable Ag, In, Sb, and Pb, with concentrations of ≤0.040 wt%, ≤0.013 wt%, ≤0.19 wt%, and ≤0.1 wt%, respectively. Iron is a common minor substituent for Zn in sphalerite (Frenzel et al., 2016) however, Fe concentrations vary only between 0.01 and 0.16 wt% (av. 0.04 wt%).

Enargite

Copper and As, the main constituents of enargite, have quite narrow concentration ranges from 49.3 to 49.7 wt%, and 17.0 to 18.0 wt%, with averages of 49.6 wt% and 17.7 wt%, thereby slightly deviating from the stoichiometric Cu and As concentrations of 48.4 wt% and 19.0 wt%. Concentration of Ga is generally <0.0036 wt%. Zinc and Ge concentrations vary distinctly, having maximum concentrations of 0.5 wt% (av. 0.19 wt%) and 0.78 wt% (av. 0.36 wt%), respectively, including concentrations <LOD. Cadmium and Sb concentrations are mostly <LOD and give maximum values of 0.13 wt% and 0.12 wt%, respectively. Concentrations of Ag and Pb are generally low, with at maximum 0.05 wt%.

Chalcopyrite

Copper and Fe concentrations range from 34.7 to 36.8 wt% (av. 35.8 wt%) and 28.1 to 29.3 wt% (av. 28.8 wt%), which is within the range of normative chalcopyrite which generally has Fe 30.5 wt% and Cu 34.5 wt% (Haldar and Tisljar, 2014). Gallium

concentrations are generally low in chalcopyrite, with an average of 0.05 wt% and a maximum concentration of 0.26 wt%. Arsenic, Ag, Cd, and Pb concentrations are mostly <<0.05 wt%.

*Table 6.6-2 Basic statistics for EMP trace element data of the different sulfide minerals in wt%. N = number, * below detection limit. Full EMP results are in Appendix 6-3.*

Elements			S	Fe	Co	Ni	Cu	Zn	Ga	Ge	As	Ag	Cd	In	Sb	Pb
Detection limit (ppm)			68	53	26	41	68	76	36	54	63	98	120	27	64	92
Renierite	$N_{analysis}$ = 38	Min	31.43	4.31	*	*	38.73	0.12	0.00	5.07	1.39	0.00	0.00	*	0.00	0.00
		Max	32.94	13.87	*	*	49.87	9.34	0.29	12.71	4.84	0.12	0.22	*	0.18	0.05
	N_{sample} = 8	Mean	32.23	12.11	*	*	44.18	2.04	0.12	8.21	2.72	0.04	0.05	*	0.04	0.01
		Median	32.17	13.42	*	*	43.49	1.90	0.14	8.32	2.27	0.03	0.04	*	0.04	0.00
		SD	0.41	2.97	*	*	2.26	1.44	0.10	1.66	1.08	0.03	0.04	*	0.04	0.02
Sphalerite	$N_{analysis}$ = 57	Min	32.15	0.00	*	*	0.01	63.40	0.00	0.00	0.02	0.00	0.40	*	*	0.00
	N_{sample} = 10	Max	33.38	0.20	*	*	2.19	66.55	0.58	0.08	0.07	0.04	2.81	*	*	0.11
		Mean	32.74	0.04	*	*	0.28	65.27	0.11	0.00	0.03	0.01	1.53	*	*	0.02
		Median	32.73	0.01	*	*	0.07	65.24	0.04	0.00	0.03	0.00	1.46	*	*	0.00
		SD	0.35	0.05	*	*	0.48	0.77	0.14	0.01	0.01	0.01	0.89	*	*	0.03
Enargite	$N_{analysis}$ = 8	Min	32.02	*	*	*	49.30	0.00	*	0.00	17.04	0.00	0.00	*	0.00	0.00
	N_{sample} = 2	Max	32.48	*	*	*	49.73	0.50	*	0.78	18.00	0.03	0.13	*	0.12	0.02
		Mean	32.23	*	*	*	49.61	0.19	*	0.36	17.66	0.01	0.07	*	0.06	0.00
		Median	32.21	*	*	*	49.63	0.12	*	0.30	17.84	0.00	0.07	*	0.06	0.00
		SD	0.13	*	*	*	0.13	0.18	*	0.30	0.37	0.01	0.05	*	0.04	0.01
Chalcopyrite	$N_{analysis}$ = 18	Min	34.17	28.13	*	*	34.71	0.00	0.00	*	0.00	0.00	0.00	*	*	0.00
	N_{sample} = 4	Max	34.65	29.32	*	*	36.81	1.76	0.26	*	0.04	0.09	0.03	*	*	0.04
		Mean	34.40	28.83	*	*	35.81	0.43	0.05	*	0.01	0.04	0.01	*	*	0.01
		Median	34.40	29.03	*	*	35.81	0.19	0.01	*	0.00	0.04	0.02	*	*	0.00
		SD	0.14	0.37	*	*	0.55	0.56	0.08	*	0.01	0.02	0.01	*	*	0.01
Pyrite	$N_{analysis}$ = 24	Min	52.97	45.57	0.00	0.00	0.00	0.00	0.00	0.00	*	0.00	0.00	*	0.00	0.00
	N_{sample} = 6	Max	55.00	46.77	0.10	0.30	0.74	0.40	0.02	0.05	*	0.04	0.06	*	0.02	0.30
		Mean	53.56	46.32	0.01	0.03	0.17	0.06	0.01	0.01	*	0.01	0.02	*	0.00	0.02
		Median	53.39	46.35	0.00	0.00	0.05	0.00	0.01	0.01	*	0.00	0.02	*	0.00	0.01
		SD	0.49	0.26	0.03	0.07	0.23	0.12	0.00	0.01	*	0.01	0.02	*	0.01	0.06

Table 6-6.2 continues……

Elements			S	Fe	Co	Ni	Cu	Zn	Ga	Ge	As	Ag	Cd	In	Sb	Pb
Detection limit (ppm)			68	53	26	41	68	76	36	54	63	98	120	27	64	92
Tennantite	$N_{analysis}$ = 61	Min	24.81	0.00	0.00	*	40.15	0.00	0.00	0.00	8.73	0.00	0.00	*	0.00	0.00
	N_{sample} = 13	Max	32.22	2.18	0.03	*	49.64	9.27	0.07	0.08	20.72	0.58	1.66	*	3.78	0.13
		Mean	27.60	0.52	0.01	*	43.89	8.10	0.02	0.01	17.72	0.06	0.42	*	0.85	0.01
		Median	27.66	0.08	0.01	*	43.95	8.49	0.01	0.00	18.41	0.03	0.27	*	0.65	0.00
		SD	0.86	0.67	0.00	*	1.55	1.27	0.02	0.01	2.33	0.10	0.36	*	0.85	0.03
Galena	$N_{analysis}$ = 94	Min	14.25	0.00	*	*	0.00	0.00	0.00	*	*	0.00	0.00	*	0.00	83.95
	N_{sample} = 14	Max	15.00	0.04	*	*	1.02	0.44	0.02	*	*	0.12	0.11	*	0.07	87.25
		Mean	14.50	0.00	*	*	0.07	0.04	0.01	*	*	0.01	0.01	*	0.00	85.77
		Median	14.48	0.00	*	*	0.02	0.00	0.01	*	*	0.00	0.00	*	0.00	86.00
		SD	0.13	0.01	*	*	0.15	0.09	0.01	*	*	0.02	0.02	*	0.01	0.91
Chalcocite	$N_{analysis}$ = 76	Min	18.73	0.00	*	*	71.55	0.00	0.00	0.00	0.00	0.00	0.00	*	0.00	0.00
	N_{sample} = 10	Max	24.44	5.55	*	*	79.95	0.54	0.74	0.04	0.09	0.65	0.16	*	0.08	0.17
		Mean	21.98	0.39	*	*	77.27	0.05	0.01	0.00	0.04	0.16	0.02	*	0.01	0.02
		Median	21.99	0.06	*	*	77.34	0.00	0.00	0.00	0.03	0.17	0.00	*	0.00	0.01
		SD	0.72	0.74	*	*	1.16	0.11	0.09	0.01	0.01	0.11	0.03	*	0.01	0.03
Bornite	$N_{analysis}$ = 56	Min	22.02	0.02	*	*	67.71	0.00	*	*	0.00	0.06	0.00	0.00	0.00	0.00
	N_{sample} = 5	Max	25.46	7.81	*	*	77.88	0.71	*	*	0.05	1.04	0.07	0.02	0.03	0.08
		Mean	23.99	5.19	*	*	72.08	0.10	*	*	0.04	0.44	0.04	0.01	0.01	0.01
		Median	24.07	5.49	*	*	71.71	0.00	*	*	0.04	0.44	0.05	0.01	0.02	0.00
		SD	0.64	1.25	*	*	1.67	0.18	*	*	0.01	0.26	0.02	0.00	0.01	0.02

Pyrite

Sulfur and Fe concentrations in pyrite range from 53.0 to 55.0 wt% (av. 53.6 wt%) and 45.6 to 46.7 wt% (av. 53.6 wt%), respectively. Gallium and Ge concentrations are generally low, ranging from <0.0036 to 0.02 wt% (av. 0.01 wt%) and <0.0054 to 0.05 wt% (av. 0.01 wt%), respectively. The Cu, Zn, and Pb contents range from <0.0068 to 0.74 wt%, <0.0076 to 0.04 wt%, and <0.0092 to 0.30 wt%, with averages of 0.17 wt%, 0.06 wt%, and 0.02 wt%, respectively. Silver and Cd contents range from <0.0098 to 0.04 wt% (av. 0.01 wt%) and <0.012 to 0.06 wt% (av. 0.02 wt%), respectively.

Tennantite

Tennantite was analysed in 13 samples, with Cu and S contents ranging from 40.2 to 49.6 wt% and 24.8 wt% to 32.2 wt%, and corresponding averages of 43.9 and 27.6 wt%, respectively. There is a great variation in As contents in tennantite, with concentrations ranging from 8.73 to 20.7 wt% (av. 17.7 wt%). Other elements detected in tennantite are Fe (<0.0053 - 2.18 wt%; av. 0.52 wt%), Co (<0.0026 - 0.03 wt%; av. 0.01 wt%), Zn (<0.0076 - 9.27 wt%; av. 8.10 wt%), Ga (<0.0036 - 0.07 wt%; av. 0.02 wt%), Ge (<0.0054 - 0.08 wt%; av. 0.01 wt%), Ag (<0.0098 - 0.58 wt%; av. 0.07 wt%), Cd (<0.012 - 0.13 wt%; av. 0.07 wt%), Sb (<0.0064 - 3.78 wt%; av. 0.85 wt%), and Pb (<0.0092 – 0.13 wt%; av. 0.01 wt%).

Galena

Galena was analysed in 14 samples with Pb and S contents ranging from 84.0 to 87.3 wt% (av. 85.8 wt%) and 14.2 to 15.0 wt% (av.14.5 wt%), respectively. Copper, Zn, and Pb contents range from <0.0068 wt% to 1.02 wt%, <0.0076 wt% to 0.44 wt%, and <0.0092 wt% to 0.17 wt%, with corresponding averages of 0.07 wt%, 0.04 wt%, and 0.02 wt%, respectively. Gallium, Ag, Cd, and Sb concentrations are generally low and range from

<0.0036 wt% to 0.02 wt%, <0.0098 wt% to 0.12 wt%, <0.012 wt% to 0.11 wt%, and <0.0064 wt% to 0.08 wt%, respectively, with all elements having averages of 0.01 wt%.

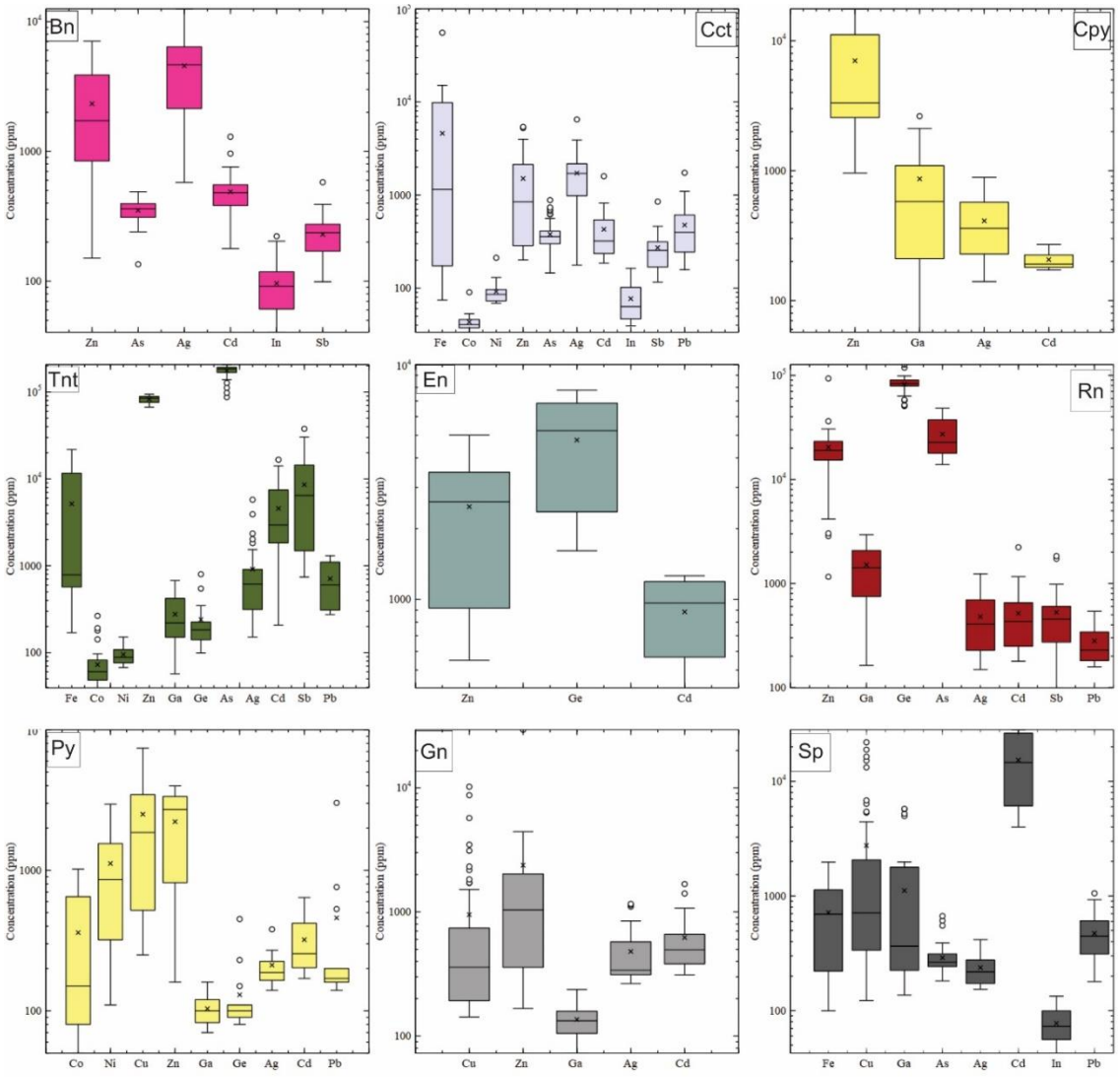

Fig. 6.6-3 Trace element content in sulfides of the Tsumeb deposit. Abbreviations: Bn-bornite, Cct-chalcocite, Ccp-chalcopyrite, En-enargite, Gn-galena, Py-pyrite, Rn-renierite, Sp-sphalerite, Tnt-tennantite.

Chalcocite

Copper and S contents in chalcocite range from 71.6 to 80.0 wt%, and 18.7 to 24.4 wt%, respectively, with averages of 72.1 wt% and 22.0 wt%, respectively. The difference to the stoichiometric Cu value of 79.9 is mostly filled by Fe having a maximum value of 5.6 wt%. Gallium is detected in chalcocite in only one sample, with concentrations ranging between 0.01 and 0.74 wt%. Silver, Zn, and Pb concentrations range between <0.0098 wt% and 0.65 wt%, <0.0076 wt% and 0.54 wt%, and <0.0092 wt% and 0.17 wt%, with averages of 0.16 wt%, 0.05 wt% and 0.02 wt%, respectively. Arsenic, Cd, and Sb concentrations are relatively low with maximum contents of 0.04 wt%, 0.16 wt%, and 0.08 wt%, respectively.

Bornite

Sulfur and Cu concentrations range from 22.0 to 25.5 wt%, and 67.7 to 77.9 wt%, with average values of 24.0 and 72.1 wt%, respectively. Iron, Ag, Pb, and Zn contents range from 0.02 to 7.81 wt%, 0.06 to 1.04 wt%, <0.0092 wt% to 0.08 wt%, and <0.0076 wt% to 0.71 wt%, with average values of 5.19 wt%, 0.44 wt%, 0.01 wt%, and 0.10 wt%, respectively. Arsenic, Cd and Sb contents are low with ≤0.07 wt%. Bornite has traces of In with concentrations ranging from <0.0027 to 0.07 wt% (av. 0.04 wt%).

6.6.4 Reconnaissance Cu and Zn Isotopes

Copper and Zn isotopic compositions of the sulfide phases are presented in Table 6.6-3. The δ^{65}Cu values of bulk ore samples from massive ore range from 0.80 to 1.18‰, while samples from oxide ore display a δ^{65}Cu range of 1.13 to 1.35‰. Four of these samples give δ^{66} Zn ratios ranging from -0.01 to +0.13‰.

Table 6.6-3 Copper and Zn isotopic data of sulfide samples from the Tsumeb deposit, Namibia. Abbreviations: Cal-calcite. Cc-chalcocite, Ccp-chalcopyrite, Dg-digenite, Gr-germanite, Gn-galena, Ren-renierite, Sph-sphalerite, Tent-tennantite, Sd-siderite.

Sample ID	Level	Ore assemblage	δ^{65}Cu (‰)	SE	δ^{66}Zn (‰)	SE	Cu (mg/kg)	Zn (mg/kg)
04546	17	Gn, Sph, Tenn, Py, Dg	1.319	0.016	-0.013	0.009	66825	35344
04618	17	Gn, Sph, Ccp, Tenn, Ren, Cc	1.132	0.001			358625	
04635	18	Gn, Sph, Py, Tenn	1.353	0.022	0.126	0.021	18794	24762
08277	30	Py, Ren, Sph, Tenn, Py, Gn, Bn	1.175	0.010	0.070	0.004	35632	135273
08298	32	Tenn, Py, Sph, Gn, Cc	0.919	0.016			342485	
08299	34	Tenn, Cc, Gn, Ren, Py, Sph, Ger, Sd	0.800	0.013	-0.110	0.002	72402	31792

6.7 Discussion

6.7.1 Paragenetic sequence

Based on ore textures, cross-cutting relations, and ore mineral assemblages, a paragenetic sequence is established alluding to at least three stages of mineralization (Fig. 6.7-1). The early stage is defined by the assemblage of pyrite (defined as pyrite 1), galena, tennantite, and renierite (brown). This stage is dominated by medium- to coarse-grained pyrite crystals of mainly subhedral to anhedral shape (Fig. 6.6-2 a). Additionally, these pyrite grains also occur as inclusions in galena. Galena grains exhibit multiple phases of

triangular deformation cleavage (Figs 6.6-1 b & 6.6-2 h). Tennantite and renierite crystals of this stage are fine- to medium-grained and are included in galena (Fig. 6.6-2 a). The second stage is defined by the assemblage carbonate-galena-pyrite-sphalerite. This stage is dominated by galena and sphalerite and only minor pyrite (defined as pyrite-2). The late stage is characterized by renierite and galena replacing pyrite and chalcopyrite, and minor bornite (Fig. 6.6-2 b, c). This late stage passes over into the alteration stage, which is defined by secondary minerals such as chalcocite (Fig. 6.6-2 f).

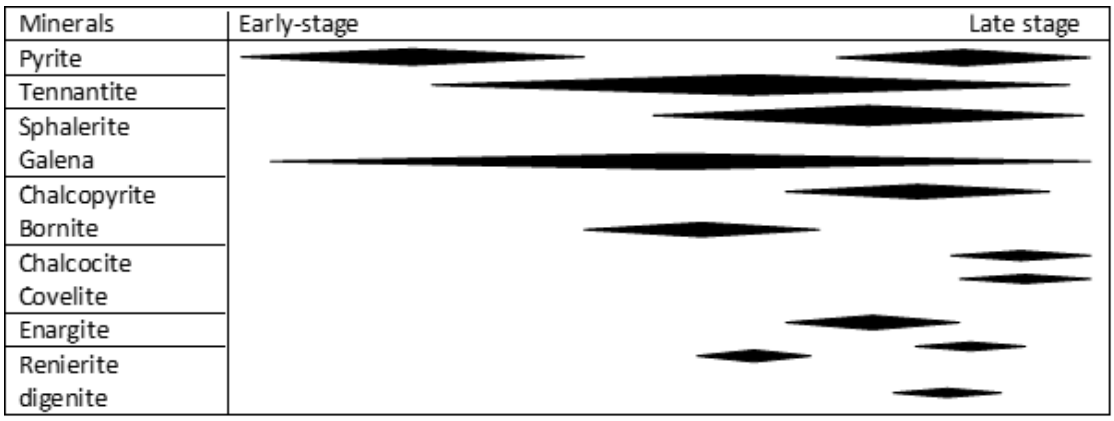

Fig. 6.7-1 Paragenetic sequence of sulfide minerals in the Tsumeb deposit samples from Level16, 17, 18, 19, 20, 29, 30, 32, and 46

6.7.2 Bulk ore geochemistry

The geochemical data of the Tsumeb ore in this study shows that the ore is dominated by concentration high of Pb (mean: 29.4 wt%), Cu (mean: 11.5 wt%), Zn (mean: 8.9 wt%) and as (mean: 1.17 wt%). Gallium (mean: 293 ppm), Ge (mean: 331 ppm), In (mean: 1.33 ppm), Cd (mean: 0.74 wt%), Fe (1.84 wt%), are all recorded in moderate concentrations.

There is a positive correlation among elements such as Ga and Sb, As, and W, which is suggestive of the relationship between Ga and the sulfide mineralisation.

6.7.3 Distribution of trace elements in sulfide minerals

Pyrite, galena, and sphalerite contain various trace elements in varying concentrations, either as inclusions or as solid solution. Concentrations of these elements can be used as a tool for mineral exploration, and they can provide useful information regarding the ore formation (e.g., Melekestseva et al. 2020; Qi et al., 2022).

Sphalerite has a high capability of incorporating minor and trace elements including critical metals such as Ga, Ge, and In (Alfantanzi and Moskalyk, 2003; Moskalyk, 2003; Höllel et al., 2007; Cook et al., 2009; Danyushevskiy, 2011; Belissont et al., 2016; Frenzel et al., 2016). Cations can be integrated in the crystal lattice by means of substitution for Zn or as microscale inclusions of other minerals (Cook et al., 2009). Fe^{2+}, Mn^{2+}, Co^{2+}, and Cd^{2+} have a similar ionic radius and the same oxidation state as Zn^{2+} (Cook et al., 2009; Bellissont et al., 2014; George et al., 2016). Their substitution within the crystal lattice of sphalerite can either be as a direct substitution for Zn^{2+} (Cook et al., 2009) and/or as a coupled substitution which is mainly defined by $2Zn^{2+} \leftrightarrow Cu^{+} + In^{3+}$ (Ye et al., 2011). Generally, Cd is the third most abundant trace element in solid solution of sphalerite (Wei et al., 2019) and its concentration can be high such that it can be extracted as a by-product (Achternbosch et al., 2009). Our data on sphalerite of the Tsumeb deposit (av. 1.53 wt% Cd) is slightly higher than the range of the average Cd concentration in sphalerite of 0.2 to 1.0 wt%, as defined by Cook et al. (2009). There is a slight correlation between Zn and Cd expressed by the coefficient of determination (R^2) at 0.63 (Fig. 6.7-2 b), suggesting

that Cd is integrated in sphalerite as solid solution defined by $Cd^{2+} \leftrightarrow Zn^{2+}$. Our data shows a clear non-correlation between Fe^{2+} and Zn^{2+} ruling out possible Zn^{2+} and Fe^{2+} substitution and suggesting that Fe could be incorporated as micro-inclusion of Fe-bearing minerals (Fig. 6.7-2 a). Gallium incorporation in sphalerite is principally possible via a coupled substitution defined by $2Zn^{2+} \leftrightarrow Cu^{+} + Ga^{3+}$ (Cook et al., 2009). Gallium concentration in our sphalerite samples ranges from few hundreds to thousand ppm, which is similar to concentrations reported in Melcher et al. (2006). There is no notable correlation between Ga and Zn, however, there is a slight positive correlation between Cu and Ga (Fig. 6.7-2 d; Fig. 6.7-2 e), suggesting a possible coupled substitution for Ga in sphalerite as defined in Cook et al. (2009). Correlation between Zn and In as defined by $R^2 = 0.5499$ is better in comparison to other trace elements such as Fe, Cu, and Ga (Fig. 6.7-2 c, a), suggesting a possible coupled substitution by $Cu^{+}In^{3+} \leftrightarrow Zn^{2+}Fe^{2+}$. Arsenic trace element concentrations above 100 ppm in Tsumeb sphalerite might indicate low temperatures during formation as proposed by Clark (1970), coupled with low Fe concentrations. Additionally, high Ga and Cd concentrations in sphalerite are also suggestive of low formation temperatures (Cook et al., 2009).

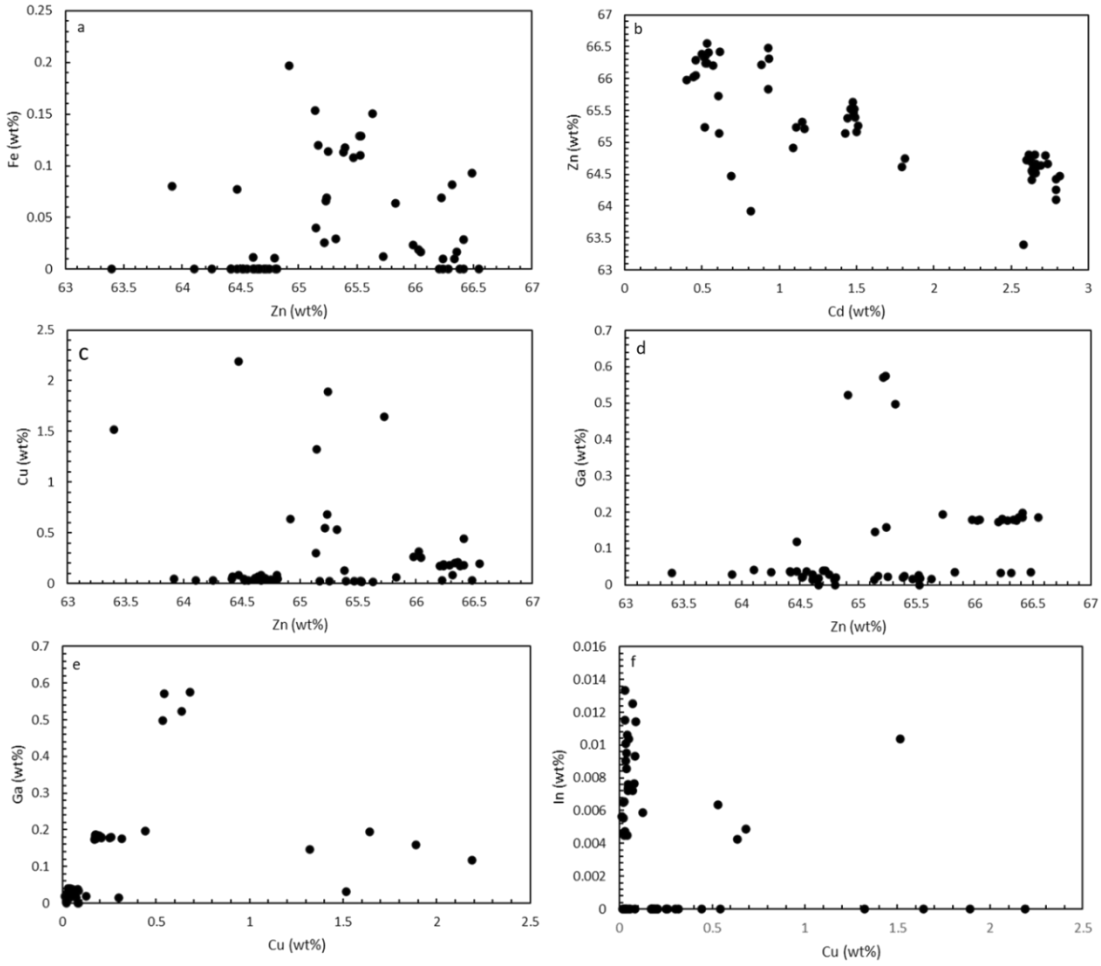

Fig. 6.7-2 Binary plots of trace elements in sphalerite of the Tsumeb deposit. A) Zn vs Fe; B) Zn vs Cd; C) Cu vs Zn; D) Ga vs Zn; E) Ga vs Cu; F) In vs Cu.

Substitution of cations such as Ag, Tl, Bi, and Sb for Pb in the crystal lattice of galena is quite common and occurs at various concentration ranges, and is mainly defined by the coupled substitutions of $Ag^{+} + (Bi,Sb)^{3+} \leftrightarrow 2Pb^{2+}$ as well as $(Ag,Cu,Tl)^{+} + (Bi,Sb)^{3+} \leftrightarrow 2Pb^{2+}$ (George et al., 2015). Traces of Cd, Cu, Fe, Mn, Ni, and Sn are mainly attributed to inclusions of other minerals in galena (Blackburn and Schwendeman, 1977). Silver concentration in Tsumeb galena ranges between hundreds to thousands ppm, which is in

accordance with general Ag concentrations in galena, as reported in Li et al. (2020). Additionally, Sb concentration in Tsumeb galena is very variable, ranging from <64 ppm to a significant concentration of about 1000 ppm. Owing to the fact, that Bi and Tl, that are typically involved in the substitution within the galena crystal, are not analysed by EMP, it is hard to determine the type of substitution involved in this case. However, Qi et al. (2022) stated that, despite the potential low concentrations of Bi and Tl, the general substitution reaction $Ag^{+} + Sb^{3+} \leftrightarrow 2Pb^{2+}$ is still the most acceptable theory for the incorporation of Ag in galena, and this is also considered for Tsumeb galena. However, Cu is the most abundant trace element in galena and occurs likely as solid solution in the galena structure.

Pyrite has the capability to incorporate various trace and minor elements in its crystal lattice either by substitution or inclusion of other mineral phases, enabling pyrite to be used over the years as a geochemical pathfinder in exploration of ore deposits (Steadman et al., 2015; 2021; Xie et al., 2020). It is noted that Tsumeb pyrite contains Cu, Zn, Ni, Cd, Pb, Ga, and Ge concentrations, with concentrations ranging from hundreds to thousands ppm. However, there is no difference in trace element abundance between the different mineral assemblages/mineral stages.

In comparison to other sulfides, such as sphalerite, galena, chalcocite and bornite, trace element incorporation in chalcopyrite is complex and rare (Cook et al., 2009; 2011; George et al., 2015, 2018). Our data shows that there is a variable Cd:Zn ratio between 0.006 and 0.04, implying that there is a variation in the physiochemical conditions during which the chalcopyrite grains crystallized, following the argumentation of George et al. (2018). This is also shown by applying the binary Zn-Cd classification proposed by Marfin et al. (2020) for discrimination of chalcopyrite environments, where the Tsumeb data are

very scattered. However, most Tsumeb chalcopyrite data plots in the high temperature field (Fig. 6.7-3).

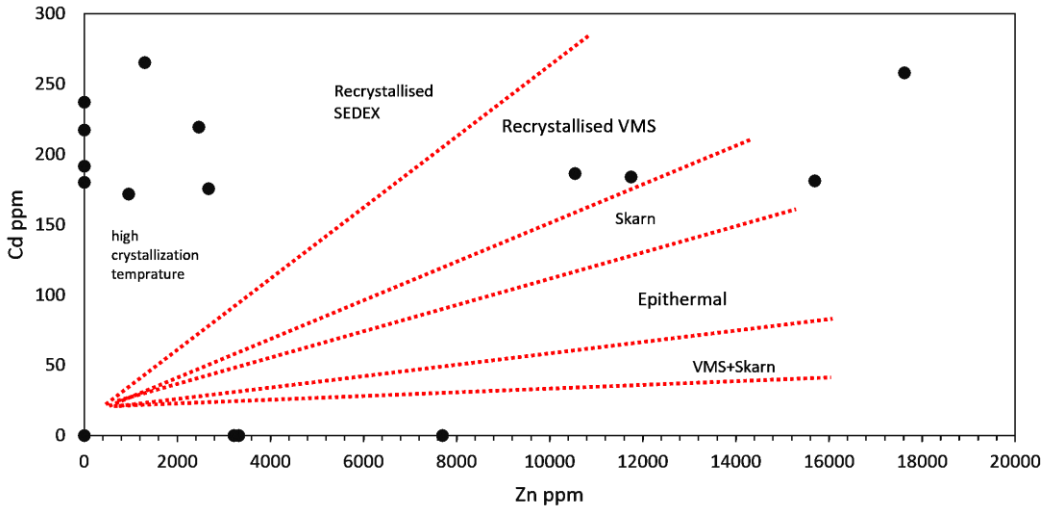

Fig. 6.7-3 Binary discrimination diagram based on Cd and Zn concentrations in chalcopyrite for Tsumeb chalcopyrite, showing formation temperature ranges for different ore types. Modified after Marfin et al. (2020).

6.7.4 Copper and zinc isotopes

Copper isotopes have been used to trace the ore forming processes especially in porphyry and epithermal environments (Mathur et al., 2012; Wu et al., 2017). The Tsumeb samples analysed for both bulk Cu and Zn isotopes consist of a mix of various sulfide minerals as summarized in Table 6.6-3. The Zn content is primarily from sphalerite, however, also renierite and tennantite contain notable amounts of Zn.

The range of bulk-ore Cu isotopes is positive and varies from 0.80 to 1.32‰ δ^{65}Cu, which is much greater than average continental crust (0.08 ± 0.17‰ δ^{65}Cu; Moynier et al., 2017).

The elevated $\delta^{65}Cu$ values likely indicate remobilization of Cu by supergene processes where reprecipitation of Cu^{1+} leads to enrichment of isotopically heavy Cu (Mathur et al., 2005). The Tsumeb Cu isotope values are also comparable to isotopic data of hypogene mineralization of porphyry deposits as described in Mathur et al. (2012) where Rayleigh fractionation leads to enrichment of isotopically heavy Cu during fluid evolution.

There is no apparent correlation between the Zn concentration and the Zn isotope composition (Fig. 6.7-4 b). The bulk-ore isotopic compositions of the Tsumeb deposit ($\delta^{66}Zn$ = -0.11 to 0.13‰) is below average continental crust (0.30 ± 0.07‰$\delta^{66}Zn$; Moynier et al., 2017), but within the range of Zn-rich massive sulfide deposits as reported in Liao et al. (2019) with a range of -0.19 to 0.14‰, or within the range of sphalerite from the Irish MVT deposits with -0.17 to 1.33‰ $\delta^{66}Zn$ (Wilkinson et al., 2005). This variability is likely due to Rayleigh fractionation on precipitation of ZnS from the ore fluid.

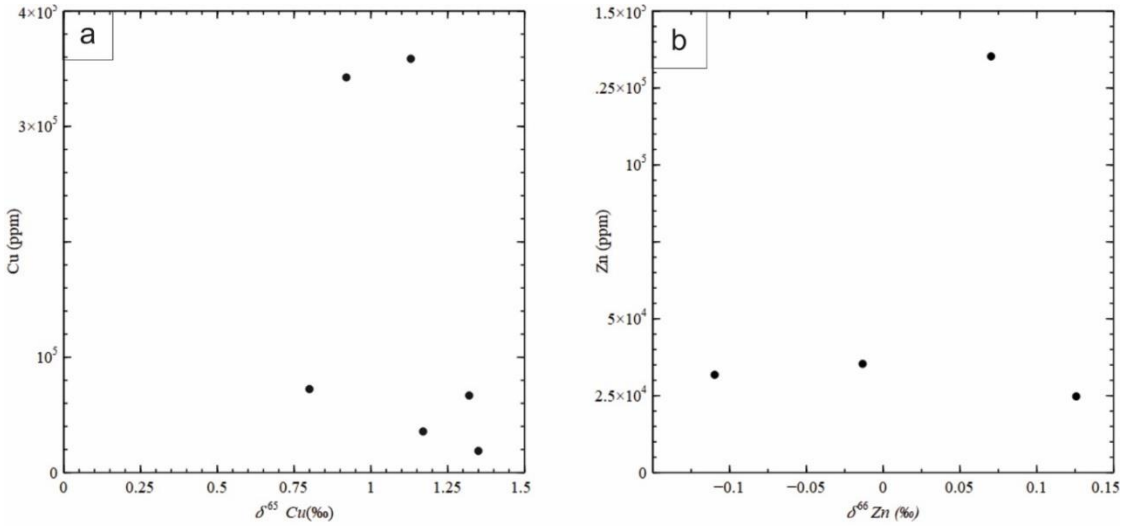

Fig. 6.7-4 Binary plots of the analysed samples (a) Cu isotopic composition vs Cu concentrations; and (b) Zinc isotopic composition vs Zn concentrations.

6.8 Conclusion

- The Tsumeb mineralization is related to at least three different stages, defined by the mineral assemblages: (1) pyrite-1-galena-tennantite-renierite (brown), (2) carbonate-galena-pyrite-2-sphalerite, (3) renierite-galena-chalcopyrite-chalcocite-digenite-renierite.
- Ga is mainly concentrated in renierite, sphalerite, and chalcopyrite, and is contained, to a lesser extent, in galena, tennantite, and chalcopyrite, while Ge is mainly concentrated in renierite and enargite with notable concentrations in tennantite and pyrite.
- Tsumeb Cu isotope values are also comparable to isotopic data of hypogene mineralization of porphyry deposits.
- Bulk-ore isotopic compositions of the Tsumeb deposit (δ 66Zn = -0.11 to 0.13 ‰) is below average continental crust but falls within the range of the massive sulfide or MVT deposits.

Declaration of Competing Interest

The authors declare that they have no known competing financial interests or personal relationships that could have appeared to influence the work reported in this paper.

7 Textural and trace element geochemical analysis of sulfide mineralisation of the Khusib Springs deposit, Namibia

Abstract

The Khusib Springs deposit, which is located in the limestone of the Maiberg Formation of the Tsumeb Subgroup, is a Cu-Zn-Pb-Ag polymetallic deposit. This chapter focuses on the sulfide mineralisation of the Khusib Springs deposit with emphasis on the concentration of trace elements in the different sulfide minerals by electron microprobe analyses (EPMA). The different sulfides show a wide range of textural features and chemical compositions. Petrographic results show that mineralisation can be categorized into two types: massive Cu-Pb-Zn sulfide mineralisation and massive to disseminated Cu-As-Ag sulfide mineralisation. Fractures, cataclastic texture and triple junction texture of pyrite crystals are suggestive of shear movement along fracture zones, while alteration of pyrite is due to metamorphism. Bulk rock composition of the analysed samples shows that the deposit is enriched in Cu, Zn, and Pb, with significant amounts of Mn, Ag, As, and Sb, and trace amounts of Cd, Cr, Co, Ga, Ge, Ni, V, and W. However, trace element concentrations of Co, Cd, Ga and Ge is below detection limit in the sulfide minerals, suggesting that trace elements are either not incorporated in the major sulfide crystals and instead occur in separate mineral phases, or the limit of detection (LOD) of the instrument is simply too high for these particular minerals, with detection limits of; Ag (LOD= 1039-1659 ppm), As (622-987 ppm), Cu (LOD=2537-3874 ppm), Fe (LOD=1155-2231 ppm), Ga (LOD= 950-2353 ppm), Ge (LOD= 1846-2506 ppm), In (LOD= 323-463 ppm), Mn (LOD= 610-973ppm), Pb (LOD= 2334-4372 ppm), S (LOD= 332-525 ppm), Sb (322-476

ppm), Zn (LOD= 3098-5192 ppm) . The negative Eu anomaly and a slight positive Gd anomaly observed from REE chondrite normalised plots are an indication of the involvement of ore formation fluids of low temperature.

Keywords: Khusib Springs, critical metals, sulfide mineralisation, EPMA, bulk rock geochemistry

7.1 Introduction

Trace elements incorporated in sulfide ore minerals have the potential of boasting the value of a deposit and can be used in aiding the understanding of the geological processes involved in the formation of a particular deposit, determining the type of deposit, and revealing mineral exploration potentiality of the deposit (e.g., Cook et al., 2009; Revan et al., 2014; George et al., 2015; Frenzel et al., 2016; Hu et al., 2020; Chu et al., 2022). Over the last decades trace element distribution within various sulfide mineralisations has been well studied (e.g., Cook et al., 2009, 2013; George et al., 2015; 2016; 2017; 2018; Li et al., 2019). The green industrial revolution depends on critical metals like Ga, Ge, In, and Cd, but because of their low crustal abundance, these are only found in association with other minerals particularly in deposits that are rich in zinc sulfide (Frenzel et al., 2014; Rudnick and Gao, 2014; Werner et al., 2017).

Neoproterozoic carbonate rock units of the Otavi Mountain Land (OML) host numerous sulfide mineralisations that have significant concentrations of the critical metals Ga, Ge and In, including the Khusib Springs deposit (Melcher et al., 2006). The Khusib Springs deposit was discovered in the early 1990s, and production took place between 1995 and 2003 (Melcher, 2003; Golden Deeps, 2020). Historically, the Khusib Springs mine had a total production of ~50 Kt of ore at grades of up to 10 wt% Cu, 1.9 wt% Zn, 1.8 wt% Pb and 584 g/t Ag (Melcher et al., 2006; Kamona and Günzel, 2007; Golden Deeps, 2020). There is a great potential for the discovery of more ores that are economically viable in the area, and exploration activities is still on going to date.

This chapter aims to characterise trace element distribution in the major sulfide ore minerals, chalcopyrite, galena, pyrite, digenite, tennantite and Ag-rich sulfides, while correlating this to ore textures. This is achieved by combining petrographic data for textural characteristics and mineralogy, with whole rock geochemical data obtained via ICP-MS, for geochemical characterisation and possible identification of the indicator elements, and EPMA analyses of the sulfide minerals for the distribution and concentration of the trace elements. Samples for this chapter were collected from the Khusib Springs' old, abandoned mine dump, as well as from two drill cores, a shallow hole KHD01 which is 50 m deep and KHD06 which is approximately 500 m deep (Fig. 7.1-1).

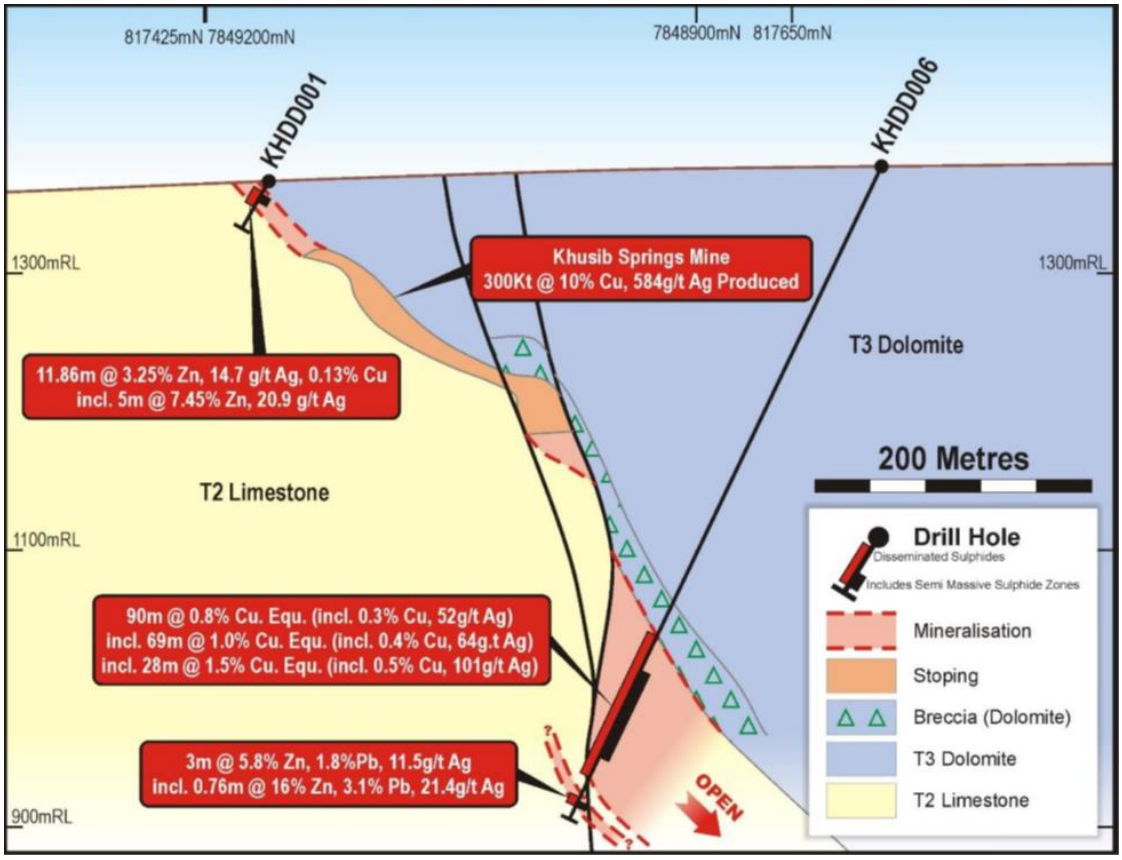

Fig. 7.1-1 Cross section outlining the two drill cores where samples were taken from for this chapter (Golden Deeps, 2022).

7.2 Geological Background

7.2.1 Regional Geology

Otavi Mountain Land is one of the most important mineral provinces in Namibia, which makes up part of the Damara Orogenic Belt (DOB) (Misiewicz, 1988). The province hosts various base metal deposits, including the Khusib Springs Cu-Zn-Pb-Ag sulfide deposit, which is hosted in the limestone of the Maiberg Formation in the Tsumeb Subgroup of the Otavi Group (Melcher et al., 2006). Tsumeb subgroup is subdivided into at least eight

lithozones namely T1 to T8 (Hedberg, 1979). Additionally, based on lithology, the Tsumeb subgroup is subdivided into four formations: the Ghaub Formation, forming up the basement of the subgroup, followed by the Maieberg and the Elandshoek Formations and the youngest, the Hüttenberg Formation (Lombaard et al., 1986; Kamona and Günzel, 2007). The Ghaub Formation is dominated by the Neoproterozoic Marinoan glaciogenic deposition as well as platform sedimentary units (Hoffmann et al., 2004; Domack and Hoffman, 2011; Bechstädt et al., 2018). The Maieberg Formation is deposited between 720 and 635 Ma and is widely distributed within the OML; it is dominated by thinly laminated limestone, associated with dolomite and cap carbonates (Hoffman et al., 1988; Kamona and Günzel, 2007). Deposition of the Maieberg Formation represents a change in environmental conditions from a glacial to a marine environment as depicted by the lithologies present in the formation (Hoffman et al., 1998; Melcher, 2003). Elandshoek Formation is made up of breccia, dolomite and sandstone (Hoffman et al., 2021). Units of this formation have been thrusted together with the Maieberg and Hüttenberg formation forming up the Mooilaagte thrust, over the Mulden Group phyllite as deduced from fold structures in the units (Miller, 2021). Hüttenberg Formation is made up of shale, limestones, dolomites and oolitic carbonate rocks that were deposited during the marine transgression on the margin of the Congo Craton (Kamona and Günzel, 2007; Delpomdor et al., 2018).

7.2.2 Deposit Geology

The at Khusib Springs exposed strata are primarily Neoproterozoic in age, which includes the limestones, various types of breccias as well as dolomite of the Maiberg Formation (Fig. 7.3-1). The deposit which is classified as a “Tsumeb-type” deposit is a small, high-

grade Cu-Zn-Pb deposit with a steeply plugging pipe-like lens structure, which is located at the contact between the T2 and T3 lithozones of the Maieberg Formation (Melcher, 2003; Melcher et al., 2006). Based on personal observations of recent KHD01 and KHD06 drill cores from Husab Energy Resources that are placed roughly about 400 meters apart (Fig. 7.1-1). The lithology in the Khusib Springs deposit is represented by meter-scale intervals of light grey dolomite, dark grey dolomite, laminated dolomite, a dolomite breccia unit, calcrete as well as calcite (Fig. 7.2-1). The uppermost part of the drill core is made up of calcareous materials that is followed by the alternation of the light and dark dolomite. The dark dolomite unit is a largely barren unit in terms of sulfide mineralization and is distinguished by fine grain texture with patches of light dolomite and calcite. The laminated dolomite layer is defined by fine grained dark dolomite bands that are embedded in a light dolomite matrix. Mineralisation is mainly found in the massive light dolomite that is characterised by brecciation (Fig. 7.2-1 c, d, g, f). The breccia is characterised by white dolomite that is replacing a grey dolomite matrix (Fig. 7.2-1 c, d). The light dolomite is characterised by a thin lamination texture that is defined by alternating light and dark layers in the millimetre to centimetre scale (Fig. 7.2-1 f). There are also sections that is characterised by the pull apart like character that is defined by dark dolomite clast that are brecciated zone of the light dolomite, associated with argillic alterations (Fig. 7.2-1 d, f).The Melcher et al. (2006) recognised at least two stages of mineralisation at the Khusib Springs deposit: a) the early stage mineralisation which is associated with the first deformation episodes of the DOB, which is characterised by sulfide minerals such as chalcopyrite, bornite, sphalerite, pyrite, tennantite, enargite, digenite, galena and Ge-colusite; and b) the later stage mineralisation, which is characterised by digenite, tennantite, pearceite-polybasite, which is linked to the 3rd

Damara Orogenic deformation episode (Melcher et al., 2006). Ore mineral textures are mainly of massive and disseminated mineralisation styles (Fig. 7.2-1 a-c).

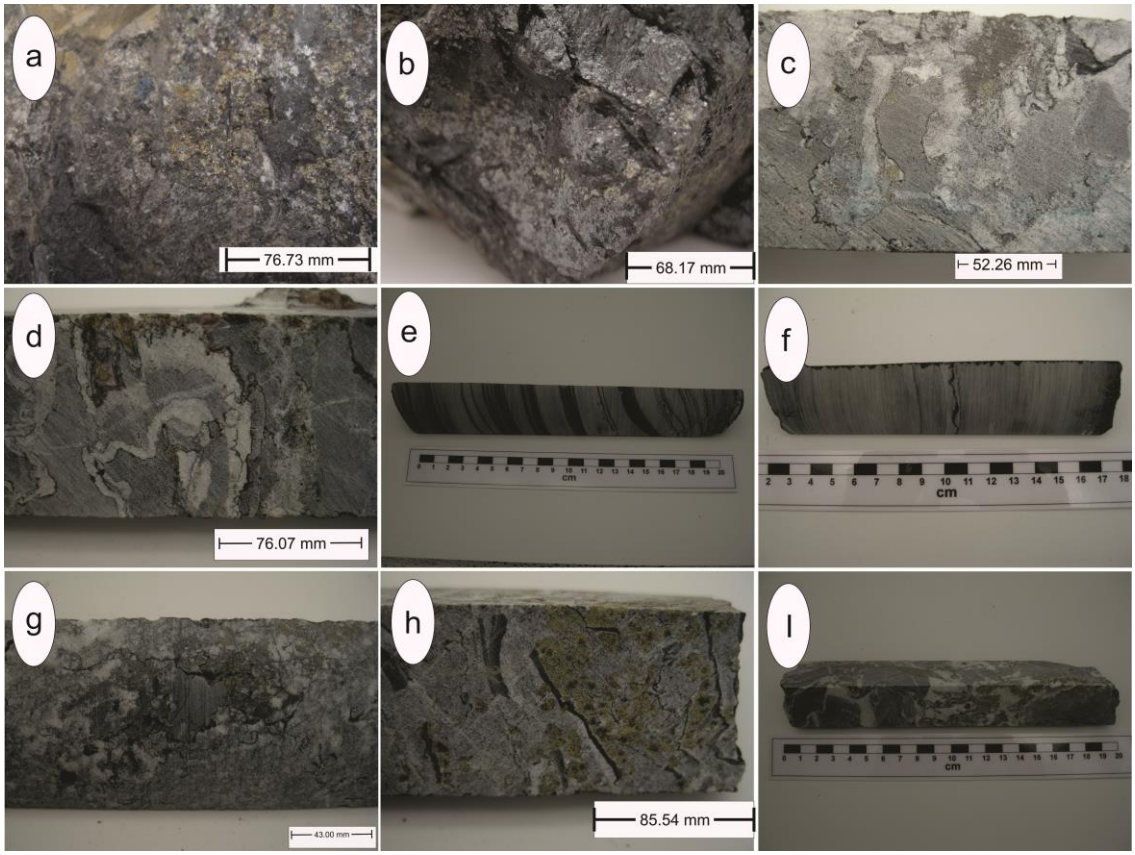

Fig. 7.2-1 Photographs showing host rock and ore textures from the Khusib Springs deposit. a) disseminated chalcopyrite and pyrite in carbonate host rock. b) massive galena associated with sphalerite in carbonate host rock. c) disseminated sulfides embedded in a brecciated zone. d) brecciated zone from one of the drill cores. e) intercalation of light and dark dolomite. f) laminated light dolomite. g) brecciated zone with patches of sulfide mineralization. h) pull apart clasts of dark dolomite embedded in the light dolomite with argillic alterations. I) brecciated zone from the footwall with veins filled with calcite.

7.3 Samples and methodology

7.3.1 Samples

About fifty-five representative samples collected for textural and chemical characterisation of the main ore minerals were taken at the Kuiseb Springs deposit. Twenty of these samples are grab samples from the historical mine dump and thirty-five were collected from recent drill cores, which were provided by Husab Energy Resources from EPL-3543 (Fig. 7.3-1). From the grab samples, twelve samples represent massive sulfide mineralisation, and from the drill core samples about twenty represent disseminated to semi-massive mineralisation. The list of samples collected is found in Appendix 7-1.

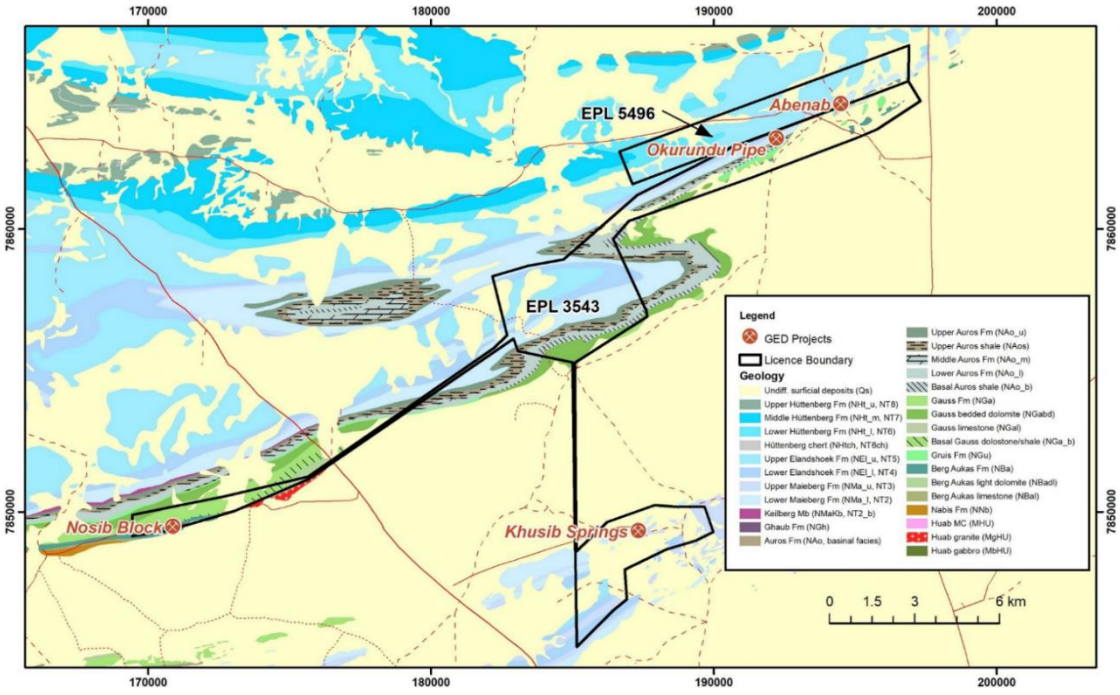

Fig. 7.3-1 Extract of the geological map of the Otavi Mountain Land showing the location of the Khusib Springs deposit and other deposits within the same vicinity (Golddeep, 2020).

7.3.2 Bulk ore geochemistry

Rock samples were submitted to Activation Laboratories LTD (ACTS LAB), Namibia, for sample preparation (crushing and pulverizing) while bulk rock trace element analysis was subsequently conducted by Activation Laboratories Ltd, Ontario, Canada. Trace elements were analysed by inductively coupled mass spectrometry (ICP-MS). Copper, Zn, Pb, As and Ag results were obtained using the 8-pre-oxide ICP assay method. The batch of samples was analysed including blanks, duplicates and standards, complying with the quality control procedures of ACTS LAB. The complete analytical results are provided in Appendix 7-2. Statistical parameters of the elemental concentrations of the bulk rock samples, as well as the correlation coefficients were determined for the samples analysed and are summarised in Table 7-4-1. The dataset with less than 25% of data that are below the lower analytical detection limit (LOD), were corrected using the methos adapted from Wood et al. (2011). This method stipulates that the data set below LOD are substituted by values of half the detection limit for the individual elements. However, it should be noted that this may lead to either an overestimation or underestimation of some of the statistical parameters.

7.3.3 Elemental analysis of sulfide minerals

Polished thin sections were prepared for petrographic analyses of all samples, whereby detailed textural and ore and host rock mineralogical analyses were carried out using a Zeiss Polarisations reflected and transmitted Axio A.1 microscope and favourable areas were chosen for compositional quantification by EPMA at the department of Mineral Resources, Clausthal University of Technology, Germany. Mineral phases quantitative

composition data were obtained using a Cameca SX Five FE electron probe microanalyser, running the Cameca own software for data capturing and processing. Quantitative analyses were performed with a beam current of 50 nA and an accelerating voltage of 15 kV. About seven trace elements were analysed: S, Mn, Fe, Cu, Zn, Ga, Pb, Ag, Sb, As, In and Ge. Full data set is presented in Appendix 7-3 a.

7.4 Results

Mineralogy and the textural characterisation of the ore mineralisation types at the Khusib Springs deposit, based on hand specimen and polished thin sections, are illustrated in Figure (7.5-1-3) whereas whole rock and trace element data of different sulfide minerals are presented in Tables 7.4-1 and 7.4-3). Sulfide minerals show a wide range of textures and chemical composition (see below).

7.4.1 Petrography

7.4.1.1 Host rock petrography

Matrix of the host rock consists of calcite, dolomite, quartz, muscovite, plagioclase, siderite, and sericite. While the most abundant minerals, dolomite and calcite, mostly do not express any specific texture, characteristic textures are observed for minor minerals. However, locally, dolomite grains occur as infill between quartz grains in the mineralized zones along with muscovite and plagioclase and exhibit a clear set of twin lamellae with high order interference colours along the twin lamellae (Fig. 7.4-1 c). Muscovite grains are frequently aligned along bedding planes and bend sometimes around quartz and feldspar grains as well as sulfide ore minerals (Fig. 7.4-1 a, e). Most of the muscovite grains show 2nd and 3rd order interference colours. Quartz grains are of fine to medium

grain size. They have subhedral to anhedral shape and exhibit an undulous extinction and a characteristic mosaic texture (Fig. 7.4-1 d, c, f). Minor plagioclase and microcline can have twin lamellae that are parallel or cross-cutting, respectively (Fig. 7.4-1 c, d).

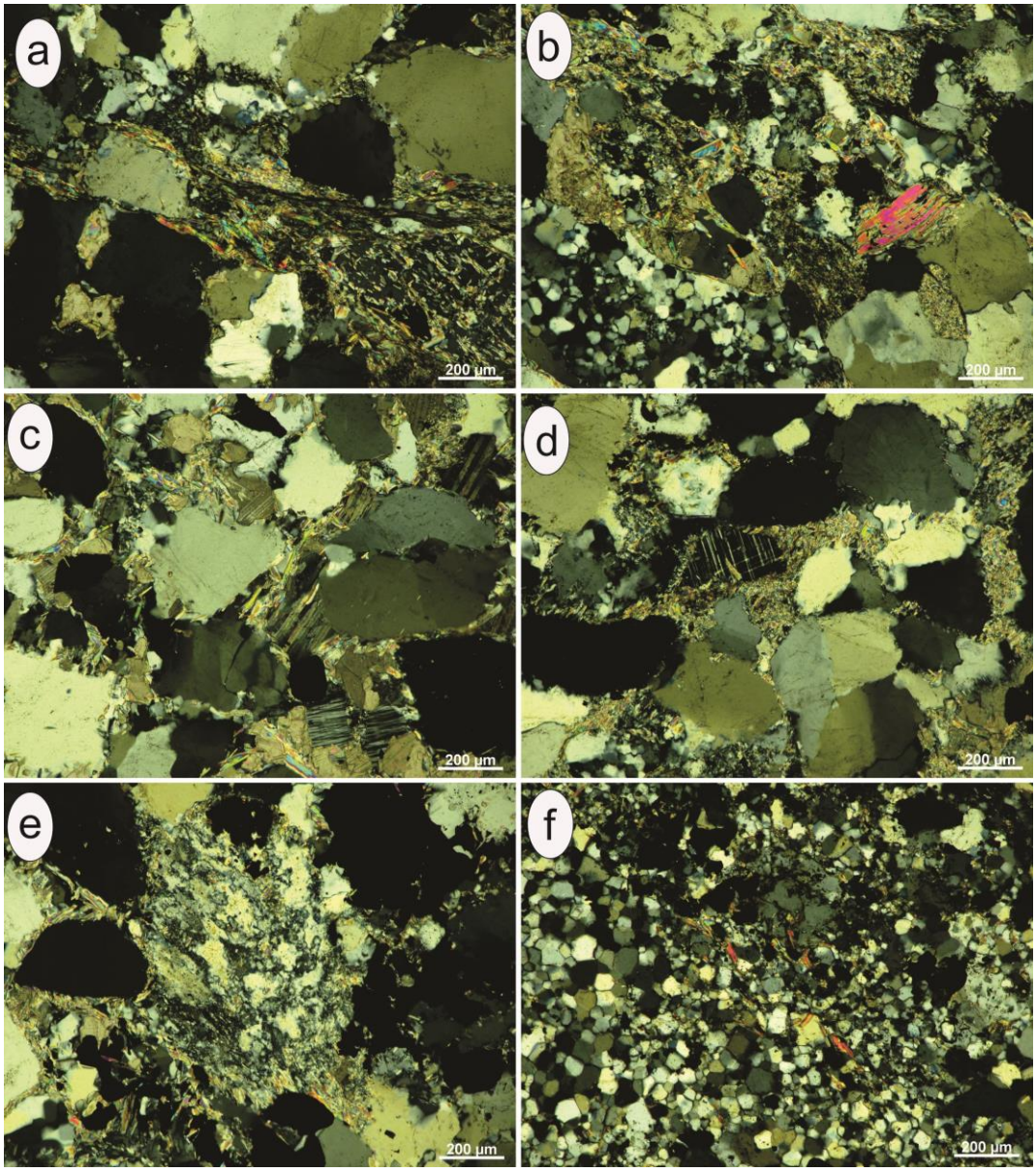

Fig. 7.4-1 Microphotographs showing various minerals and textures of the host rocks. a & b) Fine grained muscovite aligned along foliation between ore minerals and quartz grains.; c) calcite grains associated with quartz, plagioclase and sulfide minerals. d) Microcline exhibiting a tartan twinning pattern. e) Muscovite grains surrounding the opaque sulfide minerals. f) Mosaic texture defined by fine quartz grains.

7.4.1.2 Ore petrography

Pyrite grains can be fine to coarse grained and have either euhedral or subhedral shape (Fig. 7.4- 2 a-f). In some samples, pyrite has inclusions of galena, chalcopyrite, bornite and sphalerite. Disseminated pyrite crystals occur mainly within the fracture zones or in carbonate matrix (Fig. 7.4-2 b). Some of these pyrite crystals are truncated by fractures filled with tennantite and galena. Locally, a replacement texture is observed, defined by the replacement of pyrite by chalcopyrite which is then replaced by galena (Fig. 7.4-2 b) or by the replacement of pyrite by tennantite (Fig. 7.4-2a). In some samples, there are euhedral to subhedral pyrite grains embedded in a brittle deformed carbonate matrix (Fig. 7.4-2 b). There is recrystallisation of pyrite crystals that is defined by the triple-junction form texture (Fig. 7.4-2 d), which is indicative of alteration of pyrite grains due to metamorphism (Vokes and Craig, 1993). Additionally, there is an intergrowth between pyrite and sphalerite, chalcopyrite and galena and later tennantite grains (Fig. 7.4-2 c). Sphalerite is mainly a minor mineral occurring in association with tennantite, galena, pyrite and chalcopyrite (Fig. 7.4 3 b, c and h).

Galena is medium to coarse grained, having mainly subhedral to anhedral shape (Fig. 7.4-2). It occurs in assemblage with of tennantite, intergrown with pyrite, chalcopyrite, sphalerite and gangue minerals (Fig. 7.4 2 a, b, d, e - h). Most galena grains show a distinct deformation pit cleavage (Fig. 7.4 2 g). Chalcopyrite is a minor mineral phase which is typically associated with galena, pyrite, tennantite, sphalerite, and chalcocite (Fig. 7.4-2 c, e, f). It exhibits replacement texture, defined by chalcopyrite replaced galena and pyrite and as interstitial filling in microfractures of tennantite (Fig. 7.4 2 c, b and f). Bornite is a minor mineral in this, and it occurs to be replaced by pyrite, (Fig. 7.4-2i).

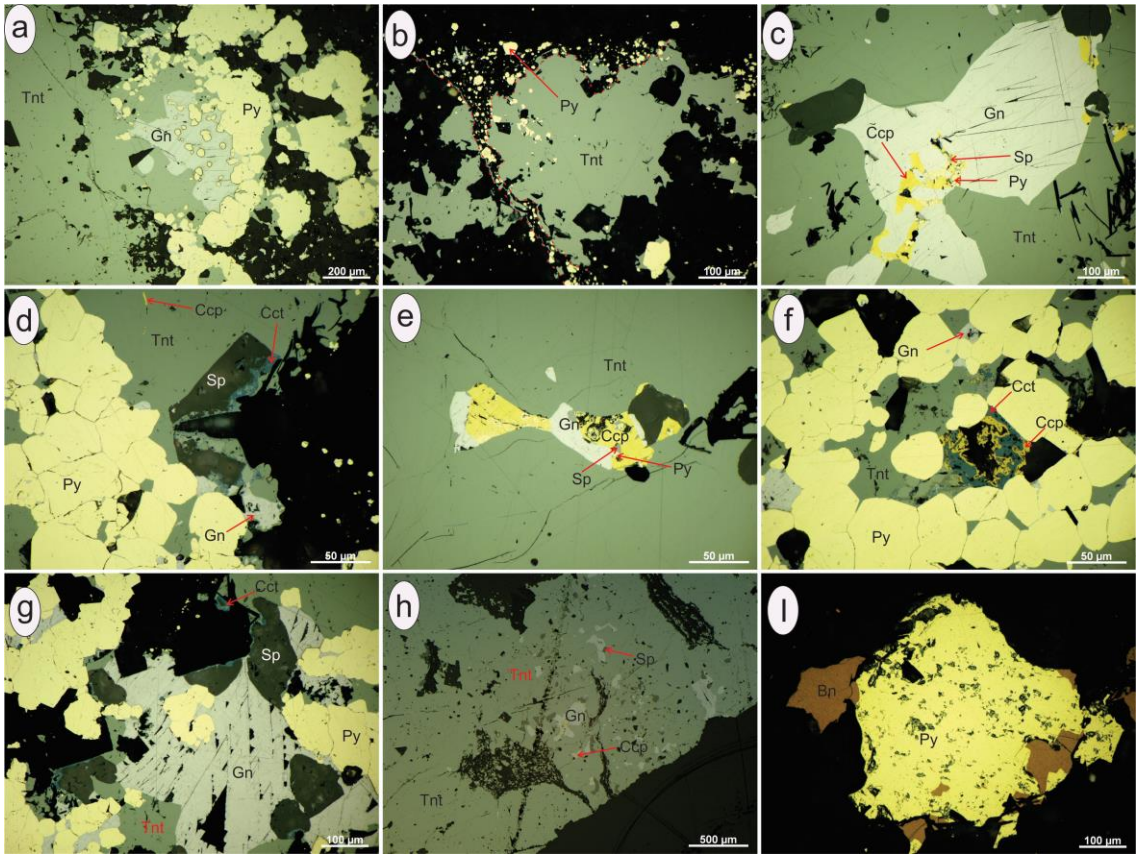

Fig. 7.4-2 Photomicrographs in reflected light of ore textures of the sulfide mineralization of the Khusib Springs deposit. A) Pyrite crystals recrystallized into subhedral grains in a galena and tennantite matrix.B) euhedral and subhedral grains of pyrite embedded in a fracture zone. C) Chalcopyrite, sphalerite and galena as inclusions in tennantite. D) triple junction boundaries between pyrite grains, in an assemblage with galena, chalcopyrite occurring as micro-inclusions in tennantite, and sphalerite being replaced by chalcocite. E) replacement texture defined by pyrite being replaced by chalcopyrite which is then replaced by galena. The assemblage sits in tennantite. F) chalcopyrite being replaced by chalcocite, and massive grains of pyrite associated with galena and tennantite. G) triangular cleavage pits in galena grains with subhedral grains of pyrite and replacement of sphalerite by chalcocite. H) tennantite with interstitial fractures filled with host rock, galena, sphalerite and chalcopyrite. I) Anhedral grains of bornite replaced by pyrite. Abbreviations: Cct- Chalcocite, Ccp-Chalcopyrite, Gn-Galena, Py-Pyrite, Sp-Sphalerite, Tnt-Tennantite.

7.4.2 Bulk rock geochemistry

Thirteen samples were chosen for whole rock geochemical analysis, of which the basic statistical parameters of selected elements are reported in Table 7.4-1. The full dataset is in Appendix 7-2. Copper is the dominant base metal element with a concentration mainly over 15 wt%, and in some instances even greater than 35 wt%, with an arithmetic mean (a.m.) of 11.8 wt% and sd 11.7%. The other known major base metal commodities at the Kuiseb Springs deposit are Zn, Pb and Ag, which have concentrations ranging between ~47 ppm and ~6.8 wt%, ~14 ppm and ~9.4 wt%, and ~1 ppm and 2000 ppm, with a.m.s of 1.7 wt%, 1.9 wt% and 655 ppm, respectively. Arsenic and Sb both have a wide range of concentrations ranging between 90 ppm and 13.7 wt% (a.m. 4.3 wt%) and 4 ppm and 1.7 wt% (a.m. 0.5 wt%), respectively. Manganese concentrations are between 220 ppm and 5110 ppm, with an a.m. of 2039 ppm and a SD of 1224 ppm. There are very strong positive correlations between Cr and Ni (r = 0.94), Cu and Sb (r = 0.92), and Zn and Bi (r = 0.91), and strong positive correlations between Ag and As (r = 0.88), Ag and Cu (r = 0.83), Ag and Cd (r = 0.83), Ag and Sb (r = 0.81), Ag and Zn (r = 0.85), Cu and Cd (r = 0.89), and Zn and Pb (r = 0.76). Additionally, there are further positive correlations between several elements as shown by the summarised correlation coefficients in Table 7.4-2.

Critical elements such as Ga and Ge, as well as the rare earth elements (REEs) occur only in low concentrations in all bulk rock samples. Gallium is above detection limit in all samples analysed, with concentrations ranging between 0.9 ppm and 14.2 ppm (a.m. 5.8 ppm; SD 3.3 ppm). Germanium is detected in 77% of the sample population, with a

concentration up to 30 ppm (a.m. 7.9 ppm; SD 11.2 ppm). Concentrations of REEs are relatively low, ranging between 0.05 and 6.2 ppm, with Tb, Tm, and Lu concentrations <LOD in 75% of the analysis. Total REE concentrations in the samples range from 4.5 ppm to 31.7 ppm. Normalizing REEs to chondrite (Fig. 7.5-3), while using the normalization values from Boynton (1984), the patterns are characterised by low enrichment of all light rare earth elements (LREEs), and heavy rare earth elements (HREEs), with a notable negative Eu anomaly and a slight positive Gd anomaly in some samples. According to Karakaya (2012), a negative Eu anomaly in sulfide mineralisations can be an indication of an involvement of fluids that are of low temperature (<200°C).

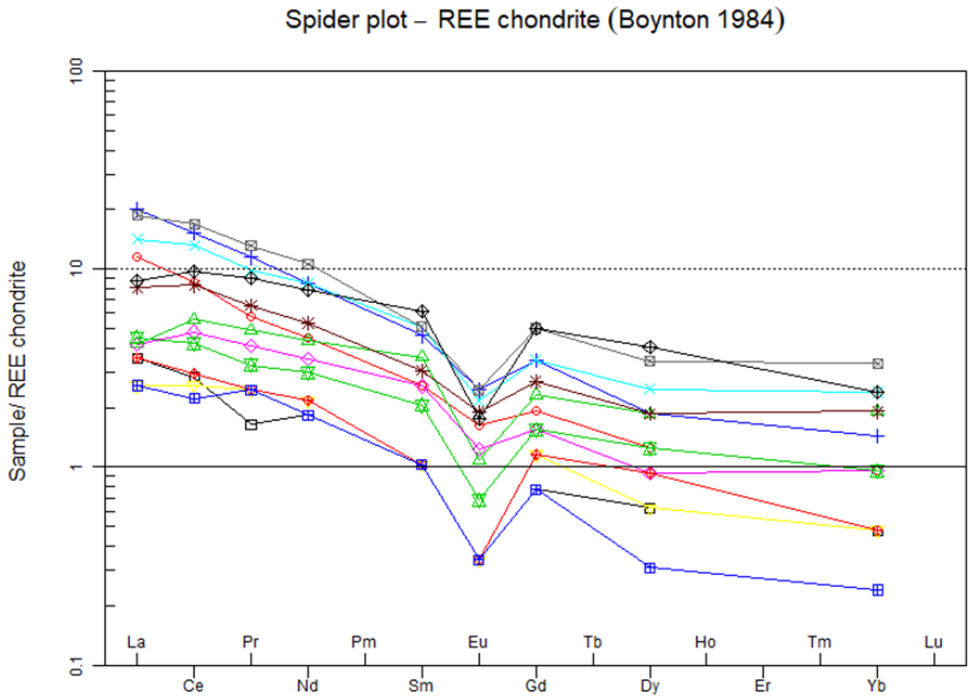

Fig. 7.4-3 Chondrite-normalised REE plots showing variations in the REE composition of Kuiseb Springs samples (normalising values used are from Boynton (1984)). All the samples shows a clear negative Eu anomaly. Some samples show in addition a slight positive Gd anomaly.

Table 7.4-1 Basic statistic parameters of trace and RE elements (in ppm; Fe in wt%) in the bulk rock samples of the Khusib Springs deposit. Number of samples analysed:13.

Elements	Min	Max	Arithmetic mean	Geometric mean	Median	Standard deviation
Ag	1.02	2000	655	168	176	748
As	97.8	137000	43341	10568	20000	45220
Ba	5	94	46.5	35.2	44	29.1
Bi	<0.02	2.02	0.7	0.5	0.3	0.7
Cd	0.3	188	56.8	25.1	31.6	53.6
Co	0.2	31.1	14.9	7.5	10.3	12.2
Cr	5	54	19.5	14.5	14	16.2
Cu	193	373000	118489	31862	166000	112874
Fe	0.08	9.41	2.6	1.5	1.8	2.4
Ga	0.9	14.2	5.8	4.6	5.4	3.4
Ge	<0.1	30.9	7.9	2.6	3.3	11.2
Hf	<0.1	0.8	0.4	0.3	0.3	0.2
Mn	220	5110	2039	1632	1870	1224.2
Mo	0.5	94.5	9.4	2.5	3	24.6
Nb	<0.1	2.8	0.96	0.6	0.6	0.9
Ni	1.6	13.9	6.515	5.3	5.5	3.9
Pb	13.9	94200	19411	3156	1480	29797
Rb	5.4	41.9	20.8	17.8	24.6	10.4
Sb	4.8	17400	5546.9	798	5400	5931
Sr	39.6	908	163	108	110	218
Th	0.5	3	1.4	1.2	1.2	0.8
U	0.5	7.2	2.1	1.6	1.5	1.7
V	5	28	14.5	12.5	17	7.3
W	0.4	28.7	4.323	1.9	2.3	7.4
Zn	47.2	67800	17438	6474	10300	18569
Zr	2	32	12.8	8.9	8	10.6
La	0.8	6.2	3.2	2.6	2.7	1.9
Ce	2.1	13.7	7.5	6.3	7	3.9
Pr	0.2	1.6	0.9	0.7	0.8	0.4
Nd	1.1	6.4	3.6	3.1	3.2	1.7
Eu	0.05	0.18	0.1	0.1	0.1	0.04
Sm	0.2	1.2	0.7	0.6	0.7	0.3
Gd	0.2	1.3	0.7	0.6	0.7	0.3
Tb	<0.1	0.2	0.1	0.1	0.1	0.04
Dy	0.2	1.3	0.6	0.5	0.6	0.3
Er	0.1	0.7	0.4	0.3	0.3	0.2
Yb	0.1	0.7	0.3	0.3	0.3	0.2

Table 7.4-2 Pearson's correlation coefficients of selected elements for bulk rock samples of the Khusib Springs deposit. Note: Pearson's correlation coefficient is based on 13 analysed samples, values with dark blue colour: r = 1; white: r = 0; red: r = -1. All other colours indicate the gradations inbetween. Correlation coefficients are interpreted as follows: r ≤0.5 = very weak correlation; r = 0.5-0.7 weak correlation; r = 0.7-0.9 strong correlation; r ≥ 0.9 very strong correlation.

	Ag	*As*	*Ba*	*Bi*	*Cd*	*Co*	*Cr*	*Cu*	*Fe*	*Ga*	*Ge*	*Hf*	*Mn*	*Mo*	*Nb*	*Ni*	*Pb*	*Rb*	*Sb*	*Sr*	*Th*	*U*	*V*	*W*	*Zn*
Ag	1.00																								
As	0.88	1.00																							
Ba	-0.66	-0.65	1.00																						
Bi	0.88	0.84	-0.55	1.00																					
Cd	0.83	0.69	-0.46	0.74	1.00																				
Co	0.70	0.76	-0.42	0.49	0.80	1.00																			
Cr	-0.31	-0.35	0.58	-0.16	-0.15	-0.16	1.00																		
Cu	0.83	0.76	-0.51	0.76	0.89	0.79	-0.13	1.00																	
Fe	0.47	0.54	-0.19	0.68	0.16	0.10	0.25	0.34	1.00																
Ga	0.39	0.32	0.12	0.39	0.52	0.44	0.22	0.40	0.21	1.00															
Ge	0.50	0.62	-0.48	0.35	0.12	0.40	-0.36	0.31	0.52	0.10	1.00														
Hf	-0.24	-0.29	0.67	-0.03	-0.13	-0.23	0.80	-0.07	0.35	0.01	-0.31	1.00													
Mn	-0.49	-0.54	0.26	-0.49	-0.44	-0.45	0.16	-0.46	-0.21	-0.08	-0.20	0.10	1.00												
Mo	-0.14	-0.10	0.28	-0.10	-0.09	-0.06	0.13	-0.17	-0.05	0.74	-0.06	-0.19	0.21	1.00											
Nb	-0.44	-0.48	0.48	-0.26	-0.38	-0.45	0.79	-0.28	0.32	-0.24	-0.28	0.78	0.28	-0.22	1.00										
Ni	-0.30	-0.28	0.65	-0.19	-0.06	0.01	0.94	-0.06	0.17	0.34	-0.37	0.75	0.12	0.24	0.69	1.00									
Pb	0.63	0.77	-0.42	0.56	0.34	0.50	-0.28	0.50	0.47	0.05	0.44	-0.14	-0.43	-0.14	-0.26	-0.17	1.00								
Rb	-0.40	-0.29	0.88	-0.27	-0.22	-0.12	0.46	-0.27	-0.11	0.28	-0.37	0.60	0.02	0.33	0.18	0.59	-0.11	1.00							
Sb	0.81	0.72	-0.48	0.64	0.80	0.78	-0.20	0.92	0.25	0.32	0.33	-0.12	-0.43	-0.17	-0.31	-0.09	0.69	-0.24	1.00						
Sr	-0.40	-0.44	-0.05	-0.39	-0.43	-0.48	-0.09	-0.43	-0.35	-0.48	-0.27	-0.26	-0.29	-0.10	0.08	-0.21	-0.30	-0.25	-0.39	1.00					
Th	-0.41	-0.44	0.86	-0.22	-0.23	-0.29	0.71	-0.23	0.04	0.22	-0.43	0.83	0.11	0.20	0.47	0.71	-0.29	0.86	-0.25	-0.16	1.00				
U	-0.39	-0.34	0.64	-0.25	-0.30	-0.26	0.47	-0.32	0.00	0.59	-0.23	0.26	0.18	0.85	0.12	0.54	-0.26	0.66	-0.32	-0.03	0.65	1.00			
V	-0.69	-0.57	0.88	-0.55	-0.51	-0.40	0.42	-0.50	-0.24	0.03	-0.45	0.56	0.41	0.31	0.32	0.53	-0.25	0.86	-0.42	-0.17	0.81	0.64	1.00		
W	0.37	0.55	-0.26	0.56	-0.06	-0.02	-0.13	0.12	0.82	0.20	0.62	-0.05	-0.18	0.22	-0.08	-0.17	0.53	-0.09	0.09	-0.23	-0.14	0.14	-0.17	1.00	
Zn	0.85	0.90	-0.55	0.91	0.56	0.48	-0.19	0.64	0.78	0.25	0.54	-0.06	-0.47	-0.15	-0.20	-0.19	0.76	-0.28	0.60	-0.41	-0.33	-0.31	-0.54	0.72	1.00

7.2.1 Trace elements in sulfide minerals

A total of 296 spots were analysed by EPMA and the results of the EPMA analyses of sulfide minerals are presented in Appendix 7-3, while in Table 7.4-3 summarised basic statistical parameters of the analysed trace elements in the different sulfide mineral phases are presented. Trace elements can be incorporated in pyrite phases either as micro-inclusions or via substitution within the crystal lattices (Thomas et al., 2011; Ciobanu et al., 2012; Cook et al., 2016). Chemical composition of pyrite is characterised by Fe and S contents ranging from 52.96 wt% to 53.92 wt%, and 44.62 wt% to 46.77 wt% with means of 53.42 wt% and 45.54 wt%, respectively (Fig. 7.4-5). Copper and Pb contents are recorded above LOD (2537-3874 ppm and 2334-4372 ppm, respectively) in 55% of the pyrite grains analysed, with concentrations ranging from 0.29 wt% to 1.36 wt% (mean: 0.74 wt%) and 0.25 wt% to 0.41 wt% (mean: 0.32 wt%), respectively. Zinc and As are generally <LOD limit of 5192 ppm and 987 ppm respectively in the analysed grains.

Lead, Ag, Sb and As are the only incorporated trace elements in chalcopyrite. Sulfur, Fe and Cu range from 30.13 wt% to 34.97 wt% (mean = 34.36 wt%; SD = 0.99), 22.41 wt% to 31.07 wt% (mean = 29.7 wt%; SD = 1.96), and 31.7 wt% to 37.47 wt% (mean = 34.13 wt%; SD = 1.02), respectively. Silver and Pb range from 0.13 wt% to 1.3 wt% (mean = 0.3 wt%; SD = 0.27) and 0.28 wt% to 7.67 wt% (mean = 2.04 wt%; SD = 2.5), respectively. Arsenic and Sb are below 987 ppm and 476 ppm respectively in most of the chalcopyrite grains. The rare detected As and Sb values range between 0.08 wt% to 6.26 wt% (mean = 0.85 wt%; SD =0.11), and 0.06 wt% and 0.32 wt% (mean = 0.18 wt%; SD = 0.11), respectively. Cupropeacite ($Cu_6As_2S_7Ag_9CuS_4$) has significant traces of Fe and Sb. Silver values range between 36.9 wt% and 51.66 wt%

(mean = 44.7 wt%; SD = 4.88). Copper and S range from 23.12 wt% to 35.26 wt% (mean =28.2 wt%; SD = 4.39) and 17.87 wt% to 18.87 wt% (mean = 18.42 wt%; SD = 0.27), respectively. Arsenic, Fe and Sb range from 5.95 wt% to 7.81 wt% (mean = 7.2 wt%; SD = 0.56), 0.57 wt% to 1.43 wt% (mean = 0.91 wt%; SD = 0.27), and 0.21 wt% to 0.64 wt% (mean = 0.40 wt%; SD = 0.13), respectively.

Table 7.4-3 Summarization of element concentrations in sulfide minerals from the Khusib Springs deposit. All elements are reported in wt%.

Mineral		S	Fe	Cu	Zn	Pb	Ag	Sb	As
Pyrite	Min	52.96	44.62	0.29	0.39	0.25	-	-	-
	Max	53.92	46.77	1.36	0.48	0.41	-	-	-
	Mean	53.42	45.56	0.74	0.43	0.32	-	-	-
Galena	Min	13.34	0.22	0.37	0.47	84.76	-	-	-
	Max	13.93	0.58	1.73	0.69	86.82	-	-	-
	Mean	13.63	0.39	0.94	0.56	86.00	-	-	-
Sphalerite	Min	32.46	0.14	0.33	65.23	0.31	0.14	-	-
	Max	33.19	0.87	1.19	68.05	0.38	0.15	-	-
	Mean	32.80	0.34	0.63	66.64	0.35	0.14	-	-
Tennantite	mean	28.03	2.17	43.65	6.24	0.33	0.64	1.73	18.12
	min	27.23	0.18	40.67	5.32	0.26	0.12	1.17	16.65
	Max	31.90	3.30	48.53	7.68	0.52	2.73	4.41	19.49
Chalcopyrite	Mean	34.37	29.73	34.13	2.24	2.04	0.32	0.18	0.85
	Min	30.13	22.41	31.70	2.24	0.28	0.13	0.06	0.08
	Max	34.97	31.07	37.47	2.24	7.67	1.30	0.32	6.26
Cupropeacite	mean	18.42	0.92	28.21	-	-	44.74	0.40	7.20
	min	17.87	0.57	23.12	-	-	36.90	0.21	5.95
	max	18.87	1.43	35.26	-	-	51.66	0.64	7.81
Digenite	min	21.53	0.16	74.45	0.43	0.27	0.14	-	0.94
	max	23.75	1.78	78.00	1.83	0.31	0.66	-	0.96
	mean	21.97	0.90	76.55	1.41	0.29	0.38	-	0.95
Peacite	Min	16.00	0.26	4.22	0.65	-	57.10	0.11	5.83
	Max	19.07	0.86	14.48	4.14	-	71.78	1.61	7.22
	Mean	16.77	0.43	9.71	1.52	-	65.59	0.82	6.51

- Throughout below the lower analytical detection limit

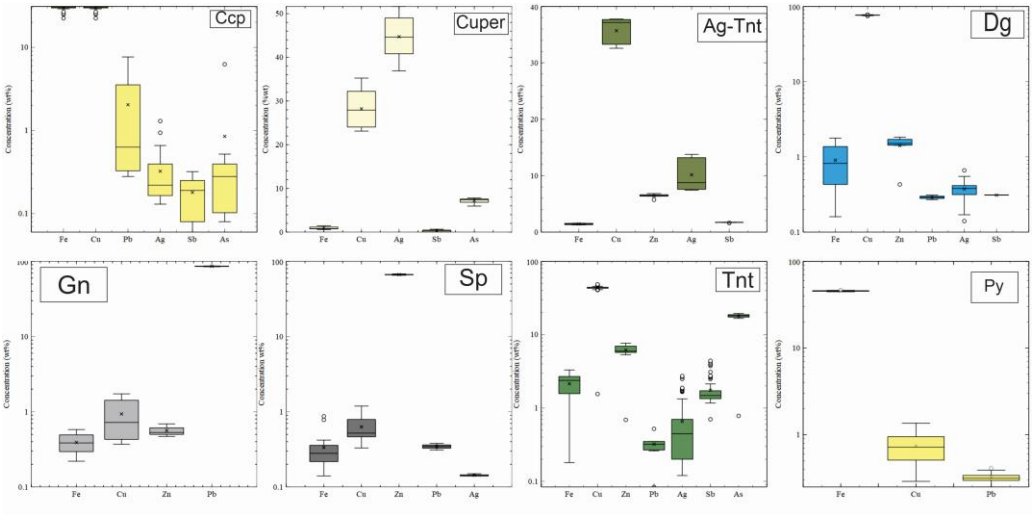

Fig. 7.4-4 Box and whisker plots of detected trace element compositions in selected ore minerals from the Khusib Springs deposit. Abbreviations: Ccp-Chalcopyrite; Cuper- Cupropeacite; Ag-Tnt- Silver-rich Tennantite; Dg-Digenite; Gn-Galena;Py-pyrite; Sp- Sphalerite; Tnt- Tennantite.

7.5 Discussion

The ore forming process of the Khusib Springs deposit involved fluids distinctly enriched in Cu, Zn and Pb, percolating and precipitating the sulfide mineralisation. The mineralisation is hosted mainly in the brecciated zone unit, that is characterised by white dolomite that is replacing the grey dolomite matrix. This can be correlated to a typical Mississippi Valley Type (MVT) deposit, which is often associated with paleokarst features in carbonate rocks, whereby, during the formation process, sulfide minerals replace carbonate minerals or occur as infills between the angular clasts, as outlined in Sangster (1988). The pull apart clasts observed in this brecciated zone may give proof of solution collapse structures, which is linked to the early mineralization stage described by Melcher et al. (2006). Sulfide mineralisation shows a wide range of textures and chemical compositions. The dominant sulfide minerals are galena, tennantite, pyrite, chalcopyrite, and pyrite, associated with dolomite, and minor

muscovite and quartz. The fracture and cataclastic texture in pyrite can be an indication of shear movement along the fracture zones bearing the ore. Mineralogical results show that mineralisation can be categorized into two types: the massive Cu, Pb, Zn sulfide mineralisation, and the massive to disseminated Cu-As-Ag sulfide mineralisation.

There is a significant amount of trace element concentrations in bulk rock; however, EPMA results show that the trace element concentrations in individual mineral phases is largely <LOD. Trace element geochemistry in sulfide mineral phases has played a major role in the understanding of ore genesis, the evolution of ore-forming fluids, the timing of mineralisation, and trace elements serve as geochemical pathfinders in the exploration of ore deposits (Cook et al., 2016; Steadman et al., 2021; Raic et al., 2022). Trace elements such as Cu and Pb are incorporated in pyrite mainly as micro-inclusions and limited via substitution (Steadman et al., 2021). Frequently, pyrite has inclusions of chalcopyrite and galena, indicating that the Cu and Pb concentrations in the pyrite is due to the inclusion of the above-mentioned minerals as micro-particles. Trace elements such as Ga, Ge and Cd in the sulfide minerals in this study are mainly <LOD. However, from the bulk rock geochemistry there is a significant amount of up to 188 ppm Cd, 30.9 ppm Ge, and 14.2 ppm Ga. Based on previous studies of sulfide ores, enrichment of Ga, Ge and Cd are good indications of ore which is formed from low temperature hydrothermal fluids (Cook et al., 2009; Ye et al., 2011; Frenzel et al., 2016). Additionally, the negative Eu anomaly and a slight positive Gd anomaly observed from the REE chondrite normalised plots (Fig. 7.4-3) from the bulk rock composition is also an indication of ore formation fluids that are of low temperature (<200°C) (Karakaya 2012; Zeng et al., 2015). However, this somewhat contradicts the

conclusion by Melcher et al. (2006), that mineralisation at the Khusib Springs deposit is attributed to precipitation from hot saline fluids.

7.6 Conclusion

- Light dolomite, grey dolomite, laminated dolomite and brecciated dolomite are the main lithological units that are associated with the Kuiseb Springs deposit.
- Mineralisation is mainly hosted in the brecciated dolomite unit, suggesting that this is an MVT-type deposit, which corroborate the suggestion from Melcher et al. (2006).
- At least two types of mineralisation are observed: massive Cu-Pb-Zn sulfide mineralisation and massive to disseminated Cu-As-Ag sulfide mineralisation.
- Ga, Ge and Cd concentrations from the bulk rock geochemistry suggest that mineralisation of the Khusib Springs deposit formed as a result of low-temperature hydrothermal fluids.
- Negative Eu anomaly and positive Gd anomaly are suggestive of low-temperature hydrothermal fluids.
- Lack of trace element detection in sulfide minerals can be due to the too high detection limits of the EPMA device for the respective elements. The re-analysis of the sulfide minerals using a LA-ICP-MS device is currently ongoing. However, results are not expected before mid of next year.

Acknowledgment

Ulf Hemmerling (Technical Univestity of Clausthal) is thanked for assistance with the preparation of the section that were studied in this chapter.

8 Discussion

This chapter is a summary of the discussions of various main aspects covered in the preceding chapters.

8.1 Sulfide mineralisation

Petrography is an essential tool in ore deposit characterization and mineral exploration as it helps to constrain the ore paragenesis and the mineralisation texture(s) as well as potential deformation events (Berrezueta et al., 2016). Textural observations between the ore minerals and the host rock mineral assemblage can be used to provide useful information to elucidate how ore minerals and rock-forming minerals are related. Kombat deposit's primary mineralisation is dominated by sulfide minerals such as chalcopyrite, bornite, covellite, galena, with minor tennantite, chalcocite, and sphalerite (Deane, 1995; Kamona and Günzel, 2007; Nghoongoloka et al., 2020). These findings are consistent with the observations made here, whereby chalcopyrite, bornite, pyrite, and galena being the dominant ore minerals (Fig. 4.5-1 and 5.4-1). Macroscopic sample observations and microscopic petrographic observations reveal three different mineralization styles: massive, disseminated, and brecciated. In detail, most sulfide minerals have anhedral shape, although few have euhedral to subhedral shape. Crystals with euhedral shape and those with almost well-developed euhedral shape such as pyrite (Fig. 5.4-1 e) are interpreted to represent the early mineralisation stage at Kombat. Later mineralisation stage is characterised by replacement and overgrown textures observed in minerals such as bornite by chalcocite and covellite (Fig. 4.5-1 c, e and f), and galena by chalcopyrite (Fig. 5.4-1 h).

The Tsumeb ore paragenesis in this study is characterised largely by bornite, chalcopyrite, chalcocite, covellite, enargite, galena, pyrite, renierite, sphalerite, and tennantite (Fig. 6.6-1b, e; Fig. 6.6-2 d). These findings are consistent with the interpretations of the ore minerals of the deposit by Lombard et al. (1986), Kamona et al. (1999), and Kamona and Günzel (2007), who reported the same mineral assemblage for the deposit. Various ore textures are observed ranging from intergrowth and replacement textures to polycrystalline (Fig. 6.6-1a) and deformation textures (Fig. 6.6-1 b). In addition, interstitial fractures filled with gangue and other sulfide minerals are detected (Fig. 6.6-1 b; e; Fig. 6.6-2 d).

Mineralisation at the Khusib Springs deposit is defined by sulfide minerals only that are embedded in dolomite, calcite, quartz, muscovite, and siderite (Fig. 7.5-1). Melcher et al. (2006) showed that the Khusib Springs mineralization is largely characterized by chalcopyrite, bornite, pyrite, enargite, digenite, Ge-colusite, and pearcite-polybasite. This confirms the observations in this study, whereby the sulfide mineralization is defined by tennantite, pyrite, galena, chalcopyrite, bornite, chalcocite, covellite, and Ag-tennantite (Fig. 7.4-4 and 5).

8.2 Bulk ore Geochemistry

Various geochemical methods (XRF, ICP-MS, ICP-AAS) were used to obtain bulk ore geochemical data from 52 samples from the Tsumeb, Kombat, and Khusib Springs deposits. This dataset contains over 50 major, minor and trace elements found in all three deposits. Several trace elements are present in significant concentrations in all three deposits (Fig. 8-1). This includes elements such as Co, Cr, Ga, Ge, and V, which are classified as critical raw material by the European Commission based on current supply and demand risks as well as their need for technological advancement

capabilities (European Commission, 2014, 2017, 2020). In general, critical commodities such as Ga and Ge occur only in low concentrations in most ore deposits due to their generally low crustal abundance, so that they are mostly only recovered as by-products (Moss et al., 2011). Provided data reveal that the Tsumeb deposit still bears a high content of these critical elements in relict ore samples and that the contents of these elements are high in comparison to those at the Khusib Springs and Kombat deposits. Tsumeb deposit contains a high content of As (n = 11; mean = 11787 ppm), Cd (n = 11; mean = 880 ppm), Cu (n = 11; mean = 115019 ppm), Ga (n = 11; mean = 293 ppm), Pb (n = 11; mean = 293607 ppm), and Zn (n = 11; mean = 89826 ppm), as well as significant contents of Ag (n = 11; mean = 136 ppm), Mn (n = 11; mean = 489 ppm), Mo (n = 11; mean = 2261 ppm), and Sb (n = 11; mean = 460 ppm). The Khusib Springs deposit is characterized by high contents of As (n = 13; mean = 43341 ppm), Cu (n = 13; mean = 118489 ppm), Mn (n = 13; mean = 2039 ppm), Pb (n = 13; mean = 19411 ppm), Sb (n = 13; mean = 5546 ppm), and Zn (n = 13; mean = 17438 ppm), with notable contents of Ga (n = 13; mean = 5.8 ppm) and Ge (n = 13; mean = 6.15 ppm), which verify the earlier work by Melcher et al. (2006). While Kombat deposit is characterized by high concentrations of As (n = 31; mean = 366 ppm), Cu (n = 31; mean = 17800 ppm), Mn (n = 31; mean = 5298 ppm), Pb (n = 31; mean = 6890 ppm), and Zn (n = 31; mean = 204 ppm), all three deposits show a depletion in Bi (Kombat: n = 19; mean = 0.033 ppm; Khusib Springs: n = 13; mean = 0.60 ppm; Tsumeb: n = 11; mean = 0.046 ppm), Nb (Kombat: n = 31; mean = 0.21 ppm; Khusib Springs: n = 13; mean = 0.75 ppm; Tsumeb: n = 11; mean = 1.06 ppm) and W (Kombat: n = 11; mean = 1.23 ppm; Khusib Springs: n = 13; mean = 4.3 ppm; Tsumeb: n = 11; mean = 177 ppm) in comparison to all the other trace elements (Fig. 8-1).

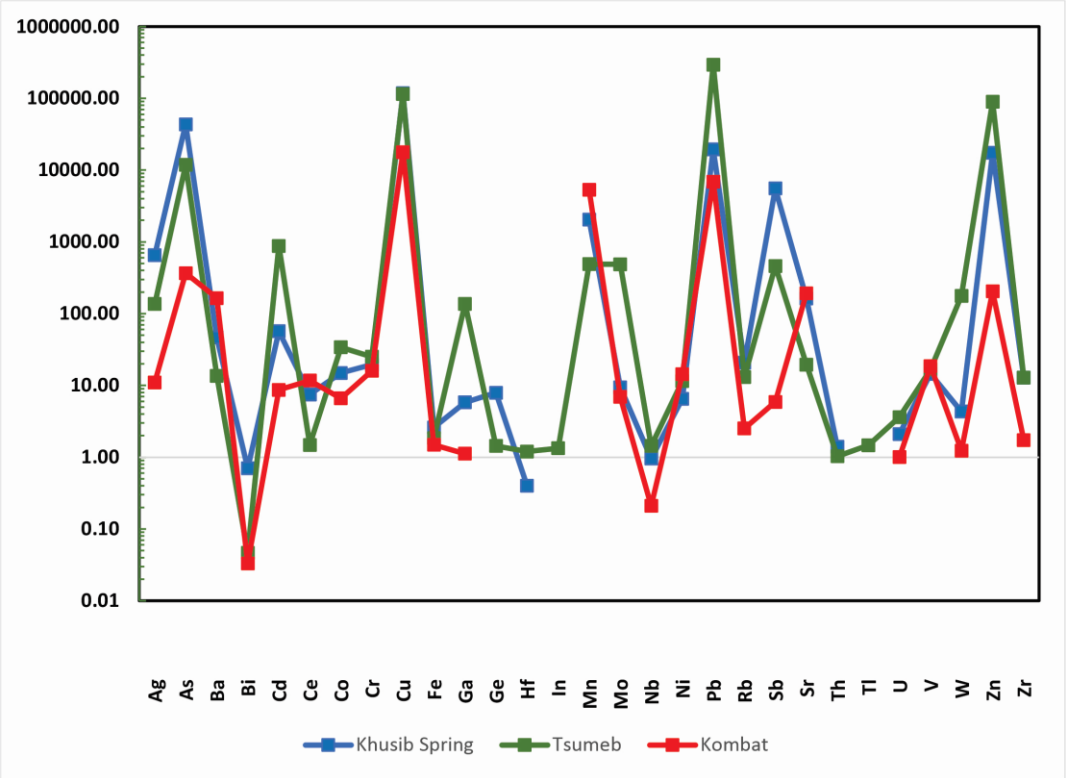

Fig. 8-1 Comparison of mean values of selected trace element contents of bulk ore samples from Khusib Springs, Tsumeb and Kombat deposit.

Bulk ore correlation diagrams indicate that there is a positive correlation between various elements (Fig. 8-2 a-c), suggesting that there is some sort of association between the respective elements and that they can be used as proxies for one another. The trace element distribution in bulk ore in the Khusib Springs deposit reveals some positive correlations, as deduced from R^2. These include As vs. Zn (R^2 = 0.81), Cu vs. Cd (R^2 = 0.80), Ag vs. As (R^2 = 0.77), Ag vs. Zn (R^2 = 0.72), Ag vs. Cu (R^2 = 0.69), and Cd vs. Ag (R^2 = 0.68). There seems to be a positive correlation between Zn and Cd in Kombat ore (R^2 = 0.69). Positive correlations are noticed for Ga vs. As (R^2 = 0.83) and Cu vs. Ag (R^2 = 0.77) in Tsumeb deposit ore.

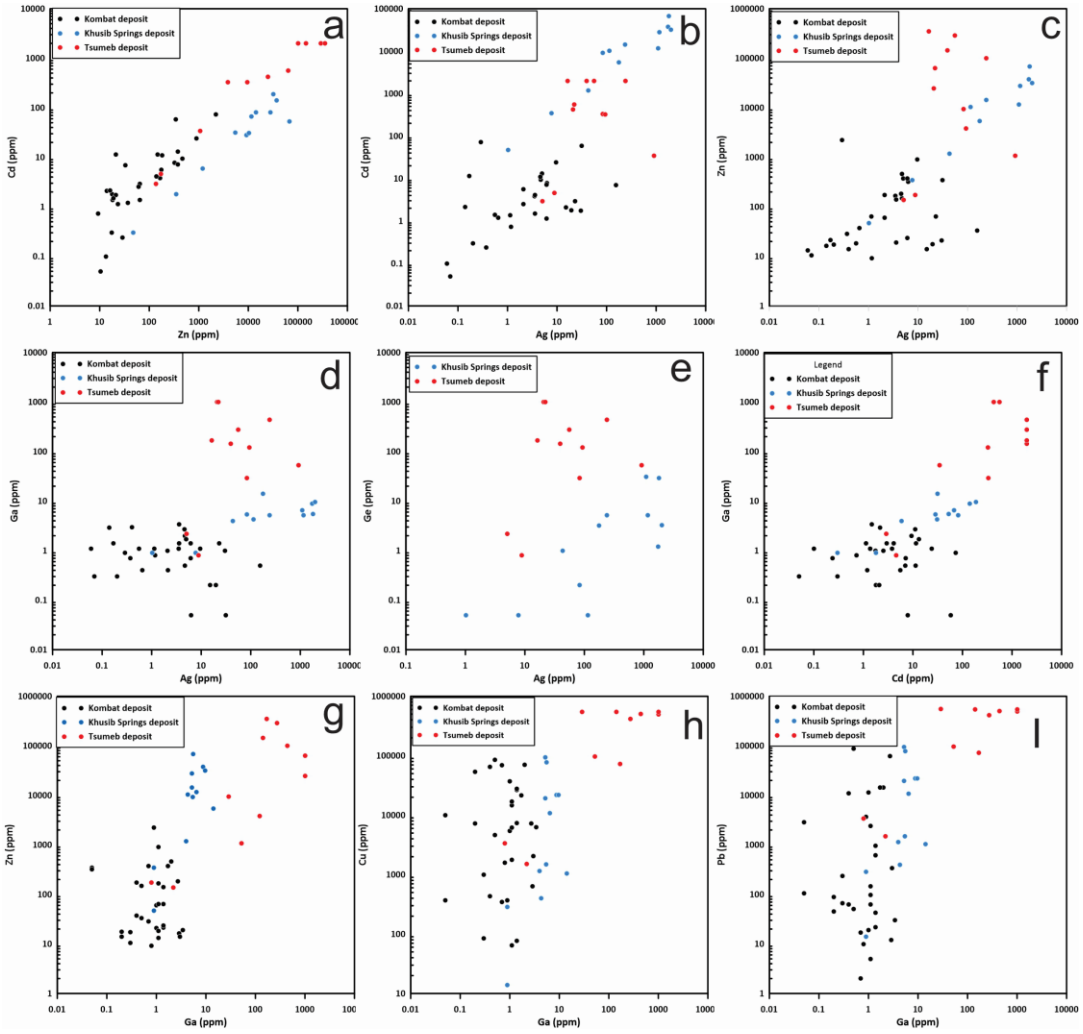

Fig. 8-2 Bivariant plots of selected trace elements (ppm) in bulk ore samples of the Tsumeb, Khusib Springs and Kombat deposits. a) Zn vs. Cd, b) Ag vs. Cd, c) Ag vs. Zn, d) Ag vs. Ga, e) Ag vs. Ge, f) Cd vs. Ga, g) Ga vs. Zn, h) Ga vs. Cu, and i) Ga vs. Pb.

This research focuses on critical raw materials with a particular emphasis on Ga, Ge, and In. All three elements are quite essential for technological advancements (Jorgenson and George, 2004; Bellisont et al., 2014; Frenzel et al., 2014; 2016; 2017; Foley et al., 2017; Shanks et al., 2017; Fontana et al., 2021). These elements are rarely found in notable amounts in nature due to their generally low crustal abundance (Taylor and McLennan, 1985; Butcher and Brown, 2014; Schwarz-Schampera, 2014).

They are commonly incorporated in ore minerals within various ore deposit types such as skarn, volcanogenic massive sulfide, Mississippi-valley type (MVT), epithermal polymetallic, and porphyry-Cu (e.g., Schwarz-Schampera and Herzig 2002; Ishihara et al., 2006; Höll et al., 2007; Cook et al., 2009; Jovic et al., 2011; Li et al., 2015; Frenzel et al., 2016a, 2019; Mondillo et al., 2018; Bauer et al., 2019a, b; Horn et al., 2019; Cugerone et al., 2021; Xu et al., 2021; Luo et al., 2022; Kumar et al., 2023). Pathfinder elements are frequently used to assess the potential of the sought element(s) in a deposit due to the rarity of the sought element(s) in nature. Pathfinder elements are those elements that occur in close association to the sought-after element(s) and are usually more abundant and easily detectable (Balaram and Sawant, 2022). However, there is little to no correlation between the more common elements in the three deposits studied and the three wanted critical elements; this means that no other element can be used as pathfinder element based on this study (Fig. 8-2 d-i).

8.3 Trace elements in Sulfide mineralization

The concentration of trace elements in similar sulfide mineralization types varies depending on the geological setting in which they formed, as shown by, for example, Ren et al. (2021), Andersson et al. (2022), Chu et al. (2022), Yang et al. 2022, Wu et al. (2023), and Xu et al. (2023). The trace element composition in sulfides can help to constrain the physiochemical conditions during which the ores formed (Bellisont et al., 2014; Frenzel et al., 2016). The incorporation of trace elements in different minerals can occur either as micro-inclusions or via element substitution into the crystal lattices (Cook et al., 2009; Ye et al., 2011; Frenzel et al., 2016). However, elements present in sulfide minerals in a solid solution are a far more useful tool for determining the deposit's genesis as shown by Xing et al. (2021). For the three deposits

in this study, trace element concentrations in the sulfide quantification were obtained via LA-ICP-MS and EPMA, whenever access was available.

Bornite can host elements such as Ag and Bi, but bornite is a poor host for other elements such as Co, Ga, and Ge (Cook et al., 2011). Bornite crystals from the Kombat deposit have a significant content of Ag and Bi, as well as of Ga, Pb, and V, with minor occurrences of Cd, Sb, and W, as detected in a few bornite grains (Fig. 8-2). In general, due to the geochemical affinity of various trace elements, positive correlations can be expected among selected elements (Ciobanu et al., 2009; Cook et al., 2011). However, in the case of Kombat mineralization, there is no notable element-element correlation (Fig. 5.5-2), suggesting that the trace elements detected are due to micro-inclusion of other sulfides in bornite phases. Bornite of the Tsumeb deposit is enriched in Ag, Pb, and Zn with minor contents of As, Cd, In, and Sb (Table 6.6-1; Fig. 8-3).

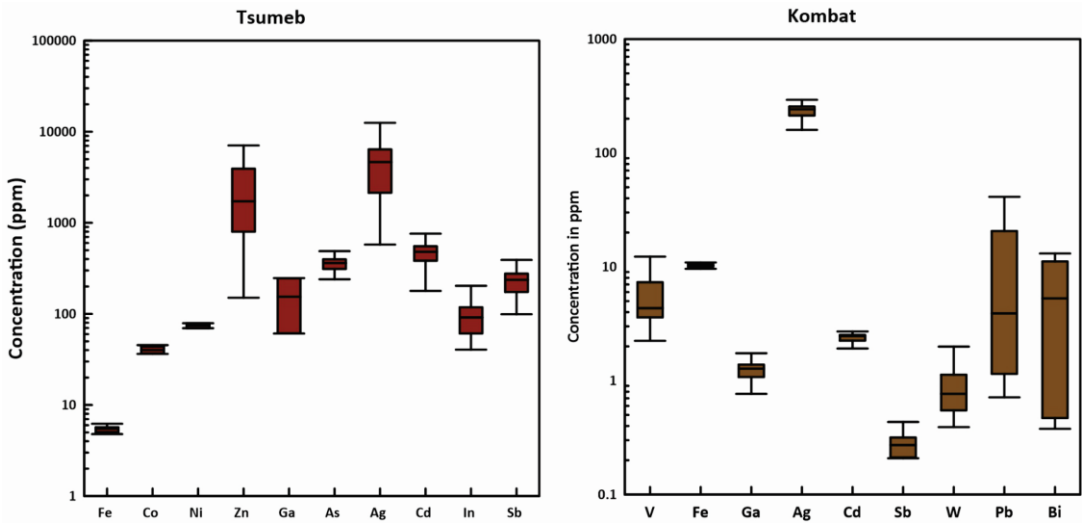

Fig. 8-3 Simple box plot of different trace element concentrations in bornite of the Tsumeb and Kombat deposits.

Because of its crystal structure, sphalerite is known to be a main carrier for various trace elements which are incorporated in the crystal lattices via substitution with Zn (Yang et al., 2022). These trace elements are incorporated in sphalerite either as micro-sulfide inclusions or via ion substitution (Cook et al., 2009; Pfaff et al., 2011; Ye et al., 2011; Belissont et al., 2014; Frenzel et al., 2016). The trace element concentrations in sphalerite have been used widely to deduce the ore-forming temperature, whereby high concentrations of Ga, Ge, and Cd paired with low concentrations of Fe and Mn are indicative of low formation temperatures while high Fe, Mn, Sn, and In concentrations combined with low Ga and Ge concentrations are indicative of high formation temperatures (Kelley et al., 2004; Ye et al., 2011; Frenzel et al., 2016; Li et al., 2020). Furthermore, trace elements such as Cd, Co, Fe, Ga, Ge, In, and Mn have been used widely to determine the type of ore deposit (e.g., Schwartz, 2000; Cook et al., 2009; Ye et al., 2011; Wen et al., 2016; Zhuang et al., 2019; Hu et al., 2020; Li et al., 2020). There is a lack of sphalerite in the samples of the Kombat deposit analyzed. Sphalerite in the Khusib Springs deposit has generally a very low abundance of trace elements, however, sphalerite at Khusib Springs is characterized by a low Fe content (Fig. 8-4 a). The Tsumeb deposit is characterized by a depletion in Fe and a relative enrichment in Ga and Cd, which is suggestive of a low formation temperature of the sulfide ore paragenesis (Fig. 8-4 b).

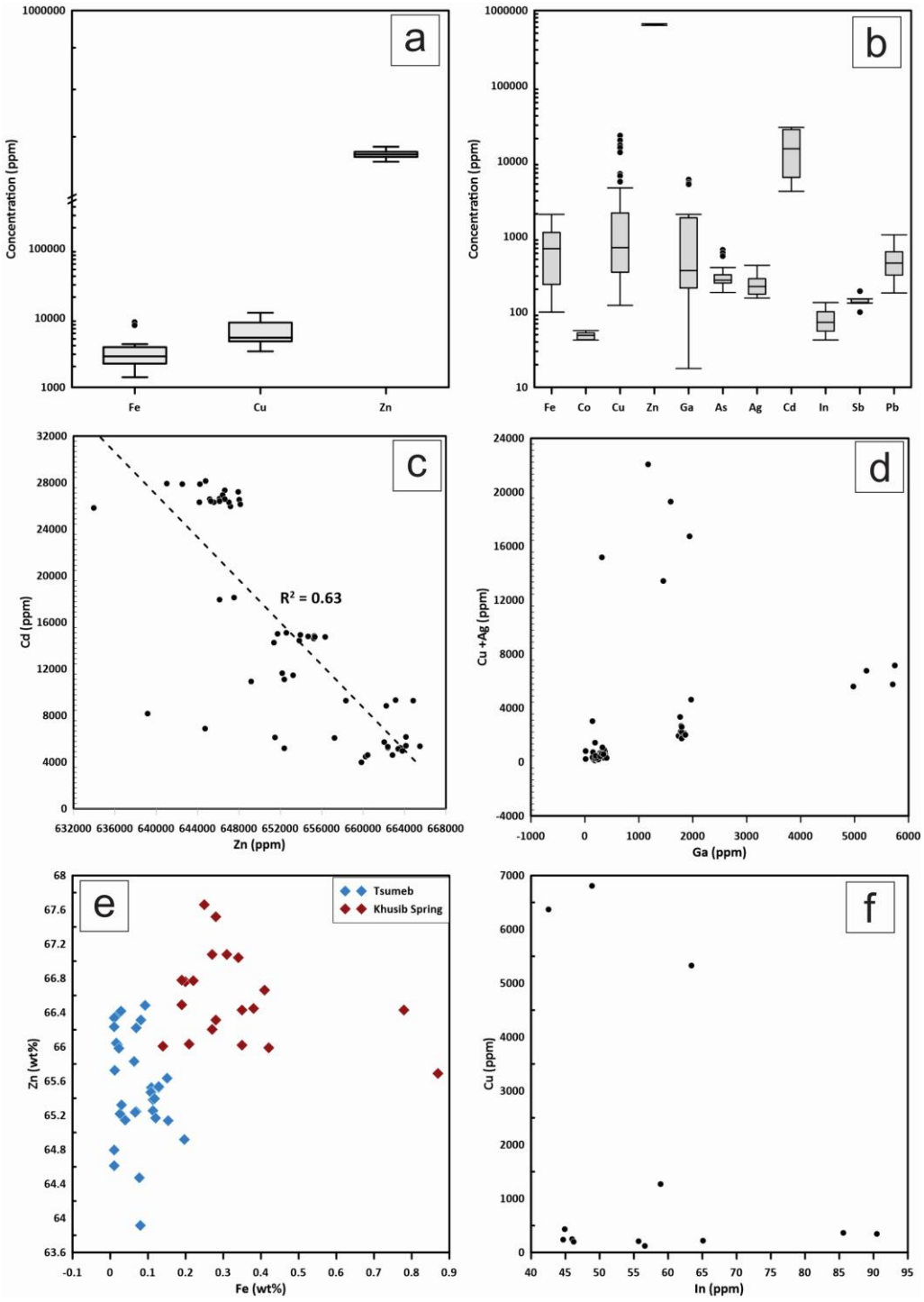

Fig. 8-4 Various plots of trace elements in sphalerite at Tsumeb and Khusib Springs, whereby a-b are box plots of the trace elements in sphalerite, and c-f are binary plots of various elements of the Tsumeb deposit. a) Simple box plot of element concentrations in sphalerite of the Khusib Springs deposit, b) simple box plot of element concentrations in sphalerite of the Tsumeb deposit. Binary plots of c) Cd vs. Zn, d) Cu+Ag vs. Ga, e) Zn vs. Fe, and f) Cu vs. In, in sphalerite of the Tsumeb deposit.

Elements that are incorporated in sphalerite such as Co^{2+}, Cd^{2+}, and Fe^{2+} have ionic radii and oxidation states comparable to Zn^{2+}, hence in general they can occur in sphalerite via a single substitution (George et al., 2016; Xing et al., 2021). The provided data reveals that there is no significant correlation between Fe and Zn, ruling out the possibility of incorporation of Fe via a single substitution in both deposits (Fig. 8-4 c). Therefore, Fe in sphalerite of Tsumeb and Khusib Springs is likely due to micro-inclusions of other sulfides such as pyrite, bornite, and chalcopyrite (Fig. 6.6-1d; Fig. 6.6-2 g). There is a slight positive correlation between Zn and Cd, and Cu and Ga, suggesting a possible substitution mechanism in the crystal lattices of $Cd^{+} \leftrightarrow Zn^{+}$ and $2\ Zn^{2+} \leftrightarrow Cu^{+} + Ga^{+}$ as defined in Cook et al. (2009) (Fig. 8-4 d & e). The composition of trace elements in sphalerite of the Tsumeb deposit is consistent with the trace element spectrum of MVT deposits as defined by other authors (Cook et al., 2009; Ye et al., 2011; Zhuang et al, 2019; Li et al., 2020). There is an expected positive correlation between Cu and In in Tsumeb sphalerite, indicating that In is present in sphalerite in solid solution via a couple substitution mechanism defined by $2\ Zn^{2+}\ Cu^{+} + In^{3+}$ (Cook et al., 2009; Murakami and Ishihara, 2013; Bellisont et al., 2016; Trigub et al., 2022). However, In in the sphalerite of the Tsumeb deposit, when occurring in detectable ranges between 42 and 125 ppm, displays no correlation with Cu, suggesting that In is possible incorporated in sphalerite due to an inclusion of a sulfide mineral that has significant amount of In (Fig. 8-4 f).

In the absence of other co-crystallizing sulfides such as sphalerite and galena, chalcopyrite is often the main carrier of other trace elements (George et al., 2018; Andersson et al., 2022). Trace elements such as Se and Co in chalcopyrite can be used to deduce the temperature of the mineralizing hydrothermal fluid in a deposit (Ren et al., 2021). In comparison to the other two deposits, the chalcopyrite from Khusib

Springs has the lowest trace element abundance, while Tsumeb chalcopyrite has the highest trace element contents (Fig. 8-5 a-c). The data reveal that chalcopyrite of the Khusib Springs and the Tsumeb deposits display only a small compositional variation with an enrichment in Pb and Ag (Fig. 8-5 d-e).

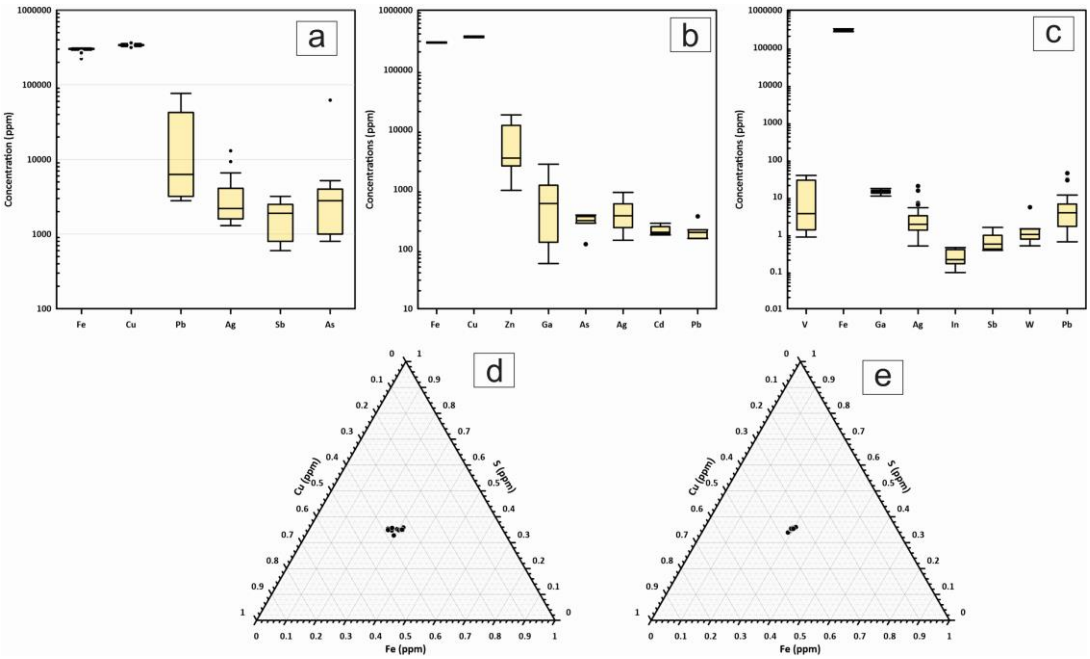

Fig. 8-5 Simple box plots and Cu-Fe-S ternary diagrams of trace elements in chalcopyrite. a) Box plot of trace elements hosted in chalcopyrite of Khusib Springs. B) Box plot of trace elements hosted in chalcopyrite of Tsumeb. c) Box plot of trace elements hosted in chalcopyrite of Kombat. Cu-Fe-S ternary plot showing the small compositional variation in chalcopyrite of d) Khusib Springs and e) Tsumeb.

Pyrite is found in a wide range of ore systems and has a simple formula that allows for the incorporation of a wide range of trace elements into its crystal structure (Huston et al., 1995; Barrie et al., 2007; Deditius et al., 2011; Reich et al., 2013; Real et al., 2020). When As is incorporated into the crystal structure of pyrite, it can cause distortion, which increases the ability of pyrite even more to incorporate other trace elements (Griffin et al., 1991; Abraitis et al., 2004). Cobalt, Ni, As, Te, and Tl are the primary

elements found in pyrite solid solutions via simple and coupled substitutions defined by $Fe^{2+} \leftrightarrow (Co^{2+}, Ni^{2+})$ and $2\ Fe^{2+} \leftrightarrow (Tl^{+} + Cu^{+} + Ag^{+}) + As^{3+}$ (Reich et al., 2013; Grant et al., 2018; Yang et al., 2022). These elements can be used to determine the depositional environment and to constrain the genesis of the ore deposit. Moreover, they can also be used as pathfinders in ore deposit exploration (Reich et al., 2013; Gregory et al., 2015; Cook et al., 2016; Del Real et al., 2020; Steadman et al., 2021). Furthermore, the Co/Ni ratio has been widely used to constrain the evolution of the mineralizing hydrothermal fluids in different ore deposit types (e.g., Bralia et al., 1979; Clark et al., 2004; Large et al., 2009; Koglin et al., 2010; Meng et al., 2019; Mukherjee et al., 2019; Ding et al., 2021). Pyrite of the Tsumeb deposit is characterized by an enrichment of Ag, Cd, Co, Cu, Ga, Ge, Ni, and Pb when detectable (Fig. 8-6 a). Most of the pyrite grains of the Tsumeb deposit with detectable Co and Ni have Co/Ni ratios of up to 0.3, which is ≤1, and which is typical of pyrite of sedimentary origin as stipulated in Bralia et al. (1979). Aside from Cu and Pb, pyrite grains from the Khusib Springs deposit are deficient in other trace elements (Fig. 8-6 b).

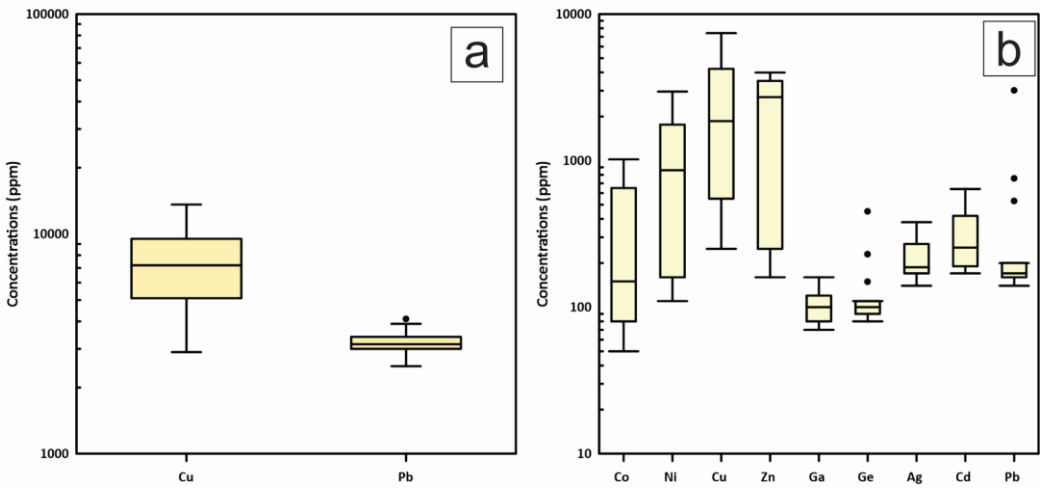

Fig. 8-6 Simple box plots of the trace element concentrations in pyrite of a) Khusib Spring deposit b) Tsumeb deposit.

Various studies have demonstrated that Ag, Bi, Cd, Se, and Sb occur in galena typically as solid solutions (George et al., 2015, 2016; Ye et al., 2020; Hu et al., 2021). Silver, Bi and Sb are typically incorporated into the galena lattice via a coupled substitution defined by $Ag^{+} + (Bi, Sb)^{3+} \leftrightarrow 2\ Pb^{2+}$ (Sharp and Buseck et al., 1993; Renock and Becker, 2011; Li et al., 2020). Other incorporations via coupled substitution include Tl and Cu which are defined by the reaction of $(Ag, Cu, Tl)^{+} + (Bi, Sb)^{3+} \leftrightarrow 2\ Pb$ (George, 2013). Additionally, Ag can also be incorporated in the galena lattice via a single substitution which is defined by $2\ Ag^{+} \leftrightarrow Pb^{2+}$ (Renock and Becker, 2011). The analytical results show that majority of the galena phases in the Tsumeb deposit have a significant concentration of Cu and Ga, while Ag, Cd, and Zn are only found in a few galena crystals (Fig. 8-7 a). Khusib Springs's galena grains that were analyzed did not yield any promising result, as trace element contents are largely below the lower analytical detection limit (Fig. 8-7 b).

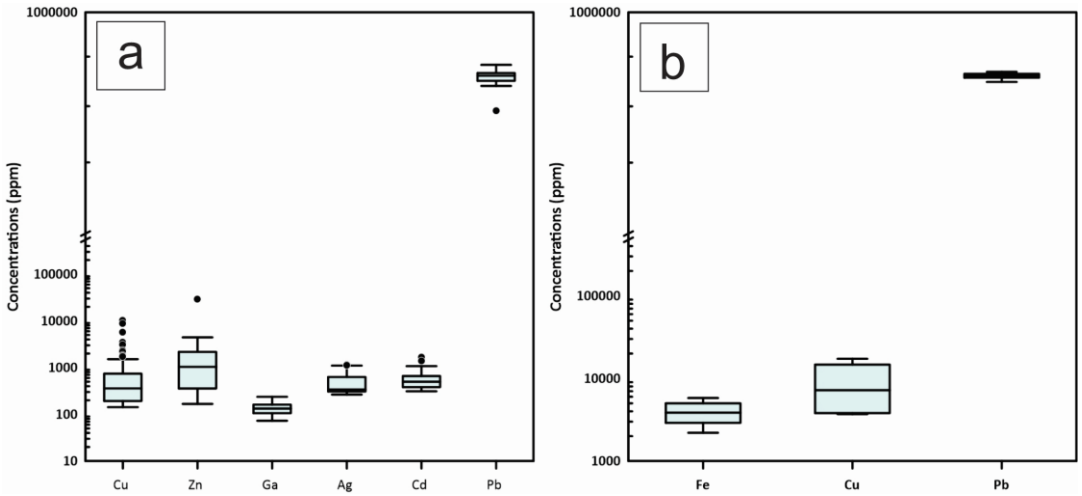

Fig. 8-7 Simple box plot of trace element concentrations in galena of a) Tsumeb ore b) Khusib Springs ore.

Tennantite is a member of the fahlore series, which has a complete solid solution extending between tetrahedrite and tennantite that is commonly found in various base metal ore deposits worldwide (Wuensch, 1964; Staude et al., 2010; George et al., 2017). In case of a co-crystallising sulfide assemblage, tennantite is a considerable to good host for Ag, As, Cu, Fe, Sb, and Zn, and rather a poor host for Ga, In, and Sn (George et al., 2017; Choi et al., 2023). Tennantite from Khusib Springs ore contains Cu (mean: 34.13 wt%), As (mean: 18.12 wt%), Zn (mean: 6.24 wt%), Fe (mean: 2.17 wt%), Sb (mean: 1.73 wt%), Ag (mean: 0.64 wt%), and Pb (mean: 0.33 wt%). Tennantite in Tsumeb ore contains Cu (mean: 43.9 wt%), As (mean: 17.7 wt%), Zn (mean: 8.10 wt%), Fe (mean: 0.52 wt%), Sb (mean: 0.85 wt%), Ag (mean: 0.07 wt%), Ga (mean: 0.02 wt%), Cd (mean: 0.07 wt%), Co (mean: 0.01 wt%), Ge (mean: 0.01 wt%), and Pb (mean: 0.01 wt%). The results show that tennantite from both Khusib Springs and Tsumeb ore is a great host for various trace elements. However, the incorporation of trace elements in tennantite is poorly studied, therefore the distinction whether the elements are in solid solution or as micro-inclusion in tennantite is not outlined here.

Other sulfide minerals that were analysed for trace elements include digenite, enargite, renierite, and chalcocite. Digenite is a supergene mineral that has the capability to incorporate Ag, As, and Fe mainly at low temperature (Reich et al., 2010). Digenite data from the Khusib Springs deposit reveals that Cu and S, have concentrations ranging between 74.45 wt% to 78 wt%, and 21.53 wt% to 23.75 wt%, respectively. Iron and Ag are recorded in more than 80% of the digenite crystals analysed with contents ranging between 0.16 wt% and 1.78 wt%, and 0.14 wt% and 0.66 wt% respectively. Other elements such as As, Pb, Sb, and Zn are all recorded only in a few grains analysed with concentrations of up to 1.83 wt%. Studies done on enargite

indicate that enargite can host Ag, Au, Cd, Bi, Fe, Ga, Ge, In, Pb, W, and Zn (Delley and Hedenquist, 2011; Liu et al., 2019). There are various substitutions in the enargite crystal structure that are known to date which include a simple substitution between As^{5+} and Sb^{5+}, and other complex ones that are defined by $(As,Sb)^{5+} \leftrightarrow (Sn,Ge)^{4+} + Cu^{+}$ and $(As,Sb)^{5+} + Cu^{+} \leftrightarrow (Sn,Ge)^{4+} + (Fe,Zn,Cu)^{2+}$ (Springer, 1969; Spry et al., 1994; Frank-Kamenetskaya et al., 2002; Liu et al., 2019). Enargite in the Tsumeb ore is dominated by As and Cu, but also has measurable amounts of other elements such as Ag, Cd, Ge, Pb, Sb, and Zn.

8.4 Copper and Zinc isotopes

Zinc has five stable isotopes: ^{64}Zn, ^{66}Zn, ^{67}Zn, ^{68}Zn, and ^{70}Zn, which can be used in the study of ore deposits, particularly in understanding the ore forming processes of deposits rich in Zn metal (Rosman, 1972; Albarède, 2004; Wilkson, 2023). The usage of Zn isotopes in the constraining of mineralisation processes is favourable in comparison to traditional stable isotopes because of the simple fractionation mechanism of Zn isotopes (Kavner et al., 2008; Liao et al., 2019). Several studies have been conducted to investigate the variation in Zn isotopes in various deposits (Zhou et al., 2004 a, b; Mason et al., 2005; Wilkson et al., 2005; Kelley et al., 2009; Gagnevin et al., 2012; Pasava et al., 2014; Gao et al., 2018; Wang et al. 2018; Zhang et al., 2020; Mathur and Zhao, 2023). Copper has two stable isotopes ^{63}Cu and ^{65}Cu which are used in the study of ore deposits to understand the ore genesis with emphasis on geochemical reactions involved in the formation of the ore minerals (Mathur and Zhao, 2023). Several studies have utilized copper isotopes for the identification of the type of Cu deposit, for interpretation of hydrothermal processes, evaluation, and exploitation of copper deposits (Larson et al., 2003; Graham et al., 2004; Mason et al., 2005; Markl et al., 2006; Mathur et al., 2009; Wang et al., 2021; Sarjoughian et al.,

2024). Zinc isotopes of the Tsumeb ore ranges between 0.11‰ and 0.13‰, which is comparable to zinc sulfide deposits in general and Irish MVT deposits in particular (Liao et al., 2019; Wilkson et al., 2005). The huge variation in the zinc isotopes analysed can be attributed to the Rayleigh fractionation during the precipitation of ZnS from the ore fluid (cf., Zhou et al., 2014b; Liao et al., 2019). Copper isotopes of the Tsumeb ore vary between 0.80‰ and 1.32‰, which indicates a positive fractionation of copper isotopes (Mathur et al., 2012; Moyier et al., 2017). These values fall within a range of isotopic data of hypogene mineralisation of porphyry deposits, whereby Rayleigh fractionation led to enrichment of isotopically heavy Cu during fluid evolution (Mathur et al., 2012).

9. Conclusions and recommendations

This is a final chapter that presents the research's closing arguments and recommendation for future work, highlighting how the different objectives were attained. Throughout the research, the primary aim has been to provide insights in the characteristic geochemical relationships between critical metals, with emphasis on Ga, Ge and In, with other trace elements in the sulfide mineralisation of Tsumeb, Kombat and Khusib Springs deposits. Four objectives that were carefully formulated to contribute to the existing knowledge and fill in the existing gaps serve as a guide towards understanding the research topic of this dissertation. Chapters 4, 5, 6, and 7 present results that assisted in addressing the objectives, and they are discussed in chapter 8. The subsection (9.1) below gives an account of how these objectives were attained.

9.1 Conclusions

A comprehensive study of the ore mineralisation which includes mineralogical investigations coupled with geochemical analyses was instrumental in the identification of mineral phases that are enriched in critical metals of interest. Tsumeb ore paragenesis in this study is characterised largely by bornite, chalcopyrite, chalcocite, covellite, enargite, galena, pyrite, renierite, sphalerite, and tennantite, and it is characterised by various ore textures observed ranging from intergrowth and replacement textures to polycrystalline, interstitial fractures filled with gangue and other sulfide minerals. Kombat ore in this study is dominated by sulfide minerals such as chalcopyrite, bornite, covellite, and galena, with minor tennantite, chalcocite, and sphalerite. Texturally, Kombat ore is characterised by massive, disseminated, and brecciated ore mineralisation styles. Khusib Springs mineralisation in this study is

defined by sulfide mineralization that includes tennantite, pyrite, galena, chalcopyrite, bornite, chalcocite, covellite, and Ag-tennantite. There are various textures that are observed including replacement, deformation, and triple junction between ore phases.

The research set out to determine the distributions and concentrations of Ga, Ge, and In in Tsumeb, Kombat, and Khusib Spring deposits, with the goal to enhance the knowledge of understanding the behaviour of these critical elements in similar geological settings. Bulk ore geochemistry data in this study reveal that the Tsumeb deposit bears a high content of Ga, Ge, and In in comparison to those at the Khusib Springs and Kombat deposits. There is little to no correlation between the minor and major elements in the three deposits studied and the critical elements of interest; this means that no other element can be used as a pathfinder element based on this study. Furthermore, the research was set out to determine the element relationships in the base metal mineralisation and to identify indicator minerals and base metal elements, which can be used as proxies or indicator elements/minerals for Ga, Ge, and In in Tsumeb, Kombat and Khusib Spring deposits. The chemistry study of individual minerals was utilised to achieve this objective, whereby EPMA results of the Tsumeb ore in this study reveal that Ga is mainly concentrated in renierite, sphalerite, and chalcopyrite, and is contained, to a lesser extent, in galena, tennantite, and chalcopyrite, while Ge is mainly concentrated in renierite and enargite with notable contents also in tennantite and pyrite. Sphalerite is the main carrier for most of the trace elements in the Tsumeb ores. Observed correlations, such as Zn-Cd and Cu-Ga, suggest a possible substitution mechanism in the crystal lattices of $Cd^{+} \leftrightarrow Zn^{+}$ and $2\ Zn^{2+} \leftrightarrow Cu^{+} + Ga^{+}$. Additionally, the As contents that are above 100 ppm in sphalerite paired with low Fe contents, and high Ga and Cd contents are suggestive of low formation temperatures. EPMA trace element data of the Khusib Springs deposit in

this study, indicate that chalcopyrite and tennantite are the main hosts for most of the trace elements in comparison to the other sulfide minerals. Trace elements such as Ga, Ge, and Cd in the sulfide minerals in the Khusib Springs ore in this study are mainly below detection limit. However, from the bulk rock geochemistry data there is a significant amount of up to 188 ppm Cd, 30.9 ppm Ge, and 14.2 ppm Ga known. For Kombat ore the LA-ICP-MS study of bornite and chalcopyrite reveals that Ga sits in both bornite and chalcopyrite, while Ge is only in chalcopyrite. In comparison to bornite, chalcopyrite is the main carrier for most of the trace elements analysed. The lack of apparent correlations between the different trace elements in both bornite and chalcopyrite suggest that trace elements are present likely via micro-inclusions.

Objective four aimed to assess whether pXRF can serve as an acceptable low-cost exploration technique for exploring for Ga, Ge, and In associated with sulfide base metal ores. This objective was attained, by comparing ICP-MS data with pXRF data for the effectiveness, accuracy and practicality evaluation of pXRF in detecting the above-mentioned critical metals and associated trace elements. Results of samples obtained from Kombat deposit reveal that pXRF data of certain trace elements (such as Ag, Cu, Fe, Pb and Zn) match adequately well with ICP-MS obtained results of the same samples. This indicates that pXRF is capable to detect the concentration of certain trace elements, with sufficient precision and accuracy, in carbonate-hosted sulphide mineralized zones; and can thus be used as a successful geochemical exploration tool for these types of sulphide ore deposits. However, pXRF has a distinct limitation in detecting the trace elements Ga, Ge, and In, mainly because they are very low in concentration (few ppm). Additionally, with low metal concentrations, there is a quantitative under-estimation of trace element values by pXRF.

9.2 Recommendation and future work

The studied deposits within the Otavi Mountain Land have been of great interest since the early 1900s, and consequently a lot of scientific works have been done, focusing on them, over the years. Despite that, because of the geological complexity of the whole province, there are still significant questions that are not yet answered pertaining to the genesis as well as the trace element distributions within the sulfide minerals. These includes aspects that might be answered in ongoing studies based on the outcomes of the research work done in this study. The key opportunities for future work related directly to this study are outlined below:

Additional studies on the trace element contents and the trace element distributions in the sulfide minerals are still needed to cover a bigger spectrum of elements. For Khusib Springs, main sulfide minerals are currently analysed for a huge variety of trace elements using LA-ICP-MS; results are expected to be received between February and March 2024 (results are distinctly delayed due to problems at the analytical facility). For the Tsumeb deposit, more Cu and Zn isotopic analyses are currently performed that would supplement the reconnaissance data obtained in this study. Results are still outstanding.

References

- Abraitis, P.K., Pattrick, R.A.D., Vaughan, D.J., 2004. Variations in the compositional, textural and electrical properties of natural pyrite: a review. International Journal of Mineral Processing 74, 41–59. https://doi.org/10.1016/j.minpro.2003.09.002
- Achternbosch, M., Kupsch, C., Sardemann, G., Bräutigam, K.R., 2009. Cadmium flows caused by the worldwide production of primary zinc metal. Industrial Ecology 13(3), 438-454. https://doi.org/10.1111/j.1530-9290.2009.00128.
- Albarède, F., 2004. The Stable Isotope Geochemistry of Copper and Zinc. Reviews in Mineralogy and Geochemistry 55(1), 409–427. https://doi.org/10.2138/gsrmg.55.1.409
- Aldis, C., Olivo, G.R., Morfin, S., 2022. LA-ICP-MS Trace Element Composition of Sphalerite and Galena of the Proterozoic Carbonate-Hosted Morro Agudo Zn-Pb Sulfide District, Brazil: Insights into Ore Genesis. Minerals 12, 1028. https://doi.org/10.3390/min12081028.
- Allsopp, H.L., Ferguson, J., 1970. Measurements relating to the genesis of the Tsumeb pipe, South West Africa. Earth and planetary science letters 9, 448-453.
- Andersson, S.S., Sahlström, F., Jonsson, E., Luth, S., Lynch, E.P., Högdahl, K., Zack, T., Gies, N., Sädbom, S., Hansson, K.S.A., Bergqvist, M., 2022. Mineral paragenesis and sulphide trace element distribution in the metamorphosed Lovisa Zn-Pb deposit, Bergslagen (Sweden), as revealed by 3D X-ray tomography, ore petrography and LA-ICP-MS analysis. Ore Geology Reviews 140, 104611. https://doi.org/10.1016/j.oregeorev.2021.104611.
- Andrew, B.S. Barker, S.L., 2017. Determination of carbonate vein chemistry using portable X-ray fluorescence and its application to mineral exploration.

Geochemistry: Exploration, Environment, Analysis 18, 85-93. https://doi.org/10.1144/geochem2016-011.

- Arne, D.C., Jeffress, G.M., 2014. Sampling and analysis for public reporting of portable X-ray fluorescence data under the 2012 edition of the JORC code. Proceedings of the Sampling 2014 Conference, Perth.
- Asael, D., Matthews, A., Bar-Matthews, M., Halicz, L., 2007. Copper isotope fractionation in sedimentary copper mineralization (Timna Valley, Israel). Chemical Geology 243, 238–254. https://doi:10.1016/j.chemgeo.2007.06.007.
- Asael, D., Matthews, A., Oszczepalski, S., Bar-Matthews, M., Halicz, L., 2009. Fluid speciation controls of low temperature copper isotope fractionation applied to the Kupferschiefer and Timna ore deposits. Chemical Geology 262, 147–158. https://doi:10.1016/j.chemgeo.2009.01.015.
- Balaram, V., Sawant, S.S., 2022. Indicator Minerals, Pathfinder Elements, and Portable Analytical Instruments in Mineral Exploration Studies. Minerals 12(4), 394. https://doi.org/10.3390/min12040394
- Barrie, C.D., Boyle, A.P., Prior, D.J., 2007. An analysis of the microstructures developed in experimentally deformed polycrystalline pyrite and minor sulphide phases using electron backscatter diffraction. Journal of Structural Geology 29(9), 1494-1511. https://doi.org/10.1016/j.jsg.2007.05.005.
- Basei, M.A.S., Frimmel, H.E., Campos Neto, M.C., De Araujo, C.E.G., De Castro, N.A., Passarelli, C.R., 2018. The Tectonic History of the Southern Adamastor Ocean Based on a Correlation of the Kaoko and Dom Feliciano Belts. In: Siegesmund, S., Basei, M., Oyhantçabal, P., Oriolo, S. (eds) Geology of Southwest Gondwana. Regional Geology Reviews. Springer, Cham. https://doi.org/10.1007/978-3-319-68920-3_3.

- Bauer, M.E., Burisch, M., Ostendorf, J., Krause, J., F., M., Seifert, T., Gutzmer, J., 2019a. Trace element geochemistry of sphalerite in contrasting hydrothermal fluid systems of the Freiberg district, Germany: insights from LA-ICP-MS analysis, nearinfrared light microthermometry of sphalerite-hosted fluid inclusions, and sulfur isotope geochemistry. Mineralium Deposita 54, 237–262. https://doi.org/10.1007/s00126-018-0850-0.
- Bauer, B.E., Seifert, T., Burisch, M., Krause, J., Richter, N., Gutzmer, J., 2019b. Indium-bearing sulfides from the Hämmerlein skarn deposit, Erzgebirge, Germany: evidence for late-stage diffusion of indium into sphalerite. Mineralium Deposita 54, 175–192. https://doi.org/10.1007/s00126-017-0773-1.
- Baumgartner, R.J., Kunzmann, M., Spinks, S., Bian, X., John, S.G., Blaikie, T.N., Hu, S., 2021. Zinc isotope composition of the Proterozoic clastic-dominated McArthur River Zn-Pb-Ag deposit, northern Australia. Ore Geology Reviews 139(B), 104545. https://doi.org/10.1016/j.oregeorev.2021.104545.
- Bechstädt, T., Jäger, H., Rittersbacher, A., Schweisfurth, B., Spence, G., Werner, G., Boni, M., 2018. The Cryogenian Ghaub Formation of Namibia – New insights into Neoproterozoic glaciations. Earth-Science Reviews 177, 678-714. https://doi.org/10.1016/j.earscirev.2017.11.028.
- Becker, T., Schreiber, U., Kampunzu, A.B., Armstrong, R., 2006. Mesoproterozoic rocks of Namibia and their plate tectonic setting. Journal of African Earth Sciences 46, 112–140. https://doi:10.1016/j.jafrearsci.2006.01.015.
- Belissont, R., Boiron, M.-C., Luais, B., Cathelineau, M., 2014. LA-ICP-MS analyses of minor and trace elements and bulk Ge isotopes in zoned Ge-rich sphalerites from the Noailhac–Saint-Salvy deposit (France): Insights into incorporation mechanisms and ore deposition processes. Geochimica and

Cosmochimica Acta 126, 518–540. https://doi.org/10.1016/j.gca.2013.10.052.

- Belissont, R., Muñoz, M., Boiron, M.C., Luais, B., Mathon, O., 2016. Distribution and oxidation state of Ge, Cu and Fe in sphalerite by μ-XRF and K-edge μ-XANES: Insights into Ge incorporation, partitioning and isotopic fractionation. Geochimica et Cosmochimica Acta 177, 298–314. https://doi.org/10.1016/j.gca.2016.01.001
- Benites, D., Torró, R., Vallance, J., Laurent, O., Valverde, P.E., Kouzmanoz, K., Chelle-Michou, C., Fontboté, L., 2021. Distribution of indium, germanium, gallium and other minor and trace elements in polymetallic ores from a porphyry system: The Morococha district, Peru. Ore Geology Reviews 136, 104236. https://doi.org/10.1016/j.oregeorev.2021.104236.
- Bernstein, L.R., 1985. Germanium geochemistry and mineralogy. Geochimica et Cosmochimica Acta 49(11), 2409–2422. https://doi.org/10.1016/0016-7037(85)90241-8.
- Berrezueta, E., Ordóñez-Casado, B., Bonilla, W., Banda, R., Castroviejo, R., Carrión, P., Puglla, S., 2016. Ore Petrography Using Optical Image Analysis: Application to Zaruma-Portovelo Deposit (Ecuador). Geosciences 6, 30. https://doi.org/10.3390/geosciences6020030
- Bial, J., Büttner, S., Schenk, V., Appel, P., 2015. The long-term high-temperature history of the central Namaqua Metamorphic Complex: Evidence for a Mesoproterozoic continental back-arc in southern Africa. Precambrian Research 268, 243-278. https://doi.org/10.1016/j.precamres.2015.07.012.
- Blackburn, W.L., Schwendeman, J.F., 1977. Trace element substitution in galena. Canadian Mineralogist 15, 365-373.

- Bobba, S., Carrara, S., Huisman, J, Mathieux, F., Pavel, C., 2020. European Commission, Critical materials for strategic technologies and sectors in the EU - a foresight study, 2020". European publication office. https://doi: 10.2873/58081.
- Boni, M., Terracciano, R., Evans, N.J., Laukamp, C., Schneider, J., Bechstädt, T., 2007. Genesis of vanadium ores in the Otavi Mountainland, Namibia. Economic Geology 102, 441–469. https://doi: 10.2113/gsecongeo.102.3.441
- Bowell, R.J., 2014. Hydrogeochemistry of the Tsumeb deposit: Implications for Arsenate Mineral stability. Mineralogy and Geochemistry 79, 589-627. https://doi.org/10.2138/rmg.2014.79.14.
- Bowell, R.J., Mocke, H., 2019. Minerals new to Tsumeb. Communications of the Geological Survey of Namibia 19, 20-46.
- Bowell, R.J., Alpers, C.N., Jamieson, H.E., Nordstrom, D.K., Majzlan, J., 2014. The environmental geochemistry of arsenic – an overview. Reviews in Mineralogy and Geochemistry 79, 1-16. https://doi.org/10.2138/rmg.2014.79.1.
- Bowyer, F.T., Shore, A.J., Wood, R.A., Alcott, L.J., Thomas, A.L., Butler, I.B., Curtis, A., Hainanan, S., Curtis-Walcott, S., Penny, A.M., Poulton, S.W., 2020. Regional nutrient decrease drove redox stabilisation and metazoan diversification in the late Ediacaran Nama Group, Namibia. Scientific Reports 10(1), 1–12. https://doi.org/10.1038/s41598-020-59335-2.
- Boynton, W.V., 1984. Geochemistry of rare earth elements: Meteorite studies. In: Henderson, P. (eds), Rare Earth Elements Geochemistry, Elsevier Pub. Co., Amsterdam, 63-114. http://dx.doi.org/10.1016/B978-0-444-42148-7.50008-3.
- Bradley, D.C., Leach, D.L., 2003. Tectonic controls of Mississippi Valley-type lead-zinc mineralization in orogenic forelands. Mineralium Deposita 38(6), 652–667. http://dx.doi.org/10.1007/s00126-003- 0355-2.

- Bralia, A., Sabatini, G., Troja, F., 1979. A revaluation of the Co/Ni ratio in pyrite as

  geochemical tool in ore genesis problems. Mineralium Deposita 14, 353–374. https://doi.org/10.1007/BF00206365
- Brand, N. W., Brand C. J., 2014. Performance comparison of portable XRF instruments. Geochemistry: Exploration, Environment, Analysis 14, 125– 138. http://dx.doi.org/10.1144/geochem2012-172
- Brandt, S., Klemd, R., Okrusch, M., 2003. Ultrahigh-temperature metamorphism and multistage evolution of garnet-orthopyroxene granulites from the Proterozoic Epupa Complex, NW Namibia. Journal of Petrology 44, 1121-1144. https://doi: 10.1093/petrology/44.6.1121.
- Brandt, S., Klemd, R., Xie, H., Bobek, P., 2021. Unravelling the P-T-t history of three high-grade metamorphic events in the Epupa Complex, NW Namibia: Implications for the Paleoproterozoic to Mesoproterozoic evolution of the Congo Craton. American Journal of Science 321(1-2), 235-296. DOI: https://doi.org/10.2475/01.2021.07.
- Brzozowski, M. J., Good, D. J., Wu, C., Li, W., 2021. Cu isotope systematics of conduit-type Cu–PGE mineralization in the Eastern Gabbro, Coldwell Complex, Canada. Mineralium Deposita 56, 707–724. https://doi.org/10.1007/s00126-020-00992-8.
- Bourke, A. Ross, P., 2016. Portable X-ray fluorescence measurements on exploration drill-cores : comparing performance on unprepared cores and powders for ‘whole-rock’ analysis. Geochemistry: Exploration, Environment, Analysis 16, 147–157, https://doi.org/10.1144/geochem2014- 326

- Bullen, T.D., 2014. Metal Stable Isotopes in Weathering and Hydrology. In: Holland, H.D., Turekian, K.K. (eds) Treatise on Geochemistry (Second Edition). Elsevier, 329-359. https://doi.org/10.1016/B978-0-08-095975-7.00511-8.
- Butcher, T., Brown, T., 2014. Gallium, In: Gunn, G. (eds), Critical Metals Handbook, First Edition. John Wiley & Sons Ltd.: 150-176.
- Butterman, W.C., Jorgenson, J.D., 2005. Mineral commodity profiles—Germanium: U.S. Geological Survey Open–File Report 2004–1218, 19.
- Cairncross, B., 1997. The Otavi Mountain Land Cu-Pb-Zn-V Deposits, Namibia. Mineralogical Record 28,109-130.
- Cairncross, B., 2017. Connoisseur's Choice: Leiteite, Tsumeb Mine, Tsumeb, Namibia, Rocks & Minerals 92(3), 264-269. http://dx.doi.org/10.1080/00357529.2017.1283661
- Cairncross, B., 2021. Minerals of Berg Aukas, Otavi Mountainland, Namibia, Rocks & Minerals 96(2), 110-147. DOI: 10.1080/00357529.2021.1848216
- Changara, L., 2009. The Lithological and structural controls on mineralisation at Kombat mines, Otavi Mountain Land, Northern Namibia. MSc thesis. University of Namibia. URI: http://hdl.handle.net/11070/448
- Chetty, D., Frimmel, H.E., 2000. The role of evaporites in the genesis of base metal sulphide mineralisation in the Northern platform of the PanAfrican Damara belt, Namibia. Geochemical and fluid inclusion evidence from carbonate wall rock alteration. Mineralium Deposita 35, 364–375. DOI: 10.1007/s001260050247.
- Chew, D.M., Petrus, J.A., Kamber, B.S., 2014. U–Pb LA–ICPMS dating using accessory mineral standards with variable common Pb. Chemical Geology 363, 185-199. https://doi.org/10.1016/j.chemgeo.2013.11.006.
- Chew, D., Drost, K., Marsh, J.H., Petrus, J.A., 2021. LA-ICP-MS imaging in the

geosciences and its applications to geochronology. Chemical Geology 559, 119917. https://doi.org/10.1016/j.chemgeo.2020.119917.

- Choi, S.K., Pak, S.J., Park, J.W, Kim, H.S., Kim, J., Choi, S.H., 2023. Trace-element distribution and ore-forming processes in Au–Ag-rich hydrothermal chimneys and mounds in the TA25 West vent field of the Tonga Arc. Mineralium Deposita 58, 135–160. https://doi.org/10.1007/s00126-022-01136-w
- Chu, X., Li, B., Shen, P., Zha, Z., Lei, Z., Wang, X., Tao, S., Hu, Q., 2022. Trace elements in sulfide minerals from the Huangshaping copper-polymetallic deposit, Hunan, China: Ore genesis and element occurrence. Ore Geology Reviews 144, 104867. https://doi.org/10.1016/j.oregeorev.2022.104867.
- Ciobanu, C. L., Cook, N. J., Pring, A., Brugger, J., Danushevsky, L., Shimizu, M., 2009b. 'Invisible gold' in bismuth chalcogenides. Geochimica et Cosmochimica Acta 73, 1970–1999. https://doi.org/10.1016/j.gca.2009.01.006
- Ciobanu, C.L., Cook, N.J., Utsunomiya, S., Kogagwa, M., Green, L., Gilbert, S., Wade, B., 2012. Gold-telluride nanoparticles revealed in arsenic-free pyrite. American Mineralogist 97, 1515-1518. https://doi.org/10.2138/am.2012.4207
- Clark, A.H., 1970. Arsenian sphalerite from Mina Alcarán, Pampa Larga, Copiapö, Chile. American Mineralogist 55 (9-10), 1794–1797.
- Clark, C., Grguric, B., Mumm, A.S., 2004. Genetic implications of pyrite chemistry from the Palaeoproterozoic Olary Domain and overlying Neoproterozoic Adelaidean sequences, northeastern South Australia. Ore Geology Reviews 25(3-4), 237-257. https://doi.org/10.1016/j.oregeorev.2004.04.003.
- Clifford, T.N., 2008. The geology of the Neoproterozoic Swakop-Otavi transition zone in the Outjo District, northern Damara Orogen, Namibia. South African Journal of Geology 111, 117-140. doi:10.2113/gssajg.111.1.117.

- Conliffe, J., King, R., Wilton, D., 2018. Genesis of carbonate-hosted Zn mineralization in the Hare Bay and Pistolet Bay areas, great Northern Peninsula, Newfoundland. Current Research; New foundland and Labrador Department of Natural Resources Geological Survey, Report 18-1, 71-93.
- Cook, N. J., Ciobanu, C. L., Pring, A., Skinner, W., Shimizu, M., Danyushevsky, L., Melcher, F., 2009. Trace and minor elements in sphalerite: A LA-ICPMS study. Geochimica et Cosmochimica Acta 73 (16), 4761–4791. https://doi:10.1016/j.gca.2009.05.045.
- Cook, N.J., Ciobanu, C., Danyushevsky, L., Gilbert, S., 2011a. Minor and trace elements in bornite and associated Cu–(Fe)-sulfides: A LA-ICP-MS study Bornite mineral chemistry. Geochimica et Cosmochimica Acta 75, 6473–6496. https://doi.org/10.1016/j.gca.2011.08.021.
- Cook, N.J., Ciobanu, C.L., Williams, T. 2011b. The mineralogy and mineral chemistry of indium in sulphide deposits and implications for mineral processing. Hydrometallurgy, 108 (3), 226–228. https://doi.org/10.1016/j.hydromet.2011.04.003
- Cook, N.J., Ciobanu, C.L., Meria, D., Silcock, D., Wade, B., 2013. Arsenopyrite-pyrite association in an orogenic gold ore: tracing mineralization history from textures and trace elements. Economic Geology 108, 1273–1283. https://doi.org/10.2113/econgeo.108.6.1273.
- Cook, N., Ciobanu, C.L., George, L., Zhu, Z.-Y., Wade, B., Ehrig, K., 2016. Trace element analysis of minerals in magmatic-hydrothermal ores by laser ablation-inductively coupled plasma mass spectrometry: Approaches and opportunities. Minerals 6(4), 111. https://doi.org/10.3390/min6040111.
- Cooke, D.R., Hollings, P., Wilkinson, J.J., Tosdal, R.M., 2014. 13.14 -

Geochemistry of Porphyry Deposits. In: Holland, H.D., Turekian, K.K. (eds) Treatise on Geochemistry (Second Edition). Elsevier, 357-381. https://doi.org/10.1016/B978-0-08-095975-7.01116-5.

- Cordeiro, P.F.O., Oliveira, C.G., Paniago, L.N., Romagna, G., Santos, R., 2018. The carbonate-hosted MVT Morro Agudo Zn-Pb deposit, central Brazil. Ore Geology Reviews 101, 437-452. https://doi.org/10.1016/j.oregeorev.2018.08.002.
- Cornell D.H., Thomas, R.J., Moen, H.F.G., Reid, D.L., Moore, J.M., Gibson, R.L., 2006. The Namaqua-Natal Province. In: Johnson, M.R., Anhaeusser, C.R., Thomas, R.J. (eds) The Geology of South Africa. Geological Society of South Africa, Johannesburg/Council for Geoscience, Pretoria, 325-379.
- Corner, B., 2000. Crustal framework of Namibia derived from magnetic and gravity data. Communications Geological Survey Namibia, Henno Martin Special 12, 13–19.
- Cugerone, A., Cenki-Tok, B., Mu˜noz, M., Kouzmanov, K., Oliot, E., Motto-Ros, V., Goff, E.L., 2021. Behavior of critical metals in metamorphosed Pb-Zn ore deposits: example from the Pyrenean Axial Zone. Mineralium Deposita 56, 685–705. https://doi.org/10.1007/s00126-020-01000-9.
- Dauteuil, O., Picart, C., Guillocheau, F., Pickford, M., Senut, B., 2018. Cenozoic deformation and geomorphic evolution of the Sperrgebiet (Southern Namibia) Communications of the Geological Survey of Namibia 18, 1-18.
- Deane, J.G., 1995. The structural evolution of the Kombat deposit, Otavi Mountain Land, Namibia, Communications of the Geological Survey of Namibia 10, 99-107.
- Deditius, A.P., Utsunomiya, S., Reich, M., Kesler, S.E., Ewing, R.C., Hough, R., Walshe, J., 2011. Trace metal nanoparticles in pyrite. Ore Geology Reviews 42 (1), 32-46. https://doi.org/10.1016/j.oregeorev.2011.03.003.

- Demir, Y., Uysal, I., Sadıklar, M.B., 2013. Mineral chemical investigation on sulfide mineralization of the Istala deposit, Gümüşhane, NE-Turkey. Ore Geology Reviews 53, 306-317. https://doi.org/10.1016/j.oregeorev.2013.01.014.
- Del Real, I., Thompson, J.F.H., Simon, A. C. Reich, M., 2020. Geochemical and Isotopic Signature of Pyrite as a Proxy for Fluid Source and Evolution in the Candelaria-Punta del Cobre Iron Oxide Copper-Gold District, Chile. Economic Geology 115(7), 1493–1518. https://doi.org/10.5382/econgeo.4765
- Delpomdor, F., Schröder, S., Préat, A., Lapointe P., Blanpied, C., 2018. Sedimentology and chemostratigraphy of the late Neoproterozoic carbonate ramp sequences of the Hüttenberg Formation (northwestern Namibia) and the C5 Formation (western central Democratic Republic of Congo): Record of the late post-Marinoan marine transgression on the margin of the Congo Craton. South African Journal of Geology. Article in South African Journal of Geology. DOI: 10.25131/sajg.121.0003.
- Deyell, C.L., Hedenquist, J.W., 2011. Trace element geochemistry of enargite in the Mankayan district, Philippines. Economic Geology 106(8), 1465-1478. https://doi.org/10.2113/econgeo.106.8.1465
- Ding, T., Wang, J., Tan, T., Ma, D., Lu, J., Zhang, R., Liang, J., Zhu, C., Wu, B., 2021.

  Accumulation of sulfides in the basement of southern Hunan Province, China: Implications for Pb-Zn mineralization related to reduced granitoids. Ore Geology Review 129, 103939. https://doi.org/10.1016/j.oregeorev.2020.103939
- Domack, E.W., Hoffman, P.F., 2011. An ice grounding-line wedge from the Ghaub glaciation (635 Ma) on the distal foreslope of the Otavi carbonate platform,

Namibia, and its bearing on the snowball Earth hypothesis. Geological Society of America Bulletin. DOI: 10.1130/B30217.1

- Donovan, J.J., Tingle, T., 1996. An improved mean atomic number background correction for quantitative microanalysis. Journal of Microscopy and Microanalysis 2, 1–7. doi:10.1017/S1431927696210013.
- Donovan, J.J., Singer, W.J., Armstrong, J.T., 2016. A new EPMA method for fast trace element analysis in simple matrices. American Mineralogist 101 (8), 1839-1853. https://doi.org/10.2138/am-2016-5628.
- Drüppel, K., Littmann, S., Romer, R.L., Okrusch, M., 2007. Petrology and isotope geochemistry of the Mesoproterozoic anorthosite and related rocks of the Kunene Intrusive Complex, NW Namibia. Precambrian Research. 156(1–2), 1-31. https://doi.org/10.1016/j.precamres.2007.02.005.
- Duran, C.J., Barnes, SJ., Corkery, J.T., 2016. Geology, petrography, geochemistry, and genesis of sulfide-rich pods in the Lac des Iles palladium deposits, western Ontario, Canada. Mineralium Deposita 51, 509–532. https://doi.org/10.1007/s00126-015-0622-z.
- European Commision, 2014. Critical Raw Materials for the EU: Report of the Ad Hoc Working Group on Defining Critical Raw Materials. European Commission: Enterprise and Industry.
- European Commision, 2017. Study on the Review of the Review List of Critical Raw Materials: Executive Summary. European Commission.
- European Comission, 2020. Study on the EU's list of Critical Raw Materials (2020) Final Report. European commission.
- Fan, M., Ni, P., Pan, J., Wang, Q., Ding, J., Chu, S., Li, W., Huang, W., Zhu, R., Chi, Z., 2023. Rare disperse elements in epithermal deposit: Insights from LA–ICP–

MS study of sphalerite at Dalingkou, South China. Journal of Geochemical Exploration 244, 107124. https://doi.org/10.1016/j.gexplo.2022.107124

- Fisher, L., Gazley, M.F., Baensch, A., Barnes, S.J., Cleverley, J., Duclaux, G., 2014. Resolution of geochemical and lithostratigraphic complexity: a workflow for application of portable X-ray fluorescence to mineral exploration. Geochemistry: Exploration, Environment, Analysis 14, 149–159. https://doi.org/10.1144/geochem2012-158.
- Fortier, S.M., Nassar, N.T., Lederer, G.W., Brainard, J., Gambogi, J., McCullough, E.A., 2018. Draft critical mineral list – summary of methodology and background information – U.S. Geological Survey technical input document in response to Secretarial order no. 3359, 15.
- Foster D.A., Goscombe B.D., Newstead, B., Mapani, B., Mueller, P.A., Gregory, L.C., Muvangua, E., 2015. U–Pb age and Lu–Hf isotopic data of detrital zircons from Neoproterozoic Damara Sequence: Implications for pre-Gondwana proximity of Congo and Kalahari. Gondwana Research 28,179–190. https://doi.org/10.1016/j.gr.2014.04.011.
- Foley, N. K., Jaskula, B. W., Kimball, B .E., Schulte, R. F., 2017. Gallium. In Schulz, K.J., DeYoung, J.H., Seal II, R.R., Bradley, D.C. (eds) Critical Mineral Resources of the United States—Economic and Environmental Geology and Prospects for Future Supply. U.S. U.S. Geological Survey Professional Paper 1802, H1–H35, https://doi.org/10.3133/pp1802H.
- Fontana, D., Forte, F., Pietrantonio, M., Pucciarmati, S., 2021. Recent developments on recycling end-of-life flat panel displays: A comprehensive review focused on indium. Critical Reviews in Environmental Science and Technology 51(5), 429-456. https://doi.org/10.1080/10643389.2020.1729073.

- Frank-Kamenetskaya, O.V., Rozhdestvenskaya, I.V., Yanulova, L.A., 2002. New data on the crystal structures of colusites and arsenosulvanites. Journal of Structural Chemistry, 43(1), 89-100.
- Frenzel, M., Ketris, M.P., Gutzmer, J., 2014. On the geological availability of germanium. Mineralium Deposit 49(4), 471–486. https://doi.org/10.1007/s00126-013-0506-z.
- Frenzel, M., Ketris, M. P., Seifert, T., Gutzmer, J., 2016. On the current and future availability of gallium. Resources Policy 47(3), 38-50. https://doi.org/10.1016/j.resourpol.2015.11.005.
- Frenzel, M., Hirsch, T., Gutzmer, J., 2016. Gallium, germanium, indium, and other trace and minor elements in sphalerite as a function of deposit type — A meta-analysis. Ore geology reviews, 76, 52-78. https://doi.org/10.1016/j.oregeorev.2015.12.017
- Frenzel, M., Bachmann, K., Carvalho, J.R.S. Relvas, J.M.R.S., Pacheco, N., Gutzmer, J., 2019. The geometallurgical assessment of by-products—geochemical proxies for the complex mineralogical deportment of indium at Neves-Corvo, Portugal. Mineralium Deposita 54, 959–982. https://doi.org/10.1007/s00126-018-0849-6
- Frimmel, H.E., Deane, J.G., Chadwick, P.J., 1996. Pan-African tectonism and the genesis of base metal sulfide deposits in the northern foreland of the Damara Orogen, Namibia. in Sangster, D.F. (eds) Carbonate-hosted lead- zinc deposits—[Society of Economic Geologists] 75th anniversary volume: Littleton, Colo. Society of Economic Geologists Special Publication 4, 204–217.
- Frimmel, H.E., Jonasson, I.R., Mubita, P., 2004. An Eburnean base metal source for sediment-hosted zinc–lead deposits in Neoproterozoic units of Namibia: lead

isotopic and geochemical evidence. Mineralium Deposita 39, 328–343. https://doi.org/10.1007/s00126-004-0410-7

- Frondel, C., Ito, J., 1957. Geochemistry of Germanium in the oxidized zone of the Tsumeb Mine, South-West Africa. The American Mineralogist 42, 743-753.
- Gallhofer, D., Lottermoser, B.G., 2018. The Influence of Spectral Interferences on Critical Element Determination with Portable X-Ray Fluorescence (pXRF). Minerals 8, 320. htts://doi:10.3390/min8080320.
- Gao, S., Luo, T.C., Zhang, B.R., Zhang, H.F., Han, Y.W., Zhao, Z.D., Hu, Y.K., 1998. Chemical composition of the continental crust as revealed by studies in East China. Geochimica et Cosmochimica Acta 62, 1959–1975. https://doi.org/10.1016/S0016-7037(98)00121-5.
- Gao, Z., Zhu, X., Sun, J., Luo, Z., Bao, C., Tang, C., Ma, J., 2018. Spatial evolution of Zn-Fe-Pb isotopes of sphalerite within a single ore body: A case study from the Dongshengmiao ore deposit, Inner Mongolia, China. Minerium Deposita 53, 55–65. https://doi.org/10.1007/s00126-017-0724-x
- Gagnevin, D., Boyce, A.J., Barrie, C.D., Menuge, J.F., Blakeman, R.J., 2012. Zn, Fe and S isotope fractionation in a large hydrothermal system. Geochimica et Cosmochimica Acta 88, 183-198. https://doi.org/10.1016/j.gca.2012.04.031.
- Gazley, M.F., Fisher, L.A., 2014a. A review of the reliability and validity of portable X-ray fluorescence spectrometry (pXRF) data. In: Gazley, M. F., Fisher, L. (eds) Mineral resource and ore reserve estimation – the AusIMM guide to good practice. The Australasian Institute of Mining and Metallurgy. Melbourne 69-82.
- Gazley, M.F., Duclaux, G., Fisher, L.A., Tutt, M.T., Latham, A.R., Hough, R.M. De Beer, S.J. Taylor, M.D., 2014b. A comprehensive approach to understanding ore deposits using portable X-ray fluorescence (pXRF) data at the Plutonic Gold

Mine, Western Australia. Geochemistry: Exploration, Environment, Analysis 15, 113– 124. https://doi.org/10.1144/geochem2014-280.

- Geier, B.H., Ottemann, J., 1970. New primary vanadium-, germanium-, gallium-, and tin-minerals from the Pb-Zn-Cu-deposit Tsumeb, South West Africa. Mineralium Deposita 5, 29–40. https://doi.org/10.1007/BF00207004
- George, L., Cook, N.J., Ciobanu, C.L., Wade, B.P., 2015. Trace and minor elements in galena: a reconnaissance LA-ICP-MS study. American Mineralogist 100(2-3), 548–569. https://doi.org/10.2138/am-2015-4862.
- George, L.L., Cook, N.J., Ciobanu, C.L., 2016. Partitioning of trace elements in cocrystallized sphalerite–galena–chalcopyrite hydrothermal ores. Ore Geology Reviews 77, 97–116. https://doi.org/10.1016/j.oregeorev.2016.02.009
- George, L.L., Cook, N.J., Ciobanu, C.L., 2017. Minor and trace elements in natural tetrahedrite-tennantite: effects on element partitioning among base metal sulphides. Minerals 7(2), 17. https://doi.org/10.3390/min7020017.
- George, L.L., Cook, N.J., Crowe, B.B.P., Ciobanu, C.L., 2018. Trace elements in hydrothermal chalcopyrite. Mineralogical Magazine 82(1), 59–88. doi:10.1180/minmag.2017.081.021.
- Germs, G.J.B., 1983. Implications of a sedimentary facies and depositional environmental analysis of the Nama Group in Southwest Africa/Namibia. Special Publication Geological Society of South Africa 11, 89–114.
- Germs, G.J.B., Knoll, A.H., Vidal, G., 1986. Latest Proterozoic microfossils from the Nama Group, Namibia (South West Africa). Precambrian Research 32, 45-62. https://doi.org/10.1016/0301-9268(86)90029-X.
- Golden deeps limited., 2020. High-grade Khusib Springs copper-silver mine comes into to golden deeps ownership. ASX announcement 18 August 2020. Report

- Golden deeps limited., 2022. ACN 054 570 777 Interim Financial Report for the Half Year Ended 31 December 2022. Report
- Göçmengil, G., Sisman T. F., Uzun, F., Guillong, M., Yilmaz, I., Aysal, N., Hanilci, N., 2022. Accurate whole-rock geochemistry analysis by combined ICP-OES and LA-ICP-MS instruments. Bulletin of The Mineral Research and Exploration 168, 157-165. https://doi.org/10.3929/ethz-b-000579637
- González-Álvarez, I., Stoppa, F., Yang, X, Y., Porwal, A., 2021. Introduction to the special Issue, insights on carbonatites and their mineral exploration approach: A challenge towards resourcing critical metals. Ore Geology Reviews 133, 104073. https://doi.org/10.1016/j.oregeorev.2021.104073.
- Goscombe, B., Gray, D., Hand, M., 2004. Variation in Metamorphic Style along the Northern Margin of the Damara Orogen, Namibia. Journal of Petrology 45(6), 1261–1295 https://doi.org/10.1093/petrology/egh013.
- Goscombe, B., Foster, D.A., Gray, D., Wade, B., Marsellos, A., Titus, J., 2017. Deformation correlations, stress field switches and evolution of an orogenic intersection: The Pan-African Kaoko-Damara orogenic junction, Namibia. Geoscience Frontiers 8, 1187-1232. //dx.doi.org/10.1016/j.gsf.2017.05.001
- Goscombe, B., Foster, D.A., Gray, D., Wade, B., 2018. The Evolution of the Damara Orogenic System: A Record of West Gondwana Assembly and Crustal Response. In: Siegesmund, S., Oyhantçabal, P., Basei, M.A.S., Oriolo, S. (eds) Geology of Southwest Gondwana. Regional Geology Reviews. Springer, Cham. https://doi.org/10.1007/978-3-319-68920-3_12.
- Graedel, T.E., Barr, R., Chandler, C., Chase, T., Choi, J., Christoffersen, L., Friedlander, E., Henly, C., Jun, C., Nassar, N., T., Schechner, D., Warren, S., Yang,

M., Zhu, C., 2012. Methodology of Metal Criticality Determination. Environmental Science & Technology 46, 1063-1070. https://doi.org/10.1021/es203534z.

- Graham, S., Pearson, N., Jackson, S., Griffin, W., O'Reilly, S.Y., 2004. Tracing Cu and Fe from source to porphyry: in situ determination of Cu and Fe isotope ratios in sulfides from the Grasberg Cu–Au deposit. Chemical Geology 207, 147– 169. doi:10.1016/j.chemgeo.2004.02.009.
- Grant, H.L.J., Hannington, M.D., Petersen, S., Frische, M., Fuchs, S.H., 2018. Constraint on the behavior of trace elements in the actively-forming TAG deposit, Mid-Atlantic Ridge, based on LA-ICP-MS analyses of pyrite. Chemical Geology 498, 45–71. https://doi. org/10.1016/j.chemgeo.2018.08.019.
- Gray, D., Foster, D., Goscombe, B., Passchier, C., Trouw, R., 2006. 40Ar/39Ar thermochronology of the Pan-African Damara Orogen, Namibia, with implications for tectonothermal and geodynamic evolution. Precambrian Research 150(1-2), 49-72. https://doi.org/10.1016/j.precamres.2006.07.003
- Gray, D., Foster, D., Meert, J., Goscombe, B., Armstrong, R., Trouw, R., Passchier, C., 2008. A Damara orogen perspective on the assembly of southwestern Gondwana. Geological Society Special Publication 294, 257-278. https://doi.org/10.1144/SP294.14
- Gregory, D.D., Large, R.R., Halpin, J.A., Baturina, E.L., Lyons, T.W., Wu, S., Danyushevsky, L., Sack, P.J., Chappaz, A., Maslennikov, V.V., Bull, S.W., 2015. Trace element content of sedimentary pyrite in black shales. Economic Geology 110, 1389–1410. https://doi.org/10.2113/econgeo.110.6.1389
- Griffin, W.L., Ashley, P.M., Ryan, C.G., Sie, S.H., Suter, G.F., 1991. Pyrite geochemistry in the North Arm epithermal Ag-Au deposit, Queensland, AustraliaA proton-microprobe study. The Canadian Mineralogist 29, 185–198.

- Haest, M., Muchez, P., 2011. Stratiform and vein-type deposits in the pan-African Orogen in Central and Southern Africa: Evidence for multiphase mineralisation. Geologica Belgica 14, 23-44.
- Haldar, S.K., Tisljar, J., 2014. Introduction to mineralogy and petrology. Elsevier. ISBN: 978-0-12-408133-8. https://doi.org/10.1016/C2019-0-00625-5
- Hall, G.E., Bonham-Carter, G.F., Buchar, A., 2014. Evaluation of portable X-ray fluorescence (pXRF) in exploration and mining: Phase 1, control reference materials. Geochemistry: Exploration, Environment, Analysis 14, 99–123. https://doi.org/10.1144/geochem2013-241.
- Halverson, G.P., Hoffman, P.F., Schrag, D.P., Kaufman, A.J., 2002. A major perturbation of the carbon cycle before the Ghaub glaciation (Neoproterozoic) in Namibia: Prelude to snowball Earth? Geochemistry, Geophysics, Geosystems, 3(6), 1–24. https://doi.org/10.1029/2001gc000244
- Halverson, G.P., Hoffman, P.F., Schrag, D.P., Maloof, A.C., Rice, A.H.N., 2005. Toward a Neoproterozoic composite carbon-isotope record. Geological Society of America Bulletin 117, 1181-1207. DOI: 10.1130/B25630.1.
- Hammerli, J., Spandler, C., Oliver, N.H., 2015. Zn and Pb mobility during metamorphism of sedimentary rocks and potential implications for some base metal deposits. Miner Deposita 50, 657–664. https://doi.org/10.1007/s00126-015-0600-5.
- Harris, M., Cornell, D.H., Mapani, B.S., Malobela, T., Lundell, C., Jonsson. A.K., 2020. The Kumbis and Nagatis Formations and the Helmeringhausen Gabbro: Oldest undeformed rocks of the Sinclair Supergroup in Namibia. Journal of African Earth Sciences 165, 103733. https://doi.org/10.1016/j.jafrearsci.2019.103733.

- Hartnady, M., Kirkland, C., Dutch, R., Bodorkos, S., Jagodzinski, E., 2020. Evaluating zircon initial Hf isotopic composition using a combined SIMS–MC-LASS-ICP-MS approach: A case study from the Coompana Province in South Australia. Chemical Geology 558, 119870. https://doi.org/10.1016/j.chemgeo.2020.119870.
- Hedberg, R.M., 1979. Stratigraphy of the Ovamboland Basin, South West Africa. Chamber of Mines Precambrian Research Unit, University of Cape Town 24. 325.
- Hoal, B.G., 1993. The Proterozoic Sinclair Sequence in southern Namibia: intracratonic rift or active continental margin setting? Precambrian Research 63(1-2), 143-162. https://doi.org/10.1016/0301-9268(93)90009-Q.
- Hoal, K.O., Hoal, B.G., Griffin, W.L., Armstrong, R., 2000. Characterization of the age and nature of the lithosphere in the Tsumkwe region, Namibia. Communs Geologic Survey Namibia 12, 21-28.
- Hoffman, P.F., Swart, R., Eckhardt, E.F., Guowei, H., 1994. Damara orogen of northwest Namibia. Geological Excursion Guide Geological Survey of Namibia.
- Hoffmann, P.F., Hawkins, D.P., Isachsen, C.E., Bowring, S.A., 1996. Precise U-Pb zircon ages for early Damaran magmatism in the Summas Mountains and Welwitschia Inlier, northern Damara belt, Namibia. Geological Survey of Namibia Communication 11, 47-52.
- Hoffman, P.F., Kaufman, A.J., Halverson, G.P., Schrag, D.P., 1998 a. A Neoproterozoic snowball earth. Science 281(5381), 1342–1346. https://doi.org/10.1126/science.281.5381.1342.
- Hoffman, P.F., Kaufman, A.J., Halverson, G.P., Schrag, D.P. 1998 b. Comings and goings of global glaciations on a Neoproterozoic tropical platform in Namibia, 8(5), 1-9. GSA today.

- Hoffmann, K.H., Condon, D.J., Bowring, S.A., Crowley, J.L., 2004. U-Pb zircon date from the Neoproterozoic Ghaub Formation, Namibia: Constrains on Marinoan glaciation. Geology 32(9), 817-820. https://doi.org/10.1130/G20519.1
- Hoffman, P.F., 2005. Hoffman, P. F. On Cryogenian (Neoproterozoic) ice-sheet dynamics and the limitations of the glacial sedimentary record. 28th DeBeers Alexander Du Toit Memorial Lecture. S. Afr. J. Geol. 108, 557-576. South African Journal of Geology - S AFR J GEOL. 108, 557-577. DOI: 10.2113/108.4.557.
- Hoffman, P.F., 2011. Strange bedfellows: glacial diamictite and cap carbonate from the Marinoan (635 Ma) glaciation in Namibia. Sedimentology 58, 57–119. https://doi.org/10.1111/j.1365-3091.2010.01206.x
- Hoffman, P.F., Halverson, G.P., Schrag, D.P., Higgins, J.A., Domack, E.W., Macdonald, F.A., Pruss, S.B., Blättler, C.L., Crockford, P.W., Hodgin, E.B., Bellefroid, E.J., Johnson, B.W., Hodgskiss, M.S.W., Lamothe, K.G. LoBianco, S.J.C., Busch, J.F., Howes, B.J., Greenman, J.W., Nelson, L.L., 2021. Snowballs in Africa: sectioning a long-lived Neoproterozoic carbonate platform and its bathyal foreslope (NW Namibia). Earth-Science Reviews 219, 103616. https://doi.org/10.1016/j.earscirev.2021.103616.
- Hoffman, P.F., Pruss, S.B., Blättler, C.L., Bellefroid, E.J. & Johnson, B.W. 2021. A Reference Section for the Otavi Group (Damara Supergroup) in Eastern Kaoko Zone near Ongongo, Namibia. Communications of the Geological Survey of Namibia 23, 1-25.
- Hoffmann, K.H., 1989. New aspects of lithostratigraphic subdivision and correlation of late Proter-ozoic to early Cambrian rocks of the southern Damara Belt and their correlation with the central and northern Damara Belt and the Gariep Belt. Communication Geological Survey Namibia 5, 61-70.

- Hoffmann, K.F., Prave, A.R., 1996. A preliminary note on a revised subdivision and regional correlation of the Otavi Group ‘based on glaciogenic diamictites and associated cap dolostones. Communations of the Geological Survey of Namibia 11, 83-88.
- Hoffmann, K.H., Condon, D.J., Bowring, S.A., Crowley, J.L., 2004. U-Pb zircon date from the Neoproterozoic Ghaub Formation, Namibia: Constraints on Marinoan glaciation. Geology 32(9), 817–820. https://doi.org/10.1130/G20519.1.
- Horn, S., Dziggel, A., Kolb, J. Sindern, S., 2019. Textural characteristics and trace element distribution in carbonate-hosted Zn-Pb-Ag ores at the Paleoproterozoic Black Angel deposit, central West Greenland. Minerium Deposita 54, 507–524. https://doi.org/10.1007/s00126-018-0821-5
- Höll, R., Kling, M., Schroll, E., 2007. Metallogenesis of germanium—A review. Ore Geology Reviews 30(3-4), 145-180. https://doi.org/10.1016/j.oregeorev.2005.07.034.
- Hu, Z., Gao, S., 2008. Upper crustal abundances of trace elements: A revision and update. Chemical Geology 253, 205–221. Hu, Z., Gao, S., 2008. Upper crustal abundances of trace elements: A revision and update. Chemical Geology 253, 205–221.
- Hu, Y., Ye, L.,Wei, C., Li, Z., Huang, Z and Wand, H., 2020. Trace Elements in Sphalerite from the Dadongla Zn-Pb Deposit, Western Hunan–Eastern Guizhou Zn-Pb Metallogenic Belt, South China. Acta Geologica Sinica (English Edition) 94(6), 2152–2164. DOI: 10.1111/1755-6724.14616.
- Hu, Y., Wei, C., Ye, L., Huang, Z., Danyushevsky, L., Wang, H., 2021. LA-ICP-MS sphalerite and galena trace element chemistry and mineralization-style fingerprinting for carbonate-hosted Pb-Zn deposits: Perspective from early

Devonian Huodehong deposit in Yunnan, South China. Ore Geology Reviews 136, 104253. https://doi.org/10.1016/j.oregeorev.2021.104253.

- Hughes, M., 1987. The Tsumeb orebody, Namibia, and related dolostone-hosted base metal ore deposits of Central Africa. PhD Thesis (unpubl.), University of the Witwatersrand, 448.
- Hughes, R., Barker, S.L., 2018. Using portable XRF to infer adularia halos within the Waihi Au-Ag system, New Zealand. Geochemistry: Exploration, Environmental, Analysis 18(2), 97-108. https://doi.org/10.1144/geochem2016-006
- Huston, D.L., Sie, S.H., Suter, G.F., Cooke, D.R., Both, R.A., 1995. Trace elements in sulfide minerals from eastern Australian volcanic-hosted massive sulfide deposits; Part I, Proton microprobe analyses of pyrite, chalcopyrite, and sphalerite, and Part II, Selenium levels in pyrite; comparison with delta 34 S values and implications for the source of sulfur in volcanogenic hydrothermal systems. Economic Geology 90, 1167-1196. https://doi.org/10.2113/gsecongeo.90.5.1167
- Ishihara, S., Hoshino, K., Murakami, H., Endo, Y., 2006. Resource Evaluation and Some Genetic Aspects of Indium in the Japanese Ore Deposits. Resource Geology 56, 347-364. https://doi.org/10.1111/j.1751-3928.2006.tb00288.x
- Jelsma, H.A., McCourt, S., Perritt, S.H., Armstrong, R.A., 2018. The geology and evolution of the Angolan Shield, Congo Craton. In: Siegesmund, S., Basei, M., Oyhantçabal, P., Oriolo, S. (eds) Geology of Southwest Gondwana. Regional Geology Reviews. Springer, Cham. https://doi.org/10.1007/978-3-319-68920-3_9.
- Jenner, G.A., Longerich, H.P., Jackson, S.E., Fryer, B.J., 1990. ICP-MS — A powerful tool for high-precision trace-element analysis in Earth sciences: Evidence from analysis of selected U.S.G.S. reference samples. Chemical Geology 83(1–2), 133-148. https://doi.org/10.1016/0009-2541(90)90145-W.

- Jorgenson, J.D., George, M.W., 2004. Mineral commodity profile—Indium: U.S. Geological Survey Open-FileReport 2004–1300, 20. https://doi.org/10.3133/ofr20041300
- Jovic, S.M., Guido, D.M., Schalamuk, I.B., Rios, F.J., Tassinari, C.C.G., Recio, C., 2011. Pingüino In-bearing polymetallic vein deposit, Deseado Massif, Patagonia, Argentina: characteristics of mineralization and ore-forming fluids. Mineralium Deposita 46, 257–271. https://doi.org/10.1007/s00126-010-0324-5
- Kamona, A.F., Lévêque, J., Friedrich, G., Haack, U., 1999. Lead isotopes of the carbonate-hosted Kabwe, Tsumeb, and Kipushi Pb-Zn-Cu sulphide deposits in relation to Pan African orogenesis in the Damaran-Lufilian Fold Belt of Central Africa. Mineralium Deposita 34, 273-283. DOI: 10.1007/s001260050203.
- Kamona, F., Günzel, A., 2007. Stratigraphy and base metal mineralization in the Otavi Mountain Land, Northern Namibia- a review and regional interpretation. Gondwana Research 11, 396-413. https://doi.org/10.1016/j.gr.2006.04.014.
- Karakaya, M.C., Karakaya, N., Küpeli, S., Yavuz, F., 2012. Mineralogy and geochemical behavior of trace elements of hydrothermal alteration types in the volcanogenic massive sulfide deposits, NE Turkey. Ore Geology Reviews 48, 197-224. https://doi.org/10.1016/j.oregeorev.2012.03.007.
- Kastanaki, E., Giannis, A., 2022. Forecasting quantities of critical raw materials in obsolete feature and smart phones in Greece: A path to circular economy. Journal of Environmental Management, 307. //doi.org/10.1016/j.jenvman.2022.114566.
- Kavner, A., John, S.G., Sass, S., Boyle, E.A., 2008. Redox-driven stable isotope fractionation in transition metals: application to Zn electroplating. Geochimica et Cosmochimica Acta 72(7), 1731-1741. https://doi.org/10.1016/j.gca.2008.01.023.

- Kearns, S., Wade, J. 2021. Electron Probe Microanalysis in Mineralogy. In Alderton, D., Elias, S.A. (eds) Encyclopedia of Geology (Second Edition). Academic Press. 532-545. https://doi.org/10.1016/B978-0-12-409548-9.12073-1.
- Kelley, K.D., Leach, D.L., Johnson, C.A., Clark, J.L., Fayek, M., Slack, J.F., Anderson, V. M., Ayuso, R.A., Ridley, W.I., 2004. Textural, compositional, and sulfur isotopevariations of sulfide minerals in the Red Dog Zn–Pb–Ag deposits, Brooks Range, Alaska: implications for ore formation. Economic Geology 99, 1509–1532. DOI: 10.2113/gsecongeo.99.7.1509
- Kelley, K.D., Wilkinson, J.J., Chapman, J.B., Crowther, H.L., Weiss, D.J., 2009. Zinc isotopes in sphalerite from base metal deposits in the red dog district, northern Alaska. Economic Geology 104(6), 767–773. https://doi.org/10.2113/gsecongeo.104.6.767
- Kleinhanns, I., Fullgraf, T., Wilsky, F., Nolte, N., Fliegel, D., Klemd, R., Hansen, B., 2013. U-Pb zircon ages and (isotope) geochemical signatures of the Kamanjab Inlier (NW Namibia): Constraints on Palaeoproterozoic crustal evolution along the southern Congo craton. Geological Society Special Publication 389(1), 165-195. DOI 10.1144/SP389.1
- Koglin, N., Frimmel, H.E., Minter, W.L., Br¨atz, H., 2010. Trace-element characteristics of different pyrite types in Mesoarchaean to Palaeoproterozoic placer deposits. Minerium Deposita 45, 259–280. https://doi.org/10.1007/s00126-009-0272-0
- Kröner, A., 1982. Rb–Sr geochronology and tectonic evolution of the Pan-African Damara belt of Namibia, southwestern Namibia. American Journal of Science 282, 1471–1507. DOI:10.2475/AJS.282.9.1471
- Kröner, S., Konopásek, J., Kröner, A., Passchier, C.W., Poller, U., Wingate, M.T.D., Hofmann, K.H., 2004. U-Pb and Pb-Pb zircon ages for metamorphic rocks

in the Kaoko Belt of Northwestern Namibia: A Palaeo- to Mesoproterozoic basement reworked during the Pan-African orogeny. South African Journal of Geology 107(3), 455–476. https://doi.org/10.2113/107.3.455

- Kröner, A., Rojas-Agramonte, Y., Hegner, E., Hoffmann, K.H., Wingate, M.T.D., 2010. SHRIMP zircon dating and Nd isotopic systematics of Palaeoproterozoic migmatitic orthogneisses in the Epupa Metamorphic Complex of northwestern Namibia. Precambrian Research 183(1), 50–69. doi:10.1016/j.precamres.2010.06.018.
- Kumar, A.A., Sanislav, I.V., Cathey, H.E. Dirks, P.H.G.M., 2023. Geochemistry of indium in magmatic-hydrothermal tin and sulfide deposits of the Herberton Mineral Field, Australia. Mineralium Deposita 58, 1297–1316. https://doi.org/10.1007/s00126-023-01179-7
- Large, R.R., Danyushevsky, L., Hollit, C., Maslennikov, V., Meffre, S., Gilbert, S., Bull, S., Scott, R., Emsbo, P., Thomas, H., 2009. Gold and trace element zonation in pyrite using a laser imaging technique: implications for the timing of gold in orogenic and Carlin-style sediment-hosted deposits. Economic Geology 104, 635–668. https://doi.org/10.2113/gsecongeo.104.5.635
- Larson, P.B., Maher, K., Ramos, F.C., Chang, Z., Gaspar, M., Meinert, L. D., 2003. Copper isotope ratios in magmatic and hydrothermal ore-forming environments. Chemical Geology 201(3-4), 337-350. https://doi.org/10.1016/j.chemgeo.2003.08.006
- Laukamp, C., 2006. Structural and fluid system evolution in the Otavi Mountain Land (Namibia) and its significance for the Genesis of sulphide and non-sulphide mineralisation. Ph.D thesis, University of Heidelberg, Germany. (Unpbl).

- Laurent, O., Guillong, M., Heinrich, C., Neubauer, K., Stephan, C., 2021. Advantages of a fast-scanning quadrupole for LA-ICP-MS analysis of fluid inclusions. Journal of Analytical Atomic Spectrometry 36, 2043–2050. https://doi.org/10.1039/D1JA00193K.
- Leach, D.L., Bradley, D.C., Huston, D., Sergei, P.A., Ryan, T.D., Steven, G.J., 2010. Sediment-hosted lead-zinc deposits in earth history. Economic Geology 105, 593–625. https://doi.org/10.2113/gsecongeo.105.3.593
- Lehmann, B., Pašava, J., Šebek, O., Andronikov, A., Frei, R., Xu, L., Mao, J. 2022., Early Cambrian highly metalliferous black shale in South China: Cu and Zn isotopes and a short review of other non-traditional stable isotopes. Mineralium Deposita, 0123456789. https://doi.org/10.1007/s00126-022-01097-0.
- Lemière, B., 2018. A review of pXRF (field portable X-ray fluorescence) applications for applied geochemistry. Journal Geochemical Exploration 188, 350–363. https://doi.org/10.1016/j.gexplo.2018.02.006.
- Le Vaillant, M., Barnes, S.J., Fisher, L., Fiorentini, M.L., Caruso, S. Use and calibration of portable X-ray fluorescence analysers: Application to lithogeochemical exploration for komatiite-hosted nickel sulphide deposits. Geochemistry: Exploration, Environment, Analysis 14, 199–209. https://doi.org/10.1144/geochem2012-166.
- Liao, S., Taoa, C., Zhua, C., Li, H., Li, X., Liang, J., Yang, W., Wang, Y., 2019. Two episodes of sulfide mineralization at the Yuhuang-1 hydrothermal field on the Southwest Indian Ridge: Insight from Zn isotopes. Chemical Geology 507, 54-63. https://doi.org/10.1016/j.chemgeo.2018.12.037.
- Li, Y., Tao, Y., Zhu, F., Liao, M.m Xiong, F., Deng, X., 2015. Distribution and existing state of indium in the Gejiu Tin polymetallic deposit, Yunnan Province,

SW China. Chinese Journal of Geochemistry 34, 469–483. https://doi.org/10.1007/s11631-015-0061-7

- Li, W., Cook, N.J., Ciobanu, C.L., Xie, G., Wade, B.P., Gilbert, S.E., 2019. Trace element distributions in (Cu)-Pb-Sb sulfosalts from the Gutaishan Au-Sb deposit, South China: Implications for formation of high fineness native gold. American Mineralogist 104, 425–437. https://doi.org/10.2138/am-2019-6674.
- Li, Z., Ye, L., Hu, Y., Wei, C., Huang, Z., Yang, Y., Danyushecsky, L., 2020. Trace elements in sulfides from the Maozu Pb-Zn deposit, Yunnan Province, China: Implications for trace-element incorporation mechanisms and ore genesis. American Mineralogist 105, 1734-1751. https://doi.org/10.2138/am-2020-6950.
- Liu, W. Cook, N., Ciobanu, C.L., Gilbert, S.E., 2019. Trace element substitution and grain-scale compositional heterogeneity in enargite. Ore Geology Reviews 111, 103004. https://doi.org/10.1016/j.oregeorev.2019.103004.
- Liu, G., Yuan, F., Deng, Y., Jowitt, S.M., Hu, X., Wang, F., Huang, L., Liu, C., Ye, Y., White, N.C., 2022. Critical metal enrichment in carbonate-hosted Pb-Zn systems: Insight from the chemistry of sphalerite within the Hehuashan Pb-Zn deposit, Middle-Lower Yangtze River Metallogenic Belt, East China. Ore Geology Reviews 151, 105209. https://doi.org/10.1016/j.oregeorev.2022.105209.
- Liu, S., Ye, L., Yang, R., Xiang, Z., Wei, C., Hu, Y., Huang, Z., Liu, S., 2023. Ore-forming processes of the Baisong carbonate-hosted Pb-Zn deposit, SW China: Constraints from in-situ sphalerite trace element and sulfide S-isotopic compositions. Ore Geology Reviews 159, 105529. https://doi.org/10.1016/j.oregeorev.2023.105529.
- Lombaard, A.F., Günzel, A., Innes, J., Krüger, T.L., 1986. The Tsumeb lead–copper–zinc–silver deposit, South West Africa/Namibia". In: Anhaeusser, C.R.,

Maske, S. (eds). Mineral Deposits of Southern Africa. Geological Society of South Africa, Johannesburg 2, 1761–1782.

- Longridge, L., Gibson, R.L., Kinnaird, J.A., Armstrong, R.A., 2017. New constraints on the age and conditions of LPHT metamorphism in the southwestern Central Zone of the Damara Belt, Namibia and implications for tectonic setting. Lithos 278-281, 361-382. //doi.org/10.1016/j.lithos.2017.02.006 .
- Luo, K., Cugerone, A., Zhou, M.F., Zhou, J.X., Sun, G.T., Xu, J., He, K.J., Lu, M.D., 2022. Germanium enrichment in sphalerite with acicular and euhedral textures: An example from the Zhulingou carbonate-hosted Zn(-Ge) deposit, South China. Mineralium Deposita 57(2), 1–23. DOI: 10.1007/s00126-022-01112-4.
- Macey, P., Thomas, R., Minnaar, H., Gresse, P., Lambert, C., Groenewald, C., Miller, J., Indongo, J., Angombe, M., Shifotoka, G., Frei, D., Diener, J., Kisters, A., Dhansay, T., Smith, H., Doggart, S., Le Roux, P., Hartnady, M., Tinguely, C., 2017. Origin and evolution of the ~1.9 Ga Richtersveld Magmatic Arc, SW Africa. Precambrian Research 292, 417-451. https://doi.org/10.1016/j.precamres.2017.01.013.
- Mapani, B., Cornell, D., Schijndel, V., 2014. Geochronology and tectonic evolution of the Hohewarte Complex, central Namibia: New insights in Paleoproterozoic to Early Neoproterozoic crustal accretion processes. Journal of African Earth Sciences 99(2), 228-244. https://doi.org/10.1016/j.jafrearsci.2014.06.021.
- Marfin, A.E., Ivanov, A.V., Abramova, V.D., Anziferova, T.N., Radomskaya, T.A., Yakich, Y., Bestemianova, K.V., 2020. A trace element classification tree for chalcopyrite from Oktyabrsk Deposit, Norilsk–Talnakh ore district, Russia: LA-ICPMS Study. Minerals 10, 716; doi:10.3390/min10080716

- Markl, G., Lahaye, Y., Schwinn, G., 2006. Copper isotopes as monitors of redox processes in hydrothermal mineralization. Geochimica et Cosmochimica Acta 70(16), 4215-4228. https://doi.org/10.1016/j.gca.2006.06.1369
- Martin, H., Porada, H., 1977. The intracratonic branch of the Damara orogen in southwest Africa I. Discussion of geodynamic models. Precambrian Research 5, 311–338. https://doi.org/10.1016/0301-9268(77)90039-0.
- Mason, T.F.D., Weiss, D.J., Chapman, J.B., Wilkinson, J.J., Tessalina, S.G., Spiro, B., Horstwood, M.S.A., Spratt, J., Coles, B.J., 2005. Zn and Cu isotopic variability in the Alexandrinka volcanic-hosted massive sulfide (VHMS) ore deposit, Urals. Russia. Chemical Geology 221, 170–187. https://doi.org/10.1016/j.chemgeo.2005.04.011.
- Mathur, R., Titley, S., Barra, F., Brantley, S., Wilson, M., Phillips, A., Munizanga, F., Maksaev, V., Vervoort, J., Hart, G., 2009. Exploration potential of Cu isotope fractionation in porphyry copper deposits. Journal of Geochemical exploration 102(1), 1-6. https://doi.org/10.1016/j.gexplo.2008.09.004
- Mathur, R., Ruiz, J., Casselman, M.J., Megaw, P., Egmond, R., 2012. Use of Cu isotopes to distinguish primary and secondary Cu mineralization in the Cañariaco Norte porphyry copper deposit, Northern Peru. Miner Deposita 47, 755–762. DOI 10.1007/s00126-012-0439-y.
- Mathur, R., Zhao, Y., 2023. Copper Isotopes Used in Mineral Exploration. In: Huston, D., Gutzmer, J. (eds) Isotopes in Economic Geology, Metallogenesis and Exploration. Mineral Resource Reviews. Springer, Cham. https://doi.org/10.1007/978-3-031-27897-6_14.
- Melcher, F., Oberthür, T., Rammlmair, D., 2003. The carbonate-hosted, Ge- and Ag-rich Khusib Springs Cu–Zn–Pb sulphide deposit, Namibia: ore geochemistry

and mineralogical variation. 11th IAGOD Quadrennial Symposium and Geocongress, Windhoek, Namibia. Geological Survey of Namibia.

- Melcher, F., 2003. The Otavi Mountainland in Namibia: Tsumeb, germanium and snowball Earth. Mitteilungen der Österreichischen Mineralogischen Gesellschaft 148, 413–435.
- Melcher, F., Oberthür, T., Rammlmair, D., 2006. Geochemical and mineralogical distribution of germanium in the Khusib Springs Cu-Zn-Pb-Ag sulphide deposit, Otavi Mountain Land, Namibia. Ore Geology Reviews 28, 32-56. https://doi.org/10.1016/j.oregeorev.2005.04.006
- Melekestseva, I., Maslennikov, V., Tret'yakov, G., Maslennikova, S., Danyushevsky, L., Kotlyarov, V., Large R., Beltenev, V., Khvorov, P., 2020. Trace element geochemistry of sulfides from the Ashadze-2 hydrothermal field (12°58' N, Mid-Atlantic Ridge): Influence of host rocks, formation conditions or seawater? Minerals 10, no. 743. https://doi.org/10.3390/min10090743
- Meng, Y.M., Hu, R.Z., Huang, X.W., Gao, J.F., Sasseville, C., 2019. The origin of the carbonate-hosted Huize Zn–Pb–Ag deposit, Yunnan province, SW China: constraints from the trace element and sulfur isotopic compositions of pyrite. 369–391. Mineralogy and Petrology 113, 369–391. https://doi.org/10.1007/s00710-019-00654-2
- Miller, R.M., 1983. The Pan-African Damara Orogen of South West Africa/Namibia. In: R. McG. Miller (Eds). Evolution of the Damara Orogen of South West Africa/Namibia. Special Publication of the Geological Society of South Africa, 11, 431-515.

- Miller, R.M., 1997. Chapter 11 The Owambo Basin of Northern Namibia, (Eds): R.C. Selley. Sedimentary Basins of the World. Elsevier 3, 237-268. https://doi.org/10.1016/S1874-5997(97)80014-7.
- Miller, R.M. ,2008a. Archaean to Mesoproterozoic. In: Miller, R.M. (Eds.), The Geology of Namibia, 1. Geological Survey of Namibia, Windhoek, 13-1–13-410
- Miller, R.M., 2008b. Neoproterozoic and early Palaeozoic rocks of the Damara Orogen. In: Miller, R.M. (Eds), The Geology of Namibia, 2. Geological Survey of Namibia, Windhoek, 13-1–13-410
- Miller, R.M., 2008c. The Geology of Namibia: Upper palaeozoic to cenozoic. In: Miller, R.M. (Eds), The Geology of Namibia, 2. Geological Survey of Namibia, Windhoek, 13-1–13-410
- Miller, R.M., 2013. Comparative Stratigraphic and Geochronological Evolution of the Northern Damara Supergroup in Namibia and the Katanga Supergroup in the Lufilian Arc of Central Africa; Paul Hoffman series. Geoscience Canada 40, http://dx.doi.org/10.12789/geocanj.2013.40.007.
- Miller, R. M. 2021. Notes on traverses across the Khorixas-Gaseneirob Thrust, Southern Khorixas and Outjo Districts, Namibia. Communications of the Geological Survey of Namibia 23, 39-89.
- Minz, F., 2008. The Kombat ore deposit, Otavi Mountain Land (Northern Namibia). http://www.geo.tufreiberg.de/Hauptseminar/2008/Friederike_minz.pdf.
- Mishra, B.P., Pati, P., Dora, M.L., Baswani, S.R., Meshram, T., Shareef, M., Pattanayak, R.S., Suryavanshi, H., Mishra, M., Raza, M.A., 2021. Trace-element systematics and isotopic characteristics of sphalerite-pyrite from volcanogenic massive sulfide deposits of Betul belt, central Indian Tectonic Zone: Insight of ore genesis to exploration. Ore Geology Reviews 134, 104149. https://doi.org/10.1016/j.oregeorev.2021.104149.

- Misiewicz, J.E. 1988. The Geology and Metallogeny of the Otavi Mountain land, Damara Orogen, SWA/Namibia, with Particular Reference to the Berg Aukas Zn-Pb-V Deposit: A Model of Ore Genesis. MSc Thesis, Rhodes University, Grahamstown.
- Mondillo, N., Arfè, G., Herrington, R., Boni, M., Wilkinson, C., Mormone, A., 2018. Germanium enrichment in supergene settings: evidence from the Cristal nonsulfide Zn prospect, Bongará district, northern Peru. Minerium Deposita 53, 155–169. https://doi.org/10.1007/s00126-017-0781-1
- Moynier, F., 2018. Zinc Isotopes. In: White, W.M. (eds) Encyclopedia of Geochemistry. Encyclopedia of Earth Sciences Series. Springer, Cham. https://doi.org/10.1007/978-3-319-39312-4_215
- Moss, R.L., Tzimas, E., Kara, H., Willis, P., Kooroshy, J., 2011. Critical metals in strategic energy technologies. Assessing rare metals as Supply-chain bottlenecks in low-carbon energy technologies. In: European Commission Joint Research Centre Institute for Energy and Transport; Publication Office of the European Union: Luxembourg, 1–159.
- Mukherjee, I., Large, R.R., Bull, S., Gregory, D.G., Stepanov, A.S., ´Avila, J., Ireland, T.R., Corkrey, R., 2019. Pyrite trace-element and sulfur isotope geochemistry of paleomesoproterozoic McArthur Basin: Proxy for oxidative weathering. American Mineralogist 104, 1256–1272. https://doi.org/10.2138/am-2019-6873
- Murakami, H., Ishihara, S., 2013. Trace elements of Indium-bearing sphalerite from tin-polymetallic deposits in Bolivia, China and Japan: A femto-second LA-ICPMS study. Ore Geology Reviews 53, 223-243. https://doi.org/10.1016/j.oregeorev.2013.01.010.

- Nascimento, D.B., Schmitt, R.S., Ribeiro, A., Trouw, R.A.J., Passchier, C.W., Baser, M.A.S., 2017. Depositional ages and provenance of the Neoproterozoic Damara Supergroup (northwest Namibia): Implications for the Angola-Congo and Kalahari cratons connection. Gondwana Research 52, 153–171. https://doi.org/10.1016/j.gr.2017.09.006.
- Nassar, N.T., Graedel, T.E., Harper, E.M., 2015. By-product metals are technologically essential but have problematic supply. Science Advances 1(3), e1400180 https://doi.org/10.1126/sciadv.1400180.
- Nghoongoloka, A., Bowell, R., Kamona, A.F., Mocke, H., 2020. Re-evaluation of Kombat-style mineralization and implications for exploration in the Otavi Mountain Land, Namibia. Open Journal of Geology 10, 1119-1152. DOI: 10.4236/ojg.2020.1011054.
- Niu, P., Jiang, S., Munoz, M., 2023. Two-stage enrichment of germanium in the giant Maoping MVT Pb-Zn deposit, southwestern China: Constraints from in situ analysis of multicolor sphalerites. Ore Geology Reviews 157, 105421. https://doi.org/10.1016/j.oregeorev.2023.105421.
- Paradis, S., 2015. Indium, germanium and gallium in volcanic- and sediment-hosted base-metal sulphide deposits. In: Simandl, G.J. and Neetz, M., (Eds.), Symposium on Strategic and Critical Materials Proceedings, November 13-14, 2015, Victoria, British Columbia. British Columbia Ministry of Energy and Mines, British Columbia Geological Survey Paper 2015-3, 23-29.
- Paradis, S., Petts, D., Simandl, G.J., Sharpe, R., Hamilton, T.S., Fayek, M., Jackson, S.E., 2023. Impact of deformation and metamorphism on sphalerite chemistry – Element mapping of sphalerite in carbonate-hosted Zn-Pb sulfide deposits of the Kootenay Arc, southern British Columbia, Canada and northeastern Washington,

USA. Ore Geology Reviews 158, 105482. https://doi.org/10.1016/j.oregeorev.2023.105482.

- Pašava, J., Tornos, F., Chrastný, V., 2014. Zinc and sulfur isotope variation in sphalerite from carbonate-hosted zinc deposits, Cantabria, Spain. Miner Deposita 49, 797–807. https://doi.org/10.1007/s00126-014-0535-2
- Piercey, S.J., Devine, M.C., 2014. Analysis of powdered reference materials and known samples with a benchtop, field portable X-ray fluorescence (pXRF) spectrometer: evaluation of performance and potential applications for exploration lithogeochemistry. Geochemistry: Exploration, Environment, Analysis 14, 139–148, https://doi.org/10.1144/geochem2013-199
- Perez, J.P.H., Folens, K., Leus, K., Vanhaecke, F., Van Der Voort, P., Du Laing, G., 2019. Progress in hydrometallurgical technologies to recover critical raw materials and precious metals from low-concentrated streams. Resources, Conservation & Recycling 142, 177-188. https://doi.org/10.1016/j.resconrec.2018.11.029.
- Pfaff, K., Koenig, A., Wenzel, T., Ridley, I., Hildebrandt, L.H., Leach, D.L., Markl, G., 2011. Trace and minor element variations and sulfur isotopes in crystalline and colloform ZnS: Incorporation mechanisms and implications for their genesis. Chemical Geology 286, 118–134. https://doi.org/10.1016/j.chemgeo.2011.04.018.
- Pirajno, F., Kinnaird, J.A., Fallick, A.E., Boyece, A.J., Petzel, V.W. F., 1992. A preliminary regional sulphur isotope study of selected samples from mineralised deposits of the Damara Orogen, Namibia. Communications of the Geological Survey of Namibia 8, 81-97.
- Pirajno, E., Joubert, B.D., 1993. An overview of carbonate-hosted mineral deposits in the Otavi Mountain Land, Namibia: Implications for ore genesis. Journal of

African Earth Sciences 6(3), 265-272. https://doi.org/10.1016/0899-5362(93)90048-U.

- Porada, H., 1979. The Damara-Ribeira orogen of the Pan-African/Brasiliano cycle in Namibia (Southwest Africa) and Brazil as interpreted in terms of continental collision. Tectonophysics 57, 237–265. https://doi.org/10.1016/0040-1951(79)90150-1
- Porada, H., Behr, H.J., 1988. Setting and sedimentary facies of late Proterozoic alkali lake (playa) deposits in the southern Damara belt of Namibia. Sedimentary Geology 58(2–4). https://doi.org/10.1016/0037-0738(88)90068-1.
- Prave, A.R., 1996. Tale of three cratons: Tectonostratigraphic anatomy of the Damara orogen in northwestern Namibia and the assembly of Gondwana. Geology 24(12), 1115–1118. doi:10.1130/0091-7613(1996)024<1115:totcta>2.3.co;2.
- Qi, Y., Hu, R., Gao, J., Leng, C., Gao, W., Gong, H., 2022. Trace and minor elements in sulfides from the Lengshuikeng Ag–Pb–Zn deposit, South China: A LA–ICP–MS study. Ore Geology Reviews 141, 104663. https://doi.org/10.1016/j.oregeorev.2021.104663.
- Quye-Sawyer, J., Vandeginste, V., Johnston, K.J., 2015. Application of handheld energy-dispersive X-ray fluorescence spectrometry to carbonate studies: Opportunities and challenges. Journal of Analytical Atomic Spectrometry 30, 1490-1499. https://doi.org/10.1039/C5JA00114E
- Raic, S. Molnár, F., Cook,N., O'Brien, H., Lahaye, Y., 2022. Application of lithogeochemical and pyrite trace element data for the determination of vectors to ore in the Raja Au–Co prospect, northern Finland. Solid Earth 13, 271–299. https://doi.org/10.5194/se-13-271-2022.
- Redlinger, M., Eggert, R., 2016. Volatility of by-product metal and mineral prices. Resources Policy 47, 69–77. https://doi.org/10.1016/j.resourpol.2015.12.002.

- Reich, M., Chryssoulis, S.L., Deditius, A., Palacios, C., Zúñiga, A., Weldt, M., Alvear, M., 2010. “Invisible” silver and gold in supergene digenite (Cu1.8S). Geochimica et Cosmochimica Acta 74(21), 6157-6173. https://doi.org/10.1016/j.gca.2010.07.026.
- Reich, M., Deditius, A., Chryssoulis, S., Li, J.-W., Ma, C.-Q., Parada, M.A., Barra, F., Mittermayr, F., 2013. Pyrite as a record of hydrothermal fluid evolution in a porphyry copper system: A SIMS/EMPA trace element study. Geochimica et Cosmochimica Acta 104, 42–62. https://doi.org/10.1016/j.gca.2012.11.006
- Ren, Y., Wohlgemuth-Ueberwasser, C.C., Huang, F., Shi, X., Li, B., Oelze, M., Schreiber, A., Wirth, R., 2021. Distribution of trace elements in sulfides from Deyin hydrothermal field, Mid-Atlantic Ridge – Implications for its mineralizing processes. Ore Geology Reviews 128, 103911. https://doi.org/10.1016/j.oregeorev.2020.103911.
- Renock, D., Becker, U., 2011. A first principles study of coupled substitution in galena. Ore Geology Reviews 42(1), 71-83. https://doi.org/10.1016/j.oregeorev.2011.04.001.
- Reuter, M.A., Verhoef, E.V., 2004. A Dynamic Model for the Assessment of the Replacement of Lead in Solders. Journal of electronic materials 33(12), 1567–1580. DOI: 10.1007/s11664-004-0100-3.
- Revan, M.K., Genç, Y., Maslennikov, V.V., Maslennikova, S.P., Large, R.R., Danyushevsky, L.V., 2014. Mineralogy and trace-element geochemistry of sulfide minerals in hydrothermal chimneys from the Upper-Cretaceous VMS deposits of the eastern Pontide orogenic belt (NE Turkey). Ore Geology Reviews 63, 129-149. https://doi.org/10.1016/j.oregeorev.2014.05.006.

- Rollinson, H., 2021. Using geochemical data: evaluation, presentation, interpretation. Cambridge University Press (2nd edition).
- Rudnick, R.L., Gao, S., 2003. The composition of the continental crust. Treatise on Geochemistry 3, 1-64. http://dx.doi.org/10.1016/b0-08-043751-6/03016-4.
- Rudnick, R.L., Gao, S., 2014. Composition of the Continental Crust. In: Heinrich D., Holland, K., Turekian, K. (eds) Treatise on Geochemistry (Second Edition). Elsevier 1-51. https://doi.org/10.1016/B978-0-08-095975-7.00301-6.
- Sadati, S.N., Yazdi, M., Mao, J., Behzadi, M., Adabi, M.H., Lingang, X., Zhenyu, C., Mokhtari, M.A.A., 2016. Sulfide mineral chemistry investigation of sediment-hosted stratiform copper deposits, Nahand-Ivand area, NW Iran. Ore Geology Reviews 72(1), 760-776. https://doi.org/10.1016/j.oregeorev.2015.09.018.
- Sahlström, F., Arribas, A., Dirks, P., Corral, I., Chang, Z., 2017. Mineralogical Distribution of Germanium, Gallium and Indium at the Mt Carlton High-Sulfidation Epithermal Deposit, NE Australia, and Comparison with Similar Deposits Worldwide. Minerals 7, 213. https://doi.org/10.3390/min7110213
- Sangster, D.F., 1988. Breccia-Hosted Lead—Zinc Deposits in Carbonate Rocks. In: James, N.P., Choquette, P.W. (eds) Paleokarst. Springer, New York, NY. https://doi.org/10.1007/978-1-4612-3748-8_5
- Sarjoughian, F., Shubin, F., Asadi, S., Moore, F., Haschke, M., 2024. Cu isotope patterns of whole rocks in the Kerman porphyry copper belt, southeastern Urumieh Dokhtar magmatic arc, Iran. Journal of Geochemical Exploration 256, 107329. https://doi.org/10.1016/j.gexplo.2023.107329.
- Saylor, B.Z., Grotzinger, J.P., Germs, G.J.B., 1995. Sequence stratigraphy and sedimentology of the Neoproterozoic Kuibis and Schwarzrand Subgroups (Nama

Group), southwestern Namibia. Precambrian Research 73(1–4), 153–171. https://doi.org/10.1016/0301-9268(94)00076-4.

- Sclar, C.B., Geier, B.H., 1957. The paragenetic relationships of germanite and renierite from Tsumeb, Southwest Africa. Economic Geology 52(6), 612–631. https://doi.org/10.2113/gsecongeo.52.6.612.
- Schlüter, T., 2006. Geological Atlas of Africa with Notes on Stratigraphy, Tectonics, Economic Geology, Geohazards, Geosites and Geoscientific Education of Each Country. Springer. DOI 10.1007/3-540-29145-8.
- Schneider, J., Boni, M., Laukamp, C., Bechstädt, T., Petzel, V., 2008. Willemite (Zn_2SiO_4) as a possible Rb–Sr geochronometer for dating nonsulfide Zn–Pb mineralization: Examples from the Otavi Mountainland (Namibia). Ore Geology Reviews 33, 152–167. https://doi.org/10.1016/j.oregeorev.2006.05.012.
- Schwarz-Schampera, U., Herzig, P.M., 2002. Indium: Geology, mineralogy, and economics. Springer Science & Business Media. https://doi.org/10.1007/978-3-662-05076-7.
- Schwartz, M.O., 2010. Cadmium in Zinc Deposits: Economic Geology of a Polluting Element. International Geology Review 42(5), 445-469. https://doi.org/10.1080/00206810009465091
- SGU. 2023. Critical and strategic raw materials. Retrieved from https://www.sgu.se/en/mineral-resources/critical-raw-materials/.
- Shanks, W.C.P., III, Kimball, B.E., Tolcin, A.C., Guberman, D.E., 2017. Germanium and indium, chap. I of Schulz, K.J.,DeYoung, J.H., Jr., Seal, R.R., II, and Bradley, D.C., eds., Critical mineral resources of the United States—Economic and environmental geology and prospects for future supply: U.S. Geological Survey Professional Paper 1802, I1–I27. https://doi.org/10.3133/pp1802I.

- Sharp, T.G., Buseck, P.R., 1993. The distribution of Ag and Sb in galena: Inclusions versus solid solution. American Mineralogist 78 (1-2), 85–95.
- Shields, W.R., Murphy, T., Garner, E., 1964. Absolute Isotopic Abundance Ratio and the Atomic Weight of a Reference Sample of Copper. Journal Of Research of the National Bureau of Standards-A. Physics and Chemistry 68a, 6.
- Shields, W. R., Goldich, S. S., Garner, E. L., and Murphy, T. J., 1965. Natural variations in the abundance ratio and the atomic weight of copper. Journal of Geophysical Research 70, 479–491. doi: 10.1029/jz070i002p00479.
- Simandl, G.J., Fajber, R., Paradis, S., 2014a. Portable X-ray fluorescence in the assessment of rare earth element enriched sedimentary phosphate deposits. Geochemistry: Exploration, Environment, Analysis 14, 161-169. https://doi.org/10.1144/geochem2012-180.
- Simandl, G.J. Stone, R.S., Paradis, S., Fajber, R., 2014b. An assessment of a handheld X-ray fluorescence instrument for use in exploration and development with an emphasis on REEs and related specialty metals. Mineralium Deposita 49, 999–1012. https://doi.org/10.1007/s00126-013-0493-0.
- Skirrow, R.G., Huston, D.L., Mernagh, T.P., Thorne, J.P., Dulfer, H., Senior, A.B., 2013. Critical commodities for a high-tech world: Australia's potential to supply global demand. Geoscience Australia. Geoscience Australia, Canberra. DOI: 10.1016/j.rcradv.2023.200137
- Söhnge, P.G., 1964. The geology of the Tsumeb Mine: Proceedings of the Geological Society of South Africa 65(2), 367-382.
- Southwood, M., 2019. Wulfenite from Tsumeb, Namibia. Rocks & Minerals 94(1), 70-83. https://doi.org/10.1080/00357529.2019.1519677

- Springer, G., 1969. Compositional variations in enargite and luzonite. Mineralium Deposita 4, 72-74. https://doi.org/10.1007/BF00206649
- Spry, P.G., Merlino, S., Wang, S., Zhang, X., Buseck, P.R., 1994. New occurrences and refined crystal chemistry of colusite, with comparisons to arsenosulvanite. American Mineralogist 79(7-8), 750-762.
- Staude, S., Mordhorst, T., Neumann, R., Prebeck, W., Markl, G., 2010. Compositional variation of the tennantite–tetrahedrite solid-solution series in the Schwarzwald ore district (SW Germany): The role of mineralization processes and fluid source. Mineralogical Magazine 74(2), 309-339. https://doi.org/10.1180/minmag.2010.074.2.309
- Steadman, J.A., Large, R.R., Olin, P.H., Danyushevsky L.V., Meffre, S., Huston, D., Fabris, A., Lisitsin, V., Wells, T., 2021. Pyrite trace element behavior in magmatic-hydrothermal environments: An LA-ICPMS imaging study. Ore Geology Reviews 128, 103878. https://doi.org/10.1016/j.oregeorev.2020.103878.
- Sylvester, P.J., Jackson, S.E., 2016. A brief history of laser ablation inductively coupled plasma mass spectrometry (LA-ICP-MS). Elements 12, 307–310. https://doi.org/10. 2113/gselements.12.5.307.
- Taylor, S.R., McLennan, S.M., 1985. The Continental Crust: Its Composition and Evolution. Blackwell, Oxford.
- Tegtmeyer, A., Kröner, A., 1985. U-Pb zircon ages for granitoid gneisses in northern Namibia and their significance for proterozoic crustal evolution of southwestern Africa. Precambrian Research 28, 311-326. https://doi.org/10.1016/0301-9268(85)90036-1.

- Thomas, R., Agenbacht, A., Cornell, D., Moore, J., 1994. The Kibaran of southern Africa: Tectonic evolution and metallogeny. Ore Geology Reviews 9(2) 131-160. https://doi.org/10.1016/0169-1368(94)90025-6.
- Thomas, H.V., Large, R.R., Bull, S.W., Maslennikov, V., Berry, R.F., Fraser, R., Froud, S., Moye, R., 2011. Pyrite and pyrrhotite textures and composition in sediments, laminated quartz veins, and reefs at Bendigo gold mine, Australia: insights for ore genesis. Economic Geology 106, 1-31. https://doi.org/10.2113/econgeo.106.1.1
- Trigon Metals Inc, 2017. NI 43-101 Technical Report on the Kombat Copper Project, Namibia Mineral Resource Report.
- Trigub, A.L., Trofimov, N.D., Tagirov, B.R., Nickolsky, M.S., Kvashnina, K.O., 2022. Probing the Local Atomic Structure of In and Cu in Sphalerite by XAS Spectroscopy Enhanced by Reverse Monte Carlo Algorithm. Minerals 10(10), 841. https://doi.org/10.3390/min10100841
- U.S. Department of the Interior, U.S. Geological Survey (USGS), 2018. Draft critical mineral list – summary of methodology and background information – U.S. Geological Survey technical input document in response to Secretarial Order 3359, 26 .
- Vaughan, D.J., Craig, J.R., 1978, Mineral chemistry of metal sulfides. Cambridge University Press. 493 p.
- Viets, J.G. O'Leary, R.M., 1992. The role of atomic absorption spectrometry in geochemical exploration. Journal of Geochemical Exploration 44(1–3), 107-138. https://doi.org/10.1016/0375-6742(92)90049-E.

- Vokes, F.M., Craig, J.R., 1993. Post-recrystallisation mobilisation phenomena in metamorphosed stratabound sulphide ores. Mineralogical Magazine 57, 19–28. doi:10.1180/minmag.1993.057.386.03.
- Wang, D., Zheng, Y., Mathur, R., Wu, S., 2018. The Fe–Zn isotopic characteristics and fractionation models: implications for the genesis of the Zhaxikang Sb–Pb–Zn–Ag deposit in southern Tibet. Geofluids 2197891, 23. https://doi.org/10.1155/2018/2197891.
- Wang, Y. H., Zhang, F. F., Xue, C. J., Liu, J. J., Zhang, Z. C., Sun, M., 2021. Geology and genesis of the Tuwu porphyry Cu deposit, Xinjiang, northwest China. Economic Geology, 116(2), 471-500. https://doi.org/10.5382/econgeo.4763
- Wang, L., Zhang, Y., Han, R., Li, X., 2023. LA-ICP-MS analyses of trace elements in zoned sphalerite: A study from the Maoping carbonate-hosted Pb-Zn(-Ge) deposit, southwest China. Ore Geology Reviews 157, 105468. https://doi.org/10.1016/j.oregeorev.2023.105468.
- Ward, F.N., Nakagawa, H., Harms, T.F., VanSickle, G.H., 1969. Atomic-Absorption Methods of Analysis Useful in Geochemical Exploration. Bulletin 1289; USGS Publications Warehouse. https://doi.org/10.3133/b1289
- Wei, C., Ye, L., Hu, Y., Danyushevskiy, L., Li, Z., Huang, Z., 2019. Distribution and occurrence of Ge and related trace elements in sphalerite from the Lehong carbonate-hosted Zn-Pb deposit, northeastern Yunnan, China: Insights from SEM and LA-ICP-MS studies. Ore Geology Reviews 115, 103175. https://doi.org/10.1016/j.oregeorev.2019.103175.
- Wei, C., Ye, L., Hu, Y., Huang, Z., Danyushevsky, L., Wang, H., 2021. LA-ICP-MS analyses of trace elements in base metal sulfides from carbonate-hosted Zn-Pb

deposits, South China: A case study of the Maoping deposit. Ore Geology Reviews 130, 103945. https://doi.org/10.1016/j.oregeorev.2020.103945.

- Wen et al., Wen, H., Zhu, C., Zhang, Y., Cloquet, C., Fan, H., Fu, S., 2016. Zn/Cd ratios and cadmium isotope evidence for the classification of lead–zinc deposits. Scientific Reports 6, 25273. https://doi.org/10.1038/srep25273
- Werner, T.T., Mudd, G.M., Jowitt, S.M., 2017. The world's by-product and critical metal resources part III: A global assessment of indium. Ore Geology Reviews 86, https://doi.org/10.1016/j.oregeorev.2017.01.015.
- Wilkinson, J.J., Weiss, D.J., Mason, T.F.D., Coles, B.J., 2005. Zinc isotope variation in hydrothermal systems: Preliminary evidence from the Irish midlands ore field. Economic Geology 100, 583-590. DOI 10.2113/gsecongeo.100.3.583.
- Wilkinson, J.J., 2023. The Potential of Zn Isotopes in the Science and Exploration of Ore Deposits. In: Huston, D., Gutzmer, J. (eds) Isotopes in Economic Geology, Metallogenesis and Exploration. Mineral Resource Reviews. Springer, Cham. https://doi.org/10.1007/978-3-031-27897-6_15.
- Wood, M.D., Beresford, N.A., Copplestone, D. 2011. Limit of detection values in data analysis: Do they matter? Radioprotection 2011, 46, S85–S90. DOI: 10.1051/radiopro/20116728s.
- Wu, L., Hu, R., Li, X., Liu, S., Tang, Y., Tang, Y., 2017. Copper isotopic compositions of the Zijinshan high-sulfidation epithermal Cu–Au deposit, South China: Implications for deposit origin. Ore Geology Reviews 83, 191–199. http://dx.doi.org/10.1016/j.oregeorev.2016.12.013
- Wu, J., Zhai, D., Zhao, Q., Zhang, H., Hong, J., Zhao, G., Liu, J., 2023. In situ trace element compositions of sulfides constraining the genesis of the worldclass

Shuangjianzishan Ag-Pb-Zn deposit, NE China. Ore Geology Reviews 162, 105675. https://doi.org/10.1016/j.oregeorev.2023.105675.

- Wuensch, B.J., 1964. The crystal structure of tetrahedrite, Cu12Sb4S13. Zeitschrift fur Kristallographie 119, 437–453. https://doi.org/10.1524/zkri.1964.119.5-6.437
- Xing, B., Mao, J., Xiao, X., Liu, H., Jia, F., Wang, S., Huang, W., Li, H., 2021. Genetic discrimination of the Dingjiashan Pb-Zn deposit, SE China, based on sphalerite chemistry. Ore Geology Reviews 135, 104212. https://doi.org/10.1016/j.oregeorev.2021.104212.
- Xiong, S.F., Jiang, S.Y., Ma, Y., Liu, T., Zhao, K.D., Jiang, M.R., Zhao, H.D., 2019. Ore genesis of Kongxigou and Nanmushu Zn-Pb deposits hosted in Neoproterozoic carbonates, Yangtze Block, SW China: Constraints from sulfide chemistry, fluid inclusions, and in situ S-Pb isotope analyses. Precambrian Research 333, 105405. https://doi.org/10.1016/j.precamres.2019.105405
- Xu, J., Cook, N.J., Ciobanu, C.L., Li., X., Kontonikas-Charos, A., Gilbert, S., Lv, Y., 2021. Indium distribution in sphalerite from sulfide–oxide–silicate skarn assemblages: a case study of the Dulong Zn–Sn–In deposit, Southwest China. Miner Deposita 56, 307–324. https://doi.org/10.1007/s00126-020-00972-y
- Xu, J., Zhang, Y., Li, K., Zheng, C., Li, X., Jin, Z., Wu, C., Zhang, Z., 2023. The ore genesis of the Shagou Ag-Pb-Zn deposit in the Southern North China Craton: Constraints from He-Ar-Pb isotopes and trace element compositions of sphalerite. Ore Geology Reviews, 105765. https://doi.org/10.1016/j.oregeorev.2023.105765.
- Yang, Q., Zhang, X., Ulrich, T., Zhang, J., Wang, J., 2022. Trace element compositions of sulfides from Pb-Zn deposits in the Northeast Yunnan and northwest Guizhou Provinces, SW China: Insights from LA-ICP-MS analyses of

sphalerite and pyrite. Ore Geology Reviews 41, 104639. https://doi.org/10.1016/j.oregeorev.2021.104639.

- Ye, L., Cook, N.J., Ciobanu, C.L., Yuping, L., Qian, Z., Tiegeng, L., Wei, G., Yulong, Y., Danyushevskiy, L., 2011. Trace and minor elements in sphalerite from base metal deposits in South China—A LA-ICPMS study. Ore Geology Reviews 39(4), 188–217. http://dx.doi.org/10.1016/j.oregeorev.2011.03.001.
- Ye, Z., Xu, J., Zhao, J., Chen, S., Chen, J., Liu, W., 2023. Mineralogy of indium mineralization in the Dajing Sn-Cu polymetallic deposit in Inner Mongolia. Ore Geology Reviews 159, 105564. https://doi.org/10.1016/j.oregeorev.2023.105564.
- Young, K. E., Evans, C. A., Hodges, K.V., Bleacher, J. E., 2016. A review of the handheld X-ray fluorescence spectrometer as a tool for field geologic investigations on Earth and in planetary surface exploration. Applied Geochemistry 72, 77-87. https://doi.org/10.1016/j.apgeochem.2016.07.003
- Zeng, Z., Ma, Y., Yin, X., Selby, D., Kong, F., Chen, S., 2015. Factors affecting the rare earth element compositions in massive sulfides from deep-sea hydrothermal systems. Geochemistry Geophysics Geosystem 16. doi:10.1002/2015GC005812.
- Zhang, Y., Bao, Z., Lv, N., Chen, K., Zong, C., Yuan, H., 2020. Copper Isotope Ratio Measurements of Cu-Dominated Minerals Without Column Chromatography Using MC-ICP-MS. Frontiers in Chemistry 8. DOI=10.3389/fchem.2020.00609.
- Zhang, W., You, H., Li, B., Zhao, K., Chen, X., Zhu, L., 2022. Ore-forming processes of the Qixiashan carbonate-hosted Pb-Zn deposit, South China: Constraints from sulfide trace elements and sulfur isotopes. Ore Geology Reviews 143, 104786. https://doi.org/10.1016/j.oregeorev.2022.104786.

- Zhou, J.X, Huang, Z.L, Zhou, M.F, Zhu, X.K, Muchez, P., 2014a. Zinc, sulfur and lead isotopic variations in carbonate-hosted Pb–Zn sulfide deposits, southwest China. Ore Geol ogy Review 58,41–54. https://doi.org/10.1016/j.oregeorev.2014.05.012.
- Zhou, J. X., Huang, Z. L., Lv, Z. C., Zhu, X. K., Gao, J. G., Mirnejad, H., 2014b. Geology, isotope geochemistry and ore genesis of the Shanshulin carbonate-hosted Pb–Zn deposit, southwest China. Ore Geology Reviews 63, 209-225. https://doi.org/10.1016/j.oregeorev.2014.05.012.
- Zhou, S., Wang, J., Wang, W., Liao, S., 2023. Evaluation of Portable X-ray Fluorescence Analysis and Its Applicability as a Tool in Geochemical Exploration. Minerals 13, 166. https://doi.org/ 10.3390/min13020166
- Zhuang, L., Song, Y., Liu, Y., Fard, M., Hou, Z., 2019. Major and trace elements and sulfur isotopes in two stages of sphalerite from the world-class Angouran Zn–Pb deposit, Iran: Implications for mineralization conditions and type. Ore Geology Reviews 109, 184-200. https://doi.org/10.1016/j.oregeorev.2019.04.009.

Appendix

Appendix 4-1a Portable XRF result of OREAS Certified reference material.

Index	Zn	Cu	Ni	Co	Fe	Mn	Cr	V	Ti	Ca	K	Al	P	Si	Cl	S	Mg	MgO	Al2O3	SiO2	P2O5	SO3	K2O	CaO	TiO2	MnO	Fe2O3
Oreas 134b	15.94	0.12	0.00	0.00	10.74	0.32	0.03	0.00	0.04	4.23	0.68	2.81	0.08	8.51	0.06	12.23	5.88	9.75	5.31	18.21	0.19	30.56	0.83	5.92	0.06	0.41	15.36
	16.20	0.13	0.00	0.00	10.81	0.35	0.01	0.00	0.03	4.18	0.65	2.98	0.07	8.61	0.06	12.41	0.00	0.00	5.64	18.42	0.16	31.01	0.78	5.85	0.05	0.46	15.46
	16.11	0.12	0.01	0.00	10.85	0.33	0.02	0.00	0.04	4.29	0.68	2.50	0.06	8.57	0.06	12.38	0.00	0.00	4.72	18.34	0.13	30.96	0.82	6.01	0.07	0.43	15.51
	15.99	0.12	0.00	0.00	10.77	0.33	0.03	0.00	0.00	4.14	0.74	3.26	0.07	8.44	0.06	12.10	8.34	13.84	6.17	18.07	0.17	30.25	0.90	5.80	0.00	0.43	15.41
	15.92	0.12	0.02	0.00	10.74	0.34	0.03	0.00	0.03	4.22	0.67	2.93	0.09	8.58	0.06	12.14	5.79	9.62	5.54	18.37	0.20	30.35	0.81	5.91	0.05	0.44	15.36
OREAS 932	0.07	5.35	0.01	0.00	14.62	0.10	0.01	0.01	0.29	0.46	2.18	11.60	0.08	29.77	0.01	3.32	1.84	3.06	21.93	63.71	0.18	8.31	2.63	0.64	0.48	0.13	20.91
	0.07	5.36	0.01	0.00	14.64	0.09	0.02	0.02	0.29	0.48	2.14	11.81	0.06	29.43	0.01	3.29	2.77	4.60	22.33	62.97	0.14	8.23	2.59	0.67	0.48	0.12	20.93
	0.07	5.37	0.01	0.00	14.69	0.10	0.02	0.02	0.29	0.47	2.30	11.48	0.08	29.40	0.01	3.28	1.84	3.06	21.70	62.92	0.18	8.20	2.78	0.66	0.49	0.13	21.00
	0.07	5.35	0.01	0.00	14.63	0.10	0.01	0.02	0.31	0.49	2.27	11.73	0.07	29.47	0.01	3.28	2.15	3.56	22.17	63.07	0.17	8.20	2.75	0.68	0.52	0.13	20.93
	0.06	5.37	0.01	0.00	14.67	0.10	0.02	0.01	0.29	0.51	2.17	11.94	0.08	29.76	0.01	3.30	3.73	6.20	22.57	63.69	0.19	8.25	2.63	0.72	0.48	0.12	20.97
OREAS 623	1.00	1.54	0.01	0.00	13.16	0.06	0.02	0.01	0.15	1.40	1.38	7.19	0.05	27.06	0.01	5.76	2.48	4.11	13.58	57.91	0.11	14.39	1.67	1.96	0.25	0.08	18.82
	1.00	1.53	0.01	0.00	13.05	0.05	0.01	0.00	0.13	1.35	1.36	7.19	0.08	26.65	0.01	5.59	1.61	2.67	13.59	57.03	0.19	13.96	1.65	1.88	0.22	0.07	18.67
	0.99	1.52	0.00	0.00	13.05	0.06	0.01	0.00	0.14	1.38	1.36	6.62	0.08	26.71	0.01	5.68	0.00	0.00	12.52	57.15	0.18	14.21	1.65	1.93	0.24	0.08	18.67
	0.99	1.55	0.01	0.00	13.13	0.06	0.02	0.00	0.16	1.41	1.39	7.89	0.07	27.35	0.01	5.77	3.82	6.34	14.91	58.53	0.16	14.43	1.68	1.97	0.27	0.07	18.78
	0.99	1.54	0.01	0.00	13.08	0.06	0.02	0.01	0.15	1.35	1.42	7.69	0.06	27.99	0.02	5.98	2.30	3.82	14.53	59.90	0.15	14.94	1.72	1.89	0.24	0.07	18.70
OREAS132b	5.29	0.05	0.00	0.00	7.57	0.24	0.01	0.00	0.17	5.11	3.23	7.53	0.07	23.23	0.02	5.12	6.48	10.76	14.23	49.71	0.15	12.80	3.91	7.15	0.28	0.31	10.83
	5.29	0.05	0.00	0.00	7.61	0.23	0.02	0.01	0.17	5.04	3.12	6.93	0.08	22.87	0.02	5.09	4.67	7.75	13.10	48.95	0.19	12.73	3.77	7.06	0.28	0.29	10.89
	5.36	0.05	0.01	0.00	7.72	0.22	0.01	0.01	0.17	5.25	3.24	8.27	0.10	23.80	0.02	5.26	7.00	11.63	15.63	50.93	0.23	13.15	3.92	7.35	0.29	0.28	11.04
	5.28	0.04	0.01	0.00	7.58	0.22	0.02	0.01	0.17	5.28	3.19	8.08	0.08	23.67	0.02	5.30	6.31	10.47	15.26	50.65	0.18	13.25	3.86	7.40	0.28	0.29	10.84
	5.34	0.05	0.00	0.00	7.66	0.24	0.01	0.00	0.16	5.18	3.22	7.30	0.04	23.04	0.02	5.10	5.17	8.58	13.79	49.31	0.09	12.74	3.89	7.25	0.27	0.31	10.95
OREAS36	3.72	0.01	0.01	0.00	18.48	1.14	0.03	0.02	0.21	0.56	1.14	5.56	0.12	23.86	0.02	10.06	0.00	0.00	10.51	51.07	0.28	25.16	1.38	0.78	0.36	1.48	26.43
	3.70	0.02	0.01	0.00	18.51	1.18	0.03	0.01	0.22	0.63	1.11	6.15	0.11	24.34	0.02	10.29	3.05	5.06	11.62	52.10	0.25	25.73	1.34	0.88	0.37	1.52	26.47
	3.69	0.02	0.01	0.00	18.41	1.15	0.02	0.00	0.20	0.58	1.14	6.40	0.11	24.23	0.02	10.15	3.10	5.15	12.10	51.85	0.25	25.38	1.38	0.82	0.34	1.48	26.32
	3.70	0.02	0.01	0.00	18.48	1.14	0.03	0.00	0.24	0.64	1.15	6.26	0.14	24.46	0.02	10.27	3.77	6.26	11.83	52.33	0.33	25.68	1.40	0.89	0.40	1.47	26.43
	3.67	0.01	0.01	0.00	18.41	1.13	0.02	0.01	0.22	0.61	1.09	5.85	0.16	24.42	0.02	10.19	0.00	0.00	11.06	52.26	0.37	25.47	1.32	0.86	0.37	1.46	26.32
OREAS37	5.45	0.02	0.01	0.00	19.74	0.64	0.03	0.01	0.21	0.25	1.18	5.95	0.09	19.35	0.02	14.13	0.00	0.00	11.24	41.41	0.21	35.31	1.42	0.36	0.34	0.82	28.22
	5.37	0.02	0.01	0.00	19.54	0.65	0.02	0.01	0.20	0.27	1.19	5.83	0.06	19.73	0.01	14.38	0.00	0.00	11.01	42.22	0.14	35.94	1.44	0.37	0.33	0.84	27.94
	5.39	0.02	0.01	0.00	19.62	0.65	0.03	0.01	0.19	0.25	1.16	5.84	0.10	19.20	0.02	14.15	0.00	0.00	11.04	41.09	0.23	35.37	1.41	0.35	0.31	0.83	28.06
	5.40	0.02	0.01	0.00	19.59	0.64	0.03	0.00	0.20	0.28	1.18	5.95	0.05	19.43	0.02	14.17	0.00	0.00	11.24	41.58	0.12	35.42	1.42	0.39	0.33	0.82	28.01
	5.35	0.02	0.02	0.00	19.46	0.62	0.03	0.01	0.19	0.27	1.16	6.09	0.09	19.12	0.02	13.93	0.00	0.00	11.51	40.91	0.21	34.81	1.40	0.37	0.32	0.81	27.82
OREAS131B	3.18	0.02	0.01	0.00	5.79	0.18	0.01	0.01	0.19	5.58	3.85	7.42	0.06	26.06	0.01	3.05	4.40	7.30	14.03	55.76	0.14	7.62	4.66	7.81	0.31	0.24	8.29
	3.14	0.02	0.00	0.00	5.78	0.19	0.01	0.01	0.20	5.55	3.77	8.05	0.08	26.43	0.01	3.08	7.21	11.96	15.22	56.55	0.18	7.70	4.56	7.77	0.33	0.24	8.26
	3.18	0.02	0.00	0.00	5.81	0.19	0.01	0.01	0.20	5.55	3.76	7.58	0.08	26.00	0.01	3.01	5.32	8.83	14.32	55.63	0.18	7.53	4.55	7.76	0.33	0.24	8.31
	3.14	0.02	0.01	0.00	5.76	0.18	0.02	0.01	0.18	5.54	3.79	8.01	0.07	26.52	0.01	3.10	7.89	13.10	15.14	56.76	0.15	7.76	4.59	7.76	0.30	0.23	8.23
	3.13	0.02	0.01	0.00	5.76	0.18	0.01	0.01	0.20	5.48	3.82	8.39	0.09	26.79	0.01	3.11	7.59	12.59	15.85	57.34	0.21	7.77	4.62	7.68	0.33	0.23	8.24

Appendix 4-1 b Portable XRF results of Kombat deposit samples.

Index	Ba	Sb	Sn	Cd	Pd	Ag	Bal	Mo	Nb	Zr	Sr	Rb	Bi	As	Se	Au	Pb	W	Zn	Cu	Ni	Co	Fe	Mn	Cr	V	Ti	Ca	K	Al	P	Si	Cl	S	Mg
KEN002	0.018	0	0.001	0	0	0	52.064	0	0	0	0.016	0	0	0	0	0	0.724	0.009	0.008	0.345	0	0	0.634	0.566	0	0	0.016	35.344	0	0.537	0	3.968	0.005	0.386	5.359
	0.016	0	0	0	0	0.001	53.233	0	0	0	0.016	0.001	0	0	0	0	0.729	0.01	0.007	0.349	0	0	0.627	0.571	0	0	0.017	35.564	0	0.26	0.028	4.094	0.01	0.378	4.09
	0.013	0	0	0	0	0	53.097	0	0	0	0.015	0	0	0	0	0	0.719	0	0.007	0.346	0	0	0.617	0.55	0	0	0.016	35.128	0	0	0.016	4.088	0.008	0.382	4.995
	0.015	0	0	0	0	0.001	49.122	0	0	0	0.016	0	0	0	0	0	0.729	0.009	0.007	0.345	0	0	0.625	0.566	0	0	0.022	35.506	0	0.36	0	4.053	0.006	0.401	8.217
	0.013	0	0	0	0	0.001	50.277	0	0	0	0.016	0.001	0	0	0	0	0.725	0	0.007	0.35	0	0	0.63	0.571	0	0	0.02	35.546	0	0.498	0	4.062	0.009	0.397	6.875
KEN003	0.014	0	0	0	0	0.001	51.299	0	0	0	0.03	0	0	0.026	0	0	0.211	0	0.018	1.087	0	0	1.178	0.584	0	0	0.017	34.552	0	0.278	0.02	7.1	0.005	0.773	2.808
	0.016	0	0	0	0	0.001	49.802	0	0	0	0.03	0	0	0.03	0	0	0.205	0	0.017	1.084	0	0	1.162	0.577	0.007	0	0.024	34.377	0	0	0.026	7.146	0.005	0.783	4.709
	0.012	0	0	0	0	0.001	54.348	0	0	0	0.031	0	0	0.027	0	0	0.209	0	0.019	1.093	0	0	1.165	0.588	0	0	0.026	34.4	0	0.213	0.028	7.063	0.006	0.77	0
	0.011	0	0	0	0	0	49.792	0	0	0	0.03	0	0	0.026	0	0	0.212	0	0.018	1.093	0	0	1.181	0.585	0	0	0.028	33.994	0.024	0.436	0.023	7.312	0.003	0.789	4.442
	0.01	0	0	0	0	0	50.38	0	0	0	0.03	0	0	0.026	0	0	0.208	0	0.018	1.083	0	0	1.172	0.576	0	0	0.018	34.38	0	0	0.029	7.305	0.005	0.802	3.959
KEN004	0.027	0	0	0	0	0.001	47.774	0.001	0.001	0	0.02	0.001	0	0.079	0	0	1.617	0.021	0.045	2.295	0	0	3.497	0.823	0.01	0	0.031	38.55	0.038	0.434	0.09	2.536	0.018	2.091	0
	0.033	0	0	0.001	0	0.002	44.172	0.001	0.001	0	0.02	0.001	0	0.064	0	0	1.626	0.022	0.047	2.279	0	0	3.5	0.819	0.008	0.007	0.035	38.461	0	0	0.068	2.694	0.018	2.109	4.012
	0.027	0.003	0	0.001	0	0.002	47.666	0.001	0.001	0	0.02	0.002	0	0.072	0	0	1.639	0.017	0.046	2.316	0	0	3.504	0.847	0.009	0.007	0.05	38.969	0	0	0.063	2.618	0.022	2.1	0
	0.029	0.004	0	0.001	0	0.001	47.394	0.001	0.001	0	0.019	0.001	0	0.071	0	0	1.617	0.018	0.049	2.274	0	0	3.493	0.823	0.007	0	0.032	39.203	0.028	0	0.063	2.643	0.021	2.206	0
	0.027	0	0	0.001	0.001	0.001	47.672	0.001	0.001	0	0.02	0.001	0	0.077	0	0	1.63	0.023	0.045	2.318	0	0	3.509	0.817	0.013	0.005	0.031	39.002	0	0	0.061	2.542	0.019	2.183	0
KEN006	0.044	0	0	0	0	0.002	42.012	0.001	0.001	0	0.019	0.002	0	0	0	0	3.733	0.046	0.026	0.546	0	0	1.317	1.066	0.014	0	0.06	41.961	0.206	1.054	0.309	2.703	0.023	1.155	3.7
	0.046	0	0	0.002	0	0.002	46.416	0	0.001	0	0.019	0.002	0	0	0	0	3.717	0.042	0.021	0.546	0.007	0	1.324	1.075	0.011	0	0.057	41.301	0.242	0.836	0.336	2.795	0.026	1.175	0
	0.045	0	0	0	0.001	0.001	42.647	0	0.001	0	0.019	0.001	0	0	0	0	3.733	0.037	0.024	0.538	0	0	1.295	1.077	0.009	0	0.052	42.043	0.201	1.299	0.347	2.756	0.023	1.144	2.706
	0.05	0	0	0.001	0.001	0.002	44.912	0.001	0.001	0	0.02	0.001	0	0	0	0	3.774	0.041	0.023	0.546	0.007	0	1.334	1.079	0.012	0	0.06	42.318	0.227	1.125	0.302	2.949	0.022	1.193	0
	0.038	0	0	0	0	0.001	38.753	0	0.001	0	0.019	0.002	0	0	0	0	3.773	0.037	0.027	0.545	0.007	0	1.3	1.074	0.01	0	0.059	41.831	0.211	0.988	0.34	2.789	0.025	1.15	7.021
KEN007	0.014	0	0	0	0	0	46.388	0.001	0	0	0.021	0	0	0.021	0	0	0.046	0	0.021	1.777	0	0	2.077	1.047	0.01	0	0.045	41.456	0	0.403	0.035	1.391	0.016	0.975	4.257
	0.016	0	0	0	0	0.001	45.049	0.001	0	0	0.021	0	0	0.023	0	0	0.045	0	0.018	1.796	0	0	2.114	1.051	0.007	0	0.053	41.875	0	0	0.028	1.404	0.018	0.955	5.526
	0.016	0	0	0	0	0.001	50.646	0	0	0	0.021	0	0	0.021	0	0	0.047	0	0.018	1.789	0	0	2.116	1.052	0.009	0	0.045	41.826	0.048	0	0	1.372	0.015	0.957	0
	0.015	0	0	0	0	0.001	44.499	0.001	0	0	0.021	0	0	0.022	0	0	0.046	0	0.019	1.799	0	0	2.106	1.066	0.01	0	0.055	41.765	0	0.442	0.037	1.378	0.019	0.958	5.742
	0.015	0	0.001	0	0	0.001	44.856	0	0	0	0.021	0	0	0.021	0	0	0.045	0	0.018	1.79	0	0	2.075	1.052	0.007	0	0.045	41.802	0	0.613	0.034	1.344	0.019	0.974	5.266
KEN008	0.033	0	0	0.001	0	0.001	43.24	0	0.001	0	0.02	0.001	0	0	0	0	3.731	0.045	0.052	0.28	0	0	1.488	1.094	0	0	0.055	43.471	0.141	0.826	0.266	1.425	0.02	1.21	2.599
	0.032	0	0.002	0.001	0.001	0.001	46.113	0	0.001	0	0.02	0.002	0	0	0	0	3.728	0.039	0.051	0.281	0	0	1.482	1.099	0.013	0	0.05	43.389	0.138	0.518	0.285	1.514	0.02	1.22	0
	0.035	0	0	0	0.001	0.002	45.575	0	0.001	0	0.02	0.002	0	0	0	0	3.758	0.042	0.054	0.281	0	0	1.483	1.101	0.009	0	0.047	43.666	0.158	0.853	0.277	1.392	0.019	1.225	0
	0.034	0	0.002	0.001	0	0.001	45.582	0	0.001	0	0.021	0.001	0	0	0	0	3.766	0.036	0.054	0.282	0.005	0	1.488	1.103	0.01	0	0.06	43.777	0.12	0.616	0.288	1.46	0.018	1.273	0
	0.039	0	0	0.002	0	0.001	45.174	0.001	0.001	0	0.021	0.001	0	0	0	0	3.787	0.043	0.05	0.285	0.007	0	1.499	1.12	0.014	0	0.058	43.896	0.134	0.827	0.312	1.472	0.019	1.238	0
	0.037	0	0	0.002	0	0.002	42.717	0	0.001	0	0.02	0.002	0	0	0	0	3.7	0.032	0.052	0.276	0	0	1.46	1.124	0.011	0	0.044	43.061	0.141	0.846	0.279	1.504	0.024	1.219	3.447
KEN009	0.016	0	0	0	0	0	49.546	0	0	0	0.018	0	0	0.012	0	0	0.001	0	0.009	0.457	0	0	0.68	0.656	0.009	0	0.056	42.405	0	0.714	0	0.593	0.01	0.293	4.523
	0.013	0	0	0	0	0.001	50.494	0	0	0	0.018	0	0	0.012	0	0.001	0.001	0	0.01	0.45	0	0	0.676	0.664	0.008	0	0.056	42.529	0.024	0	0.029	0.561	0.01	0.291	4.151
	0.017	0	0	0	0	0	49.665	0	0	0	0.018	0	0	0.012	0	0.001	0.001	0	0.01	0.457	0	0	0.674	0.676	0	0	0.054	42.14	0	0.487	0	0.54	0.008	0.278	4.963
	0.016	0	0	0	0	0	54.849	0	0	0	0.019	0	0	0.012	0	0	0.001	0	0.01	0.456	0	0	0.681	0.673	0	0	0.056	42.303	0	0	0.064	0.574	0.011	0.274	0
	0.013	0	0	0	0	0	50.131	0	0	0	0.019	0	0	0.012	0	0	0.001	0	0.009	0.457	0	0	0.679	0.656	0.013	0	0.06	42.522	0	0.295	0.034	0.576	0.007	0.267	4.248
KEN010	0.013	0	0	0	0	0.001	51.066	0	0	0	0.019	0	0	0.012	0	0	0.001	0	0.01	0.456	0	0	0.671	0.665	0.007	0	0.052	42.139	0	0.408	0.04	0.559	0.007	0.272	3.603
	0.013	0	0	0.002	0	0.001	49.971	0	0	0	0.018	0	0	0.228	0	0	0.008	0	0.094	1.364	0	0	1.049	0.645	0	0	0.032	36.335	0.044	0.422	0.114	5.468	0.012	0.584	3.598
	0.014	0.002	0	0.002	0	0.002	49.765	0	0	0	0.018	0	0	0.227	0	0	0.008	0	0.095	1.354	0	0	1.028	0.666	0.007	0	0.022	36.272	0.045	0	0.104	5.583	0.011	0.601	4.174
	0.017	0.002	0	0.002	0	0.001	53.47	0	0	0	0.018	0	0	0.228	0	0	0.008	0	0.094	1.353	0	0	1.044	0.647	0	0	0.03	36.24	0.031	0.327	0.112	5.758	0.009	0.606	0
	0.016	0	0	0.003	0	0.001	49.778	0	0	0	0.018	0	0	0.225	0	0	0.008	0	0.093	1.345	0	0	1.037	0.643	0.008	0	0.034	36.206	0.058	0.638	0.125	5.698	0.014	0.611	3.441

Appendix 4-1 b continues……

Index	Ba	Sb	Sn	Cd	Pd	Ag	Bal	Mo	Nb	Zr	Sr	Rb	Bi	As	Se	Au	Pb	W	Zn	Cu	Ni	Co	Fe	Mn	Cr	V	Ti	Ca	K	Al	P	Si	Cl	S	Mg
KEN011	0.017	0	0	0	0	0.002	53.02	0	0.001	0	0.019	0	0	0	0	0.001	0.004	0	0.007	1.738	0	0	0.667	0.933	0	0	0.046	41.938	0.03	0.412	0.13	0.725	0.011	0.298	0
	0.019	0	0	0	0	0.003	45.573	0	0	0	0.019	0	0	0	0	0	0.005	0	0.007	1.731	0	0	0.665	0.941	0.008	0	0.046	41.085	0	0.629	0.131	0.662	0.012	0.3	8.164
	0.018	0	0	0	0	0.002	49.628	0	0	0	0.019	0	0	0.001	0	0.001	0.004	0	0.008	1.746	0	0	0.667	0.938	0	0	0.04	41.553	0.029	0.601	0.135	0.781	0.013	0.321	3.495
	0.016	0	0	0	0	0.003	47.978	0	0	0	0.019	0	0	0	0	0.001	0.005	0	0.007	1.733	0	0	0.663	0.945	0.007	0	0.049	41.5	0.024	0.33	0.162	0.866	0.011	0.321	5.361
	0.016	0	0	0	0	0.003	47.506	0	0	0.001	0.018	0	0	0	0	0	0.005	0	0.007	1.732	0	0	0.667	0.954	0	0	0.048	41.856	0.031	0.692	0.135	0.833	0.01	0.311	5.175
KC001	0.014	0	0	0	0	0	57.419	0	0	0	0.009	0	0	0	0	0	0	0	0.003	0.029	0	0	0.098	0.028	0.004	0	0.031	25.365	0.025	0.524	0.175	1.488	0.01	0.064	14.715
	0.012	0	0	0	0	0.001	57.307	0	0	0	0.009	0	0	0	0	0	0	0	0.003	0.026	0	0	0.101	0.029	0.004	0	0.026	25.285	0.017	0.409	0.183	1.612	0.011	0.062	14.903
	0.015	0	0	0	0	0	58.916	0	0	0	0.009	0	0	0.001	0	0	0	0	0.005	0.027	0	0	0.097	0.026	0	0	0.026	25.325	0	0	0.19	1.548	0.012	0.053	13.749
	0.014	0	0	0	0	0	59.447	0	0	0	0.009	0	0	0	0	0	0	0	0.005	0.029	0	0	0.095	0.029	0.007	0	0.028	25.525	0.016	0.261	0.169	1.506	0.012	0.057	12.79
	0.013	0	0	0	0	0	58.44	0	0	0	0.009	0	0	0	0	0	0	0	0.004	0.027	0	0	0.095	0.024	0.005	0	0.029	25.486	0.024	0.286	0.158	1.411	0.01	0.058	13.919
KC002	0.063	0	0	0	0	0.001	52.252	0	0	0	0.011	0	0	0	0	0	0.067	0	0.006	0.654	0	0	0.278	0.412	0	0	0.055	40.003	0.05	0.735	1.13	0.799	0.003	0.073	3.408
	0.061	0	0	0	0	0	51.577	0	0.001	0	0.011	0	0	0	0	0	0.066	0	0.006	0.647	0	0	0.273	0.415	0.008	0	0.044	39.561	0.07	0.589	1.204	0.847	0.006	0.074	4.542
	0.065	0	0	0	0	0.001	50.706	0	0	0	0.011	0	0	0	0	0	0.066	0	0.003	0.65	0	0	0.284	0.416	0	0	0.049	40.156	0.078	0.522	1.193	0.849	0.007	0.072	4.871
	0.061	0	0	0	0	0.001	51.059	0	0.001	0	0.011	0	0	0	0	0	0.064	0	0.005	0.655	0	0	0.281	0.425	0.008	0	0.046	40.238	0.077	0.777	1.15	0.833	0.004	0.07	4.234
	0.064	0	0	0	0	0.001	52.287	0	0	0	0.011	0	0	0	0	0	0.065	0	0.005	0.655	0	0	0.282	0.419	0.008	0	0.051	40.284	0.077	0.735	1.157	0.816	0.005	0.073	3.004
KC005	0	0	0	0.001	0	0.001	55.879	0	0	0	0.006	0	0	0	0	0	0.013	0	0.007	0.126	0	0	0.14	0.189	0	0	0.014	17.97	0	0	0.11	18.179	0.01	0.085	7.271
	0.005	0	0.001	0.001	0	0.001	54.907	0	0	0	0.006	0	0	0	0	0	0.012	0	0.008	0.128	0	0	0.143	0.189	0.003	0	0.018	17.97	0	0.277	0.105	18.643	0.009	0.087	7.484
	0	0	0	0.001	0	0	53.921	0	0	0	0.006	0	0	0	0	0	0.013	0	0.008	0.127	0	0	0.134	0.191	0.004	0	0.015	18.108	0	0.173	0.089	18.461	0.011	0.081	8.657
	0	0	0	0.001	0	0	55.621	0	0	0	0.006	0	0	0	0	0	0.012	0	0.007	0.126	0	0	0.142	0.189	0.004	0	0.018	17.982	0	0.346	0.11	19.028	0.007	0.084	6.316
	0.006	0	0.002	0.001	0	0.001	54.549	0	0	0	0.007	0	0	0	0	0	0.012	0	0.007	0.125	0	0	0.14	0.19	0.005	0	0.021	18.066	0	0.249	0.086	18.472	0.01	0.085	7.967
KC006	0.038	0	0	0	0	0	53.006	0	0	0	0.019	0	0	0	0	0	0.002	0	0.004	0.008	0	0	0.557	0.558	0.007	0	0.057	37.291	0.082	0.477	0.619	1.41	0.012	0.124	5.728
	0.038	0	0	0.001	0	0	50.922	0	0	0	0.018	0	0	0.001	0	0	0.002	0	0.004	0.007	0	0	0.559	0.547	0.009	0	0.05	36.618	0.113	0.813	0.618	1.506	0.01	0.123	8.04
	0.041	0	0	0.001	0	0	51.437	0	0	0	0.019	0	0	0	0	0	0.003	0	0.004	0.008	0	0	0.56	0.546	0.007	0	0.051	37.203	0.1	0.836	0.587	1.324	0.011	0.114	7.145
	0.036	0	0	0	0	0	52.862	0	0	0	0.018	0	0	0.001	0	0.001	0.002	0	0.005	0.007	0	0	0.567	0.543	0.007	0	0.054	37.04	0.116	0.6	0.677	1.34	0.009	0.127	5.987
	0.07	0	0	0	0	0	48.712	0	0	0.001	0.02	0.001	0	0.002	0	0.001	0.001	0	0.004	0.051	0	0	0.394	0.438	0.006	0	0.072	35.791	0.388	1.095	1.039	2.503	0.009	0.107	9.294
KC008	0.075	0	0	0	0	0	53.758	0	0	0.001	0.021	0.001	0	0.001	0	0	0.001	0	0.003	0.052	0	0	0.394	0.448	0.006	0	0.068	36.228	0.411	0.857	1.03	2.642	0.004	0.113	3.885
	0.073	0	0	0.001	0	0	48.265	0	0	0.001	0.02	0.001	0	0.001	0	0	0.002	0	0.005	0.047	0	0	0.382	0.447	0.005	0	0.08	36.568	0.383	1.279	1.036	2.636	0.008	0.106	8.653
	0.072	0	0.001	0	0	0	53.561	0	0.001	0.001	0.021	0.001	0	0.001	0	0	0.001	0	0.004	0.051	0	0	0.394	0.436	0.007	0	0.062	36.256	0.393	0.925	1.101	2.628	0.006	0.101	3.975
	0.069	0	0	0	0	0	53.389	0	0	0.001	0.02	0.001	0	0.001	0	0	0.002	0	0.003	0.05	0	0	0.387	0.438	0	0	0.069	35.846	0.369	0.99	1.048	2.667	0.007	0.118	4.524
	0.071	0	0	0	0	0	46.342	0	0	0.001	0.02	0.001	0	0.001	0	0.001	0.001	0	0.003	0.05	0	0	0.405	0.443	0	0	0.079	36.303	0.378	0.951	1.052	2.626	0.008	0.099	11.165
KC009	0.144	0	0	0	0	0.001	51.88	0.001	0	0	0.034	0	0	0.004	0	0.001	0.002	0	0.005	0.457	0	0	0.656	0.3	0.006	0	0.058	43.845	0.082	0.321	0.996	0.932	0.009	0.264	0
	0.136	0	0	0	0	0.001	50.746	0.001	0	0.001	0.033	0	0	0.004	0	0	0.002	0	0.006	0.459	0	0	0.643	0.307	0.007	0	0.059	44.668	0.064	0.672	0.998	0.918	0.006	0.268	0
	0.137	0	0	0	0	0	51.144	0.001	0.001	0	0.033	0	0	0.004	0	0	0.002	0	0.005	0.451	0	0	0.646	0.306	0.011	0	0.07	44.457	0.077	0.398	1.006	0.99	0.007	0.254	0
	0.138	0	0	0	0	0.001	44.727	0.001	0	0.001	0.033	0	0	0.004	0	0	0.002	0	0.006	0.454	0	0	0.651	0.303	0.006	0	0.061	44.254	0.092	0.399	1.005	1.008	0.01	0.256	6.587
	0.137	0	0	0	0	0.001	48.966	0.001	0.001	0	0.034	0	0	0.004	0	0.001	0.003	0	0.005	0.46	0	0	0.639	0.295	0.009	0	0.061	44.078	0.091	0.54	1.019	1.024	0.009	0.267	2.358
KC010	0.005	0	0	0	0	0.001	52.133	0	0	0	0.012	0	0	0	0	0	0.001	0	0.003	0.141	0	0	0.143	0.269	0.004	0	0.023	24.877	0.022	0.315	0.467	18.913	0.009	0.061	2.601
	0.005	0	0	0	0	0.001	52.622	0	0	0	0.012	0	0	0	0	0	0.001	0	0.003	0.139	0	0	0.146	0.278	0	0	0.025	25.18	0	0.282	0.461	18.817	0.005	0.062	1.96
	0.006	0	0	0	0	0.001	52.777	0	0	0	0.012	0	0	0.001	0	0	0.001	0	0.002	0.141	0	0	0.15	0.278	0	0	0.018	25.21	0	0.189	0.465	18.752	0.007	0.064	1.925
	0.004	0	0	0	0	0.001	52.365	0	0	0	0.012	0	0	0	0	0	0.001	0	0.003	0.137	0	0	0.145	0.276	0	0	0.029	25.142	0.032	0.185	0.475	19.007	0.01	0.061	2.115
	0.006	0	0	0	0	0	54.122	0	0	0	0.012	0	0	0	0	0	0.001	0	0.002	0.142	0	0	0.143	0.279	0	0	0.031	25.264	0.029	0.192	0.475	19.225	0.007	0.069	0

Appendix 4-1 b Continues……

Index	Ba	Sb	Sn	Cd	Pd	Ag	Bal	Mo	Nb	Zr	Sr	Rb	Bi	As	Se	Au	Pb	W	Zn	Cu	Ni	Co	Fe	Mn	Cr	V	Ti	Ca	K	Al	P	Si	Cl	S	Mg
KC011	0.019	0	0	0	0	0.003	46.482	0.001	0	0	0.016	0	0	0.001	0	0	0.003	0	0.003	2.905	0	0	0.624	0.632	0	0	0.081	38.174	0.03	0.51	0.074	1.756	0.007	0.144	8.536
	0.019	0	0	0	0	0.003	48.362	0.001	0	0	0.016	0	0	0.001	0	0.001	0.003	0	0.008	2.905	0	0	0.627	0.63	0.006	0	0.078	38.876	0	0.334	0.048	1.649	0.008	0.148	6.278
	0.017	0	0	0	0	0.003	48.97	0.001	0	0	0.016	0	0	0	0	0.001	0.003	0	0.004	2.909	0	0	0.622	0.629	0	0	0.087	38.402	0.029	0.387	0.044	1.694	0.007	0.149	6.026
	0.014	0	0	0	0	0.003	50.11	0.001	0	0	0.016	0	0	0	0	0	0.003	0	0.003	2.913	0	0	0.62	0.613	0	0	0.083	39.101	0	0.323	0.051	1.652	0.006	0.15	4.339
	0.014	0	0	0	0	0.003	50.835	0.001	0	0	0.016	0	0	0	0	0	0.003	0	0.004	2.922	0	0	0.639	0.637	0	0	0.084	38.396	0.025	0.3	0.059	1.736	0.006	0.157	4.164
KC012	0.024	0	0	0	0	0	51.963	0	0	0	0.019	0	0	0.001	0	0	0.008	0	0.005	0.113	0	0	0.328	0.438	0.01	0	0.101	43.455	0.029	0.426	0.096	0.69	0.007	0.12	2.167
	0.027	0	0	0	0	0	49.134	0	0	0	0.019	0	0	0	0	0	0.008	0	0.005	0.113	0	0	0.327	0.448	0.008	0	0.107	43.55	0.034	0.449	0.135	0.733	0.012	0.121	4.769
	0.027	0	0	0	0	0	50.136	0	0	0	0.019	0	0	0	0	0	0.008	0	0.005	0.115	0	0	0.323	0.446	0.009	0	0.091	43.409	0.037	0.326	0.114	0.727	0.011	0.131	4.063
	0.032	0	0	0	0	0	51.708	0	0	0	0.019	0	0	0	0	0	0.009	0	0.005	0.111	0	0	0.322	0.45	0	0	0.094	42.945	0.029	0.405	0.111	0.693	0.012	0.129	2.927
	0.033	0	0	0.001	0	0.001	53.49	0	0	0	0.019	0	0	0.001	0	0	0.008	0	0.005	0.117	0	0	0.33	0.459	0	0	0.099	43.792	0.041	0.63	0.124	0.715	0.011	0.124	0
KH002	0.009	0.005	0.001	0.001	0	0.002	44.594	0.001	0.001	0	0.015	0	0	0.052	0	0.001	0.002	0	0.047	4.699	0	0	4.901	0.523	0	0	0.071	32.174	0.027	0.472	0	6.761	0.011	2.443	3.186
	0.008	0.003	0	0	0	0.001	44.696	0.001	0	0	0.014	0	0	0.051	0	0	0.002	0	0.045	4.622	0	0	4.87	0.514	0	0	0.067	32.226	0.031	0.36	0.048	6.833	0.011	2.464	3.134
	0.008	0.004	0	0	0	0.001	47.81	0.001	0	0	0.014	0	0	0.051	0	0	0.003	0	0.044	4.657	0	0	4.902	0.53	0.01	0	0.073	32.415	0.03	0	0	6.922	0.009	2.516	0
	0.008	0.003	0	0.001	0	0.001	45.695	0.001	0	0	0.014	0	0	0.05	0	0	0.003	0	0.044	4.658	0	0	4.897	0.525	0	0	0.076	31.868	0	0.301	0.033	6.669	0.01	2.374	2.767
	0.012	0.006	0.001	0	0.001	0.001	47.892	0	0.001	0	0.014	0	0	0.052	0	0.002	0.003	0	0.049	4.673	0	0	4.897	0.523	0	0	0.061	32.11	0.026	0.419	0	6.821	0.009	2.427	0
KH010	0.018	0	0.002	0	0	0.015	45.848	0.001	0.001	0	0.017	0	0	0.007	0	0	0.005	0	0.005	5.164	0	0	1.183	0.595	0.007	0	0.096	41.61	0.051	0	0.059	1.143	0.006	0.645	3.521
	0.023	0	0.002	0	0	0.017	45.408	0.001	0	0	0.017	0	0	0.007	0	0.001	0.005	0.006	0	5.185	0	0	1.173	0.596	0.007	0	0.104	42.129	0	0.358	0.04	1.133	0.009	0.612	3.166
	0.024	0	0.002	0	0	0.016	46.408	0.001	0	0	0.017	0	0	0.006	0	0	0.006	0.005	0	5.129	0	0	1.163	0.584	0.008	0	0.095	41.507	0	0	0.053	1.136	0.007	0.648	3.185
	0.031	0	0.004	0	0	0.016	48.064	0	0	0	0.017	0	0	0.006	0	0	0.005	0	0	5.154	0	0	1.172	0.593	0	0	0.105	42.303	0	0.596	0.022	1.252	0.011	0.647	0
	0.023	0	0.001	0	0	0.016	48.243	0	0.001	0	0.017	0	0	0.006	0	0	0.006	0	0	5.224	0	0	1.196	0.603	0.006	0	0.082	42.09	0	0.642	0.037	1.143	0.009	0.652	0
KM005	11.794	0	0	0	0	0	25.86	0.002	0.001	0	0.412	0	0	0.011	0	0	0.035	0	0.012	0.191	0.041	0	47.957	0.351	0.059	0.052	0.209	6.685	0.045	1.473	0.539	1.884	0	2.39	0
	12.118	0	0	0	0	0	24.637	0.002	0.001	0	0.428	0	0	0.013	0	0	0.035	0	0.012	0.191	0.046	0	48.925	0.361	0.056	0	0.328	6.728	0	1.359	0.571	1.818	0	2.371	0
	11.929	0	0	0	0	0	26.384	0.002	0.001	0	0.414	0	0	0.014	0	0	0.034	0	0.012	0.184	0.053	0	48.133	0.357	0.044	0	0	6.45	0	1.438	0.548	1.742	0	2.26	0
	12.059	0	0	0	0	0	25.861	0.002	0.001	0	0.419	0.001	0	0.013	0	0	0.034	0	0.009	0.179	0.039	0	48.307	0.367	0.046	0	0.193	6.623	0	1.339	0.526	1.712	0	2.27	0
	12.095	0	0	0	0	0	24.66	0.002	0.001	0	0.423	0	0	0.013	0	0.004	0.039	0	0.011	0.19	0.055	0	48.716	0.381	0.068	0	0.204	6.751	0	1.48	0.554	1.931	0	2.421	0

Appendix 4-2 ICP-MS and AAS results of major and trace elements of the Kombat ore.

	Ag	Al	As	Ba	Cd	Ce	Co	Cr	Cs	Cu	Fe	Ga	K	La	Li	Lu	Mg	Mn	Mo	Na	Nb	Ni	P	Pb	Rb	S	Sb	Sr	Tb	Tl	U	V	W	Y	Yb	Zn	Zr
	ppm	%	ppm	ppm	ppm	ppm	ppm	ppm	ppm	ppm	%	ppm	%	ppm	ppm	ppm	%	ppm	ppm	ppm	ppm	ppm	ppm	ppm	ppm	%	ppm	ppm	ppm	ppm	ppm	ppm	ppm	ppm	ppm	ppm	ppm	ppm
KC011	30	600	2.2	31	1.75	13	1.9	13.1	0.23	37300	6400	1	500	5.2	2.8	0.07	32700	6434	5.29	100	0.3	19.7	500	19	1.5	16000	0.32	156	0.32	0.12	0.5	13.2	0.4	12	0.6	21.1	0.8
KC012	0.56	500	6.7	138	1.39	7.54	2.6	15.9	0.26	1775	3800	1.1	500	4.2	3.7	0.07	17300	4996	1.34	200	0.4	28.2	1100	63	1.2	17000	0.49	180	0.21	0.07	0.6	8.7	0.2	10.4	0.5	18.2	0.6
KC008	0.14	5000	12.6	650	2.16	28.3	3	19.3	0.83	636	4400	2.9	3700	13.8	12.3	0.1	44700	4805	1.35	200	0.4	24.4	17100	12	16.2	15000	0.24	219	0.52	0.61	0.8	15.5	0.3	19.6	0.9	16.3	6.5
KC010	1.17	500	1.3	34	0.73	12	1.1	53	0.22	1590	1800	0.8	400	12.8	3.6	0.04	7200	3092	3.69	100	0.2	17.1	4000	10	1.5	14000	0.17	114	0.27	0.03	0.3	6.8	0.3	10.6	0.3	9.2	0.6
KC006	0.17	1700	7.6	278	11.51	14.7	2.3	17.6	0.29	77	6700	1.4	1400	7	7.5	0.07	46100	6010	1.07	200	0.3	24.6	6900	22	4.4	16000	0.33	187	0.29	0.37	0.6	7.4	0.3	12.9	0.5	21.4	2.4
KEN003	3.5	300	380	6	3.82	6.41	1.8	20.4	0.22	14700	13700	1.1	300	2.3	9.1	0.03	12600	6176	1.29	100	0.2	19.9	300	2405	1.2	25000	2.61	155	0.14	0.05	0.2	5.8	0.2	6.2	0.3	166	-0.5
KEN004	5	300	1100	11	13.09	22.1	10.7	25.6	0.21	21500	39300	1.7	300	6.3	3.5	0.08	8800	7839	11.4	200	0.2	16.8	500	14500	2.9	43000	14.4	177	0.32	0.91	0.4	67.9	0.5	14.2	0.6	377	1
KEN006	4.6	3100	580	190	11.01	16.2	10.7	20.5	0.33	7201	15300	2.7	1600	4.5	3.5	0.08	11600		4.13	300	0.6	20	3300	62200	7.1	26000	5.21	191	0.45	1.13	3	70.9	0.3	14	0.7	183	4.6
KEN010	9.58	500	2420	11	23.9	8.81	3.9	25.2	0.34	17000	11800	1.1	500	2.4	3.4	0.04	15200	6924	2.19	200	0.2	20.4	1000	147	2.6	23000	15.7	165	0.24	0.43	0.3	12.7	0.3	7.6	0.3	900	0.6
KEN011	23	400	5.4	7	2.94	6.72	1.9	13.1	0.11	26500	7100	1.4	400	2.4	2.7	0.04	24500	9975	0.66	200	0.3	25.2	1400	43	2.3	21000	0.52	187	0.19	0.12	1.5	15.2	0.4	6.9	0.3	64.5	0.8
KM002	0.4	2100	59.3	1528		17.8	0.7	19.8	0.18	2050	335000	3	600	9.9	1.8	0.18	700	2652	16.1	1200	0.2	2.9	2900	340	2.9	-5000	1.53	1149	0.75	0.03	7.1	82.5	29.4	21.2	1.5	14	0.7
KH002	6.1	500	568	16	7.21	7.61	2.5	25.7	0.12	69100	52700	0.7	300	3.1	2.8	0.05	6400	4879	2.31	-100	0.2	11.5	100	17	2.5	35000	29.7	134	0.15	0.06	0.4	9	0.6	6.6	0.4	375	1
KH010	155	-100	62.9		6.97	3.57	1.4	9.8	0.15	85900	11600	0.5	100	1.4	1.6	0.02	13300	5819	0.78	-100	-0.1	18	100	51	0.4	22000	0.4	147	0.08	0.09	0.2	4.1	0.3	3.1	0.1	33.3	-0.5
KEN007	3.6	0	301	5	4.1	16.1	4.6	15.2	0.12	27900	25200	1.4	200	5.5	1.7	0.06	10900		3.3	200	-0.1	20.8	100	612	0.6	28000	7.93	198	0.33	0.1	0.1	7.5	0.2	14.4	0.6	140	-0.5
KEN002	2.1	200	147	8	2.53	5.08	2.8	13.3	0.07	5443	8900	1	300	1.5	2.3	0.02	46300	6176	2.35	100	0.1	22.3	100	11500	1.6	21000	1.56	150	0.1	0.36	0.3	12.7	0.3	4.7	0.3	60.7	-0.5
KC009	3.6	1200	36.7	1272	1.49	28.5	3	16.3	0.15	6318	8200	3.4	1000	25.1	1.7	0.12	6500	3159	11.7	200	0.2	27.9	12400	30	2.2	20000	1.51	342	0.63	0.9	0.9	7.8	0.5	27.7	1	19	1.9
KC002	6.1	1400	16	513	1.14	18.8	1.9	14.4	0.27	7368	2600	1.4	800	18.4	3.3	0.07	32600	4580	0.85	200	0.2	25.6	13100	952	2.3	13000	0.24	106	0.47	0.06	1	10.1	0.3	17.2	0.6	23.5	1.9
KEN009	1.14	0	138		1.38	6.65	2.2	14.8	0.08	6213	7100	1.1	200	2.4	2.2	0.04	22800	7091	0.74	100	-0.1	27.6	100	5	0.4	20000	1.87	174	0.11	0.03	0.2	3.4	0.2	5.4	0.2	64.5	-0.5
KC001	0.37	400	1.7	57	0.24	2.2	1.4	19.1	0.2	345	1900	0.7	400	1	2.9	0.01	133500	536	0.78	100	0.3	17.7	2200	2	0.8	16000	-0.05	96.4	-0.05	-0.02	0.2	3.4	0.2	2	0.1	28.7	1.9

Appendix 4-3 Assessment summary table of CRMS (OREAS, 932, 134b and 623).

	Index	Ba	Ag	Sr	Pb	Zn	Cu	Fe	Mn	Cr	Ti	S
Oreas 134b	Mean	0.235	0.025	0.004	11.298	16.030	0.118	10.781	0.335	0.023	0.027	12.251
	SD	0.009	0.001	0.000	0.054	0.120	0.004	0.047	0.012	0.006	0.016	0.138
	RSD	3.920	5.174	10.648	0.482	0.748	3.442	0.434	3.674	27.498	58.969	1.130
	% diff	57.584	23.529	57.303	-14.409	-9.435	-11.743	-11.992	-2.588	1337.500	-38.497	-36.555
OREAS 932	Mean	0.063	0.003	0.005	0.015	0.067	5.359	14.649	0.096	0.015	0.293	3.295
	SD	0.005	0.000	0.001	0.001	0.002	0.007	0.027	0.003	0.003	0.009	0.018
	RSD	7.943	13.975	10.143	7.404	2.728	0.132	0.184	3.409	18.708	3.119	0.548
	% diff	1376.636	42.793	182.723	-15.385	11.185	-12.285	-0.755	9.545	190.566	396.610	-44.061
OREAS 623	Mean	0.170	0.003	0.016	0.229	0.994	1.535	13.095	0.057	0.014	0.146	5.754
	SD	0.005	0.000	0.001	0.003	0.003	0.012	0.049	0.003	0.003	0.010	0.144
	RSD	2.837	15.972	3.340	1.293	0.279	0.794	0.372	5.445	18.228	6.984	2.509
	% diff		37.255		-8.240	-3.515	-11.272					-36.556

Appendix 5-1a LA-ICP-MS results of trace elements in bornite of the Kombat ore.

	int. Std (S)	S34 (%)	V51 (ppm)	Fe57 (%)	Ga69 (ppm)	Ag107 (ppm)	Cd111 (ppm)	Sn118 (ppm)	Sb121 (ppm)	W184 (ppm)	Pb208 (ppm)	Bi209 (ppm)
KH0517 P1 3	25.560	25.560	2.256	10.271	1.008	267.849	2.705				2.108	0.459
KH0517 P2 4	25.560	25.560	2.800	9.981	0.788	281.360			0.272		21.779	0.469
KH0517 P3 5	25.560	25.560	6.048	9.613	1.249	252.297					2.539	0.456
KH0517 P4 6	25.560	25.560	3.812	10.146	1.056	272.238					9.920	0.477
KH0517 P5 7	25.560	25.560	4.638	9.927	1.087	262.019	2.244			0.953	10.698	0.455
KH0517 P6 8	25.560	25.560	6.118	10.237	1.351	279.596	2.248			0.766	38.981	0.499
KH0517 P7 11	25.560	25.560	4.665	10.400	1.051	273.536			0.292	0.588	1270.306	0.474
KH0517 P8 12	25.560	25.560	3.483	9.969	1.094	252.650			0.434		298.702	0.453
KH0517 P9 13	25.560	25.560	3.576	9.852	1.115	252.185					3.806	0.429
KH0517 P10 14	25.560	25.560	12.292	9.830	1.544	274.953			0.317	1.129	30.527	0.470
KH0517 P11 15	25.560	25.560	6.020	9.648	1.090	256.159	1.991		0.208	0.548	5.138	0.454
KH0517 P12 16	25.560	25.560	3.736	9.770	1.075	264.197				0.687	5.088	0.458
KH0517 P13 19	25.560	25.560	4.150	9.867	0.797	250.656				2.329	3.206	0.469
KH0517 P14 20	25.560	25.560	3.340	9.608	1.104	217.703			0.211	0.792	4.160	0.447
KH0517 P15 21	25.560	25.560	7.327	9.797	1.245	254.858	2.465		0.218	1.991	8.107	0.452
KH0517 P16 22	25.560	25.560	2.238	9.843	1.473	261.961	2.524			0.541	6.738	0.450
KH0517 P17 23	25.560	25.560	2.339	9.714	1.082	249.953				0.391	133.112	0.385
KH0517 P18 24	25.560	25.560		9.808	1.385	250.549	2.468				2.490	0.403
KH0517 P19 27	25.560	25.560		9.859	1.965	267.210					1.865	0.378
KH0517 P20 28	25.560	25.560		10.422	7.661	207.612	2.539				1.422	0.386
KH0516 P1 45	25.560	25.560	2.275	10.592	1.067	232.782					1.012	11.044
KH0516 P2 46	25.560	25.560	9.132	10.585	1.241	240.064					0.843	11.452
KH0516 P3 47	25.560	25.560	75.128	10.373	2.978	232.504					1.067	11.050
KH0516 P4 48	25.560	25.560	4.779	10.545	0.957	213.495					0.975	11.483
KH0516 P5 49	25.560	25.560	44.583	10.274	2.173	243.802		5.716			1.020	11.265
KH0516 P6 50	25.560	25.560	10.449	10.171	1.399	221.847					1.040	10.817
KH0516 P7 53	25.560	25.560	6.629	10.156	1.349	252.794					0.917	11.154

Appendix 5-1 a continues

	int. Std (S)	S34 (%)	V51 (ppm)	Fe57 (%)	Ga69 (ppm)	Ag107 (ppm)	Cd111 (ppm)	Sn118 (ppm)	Sb121 (ppm)	W184 (ppm)	Pb208 (ppm)	Bi209 (ppm)
KH0516 P8 54	25.560	25.560	3.682	10.171	1.282	258.479					0.713	11.382
KH0516 P9 55	25.560	25.560	11.427	10.158	1.305	220.866					1.089	10.796
KH0516 P10 56	25.560	25.560	8.112	10.500	1.338	256.874					1.004	11.604
KH0516 P11 57	25.560	25.560	2.748	10.374	1.304	229.166					0.943	11.411
KH0516 P12 58	25.560	25.560	4.058	10.289	1.217	244.346					1.259	11.624
KH0516 P13 61	25.560	25.560	3.675	10.731	1.301	255.543					1.328	13.086
KH0516 P14 62	25.560	25.560	5.799	10.761	1.350	249.073					1.146	12.563
KH0516 P15 63	25.560	25.560	4.378	10.921	1.499	220.511					1.810	12.240
KH0516 P16 64	25.560	25.560	33.963	10.871	1.948	292.778					1.097	12.760
KH0516 P17 65	25.560	25.560	4.288	10.653		250.588					1.139	12.350
KH0516 P18 66	25.560	25.560	3.695	10.717		249.322					1.106	12.415
KH0515 P1 3	25.560	25.560		10.358	1.332	188.657					3.215	5.290
KH0515 P2 4	25.560	25.560		10.326	1.350	159.571					2.562	5.179
KH0515 P3 5	25.560	25.560		10.434	1.346	183.620					28.072	5.387
KH0515 P4 6	25.560	25.560		10.407	1.684	100.236					14.647	5.039
KH0515 P5 7	25.560	25.560		10.689	1.284	133.170					22.117	5.263
KH0515 P6 8	25.560	25.560		10.459	1.008	164.376					245.222	5.109
KH0515 P7 11	25.560	25.560		10.384	3.140	197.174					3.995	4.766
KH0515 P8 12	25.560	25.560		10.211	1.741	214.965					41.189	4.971
KH0515 P9 13	25.560	25.560		10.251	1.267	179.631					6.637	5.445
KH0515 P10 14	25.560	25.560		10.199	1.216	191.143					10.482	5.118
KH0515 P11 15	25.560	25.560		10.287	1.298	193.887	1.916				3.430	5.383
KH0515 P12 16	25.560	25.560		10.350	1.254	212.988					656.522	5.742
KH0515 P13 19	25.560	25.560		10.098	0.808	202.701					40.216	5.241
KH0515 P14 20	25.560	25.560		10.754	0.798	234.980					20.628	6.066
KH0515 P15 21	25.560	25.560		10.462	0.920	209.080					8.825	5.637
KH0515 P16 22	25.560	25.560	3.591	10.720	1.692	238.847					215.801	6.297
KH0515 P17 23	25.560	25.560		10.684	0.850	210.780					6.132	5.867
KH0515 P18 24	25.560	25.560		10.595	0.766	237.801					4.814	5.893

Appendix 5-1b LA-ICP-MS results of trace elements in chalcopyrite of the Kombat ore.

	int. Std (S)	S34 (%)	V51 (ppm)	Fe57 (ppm)	Ga69 (ppm)	Zn70 (ppm)	Ge73 (ppm)	Ag107 (ppm)	In115 (ppm)	Sb121(ppm)	W184 (ppm)	Pb208 (ppm)	Bi209 (ppm)
KH0517 P21 29	34.940	34.940	5.078	27.926	11.661			2.237		0.378	1.364	3.969	
KH0517 P22 30	34.940	34.940		28.241	12.163			1.923		0.526		4.791	
KH0517 P23 31	34.940	34.940	0.834	28.457	13.095			1.309		0.460	1.384	3.469	
KH0517 P24 32	34.940	34.940		28.219	11.574			0.953		0.367	0.596	3.253	
KH0517 P25 35	34.940	34.940	1.347	28.886	12.786			6.807		1.508	0.736	10.230	
KH0517 P26 36	34.940	34.940	2.010	28.006	14.995		2.937	1.328		0.398	1.330	4.148	
KH0517 P27 37	34.940	34.940		27.975	16.612			1.337		0.578	0.799	11.106	
KH0517 P28 38	34.940	34.940		26.431	12.423			14.575		0.553		4.983	
KH0517 P29 39	34.940	34.940	1.064	27.644	13.069			2.246		0.988	0.484	6.189	
KH0517 P30 40	34.940	34.940	1.299	28.013	13.848			2.936	0.093	0.927	0.977	8.870	
KH0516 P19 69	34.940	34.940	23.392	28.969	13.713			5.099	0.385			1.104	
KH0516 P20 70	34.940	34.940	27.778	29.006	13.801			2.868	0.395			2.043	
KH0516 P21 71	34.940	34.940		29.117	12.733			1.162	0.412			1.587	
KH0516 P22 72	34.940	34.940	37.357	29.015	13.912			1.740	0.434			1.611	
KH0516 P23 73	34.940	34.940		29.988	10.448			4.301	0.343			0.800	
KH0516 P24 74	34.940	34.940	33.402	29.554	10.650			1.366	0.315			2.282	
KH0515 P19 27	34.940	34.940		27.434	10.837			19.237	0.217			43.270	
KH0515 P20 28	34.940	34.940		27.615	12.534				0.235			2.271	
KH0515 P21 29	34.940	34.940		27.690	15.078			4.715	0.173			10.661	
KH0515 P22 30	34.940	34.940		28.045	14.613			1.279				1.855	
KH0515 P23 31	34.940	34.940		28.595	14.789			2.350			5.314	5.077	
KH0515 P24 32	34.940	34.940		27.841	13.856				0.114			0.621	
KH0515 P25 35	34.940	34.940		29.825	15.756			0.762	0.197			1.388	
KH0515 P26 36	34.940	34.940		30.311	15.724	0.058		2.026				6.376	0.161
KH0515 P27 37	34.940	34.940		30.246	13.917		3.860	1.143	0.161			1.635	
KH0515 P28 38	34.940	34.940		31.599	16.307		3.580	0.826				0.998	
KH0515 P29 39	34.940	34.940		30.798	16.628			1.699	0.159			4.059	
KH0515 P30 40	34.940	34.940		31.307	14.365			1.031	0.138			1.394	
KH0515 P31 43	34.940	34.940		27.968	10.863			0.480	0.183			0.641	
KH0515 P32 44	34.940	34.940		29.138	12.724			1.348				1.748	
KH0515 P33 45	34.940	34.940		30.155	12.778			6.185				27.545	
KH0515 P34 46	34.940	34.940		30.518	14.264			3.101				29.026	
KH0515 P35 47	34.940	34.940		30.497	13.417			2.894				10.006	
KH0515 P36 48	34.940	34.940		30.075	14.817			0.924				4.061	

Appendix 5-2 Whole ore geochemistry of the Kombat ore deposit.

Analyte Symbol	Li	Na	Mg	Al	K	Ca	Cd	V	Cr	Mn	Fe	Hf	Ni	Er	Be	Ho	Ag	Cs	Co	Eu	Bi	Se	Zn	Ga	As
Unit Symbol	ppm	%	%	%	%	%	ppm	ppm	ppm	ppm	%	ppm	ppm	ppm	ppm	ppm	ppm	ppm	ppm	ppm	ppm	ppm	ppm	ppm	ppm
Detection Limit	0.5	0.01	0.01	0.01	0.01	0.01	0.1	1	1	1	0.01	0.1	0.5	0.1	0.1	0.1	0.05	0.05	0.1	0.05	0.02	0.1	0.2	0.1	0.1
KEN026	2.1	0.02	10.5	0.28	0.15	25.1	0.1	8	6	2760	0.15	< 0.1	1.6	0.3	< 0.1	0.1	0.06	0.15	0.2	0.07	< 0.02	0.2	13.3	1.1	10.5
KEN29	0.7	< 0.01	5.87	< 0.01	< 0.01	34.4	< 0.1	5	8	6360	0.14	< 0.1	1.7	0.4	< 0.1	0.2	0.07	< 0.05	0.2	0.09	< 0.02	< 0.1	10.5	0.3	14.2
KEN31	3.8	0.01	1.74	0.42	0.27	31.2	58.5	31	17	7550	1.64	0.2	18.1	1.2	< 0.1	0.5	31.2	0.43	32.9	0.5	< 0.02	0.2	345	< 0.1	73.6
KEN32	0.9	< 0.01	0.99	< 0.01	0.04	28.2	9.4	14	12	8720	5.9	< 0.1	2.5	0.8	< 0.1	0.3	4.71	0.07	9.5	0.19	0.03	0.3	463	2	712
KEN33	0.7	< 0.01	0.71	0.07	0.04	32.1	11.3	16	3	8890	1.89	< 0.1	8.1	2.2	< 0.1	0.8	4.71	0.08	49.4	0.44	0.05	< 0.1	148	0.5	438
KEN34	0.8	< 0.01	3.84	< 0.01	< 0.01	35.2	1.8	4	2	6120	0.24	< 0.1	1.3	0.2	< 0.1	< 0.1	19.6	< 0.05	< 0.1	0.1	< 0.02	< 0.1	17.7	0.2	28.5
KEN35	0.6	< 0.01	5.02	< 0.01	< 0.01	34	0.3	6	3	6120	0.2	< 0.1	2.5	0.3	< 0.1	0.1	0.2	< 0.05	< 0.1	0.1	< 0.02	0.1	17.4	0.3	40.6
KEN36	1	< 0.01	3.84	< 0.01	< 0.01	34.7	2.1	4	6	6230	0.21	< 0.1	1.7	0.2	< 0.1	< 0.1	15.1	0.07	< 0.1	0.1	< 0.02	< 0.1	13.9	0.2	21.4
KEN023	2.3	0.01	13.2	< 0.01	0.01	23.2	1.2	83	4	2280	0.21	< 0.1	1.7	< 0.1	< 0.1	< 0.1	0.65	< 0.05	7.6	< 0.05	< 0.02	0.2	37.3	0.4	102
KEN025	1.4	< 0.01	5.17	< 0.01	0.02	25.6	72.9	7	27	2670	3.32	< 0.1	5.6	0.4	0.5	0.2	0.29	< 0.05	7.3	0.09	< 0.02	< 0.1	2230	0.9	2080
KEN027	0.9	0.01	1.33	< 0.01	0.01	29.7	7.8	29	31	8830	7.28	< 0.1	9.3	0.7	< 0.1	0.3	6.28	0.06	37.1	0.28	< 0.02	0.4	322	< 0.1	1820
KEN30	0.5	< 0.01	6.36	< 0.01	< 0.01	31	5.6	4	5	4570	1.42	< 0.1	1.4	0.2	< 0.1	< 0.1	2.11	< 0.05	0.3	0.06	< 0.02	< 0.1	174	0.4	172

Appendix 6-1 List of samples collected from the Schneiderhöhn collection housed at the Geological Survey of Namibia.

Sample Number	Level/tray	description
04029	A12	Dolomite with clasts of sulfide mineralsiation
04050	A12	Massive sulfide mineralisatiom
04044	A12	Massive sulfide mineralisation
04236	A12	Bands of chalcopyrite, embended in dolomite
04261	A12	Brecciated zone, with primary sulfide minerals
04416	B2	Sphalerite and galena rich
04399	B2	Sphalerite and galena rich
04769	B2	Silica rich veins, with bornite and chalcopyrite in the vein
04767	B2	Veinlets filled with chalcopyrite and bornite in the silica rich vein
08277	Level 30 stope E9	Smithsonite, galena, sphalerite, dolomite and chalcopyrite
08280	Level 30 stope E10	Smithsonite, cobaltian, galena, sphalerite and pyrite
08269	Level 32, st W50	Smithsonite, mimekite, cerrusite, tennantite, galena and sphalerite
08205	Level 32 Stw40	Smithsonite, galena, sphalerite, pyrite, chalcocite, tennantite
08241	Level 32 north stope	Smithsonite, sphalerite, galena, pyrite, chalcocite, dolomite, goethite
08298	Level 32, St w30	Tennantite, galena, pyrite, renierite, germanite, calcite, siderite cement with vugs
08239	Level 32crown sublevel 96	Smithsonite, Tsumicorite, willemite
08299	Level 34. St w40	Tennantite, pyrite, galena, renierite, germanite, calcite, siderite
08107	Level 46 crown pillar	Smithsonite, tennantite, pyrite, galena
08111	Level 29	Smithsonite replacing galena in a sphalerite matrix
04236	Level XIV A12	Chalcopyrite rich
04196	Level XIV 0.7	Carbonate rock
04306	Level XV	Carbonate primary sulfide rich
04546	XVII	Chalcopyrite, galena, sphalerite
04495	Level 17	Massive sulfide ore
04618	A20	Massive sulfide ore
04612	Drawer 6	Massive
04635	XVIII A20	
04807	Level 18	Quartz veins (~1cm) with clusts of malachite
04847	Level 18	
04803	XIX	
04884	XIX	
04898	XIX	
05143	XXL	
05104	XIX	
05254	XXL	
05246	XXL	
05263	XX	

Appendix 6-2, bulk ore geochemistry of the Tsumeb ore.

Analyte Symbol	Li	Na	Mg	Al	K	Ca	Cd	V	Cr	Mn	Fe	Hf	Ni	Er	Be	Ho	Ag	Cs	Co	Eu	Bi	Se	Zn	Ga	As	Rb	Y
Unit Symbol	ppm	%	%	%	%	%	ppm	ppm	ppm	ppm	%	ppm	ppm	ppm	ppm	ppm	ppm	ppm	ppm	ppm	ppm	ppm	ppm	ppm	ppm	ppm	ppm
Detection Limit	0.5	0.01	0.01	0.01	0.01	0.01	0.1	1	1	1	0.01	0.1	0.5	0.1	0.1	0.1	0.05	0.05	0.1	0.05	0.02	0.1	0.2	0.1	0.1	0.2	0.1
04502	3	< 0.01	0.03	0.13	0.08	0.13	> 1000	7	34	433	0.37	< 0.1	11.6	< 0.1	< 0.1	< 0.1	39.2	0.11	8.6	< 0.05	0.07	5.1	145000	143	20000	3.4	0.2
04884	14	< 0.01	0.14	0.64	0.42	2.72	330	27	23	256	0.37	0.4	7.3	0.3	< 0.1	0.1	83.8	0.47	10.7	< 0.05	0.09	4.3	9460	29	9070	16.8	2.6
04618	< 0.5	< 0.01	0.01	0.01	< 0.01	0.05	34.3	1	31	177	3.1	< 0.1	1.5	< 0.1	< 0.1	< 0.1	914	< 0.05	0.4	< 0.05	0.04	31	1070	52.7	268	0.3	< 0.1
04196	7.8	< 0.01	6.22	< 0.01	0.03	12.1	4.6	11	21	1340	0.27	< 0.1	1.9	< 0.1	< 0.1	< 0.1	8.83	0.14	0.8	< 0.05	0.08	3.6	173	0.8	178	1.9	0.3
04236	38.3	< 0.01	6.37	0.14	0.16	10.1	2.9	8	18	393	0.29	< 0.1	2	< 0.1	< 0.1	< 0.1	5.09	0.79	0.6	< 0.05	< 0.02	0.4	137	2.2	64.1	10.8	0.8
04898	0.8	< 0.01	< 0.01	< 0.01	< 0.01	0.02	425	1	6	135	3.02	< 0.1	26.4	< 0.1	< 0.1	< 0.1	20.8	< 0.05	28.5	< 0.05	< 0.02	164	24700	1000	47800	< 0.2	< 0.1
04807	2.8	< 0.01	0.04	0.22	0.03	0.07	> 1000	8	12	471	0.4	0.2	43.1	< 0.1	< 0.1	< 0.1	239	0.11	262	< 0.05	0.09	108	101000	441	8500	1.7	0.5
05254	87.7	0.03	4.03	5.61	1.95	5.6	327	112	67	668	1.82	3	7.6	1.1	1.6	0.3	93.1	3.47	15	0.13	0.03	6.7	3850	121	686	106	7.3
08107	< 0.5	0.01	0.04	0.03	< 0.01	0.03	> 1000	1	15	608	1.43	< 0.1	11.3	< 0.1	< 0.1	< 0.1	55.4	< 0.05	30.3	< 0.05	< 0.02	27.1	289000	275	4050	0.4	< 0.1
08298	3.3	< 0.01	0.02	0.07	< 0.01	0.1	> 1000	6	23	744	8.34	< 0.1	12.6	< 0.1	< 0.1	< 0.1	16.4	< 0.05	15.3	< 0.05	0.05	8.9	350000	168	3250	2	0.3
08299	0.6	< 0.01	< 0.01	< 0.01	< 0.01	0.12	558	< 1	26	157	0.87	< 0.1	1.5	< 0.1	< 0.1	< 0.1	22.1	< 0.05	2.5	< 0.05	0.03	175	63700	1000	36400	< 0.2	< 0.1

Appendix 6-2 continues.

	Sr	Zr	Nb	Mo	In	Sn	Sb	Te	Ba	La	Ce	Pr	Nd	Sm	Gd	Tb	Dy	Cu	Ge	Tm	Yb	Lu	Ta	W	Re	Tl	Pb	Sc	Th	U	Ti	P	S
	ppm	ppm	ppm	ppm	ppm	ppm	ppm	ppm	ppm	ppm	ppm	ppm	ppm	ppm	ppm	ppm	ppm	ppm	ppm	ppm	ppm	ppm	ppm	ppm	ppm	ppm	ppm	ppm	ppm	ppm	%	%	%
	0.2	1	0.1	0.05	0.1	1	0.1	0.1	1	0.1	0.1	0.1	0.1	0.1	0.1	0.1	0.1	0.2	0.1	0.1	0.1	0.1	0.1	0.1	0.001	0.05	0.5	1	0.1	0.1	0.0005	0.001	0.01
04502	1.3	2	0.1	1950	0.7	< 1	77.8	0.1	8	0.2	0.4	< 0.1	0.1	< 0.1	< 0.1	< 0.1	< 0.1	50200	1.6	< 0.1	< 0.1	< 0.1	< 0.1	0.5	1.3	1.61	547000	< 1	0.3	1.9	0.0104	0.022	19.9
04884	23.4	14	1	1210	< 0.1	< 1	700	< 0.1	26	1.5	3.1	0.4	1.7	0.5	0.5	< 0.1	0.5	26100	12.5	< 0.1	0.3	< 0.1	< 0.1	0.8	1.68	1.77	549000	1	1.4	5.8	0.0524	0.063	11
04618	0.2	3	0.2	245	0.1	1	11.4	< 0.1	2	0.1	0.3	< 0.1	< 0.1	< 0.1	< 0.1	< 0.1	< 0.1	627000	1.3	< 0.1	< 0.1	< 0.1	< 0.1	1.8	0.447	0.16	96600	< 1	0.1	< 0.1	0.0034	0.17	21.6
04196	57.9	2	0.2	21.6	< 0.1	< 1	19.4	< 0.1	11	0.5	1	0.1	0.3	< 0.1	< 0.1	< 0.1	< 0.1	497	< 0.1	< 0.1	< 0.1	< 0.1	< 0.1	0.8	0.035	0.07	3380	< 1	0.1	2.6	0.0036	0.048	0.15
04236	87.5	4	0.3	6.72	< 0.1	1	5.5	< 0.1	16	0.7	1.5	0.2	0.6	0.1	0.1	< 0.1	0.1	3520	0.1	< 0.1	< 0.1	< 0.1	< 0.1	0.6	0.008	0.24	1500	< 1	0.2	1	0.0081	0.008	0.3
04898	1.5	< 1	< 0.1	483	2.3	49	478	2.7	3	0.1	0.2	< 0.1	< 0.1	< 0.1	< 0.1	< 0.1	< 0.1	209000	> 500	< 0.1	< 0.1	< 0.1	< 0.1	1390	0.04	0.18	497000	< 1	< 0.1	0.1	0.0007	0.06	21.4
04807	1	5	0.3	20000	5.2	9	3000	2.3	4	0.2	0.6	< 0.1	0.4	< 0.1	0.1	< 0.1	0.1	49200	81.7	< 0.1	< 0.1	< 0.1	< 0.1	57.3	> 100	7.4	502000	< 1	0.6	0.7	0.0206	0.04	19.2
05254	36.7	108	9.2	45.4	1.4	3	13.2	0.1	67	2.3	6.9	1	4.5	1.2	1.3	0.2	1.4	45800	148	0.2	1.3	0.2	0.6	6.7	0.299	3.29	3780	10	8.3	5.6	0.347	0.132	3.67
08107	1.4	< 1	< 0.1	198	1.5	3	151	0.7	2	0.1	0.2	< 0.1	< 0.1	< 0.1	< 0.1	< 0.1	< 0.1	28400	397	< 0.1	< 0.1	< 0.1	< 0.1	28.9	2.01	0.54	413000	< 1	< 0.1	21.6	0.0026	0.01	23.3
08298	1.3	2	0.2	182	< 0.1	< 1	157	< 0.1	8	0.9	1.7	0.2	0.6	0.1	< 0.1	< 0.1	< 0.1	23500	> 500	< 0.1	< 0.1	< 0.1	< 0.1	35.6	1.81	0.63	72200	< 1	0.2	0.4	0.0052	0.018	32.2
08299	1.9	< 1	< 0.1	530	3.3	28	450	1.4	3	0.2	0.4	< 0.1	< 0.1	< 0.1	< 0.1	< 0.1	< 0.1	202000	> 500	< 0.1	< 0.1	< 0.1	< 0.1	430	0.113	0.24	548000	< 1	< 0.1	0.1	0.0053	0.057	20.3

Appendix 6-3 Full EPMA results of the sulfide mineralisation of Tsumeb deposit.

SAMPLE	Mineral	S WT%	Fe WT%	Co WT%	Ni WT%	Cu WT%	Zn WT%	Ga WT%	Ge WT%	As WT%	Ag WT%	Cd WT%	In WT%	Sb WT%	Pb WT%	TOTAL
MS496_04495_BSE1_1	galena	14.997	0.000	0.000	0.000	0.000	0.000	0.010	0.000	0.000	0.034	0.040	0.000	0.000	85.319	100.399
MS496_04495_BSE1_2	tennantite	27.835	0.064	0.004	0.000	43.106	8.063	0.045	0.000	18.227	0.023	1.014	0.000	1.311	0.093	99.784
MS496_04495_BSE1_3	reniérite	32.503	13.631	0.000	0.000	43.135	1.766	0.252	8.237	2.259	0.000	0.076	0.000	0.046	0.049	101.954
MS496_04495_BSE2_2	reniérite	32.545	13.563	0.000	0.000	43.318	1.530	0.288	7.920	2.519	0.016	0.072	0.000	0.043	0.000	101.813
MS496_04495_BSE2_3	galena	14.473	0.000	0.000	0.000	0.022	0.000	0.000	0.000	0.000	0.000	0.000	0.000	0.000	84.836	99.330
MS496_04495_BSE2_4	reniérite	32.371	13.545	0.000	0.000	43.167	1.613	0.279	8.155	2.361	0.017	0.058	0.000	0.034	0.017	101.618
MS496_04495_BSE2_5	reniérite	32.546	13.501	0.000	0.000	43.382	1.586	0.279	8.051	2.458	0.000	0.063	0.000	0.043	0.000	101.910
MS496_04495_BSE2_6	galena	14.685	0.000	0.000	0.000	0.000	0.000	0.008	0.000	0.000	0.000	0.000	0.000	0.000	85.402	100.095
MS496_04495_BSE3_1	tennantite	25.665	0.066	0.004	0.000	43.185	9.273	0.048	0.000	16.539	0.000	0.722	0.000	1.147	0.000	96.649
MS496_04495_BSE3_2	tennantite	27.271	0.106	0.005	0.000	42.892	8.663	0.051	0.015	18.267	0.000	0.669	0.000	1.250	0.000	99.190
MS496_04495_BSE3_3	reniérite	32.431	13.457	0.000	0.000	43.364	1.816	0.000	8.458	2.212	0.000	0.069	0.000	0.039	0.020	101.867
MS496_04495_BSE3_4	reniérite	32.531	13.521	0.000	0.000	43.198	1.764	0.294	8.481	2.180	0.024	0.070	0.000	0.029	0.054	102.146
MS496_04495_BSE3_5	galena	14.539	0.000	0.000	0.000	0.018	0.000	0.000	0.000	0.000	0.000	0.000	0.000	0.000	85.023	99.579
MS496_04495_BSE3_6	galena	14.592	0.000	0.000	0.000	0.017	0.000	0.014	0.000	0.000	0.000	0.000	0.000	0.000	85.968	100.592
MS496_04546_BSE1a_001	galena	14.400	0.000	0.000	0.000	0.000	0.000	0.011	0.000	0.000	0.000	0.000	0.000	0.000	86.474	100.885
MS496_04546_BSE1a_002	galena	14.445	0.000	0.000	0.000	0.015	0.000	0.016	0.000	0.000	0.000	0.000	0.000	0.000	87.017	101.494
MS496_04546_BSE1a_003	galena	14.367	0.000	0.000	0.000	0.000	0.000	0.012	0.000	0.000	0.000	0.000	0.000	0.000	86.481	100.859
MS496_04546_BSE1a_004	galena	14.415	0.000	0.000	0.000	0.014	0.000	0.016	0.000	0.000	0.000	0.000	0.000	0.000	86.675	101.120
MS496_04546_BSE1b_005	tennantite	27.195	0.053	0.005	0.000	41.013	8.945	0.008	0.000	19.275	0.000	0.729	0.000	0.313	0.000	97.536
MS496_04546_BSE1b_10	sphalerite	32.350	0.000	0.000	0.000	0.039	64.718	0.039	0.000	0.024	0.000	2.597	0.010	0.000	0.043	99.820
MS496_04546_BSE1b_11	sphalerite	32.437	0.000	0.000	0.000	0.033	64.555	0.038	0.000	0.030	0.000	2.633	0.010	0.000	0.023	99.759
MS496_04546_BSE1b_6	tennantite	27.943	0.046	0.000	0.000	40.426	8.520	0.000	0.000	20.724	0.000	0.814	0.000	0.278	0.027	98.779
MS496_04546_BSE1b_8	sphalerite	32.586	0.000	0.000	0.000	0.052	64.702	0.038	0.000	0.026	0.000	2.630	0.010	0.000	0.024	100.068
MS496_04546_BSE1b_9	sphalerite	32.257	0.000	0.000	0.000	0.043	64.417	0.038	0.000	0.026	0.000	2.631	0.011	0.000	0.054	99.477
MS496_04546_BSE1c_12	tennantite	27.539	0.050	0.000	0.008	41.163	8.656	0.006	0.000	18.643	0.000	0.692	0.000	0.553	0.000	97.309
MS496_04546_BSE1c_13	sphalerite	32.368	0.000	0.000	0.000	1.516	63.397	0.032	0.000	0.035	0.000	2.581	0.010	0.000	0.000	99.940
MS496_04546_BSE1c_14	tennantite	27.920	0.059	0.004	0.000	40.149	8.571	0.000	0.000	19.393	0.000	0.788	0.000	0.657	0.000	97.541
MS496_04546_BSE1c_15	enargite	32.124	0.000	0.000	0.000	49.584	0.000	0.000	0.000	17.999	0.000	0.000	0.000	0.104	0.000	99.811

Appendix 6-3 continues……

MS496_04546_BSE2a_1	galena	14.453	0.000	0.000	0.000	0.015	0.000	0.013	0.000	0.000	0.000	0.000	0.000	0.000	86.521	101.003
MS496_04546_BSE2a_2	galena	14.437	0.000	0.000	0.000	0.026	0.000	0.013	0.000	0.000	0.000	0.000	0.000	0.000	86.571	101.047
MS496_04546_BSE2a_3	galena	14.460	0.000	0.000	0.000	0.000	0.000	0.011	0.000	0.000	0.000	0.000	0.000	0.000	87.253	101.724
MS496_04546_BSE2a_4	galena	14.501	0.000	0.000	0.000	0.026	0.000	0.014	0.000	0.000	0.000	0.000	0.000	0.000	86.619	101.161
MS496_04546_BSE2a_5	enargite	32.481	0.000	0.000	0.000	49.301	0.350	0.000	0.705	17.563	0.000	0.126	0.000	0.000	0.000	100.527
MS496_04546_BSE2a_6	tennantite	27.947	0.058	0.005	0.000	41.312	8.472	0.000	0.000	19.682	0.000	0.796	0.000	0.357	0.000	98.628
MS496_04546_BSE2a_7	enargite	32.328	0.000	0.000	0.000	49.731	0.181	0.000	0.421	17.755	0.000	0.095	0.000	0.024	0.000	100.535
MS496_04546_BSE2b_10	tennantite	26.400	0.065	0.000	0.000	43.126	9.014	0.000	0.000	17.118	0.000	0.666	0.000	0.074	0.000	96.465
MS496_04546_BSE2b_11	enargite	32.179	0.000	0.000	0.000	49.727	0.000	0.000	0.000	17.975	0.000	0.000	0.000	0.118	0.000	99.998
MS496_04546_BSE2b_12	sphalerite	32.484	0.000	0.000	0.000	0.086	64.663	0.000	0.000	0.030	0.000	2.736	0.011	0.000	0.000	100.010
MS496_04546_BSE2b_13	enargite	32.287	0.000	0.000	0.000	49.568	0.062	0.000	0.174	17.918	0.000	0.042	0.000	0.044	0.000	100.095
MS496_04546_BSE2b_8	tennantite	26.537	0.057	0.007	0.000	41.646	9.089	0.000	0.000	18.397	0.000	0.691	0.000	0.091	0.000	96.514
MS496_04546_BSE2b_9	tennantite	32.221	0.000	0.000	0.000	49.638	0.000	0.000	0.000	18.025	0.000	0.000	0.000	0.135	0.000	100.019
MS496_04546_BSE3a_1	galena	14.466	0.000	0.000	0.000	0.000	0.000	0.015	0.000	0.000	0.000	0.000	0.000	0.000	87.014	101.495
MS496_04546_BSE3a_2	sphalerite	32.338	0.000	0.000	0.000	0.030	64.253	0.036	0.000	0.026	0.000	2.788	0.013	0.000	0.036	99.520
MS496_04546_BSE3a_3	sphalerite	32.366	0.000	0.000	0.000	0.082	64.475	0.037	0.000	0.033	0.000	2.812	0.009	0.000	0.032	99.847
MS496_04546_BSE3a_4	tennantite	28.037	0.035	0.000	0.000	40.673	8.560	0.000	0.000	20.212	0.025	0.939	0.000	0.643	0.000	99.124
MS496_04546_BSE3a_5	galena	14.411	0.000	0.000	0.000	0.020	0.029	0.000	0.000	0.000	0.000	0.000	0.000	0.000	85.924	100.383
MS496_04546_BSE3b_10	sphalerite	32.436	0.000	0.000	0.000	0.028	64.104	0.040	0.000	0.028	0.000	2.790	0.012	0.000	0.046	99.483
MS496_04546_BSE3b_11	galena	14.518	0.000	0.000	0.000	0.041	0.000	0.011	0.000	0.000	0.000	0.000	0.000	0.000	86.471	101.041
MS496_04546_BSE3b_6	sphalerite	32.399	0.000	0.000	0.000	0.070	64.421	0.034	0.000	0.024	0.000	2.789	0.013	0.000	0.024	99.773
MS496_04546_BSE3b_7	tennantite	28.093	0.030	0.000	0.000	41.150	8.998	0.006	0.000	19.723	0.023	0.870	0.000	0.378	0.033	99.304
MS496_04546_BSE3b_8	tennantite	27.655	0.023	0.000	0.000	41.354	8.589	0.000	0.000	19.351	0.000	0.852	0.000	1.206	0.030	99.058
MS496_04546_BSE3b_9	enargite	32.247	0.000	0.000	0.000	49.691	0.055	0.000	0.161	17.948	0.000	0.044	0.000	0.060	0.019	100.224
MS496_04612_BSE1a_10	galena	14.427	0.000	0.000	0.000	0.000	0.000	0.000	0.000	0.000	0.000	0.000	0.000	0.000	85.892	100.319
MS496_04612_BSE1a_7	galena	14.524	0.000	0.000	0.000	0.000	0.000	0.015	0.000	0.000	0.000	0.000	0.000	0.000	86.237	100.775
MS496_04612_BSE1a_8	galena	14.464	0.000	0.000	0.000	0.015	0.000	0.012	0.000	0.000	0.000	0.000	0.000	0.000	86.544	101.035
MS496_04612_BSE1a_9	galena	14.507	0.000	0.000	0.000	0.000	0.000	0.018	0.000	0.000	0.000	0.000	0.000	0.000	86.557	101.082
MS496_04612_BSE1b_1	tennantite	27.488	1.438	0.007	0.008	43.599	7.418	0.000	0.000	18.660	0.042	0.270	0.000	0.654	0.000	99.583
MS496_04612_BSE1b_2	tennantite	27.688	1.418	0.000	0.000	43.542	7.341	0.000	0.080	19.269	0.067	0.305	0.000	0.630	0.000	100.340
MS496_04612_BSE1b_3	tennantite	27.161	1.454	0.007	0.011	43.637	7.527	0.006	0.055	18.509	0.038	0.270	0.000	0.647	0.000	99.321
MS496_04612_BSE1b_4	sphalerite	32.736	0.153	0.000	0.000	0.301	65.138	0.014	0.080	0.067	0.000	1.426	0.000	0.013	0.000	99.929
MS496_04612_BSE1b_5	sphalerite	32.670	0.110	0.000	0.000	0.021	65.526	0.000	0.000	0.025	0.000	1.483	0.006	0.000	0.000	99.841
MS496_04612_BSE1b_6	sphalerite	32.852	0.129	0.005	0.000	0.024	65.521	0.027	0.000	0.026	0.000	1.463	0.004	0.000	0.000	100.050
MS496_04612_BSE2a_1	galena	14.643	0.000	0.000	0.000	0.000	0.048	0.023	0.000	0.000	0.000	0.000	0.000	0.000	86.474	101.188
MS496_04612_BSE2a_2	galena	14.464	0.000	0.000	0.000	0.000	0.000	0.012	0.000	0.000	0.000	0.000	0.000	0.000	86.303	100.779
MS496_04612_BSE2a_3	sphalerite	32.721	0.108	0.000	0.000	0.022	65.467	0.016	0.000	0.026	0.017	1.480	0.007	0.000	0.000	99.864
MS496_04612_BSE2a_4	tennantite	27.995	1.554	0.000	0.007	43.782	7.150	0.000	0.035	18.781	0.075	0.306	0.000	0.692	0.000	100.375
MS496_04612_BSE2a_5	sphalerite	32.855	0.150	0.000	0.000	0.017	65.631	0.016	0.000	0.030	0.000	1.474	0.000	0.000	0.000	100.173
MS496_04612_BSE2a_6	galena	14.524	0.000	0.000	0.000	0.000	0.000	0.010	0.000	0.000	0.000	0.000	0.000	0.000	86.647	101.181
MS496_04612_BSE2b_10	sphalerite	33.046	0.113	0.000	0.000	0.127	65.382	0.019	0.000	0.023	0.017	1.443	0.006	0.000	0.000	100.175
MS496_04612_BSE2b_11	tennantite	27.660	1.571	0.004	0.000	43.490	7.435	0.000	0.000	19.102	0.061	0.267	0.000	0.694	0.000	100.283
MS496_04612_BSE2b_12	galena	14.470	0.000	0.000	0.000	0.000	0.000	0.012	0.000	0.000	0.000	0.000	0.000	0.000	86.869	101.351
MS496_04612_BSE2b_13	tennantite	27.561	1.573	0.000	0.008	43.237	8.181	0.000	0.000	18.843	0.044	0.276	0.000	0.693	0.000	100.415

MS496_04612_BSE2b_7	sphalerite	32.721	0.128	0.000	0.000	0.012	65.535	0.018	0.000	0.031	0.000	1.474	0.006	0.000	0.000	99.926
MS496_04612_BSE2b_8	galena	14.452	0.000	0.000	0.000	0.016	0.000	0.013	0.000	0.000	0.000	0.000	0.000	0.000	86.779	101.260
MS496_04612_BSE2b_9	tennantite	27.280	1.833	0.005	0.008	43.770	7.645	0.006	0.012	16.847	0.000	0.248	0.000	0.622	0.000	98.277
MS496_04612_BSE3a_1	galena	14.465	0.000	0.000	0.000	0.000	0.026	0.012	0.000	0.000	0.000	0.000	0.000	0.000	86.313	100.815
MS496_04612_BSE3a_2	galena	14.471	0.000	0.000	0.000	0.172	0.188	0.017	0.000	0.000	0.000	0.000	0.000	0.000	86.541	101.390
MS496_04612_BSE3a_3	galena	14.542	0.000	0.000	0.000	0.000	0.000	0.014	0.000	0.000	0.000	0.000	0.000	0.000	86.569	101.125
MS496_04612_BSE3a_4	galena	14.523	0.000	0.000	0.000	0.056	0.306	0.015	0.000	0.000	0.000	0.000	0.000	0.000	86.305	101.204
MS496_04612_BSE3b_10	sphalerite	32.729	0.114	0.000	0.000	0.019	65.256	0.022	0.000	0.023	0.000	1.509	0.000	0.000	0.018	99.689
MS496_04612_BSE3b_5	tennantite	27.781	2.180	0.000	0.000	43.064	7.131	0.000	0.000	18.949	0.050	0.234	0.000	0.709	0.000	100.097
MS496_04612_BSE3b_6	tennantite	28.137	1.398	0.000	0.007	43.462	7.189	0.000	0.000	19.274	0.100	0.365	0.000	0.760	0.000	100.691
MS496_04612_BSE3b_7	tennantite	27.684	1.449	0.004	0.008	43.417	7.327	0.000	0.000	19.283	0.062	0.292	0.000	0.696	0.000	100.221
MS496_04612_BSE3b_8	sphalerite	32.760	0.120	0.000	0.000	0.024	65.171	0.024	0.000	0.039	0.000	1.501	0.005	0.000	0.000	99.642
MS496_04612_BSE3b_9	sphalerite	32.726	0.117	0.000	0.000	0.020	65.395	0.024	0.000	0.026	0.000	1.491	0.005	0.000	0.000	99.804
MS496_04618_area1_1	Cu-Fe-sulfide	23.982	5.570	0.000	0.000	72.117	0.000	0.000	0.000	0.014	0.688	0.000	0.000	0.000	0.000	102.371
MS496_04618_area1_2	galena	14.456	0.000	0.000	0.000	0.089	0.000	0.010	0.000	0.000	0.044	0.000	0.000	0.000	85.987	100.586
MS496_04618_area1_3	Cu-sulfide	22.473	1.021	0.004	0.000	76.714	0.000	0.000	0.000	0.030	0.156	0.000	0.004	0.000	0.000	100.402
MS496_04618_area1_4	Cu-sulfide	21.543	0.000	0.000	0.000	76.809	0.000	0.000	0.000	0.074	0.363	0.000	0.000	0.000	0.000	98.788
MS496_04618_area10_1	reniérite	32.125	13.870	0.000	0.000	44.887	0.285	0.087	5.743	4.036	0.097	0.031	0.000	0.173	0.000	101.333
MS496_04618_area10_2	Cu-Fe-sulfide	24.345	5.681	0.004	0.000	71.567	0.000	0.000	0.000	0.026	0.737	0.027	0.006	0.000	0.000	102.394
MS496_04618_area10_3	Cu-sulfide	22.423	1.007	0.005	0.000	76.605	0.000	0.000	0.000	0.028	0.178	0.000	0.007	0.000	0.000	100.253
MS496_04618_area11_1	Cu-sulfide	22.090	1.035	0.004	0.000	76.470	0.000	0.000	0.000	0.036	0.176	0.000	0.000	0.000	0.000	99.811
MS496_04618_area11_2	chalcopyrite	34.444	29.186	0.000	0.000	36.045	0.000	0.045	0.000	0.000	0.072	0.022	0.000	0.000	0.000	99.814
MS496_04618_area11_3	galena	14.522	0.039	0.000	0.000	0.037	0.000	0.013	0.000	0.000	0.000	0.000	0.000	0.000	85.960	100.570
MS496_04618_area11_4	Cu-Fe-sulfide	24.090	5.483	0.000	0.000	71.647	0.000	0.000	0.000	0.033	1.006	0.047	0.013	0.015	0.000	102.334
MS496_04618_area11_6	Cu-sulfide	22.152	0.013	0.000	0.010	77.742	0.000	0.000	0.000	0.027	0.265	0.026	0.004	0.000	0.000	100.240
MS496_04618_area11_7	pyrite	53.382	46.108	0.006	0.000	0.211	0.000	0.007	0.011	0.000	0.015	0.026	0.000	0.000	0.014	99.779
MS496_04618_area11_8	galena	14.373	0.000	0.000	0.000	0.217	0.000	0.012	0.000	0.000	0.028	0.000	0.000	0.000	86.124	100.755
MS496_04618_area12_1	chalcopyrite	34.649	29.055	0.000	0.000	36.491	0.000	0.069	0.000	0.000	0.057	0.000	0.000	0.000	0.000	100.321
MS496_04618_area12_2	Cu-Fe-sulfide	24.054	5.491	0.000	0.000	71.513	0.000	0.000	0.000	0.031	1.035	0.057	0.014	0.016	0.000	102.211
MS496_04618_area13_1	pyrite	53.404	46.272	0.000	0.000	0.423	0.000	0.008	0.000	0.000	0.018	0.026	0.000	0.000	0.000	100.152
MS496_04618_area13_2	galena	14.456	0.041	0.000	0.000	0.349	0.000	0.016	0.000	0.000	0.116	0.000	0.000	0.000	85.969	100.946
MS496_04618_area13_3	reniérite	32.115	13.863	0.000	0.000	44.666	0.303	0.083	5.776	3.943	0.124	0.021	0.000	0.183	0.000	101.078
MS496_04618_area13_4	Cu-Fe-sulfide	24.032	5.810	0.007	0.008	71.182	0.000	0.000	0.000	0.000	0.559	0.000	0.000	0.000	0.000	101.597
MS496_04618_area13_5	chalcopyrite	34.549	29.182	0.000	0.000	35.976	0.000	0.006	0.000	0.000	0.044	0.018	0.000	0.000	0.000	99.775
MS496_04618_area15_1	Cu-Fe-sulfide	24.160	5.409	0.000	0.000	71.844	0.000	0.000	0.000	0.038	0.882	0.063	0.016	0.029	0.000	102.440
MS496_04618_area15_2	chalcopyrite	34.557	29.322	0.000	0.000	35.987	0.000	0.000	0.000	0.000	0.089	0.019	0.000	0.000	0.000	99.975
MS496_04618_area15_3	Cu-sulfide	22.446	1.168	0.000	0.009	76.329	0.000	0.000	0.000	0.034	0.175	0.021	0.007	0.000	0.020	100.209
MS496_04618_area15_4	Cu-Fe-sulfide	24.530	5.685	0.000	0.000	71.464	0.000	0.000	0.000	0.034	0.667	0.051	0.015	0.028	0.000	102.474
MS496_04618_area15_5	Cu-sulfide	22.470	1.006	0.004	0.000	76.586	0.000	0.000	0.000	0.025	0.166	0.019	0.006	0.000	0.000	100.282
MS496_04618_area16_1	Cu-Fe-sulfide	22.096	0.023	0.000	0.000	77.824	0.000	0.000	0.000	0.027	0.219	0.032	0.005	0.011	0.000	100.238
MS496_04618_area16_2	Cu-sulfide	24.442	5.550	0.000	0.000	71.551	0.000	0.000	0.000	0.037	0.649	0.068	0.015	0.025	0.000	102.337
MS496_04618_area16_3	chalcopyrite	34.432	28.598	0.000	0.000	36.702	0.000	0.008	0.000	0.000	0.069	0.024	0.000	0.000	0.018	99.851
MS496_04618_area16_4	Cu-sulfide	22.483	1.023	0.000	0.007	76.415	0.000	0.000	0.000	0.034	0.186	0.031	0.007	0.000	0.000	100.185
MS496_04618_area17_1	Cu-Fe-sulfide	24.804	5.819	0.000	0.000	71.554	0.000	0.000	0.000	0.029	0.556	0.054	0.015	0.025	0.000	102.855
MS496_04618_area17_2	Cu-sulfide	22.615	1.076	0.000	0.000	76.466	0.000	0.000	0.000	0.027	0.186	0.029	0.005	0.012	0.000	100.415
MS496_04618_area17_3	Cu-sulfide	21.991	0.000	0.000	0.000	77.742	0.000	0.000	0.000	0.039	0.215	0.032	0.011	0.013	0.000	100.045

MS496_04618_area17_3	Cu-sulfide	22.170	0.000	0.003	0.010	77.676	0.000	0.000	0.000	0.037	0.217	0.039	0.010	0.012	0.000	100.176
MS496_04618_area2_1	Cu-Fe-sulfide	24.387	5.737	0.000	0.000	71.626	0.000	0.000	0.000	0.031	0.651	0.039	0.016	0.011	0.000	102.499
MS496_04618_area2_2	chalcopyrite	34.241	29.012	0.000	0.000	36.180	0.000	0.046	0.000	0.000	0.060	0.000	0.000	0.000	0.000	99.539
MS496_04618_area2_3	Cu-Fe-sulfide	24.323	5.817	0.000	0.000	71.196	0.000	0.000	0.000	0.040	0.758	0.042	0.013	0.000	0.000	102.188
MS496_04618_area2_4	Cu-sulfide	22.340	1.017	0.000	0.009	76.432	0.000	0.000	0.000	0.029	0.175	0.000	0.000	0.000	0.000	100.003
MS496_04618_area2_5	Cu-sulfide	21.861	0.000	0.000	0.000	77.875	0.000	0.000	0.000	0.024	0.161	0.000	0.000	0.000	0.000	99.921
MS496_04618_area2_6	Cu-sulfide	22.339	0.983	0.000	0.000	76.333	0.000	0.000	0.000	0.031	0.148	0.000	0.000	0.000	0.000	99.835
MS496_04618_area3_1	pyrite	52.972	46.242	0.000	0.000	0.221	0.000	0.010	0.009	0.000	0.000	0.000	0.000	0.000	0.000	99.453
MS496_04618_area3_2	Cu-Fe-sulfide	23.755	5.328	0.000	0.000	72.029	0.000	0.000	0.000	0.037	0.731	0.030	0.012	0.000	0.000	101.921
MS496_04618_area3_3	Cu-sulfide	22.298	0.995	0.004	0.000	76.424	0.000	0.000	0.000	0.037	0.168	0.000	0.004	0.000	0.000	99.932
MS496_04618_area3_4	Cu-sulfide	22.368	0.987	0.000	0.000	76.680	0.000	0.000	0.000	0.031	0.159	0.000	0.000	0.000	0.000	100.225
MS496_04618_area3_5	Cu-Fe-sulfide	24.290	5.822	0.000	0.000	71.476	0.000	0.000	0.000	0.037	0.540	0.022	0.012	0.000	0.000	102.199
MS496_04618_area3_6	pyrite	53.243	46.459	0.000	0.000	0.000	0.000	0.010	0.009	0.000	0.000	0.000	0.000	0.000	0.017	99.737
MS496_04618_area3_7	pyrite	53.083	46.276	0.000	0.000	0.000	0.000	0.008	0.009	0.000	0.000	0.019	0.000	0.000	0.000	99.395
MS496_04618_area4_1	pyrite	53.157	46.558	0.000	0.000	0.000	0.000	0.009	0.000	0.000	0.000	0.024	0.000	0.000	0.000	99.747
MS496_04618_area4_2	Cu-sulfide	22.388	1.000	0.000	0.000	76.526	0.000	0.000	0.000	0.032	0.208	0.000	0.005	0.000	0.032	100.190
MS496_04618_area4_3	Cu-sulfide	21.605	0.016	0.000	0.000	77.587	0.000	0.000	0.000	0.042	0.207	0.000	0.000	0.000	0.029	99.486
MS496_04618_area4_4	Cu-sulfide	22.421	1.014	0.004	0.009	76.659	0.000	0.000	0.000	0.043	0.210	0.000	0.008	0.000	0.024	100.391
MS496_04618_area4_5	Cu-sulfide	22.221	0.017	0.005	0.000	77.065	0.000	0.000	0.000	0.049	0.390	0.034	0.016	0.000	0.098	99.895
MS496_04618_area4_6	galena	14.550	0.028	0.000	0.000	0.171	0.000	0.023	0.000	0.000	0.000	0.000	0.000	0.000	86.124	100.896
MS496_04618_area4_7	galena	14.485	0.000	0.000	0.000	0.074	0.000	0.015	0.000	0.000	0.000	0.000	0.000	0.000	86.010	100.583
MS496_04618_area4_8	pyrite	53.111	46.404	0.000	0.000	0.000	0.000	0.011	0.000	0.000	0.000	0.025	0.000	0.000	0.016	99.566
MS496_04618_area5_1	Cu-sulfide	22.457	1.027	0.004	0.000	76.582	0.000	0.000	0.000	0.038	0.218	0.000	0.006	0.000	0.000	100.331
MS496_04618_area5_2	pyrite	53.218	46.534	0.000	0.000	0.096	0.000	0.000	0.010	0.000	0.000	0.017	0.000	0.000	0.000	99.876
MS496_04618_area5_3	pyrite	53.062	46.249	0.000	0.000	0.320	0.000	0.012	0.000	0.000	0.000	0.000	0.000	0.000	0.015	99.657
MS496_04618_area5_4	pyrite	53.171	46.659	0.000	0.000	0.000	0.000	0.007	0.008	0.000	0.000	0.017	0.000	0.000	0.018	99.880
MS496_04618_area5_5	pyrite	53.222	46.496	0.000	0.000	0.000	0.000	0.011	0.000	0.000	0.000	0.000	0.000	0.000	0.020	99.748
MS496_04618_area6_1	Cu-sulfide	22.297	0.999	0.000	0.008	76.542	0.000	0.000	0.000	0.028	0.161	0.000	0.006	0.000	0.000	100.041
MS496_04618_area6_2	Cu-Fe-sulfide	23.844	5.808	0.000	0.000	71.419	0.000	0.007	0.000	0.026	0.515	0.000	0.000	0.000	0.000	101.619
MS496_04618_area6_3	chalcopyrite	34.454	29.198	0.000	0.000	36.205	0.000	0.013	0.000	0.000	0.034	0.000	0.000	0.000	0.000	99.904
MS496_04618_area8_1	Cu-Fe-sulfide	24.463	5.651	0.000	0.000	71.551	0.000	0.000	0.000	0.036	0.670	0.055	0.010	0.014	0.000	102.450
MS496_04618_area8_2	galena	14.504	0.000	0.000	0.000	0.116	0.000	0.012	0.000	0.000	0.085	0.000	0.000	0.000	85.923	100.640
MS496_04618_area8_3	Cu-sulfide	21.798	0.010	0.005	0.011	78.196	0.000	0.000	0.000	0.015	0.246	0.000	0.000	0.000	0.000	100.280
MS496_04618_area8_4	Cu-sulfide	22.432	1.074	0.000	0.000	76.416	0.000	0.000	0.000	0.038	0.205	0.000	0.000	0.000	0.000	100.165
MS496_05143_area1_1	tennantite	27.560	1.161	0.005	0.000	44.145	7.667	0.016	0.000	19.293	0.015	0.160	0.000	0.126	0.000	100.148
MS496_05143_area1_2	chalcopyrite	34.169	28.909	0.000	0.000	35.661	0.246	0.117	0.000	0.035	0.023	0.022	0.000	0.000	0.000	99.182
MS496_05143_area1_3	Cu-sulfide	24.139	0.030	0.000	0.000	75.313	0.029	0.000	0.000	0.070	0.255	0.024	0.000	0.000	0.105	99.965
MS496_05143_area1_4	galena	14.247	0.000	0.000	0.000	0.232	0.036	0.011	0.000	0.000	0.000	0.000	0.000	0.000	84.871	99.396
MS496_05143_area1_5	galena	14.308	0.000	0.000	0.000	0.311	0.046	0.000	0.000	0.000	0.000	0.000	0.000	0.000	84.405	99.070
MS496_05143_area2_1	tennantite	27.814	1.113	0.004	0.000	44.502	7.588	0.016	0.000	19.541	0.022	0.199	0.000	0.139	0.000	100.938
MS496_05143_area2_2	tennantite	27.360	1.114	0.006	0.000	44.464	7.798	0.020	0.010	17.975	0.021	0.165	0.000	0.122	0.000	99.056
MS496_05143_area2_3	sphalerite	32.500	0.077	0.000	0.000	2.190	64.473	0.118	0.000	0.055	0.016	0.688	0.000	0.000	0.000	100.117
MS496_05143_area2_4	Cu-sulfide	22.307	0.188	0.004	0.000	75.611	0.249	0.743	0.041	0.088	0.171	0.023	0.000	0.000	0.018	99.441
MS496_05143_area2_5	galena	14.330	0.000	0.000	0.000	0.872	0.163	0.000	0.000	0.000	0.000	0.000	0.000	0.000	84.669	100.034
MS496_05143_area4_1	tennantite	27.716	1.222	0.006	0.000	44.026	7.482	0.015	0.000	19.327	0.027	0.200	0.000	0.142	0.000	100.162
MS496_05143_area4_2	chalcopyrite	34.245	29.074	0.000	0.000	35.780	0.096	0.086	0.000	0.027	0.018	0.017	0.000	0.000	0.000	99.344

MS496_05143_area4_3	galena	14.355	0.000	0.000	0.000	0.571	0.104	0.012	0.000	0.000	0.032	0.032	0.000	0.000	85.247	100.354
MS496_05143_area4_4	Cu-sulfide	22.147	0.149	0.005	0.000	77.142	0.529	0.034	0.000	0.061	0.155	0.019	0.000	0.000	0.000	100.240
MS496_05143_area5_1	tennantite	27.590	1.174	0.006	0.000	44.397	7.609	0.017	0.000	18.936	0.000	0.181	0.000	0.112	0.000	100.022
MS496_05143_area5_2	chalcopyrite	34.261	28.280	0.000	0.000	35.612	0.333	0.263	0.010	0.037	0.014	0.000	0.000	0.000	0.021	98.832
MS496_05143_area5_3	Cu-sulfide	21.758	0.031	0.000	0.000	73.918	0.067	0.000	0.000	0.063	0.133	0.000	0.000	0.000	0.029	95.999
MS496_05143_area7_1	tennantite	27.817	1.145	0.007	0.000	44.345	7.529	0.015	0.000	19.264	0.032	0.183	0.000	0.128	0.000	100.467
MS496_05143_area7_2	chalcopyrite	34.249	28.293	0.000	0.000	35.833	0.322	0.211	0.000	0.030	0.000	0.000	0.000	0.000	0.015	98.953
MS496_05143_area7_3	Cu-sulfide	22.112	0.102	0.000	0.000	76.885	0.398	0.010	0.000	0.067	0.126	0.026	0.000	0.000	0.000	99.727
MS496_05143_area7_4	sphalerite	32.256	0.040	0.000	0.000	1.322	65.146	0.146	0.000	0.061	0.021	0.610	0.000	0.000	0.000	99.603
MS496_05143_area7_5	Cu-sulfide	21.985	0.043	0.000	0.000	76.936	0.246	0.187	0.000	0.062	0.172	0.000	0.000	0.000	0.000	99.631
MS496_05143_area7_6	tennantite	27.814	1.148	0.007	0.000	44.367	7.518	0.017	0.000	19.231	0.028	0.169	0.000	0.121	0.000	100.420
MS496_05143_area8_1	tennantite	27.764	1.296	0.000	0.000	44.098	7.341	0.011	0.000	19.708	0.071	0.214	0.000	0.111	0.000	100.616
MS496_05164_area1_1	tennantite	27.678	0.039	0.000	0.000	43.780	8.544	0.000	0.000	18.080	0.000	0.609	0.000	1.623	0.000	100.352
MS496_05164_area1_2	galena	14.394	0.000	0.000	0.000	0.000	0.000	0.007	0.000	0.000	0.000	0.000	0.000	0.000	84.897	99.299
MS496_05164_area10_1	Cu-Fe-sulfide	23.739	5.059	0.000	0.000	72.445	0.423	0.000	0.000	0.035	0.350	0.074	0.007	0.031	0.000	102.162
MS496_05164_area10_2	reniérite	32.095	13.638	0.000	0.000	44.312	0.857	0.039	6.332	3.524	0.079	0.032	0.000	0.068	0.017	100.993
MS496_05164_area10_3	chalcopyrite	34.383	29.134	0.000	0.000	35.345	1.175	0.000	0.000	0.000	0.037	0.018	0.000	0.000	0.015	100.107
MS496_05164_area10_4	Cu-sulfide	21.350	0.199	0.000	0.000	77.582	0.215	0.000	0.000	0.047	0.075	0.000	0.000	0.000	0.037	99.505
MS496_05164_area10_5	Cu-Fe-sulfide	23.494	4.929	0.000	0.000	72.697	0.141	0.000	0.000	0.036	0.592	0.055	0.006	0.027	0.000	101.977
MS496_05164_area10_6	galena	14.414	0.000	0.000	0.000	0.028	0.325	0.011	0.000	0.000	0.031	0.034	0.000	0.000	84.977	99.819
MS496_05164_area11_1	Cu-Fe-sulfide	23.648	5.030	0.000	0.000	72.489	0.000	0.000	0.000	0.032	0.266	0.039	0.000	0.022	0.032	101.558
MS496_05164_area11_2	reniérite	32.143	11.736	0.000	0.000	38.735	9.344	0.000	5.067	4.052	0.022	0.223	0.000	0.053	0.025	101.398
MS496_05164_area11_3	reniérite 2	31.547	4.308	0.000	0.000	49.785	0.929	0.000	9.777	4.681	0.031	0.044	0.000	0.048	0.031	101.180
MS496_05164_area11_4	Cu-Fe-sulfide	23.675	5.081	0.000	0.000	72.831	0.089	0.000	0.000	0.038	0.363	0.057	0.006	0.024	0.000	102.165
MS496_05164_area11_5	Cu-Fe-sulfide	23.344	4.797	0.000	0.000	73.031	0.089	0.000	0.000	0.043	0.472	0.044	0.005	0.028	0.000	101.852
MS496_05164_area11_6	Cu-sulfide	21.524	0.038	0.005	0.000	78.101	0.022	0.000	0.000	0.038	0.115	0.035	0.000	0.000	0.063	99.941
MS496_05164_area11_7	galena	14.581	0.000	0.000	0.000	0.033	0.000	0.009	0.000	0.000	0.029	0.043	0.000	0.025	84.652	99.372
MS496_05164_area12_1	enargite	32.169	0.000	0.000	0.000	49.598	0.501	0.000	0.778	17.035	0.027	0.126	0.000	0.069	0.000	100.304
MS496_05164_area12_2	enargite	32.015	0.011	0.000	0.000	49.668	0.340	0.000	0.624	17.068	0.033	0.098	0.000	0.052	0.000	99.910
MS496_05164_area12_3	galena	14.497	0.000	0.000	0.000	0.016	0.000	0.012	0.000	0.000	0.029	0.061	0.000	0.000	84.322	98.937
MS496_05164_area13_1	galena	14.487	0.000	0.000	0.000	0.033	0.000	0.000	0.000	0.000	0.000	0.000	0.000	0.000	84.511	99.030
MS496_05164_area13_2	Cu-Fe-sulfide	23.168	4.791	0.000	0.000	73.173	0.015	0.000	0.000	0.030	0.477	0.032	0.000	0.010	0.000	101.698
MS496_05164_area13_3	Cu-sulfide	21.396	0.021	0.000	0.000	78.029	0.020	0.000	0.000	0.048	0.115	0.051	0.004	0.027	0.030	99.740
MS496_05164_area13_4	Cu-Fe-sulfide	23.440	4.826	0.000	0.000	72.757	0.097	0.000	0.000	0.049	0.572	0.063	0.006	0.025	0.000	101.833
MS496_05164_area13_5	reniérite	32.067	13.606	0.005	0.000	44.506	0.958	0.040	5.824	3.809	0.070	0.025	0.000	0.062	0.000	100.971
MS496_05164_area13_6	reniérite 2	31.553	4.477	0.000	0.000	49.871	1.227	0.000	9.755	4.724	0.109	0.038	0.000	0.050	0.000	101.805
MS496_05164_area14_1	Cu-sulfide	22.297	0.011	0.000	0.000	77.680	0.140	0.000	0.000	0.035	0.160	0.063	0.004	0.030	0.025	100.446
MS496_05164_area14_2	Cu-Fe-sulfide	24.581	5.709	0.000	0.000	71.664	0.225	0.000	0.000	0.032	0.261	0.054	0.004	0.025	0.000	102.555
MS496_05164_area14_3	Cu-sulfide	22.317	0.015	0.003	0.000	77.804	0.047	0.000	0.000	0.026	0.138	0.049	0.000	0.022	0.043	100.464
MS496_05164_area14_4	Cu-sulfide	22.137	0.012	0.000	0.000	77.943	0.022	0.000	0.000	0.032	0.101	0.042	0.000	0.018	0.042	100.350
MS496_05164_area14_5	galena	14.475	0.000	0.000	0.000	0.032	0.000	0.019	0.000	0.000	0.032	0.000	0.000	0.000	84.641	99.199
MS496_05164_area15_1	galena	14.554	0.000	0.000	0.000	0.015	0.000	0.000	0.000	0.000	0.033	0.045	0.000	0.000	83.952	98.600
MS496_05164_area15_2	Cu-sulfide	21.688	0.115	0.000	0.000	77.496	0.120	0.000	0.000	0.041	0.085	0.000	0.000	0.000	0.056	99.601
MS496_05164_area15_3	Cu-Fe-sulfide	24.028	5.336	0.000	0.000	72.072	0.172	0.000	0.000	0.036	0.354	0.059	0.004	0.025	0.000	102.087
MS496_05164_area15_4	Cu-sulfide	22.365	0.017	0.000	0.000	76.881	0.020	0.000	0.000	0.029	0.271	0.159	0.005	0.085	0.024	99.857
MS496_05164_area15_5	galena	14.431	0.000	0.000	0.000	0.026	0.017	0.010	0.000	0.000	0.000	0.000	0.000	0.000	84.811	99.295

MS496_05164_area16_1	galena	14.599	0.000	0.000	0.000	0.051	0.444	0.009	0.000	0.000	0.028	0.034	0.000	0.000	84.864	100.029
MS496_05164_area16_2	Cu-sulfide	22.506	0.034	0.000	0.000	76.741	0.085	0.000	0.000	0.030	0.224	0.073	0.000	0.027	0.045	99.765
MS496_05164_area16_3	Cu-Fe-sulfide	24.376	5.613	0.000	0.000	71.484	0.093	0.000	0.000	0.037	0.281	0.061	0.005	0.025	0.000	101.976
MS496_05164_area16_4	? Cu-Fe-sulfide	25.456	7.814	0.000	0.000	67.712	0.704	0.000	0.000	0.038	0.170	0.055	0.000	0.029	0.000	101.977
MS496_05164_area16_5	galena	14.482	0.000	0.000	0.000	0.000	0.104	0.009	0.000	0.000	0.000	0.034	0.000	0.000	84.238	98.867
MS496_05164_area16_6	galena	14.477	0.000	0.000	0.000	0.000	0.036	0.007	0.000	0.000	0.000	0.000	0.000	0.000	85.130	99.649
MS496_05164_area16_7	Cu-Fe-sulfide	24.599	5.886	0.000	0.000	70.746	0.393	0.000	0.000	0.041	0.174	0.056	0.000	0.030	0.000	101.924
MS496_05164_area16_8	Cu-Fe-sulfide	24.682	6.111	0.000	0.000	70.573	0.459	0.000	0.000	0.039	0.214	0.052	0.000	0.023	0.000	102.152
MS496_05164_area2_1	Cu-sulfide	22.087	0.124	0.000	0.000	76.691	0.540	0.000	0.000	0.035	0.090	0.000	0.000	0.000	0.016	99.583
MS496_05164_area2_2	galena	14.405	0.000	0.000	0.000	0.000	0.068	0.000	0.000	0.000	0.000	0.031	0.000	0.000	84.551	99.054
MS496_05164_area2_3	Cu-Fe-sulfide	24.564	6.110	0.000	0.000	69.912	0.706	0.000	0.000	0.038	0.181	0.050	0.000	0.020	0.000	101.582
MS496_05164_area2_4	chalcopyrite	34.378	28.457	0.000	0.000	34.714	1.762	0.000	0.000	0.000	0.036	0.026	0.000	0.000	0.000	99.373
MS496_05164_area2_5	galena	14.446	0.000	0.000	0.000	0.152	0.165	0.010	0.000	0.000	0.000	0.000	0.000	0.000	84.459	99.232
MS496_05164_area3_1	galena	14.437	0.000	0.000	0.000	0.000	0.022	0.000	0.000	0.000	0.028	0.000	0.000	0.000	84.448	98.936
MS496_05164_area3_2	Cu-sulfide	21.467	0.012	0.000	0.000	77.579	0.062	0.000	0.000	0.034	0.078	0.000	0.000	0.000	0.000	99.232
MS496_05164_area3_3	Cu-Fe-sulfide	23.570	5.029	0.000	0.000	72.144	0.063	0.000	0.000	0.040	0.390	0.054	0.004	0.029	0.000	101.325
MS496_05164_area4_1	galena	14.374	0.000	0.000	0.000	0.017	0.000	0.010	0.000	0.000	0.000	0.000	0.000	0.000	84.380	98.782
MS496_05164_area4_2	Cu-Fe-sulfide	23.637	4.985	0.000	0.000	72.580	0.172	0.000	0.000	0.044	0.488	0.064	0.005	0.021	0.000	101.995
MS496_05164_area4_3	reniérite	31.490	4.374	0.000	0.000	49.606	2.086	0.000	9.655	4.840	0.097	0.043	0.000	0.070	0.000	102.261
MS496_05164_area4_4	Cu-Fe-sulfide	22.021	0.034	0.004	0.000	77.885	0.047	0.000	0.000	0.026	0.131	0.048	0.000	0.024	0.078	100.299
MS496_05164_area4_5	chalcopyrite	34.235	28.130	0.000	0.000	36.811	0.131	0.000	0.000	0.012	0.040	0.027	0.000	0.000	0.000	99.386
MS496_05164_area5_1	galena	14.512	0.000	0.000	0.000	0.000	0.401	0.008	0.000	0.000	0.044	0.053	0.000	0.020	84.265	99.303
MS496_05164_area5_2	reniérite	32.227	13.410	0.000	0.000	43.904	1.715	0.037	7.226	3.023	0.018	0.043	0.000	0.047	0.000	101.648
MS496_05164_area5_3	galena	14.477	0.000	0.000	0.000	0.016	0.000	0.010	0.000	0.000	0.000	0.000	0.000	0.000	84.237	98.740
MS496_05164_area6_1	Cu-Fe-sulfide	24.038	5.617	0.000	0.000	71.511	0.080	0.000	0.000	0.034	0.219	0.053	0.000	0.024	0.000	101.575
MS496_05164_area6_2	chalcopyrite	34.417	28.552	0.000	0.000	35.318	1.055	0.000	0.000	0.000	0.021	0.019	0.000	0.000	0.000	99.382
MS496_05164_area6_3	reniérite	31.591	4.335	0.000	0.000	49.704	1.510	0.000	9.892	4.631	0.029	0.043	0.000	0.045	0.000	101.780
MS496_05164_area6_4	galena	14.408	0.000	0.000	0.000	0.048	0.186	0.000	0.000	0.000	0.000	0.038	0.000	0.000	83.979	98.658
MS496_05164_area6_5	Cu-sulfide	21.373	0.026	0.000	0.000	77.301	0.134	0.000	0.000	0.038	0.103	0.000	0.000	0.000	0.039	99.014
MS496_05164_area6_6	Cu-Fe-sulfide	23.883	5.273	0.000	0.000	72.071	0.046	0.000	0.000	0.037	0.314	0.055	0.006	0.027	0.000	101.712
MS496_05164_area6_7	galena	14.387	0.000	0.000	0.000	0.000	0.217	0.000	0.000	0.000	0.000	0.000	0.000	0.000	84.147	98.751
MS496_05164_area6_8	chalcopyrite	34.616	29.060	0.000	0.000	35.432	0.267	0.000	0.000	0.000	0.019	0.018	0.000	0.000	0.000	99.412
MS496_05164_area6_9	sphalerite	32.631	0.000	0.000	0.000	0.050	64.611	0.028	0.000	0.032	0.015	1.794	0.000	0.000	0.000	99.163
MS496_05164_area8_1	Cu-Fe-sulfide	24.233	5.545	0.000	0.000	71.241	0.395	0.000	0.000	0.033	0.305	0.063	0.007	0.030	0.000	101.853
MS496_05164_area8_2	Cu-sulfide	21.663	0.061	0.000	0.000	77.162	0.197	0.000	0.000	0.041	0.102	0.000	0.000	0.000	0.000	99.226
MS496_05164_area8_3	Cu-Fe-sulfide	24.150	5.522	0.000	0.000	71.477	0.210	0.000	0.000	0.034	0.206	0.049	0.000	0.019	0.000	101.667
MS496_05164_area8_4	galena	14.458	0.000	0.000	0.000	0.018	0.000	0.009	0.000	0.000	0.000	0.000	0.000	0.000	84.131	98.616
MS496_05164_area8_5	sphalerite	32.528	0.000	0.000	0.000	0.038	64.750	0.028	0.000	0.029	0.017	1.812	0.000	0.000	0.000	99.201
MS496_05164_area9_1	galena	14.357	0.000	0.000	0.000	0.000	0.103	0.000	0.000	0.000	0.000	0.000	0.000	0.000	83.958	98.418
MS496_05164_area9_2	reniérite	31.915	13.344	0.000	0.000	43.496	1.993	0.039	6.524	3.315	0.069	0.034	0.000	0.060	0.000	100.789
MS496_05164_area9_3	Cu-sulfide	21.615	0.014	0.000	0.000	77.383	0.363	0.000	0.000	0.041	0.099	0.020	0.000	0.000	0.017	99.552
MS496_05164_area9_4	chalcopyrite	34.513	28.507	0.000	0.000	34.932	1.570	0.000	0.000	0.000	0.030	0.018	0.000	0.000	0.020	99.590
MS496_05164_area9_5	Cu-sulfide	21.878	0.124	0.000	0.000	77.205	0.526	0.000	0.009	0.034	0.122	0.044	0.000	0.017	0.022	99.981
MS496_05164_area9_6	Cu-Fe-sulfide	24.105	5.458	0.000	0.007	71.686	0.382	0.000	0.000	0.041	0.320	0.053	0.005	0.027	0.000	102.085
MS496_05246_BSE1_1	sphalerite	32.152	0.011	0.000	0.000	0.036	64.610	0.014	0.000	0.026	0.000	2.663	0.009	0.000	0.105	99.626
MS496_05246_BSE1_2	Cu-sulfide	22.155	0.943	0.000	0.000	76.534	0.000	0.000	0.000	0.035	0.271	0.000	0.000	0.000	0.066	100.003

MS496_05246_BSE1_3	galena	14.293	0.000	0.000	0.000	0.017	0.000	0.012	0.000	0.000	0.000	0.000	0.000	0.000	85.969	100.291
MS496_05246_BSE1_4	tennantite	27.389	0.033	0.010	0.000	43.935	8.223	0.000	0.000	17.157	0.088	0.827	0.000	2.171	0.110	99.942
MS496_05246_BSE1_5	Cu-Fe-sulfide	24.539	5.783	0.000	0.000	71.087	0.000	0.000	0.000	0.030	0.996	0.000	0.006	0.000	0.042	102.482
MS496_05246_BSE2_2	sphalerite	32.245	0.011	0.004	0.000	0.035	64.793	0.014	0.000	0.032	0.000	2.722	0.009	0.000	0.048	99.912
MS496_05246_BSE2_4	Cu-Fe-sulfide	24.428	5.838	0.000	0.000	71.045	0.197	0.006	0.000	0.034	0.521	0.018	0.011	0.000	0.030	102.128
MS496_05246_BSE3_1	sphalerite	32.298	0.000	0.006	0.000	0.079	64.803	0.000	0.000	0.028	0.000	2.655	0.008	0.000	0.037	99.913
MS496_05246_BSE3_2	galena	14.400	0.000	0.000	0.000	0.066	0.000	0.014	0.000	0.000	0.000	0.000	0.000	0.000	86.331	100.811
MS496_05246_BSE3_3	tennantite	27.521	0.032	0.008	0.000	43.839	8.198	0.000	0.000	18.329	0.073	0.845	0.000	2.244	0.031	101.121
MS496_05246_BSE3_4	Cu-sulfide	22.041	0.008	0.004	0.000	77.267	0.000	0.000	0.000	0.031	0.302	0.000	0.000	0.000	0.052	99.704
MS496_05246_BSE3_5	Cu-Fe-sulfide	24.788	5.841	0.000	0.000	70.822	0.000	0.000	0.000	0.040	1.031	0.043	0.013	0.010	0.023	102.611
MS496_05246_BSE4_1	galena	14.422	0.000	0.000	0.000	0.019	0.000	0.014	0.000	0.000	0.000	0.000	0.000	0.000	86.081	100.536
MS496_05246_BSE4_2	Cu-sulfide	22.234	0.918	0.000	0.000	76.753	0.000	0.000	0.000	0.037	0.266	0.000	0.000	0.000	0.066	100.275
MS496_05246_BSE4_3	Cu-Fe-sulfide	24.483	5.603	0.000	0.000	71.543	0.000	0.000	0.000	0.042	0.506	0.038	0.009	0.000	0.050	102.275
MS496_05246_BSE4_4	sphalerite	32.331	0.000	0.000	0.000	0.071	64.642	0.015	0.000	0.033	0.000	2.693	0.007	0.000	0.068	99.862
MS496_05246_BSE4_5	tennantite	27.483	0.033	0.009	0.000	43.938	8.108	0.000	0.000	17.838	0.041	0.853	0.000	2.172	0.123	100.598
MS496_05246_BSE4_6	Cu-sulfide	22.184	0.821	0.000	0.000	76.227	0.000	0.000	0.000	0.038	0.295	0.000	0.000	0.000	0.173	99.740
MS496_05246_BSE4_7	Cu-Fe-sulfide	24.731	5.669	0.000	0.000	71.472	0.000	0.000	0.000	0.042	0.640	0.037	0.012	0.000	0.061	102.664
MS496_05263_BSE1_1	sphalerite	32.333	0.000	0.000	0.000	0.027	64.663	0.018	0.000	0.030	0.000	2.659	0.007	0.000	0.043	99.780
MS496_05263_BSE1_2	Cu-sulfide	21.847	0.000	0.000	0.008	77.636	0.000	0.000	0.000	0.033	0.216	0.000	0.000	0.000	0.040	99.781
MS496_05263_BSE1_3	Cu-sulfide	21.610	0.012	0.004	0.000	77.746	0.000	0.000	0.000	0.044	0.170	0.000	0.000	0.000	0.045	99.630
MS496_05263_BSE1_4	Cu-Fe-sulfide	24.346	5.640	0.000	0.000	71.783	0.000	0.000	0.000	0.040	0.328	0.029	0.006	0.000	0.018	102.189
MS496_05263_BSE1_5	Cu-Fe-sulfide	24.644	5.815	0.000	0.000	71.269	0.032	0.000	0.000	0.039	0.491	0.035	0.009	0.000	0.025	102.359
MS496_05263_BSE1_6	galena	14.309	0.000	0.000	0.000	0.023	0.000	0.008	0.000	0.000	0.000	0.000	0.000	0.000	85.159	99.499
MS496_05263_BSE1_7	Cu-sulfide	22.143	0.016	0.000	0.000	78.092	0.020	0.000	0.000	0.025	0.224	0.000	0.000	0.000	0.030	100.550
MS496_05263_BSE2_1	sphalerite	32.402	0.000	0.000	0.000	0.045	64.811	0.021	0.000	0.026	0.000	2.615	0.007	0.000	0.051	99.979
MS496_05263_BSE2_2	tennantite	27.571	0.065	0.009	0.000	44.032	8.144	0.000	0.000	18.433	0.060	0.779	0.000	1.584	0.000	100.677
MS496_05263_BSE2_3	reniérite	31.970	13.508	0.000	0.000	44.866	0.417	0.020	5.190	4.403	0.059	0.000	0.000	0.092	0.041	100.564
MS496_05263_BSE2_4	Cu-Fe-sulfide	23.434	5.492	0.000	0.000	68.171	0.078	0.000	0.000	0.027	0.476	0.000	0.000	0.000	0.000	97.677
MS496_05263_BSE2_5	Cu-sulfide	22.167	0.064	0.000	0.000	77.720	0.058	0.000	0.000	0.028	0.196	0.000	0.000	0.000	0.000	100.232
MS496_05263_BSE3_1	galena	14.329	0.000	0.000	0.000	0.021	0.000	0.011	0.000	0.000	0.000	0.000	0.000	0.000	85.206	99.568
MS496_05263_BSE3_2	Cu-Fe-sulfide	24.357	5.613	0.000	0.000	71.692	0.000	0.000	0.000	0.039	0.410	0.030	0.004	0.000	0.016	102.162
MS496_05263_BSE3_3	chalcopyrite	34.375	29.061	0.000	0.000	35.594	0.770	0.000	0.000	0.000	0.036	0.000	0.000	0.000	0.035	99.871
MS496_05263_BSE3_4	Cu-sulfide	21.809	0.063	0.000	0.000	77.215	0.000	0.000	0.000	0.043	0.197	0.000	0.000	0.000	0.067	99.394
MS496_05263_BSE3_5	sphalerite	32.295	0.000	0.000	0.000	0.046	64.515	0.021	0.000	0.030	0.000	2.659	0.008	0.000	0.032	99.606
MS496_05263_BSE3_6	Cu-Fe-sulfide	22.108	1.114	0.000	0.000	76.593	0.559	0.000	0.000	0.028	0.199	0.024	0.006	0.000	0.033	100.665
MS496_05263_BSE3_7	galena	14.377	0.000	0.000	0.000	0.017	0.000	0.009	0.000	0.000	0.000	0.000	0.000	0.000	85.689	100.093
MS496_05263_BSE4_1	galena	14.383	0.000	0.000	0.000	0.019	0.000	0.015	0.000	0.000	0.000	0.000	0.000	0.000	86.041	100.458
MS496_05263_BSE4_2	Cu-sulfide	21.699	0.023	0.000	0.000	77.540	0.000	0.000	0.000	0.037	0.271	0.000	0.000	0.000	0.075	99.644
MS496_05263_BSE4_3	sphalerite	32.206	0.000	0.005	0.000	0.031	64.526	0.022	0.000	0.028	0.000	2.639	0.005	0.000	0.049	99.510
MS496_05263_BSE4_4	Cu-Fe-sulfide	24.050	5.199	0.000	0.000	72.175	0.000	0.000	0.000	0.043	0.582	0.042	0.009	0.000	0.022	102.123
MS496_05263_BSE4_5	tennantite	27.332	0.072	0.009	0.000	44.159	8.320	0.000	0.000	17.746	0.018	0.748	0.000	1.263	0.000	99.666
MS496_05263_BSE5_1	galena	14.318	0.000	0.000	0.000	0.038	0.000	0.011	0.000	0.000	0.000	0.000	0.000	0.000	85.456	99.823
MS496_05263_BSE5_2	Cu-Fe-sulfide	24.253	5.457	0.000	0.000	71.736	0.000	0.000	0.000	0.036	0.464	0.048	0.010	0.013	0.045	102.062
MS496_05263_BSE5_3	reniérite	32.042	13.264	0.000	0.000	45.704	0.116	0.016	5.125	4.449	0.079	0.000	0.000	0.098	0.030	100.923
MS496_05263_BSE5_4	Cu-sulfide	21.751	0.059	0.000	0.009	77.554	0.000	0.000	0.000	0.031	0.198	0.000	0.000	0.000	0.055	99.657
MS496_05263_BSE5_5	Cu-Fe-sulfide	24.313	5.532	0.004	0.000	71.779	0.000	0.000	0.000	0.041	0.504	0.042	0.010	0.013	0.033	102.269

MS496_05263_BSE5_6	Cu-sulfide	21.750	0.104	0.000	0.007	77.618	0.212	0.000	0.000	0.037	0.212	0.000	0.000	0.000	0.054	99.992
MS496_05263_BSE5_7	sphalerite	32.361	0.000	0.000	0.000	0.047	64.613	0.019	0.000	0.032	0.000	2.643	0.007	0.000	0.048	99.770
MS496_08239_BSE1_1	Cu-sulfide (low total)	17.647	0.000	0.000	0.000	76.649	0.000	0.000	0.000	0.000	0.141	0.000	0.000	0.000	0.710	95.147
MS496_08239_BSE1_2	galena	14.424	0.000	0.000	0.000	1.021	0.000	0.000	0.000	0.000	0.000	0.000	0.000	0.000	85.623	101.067
MS496_08239_BSE1_3	? low total (Cu-Pb-S)	20.058	0.000	0.000	0.000	62.989	0.000	0.000	0.000	0.000	0.042	0.000	0.000	0.000	12.121	95.209
MS496_08239_BSE1_4	Cu-sulfide (low total)	18.183	0.000	0.006	0.018	78.334	0.000	0.000	0.000	0.000	0.000	0.000	0.000	0.000	0.372	96.913
MS496_08239_BSE1_5	Cu-Fe-Sulfide	23.753	5.085	0.000	0.000	73.005	0.000	0.000	0.000	0.041	0.065	0.031	0.007	0.014	0.000	102.001
MS496_08239_BSE1_6	Cu-sulfide	21.252	0.187	0.004	0.000	78.225	0.000	0.000	0.000	0.048	0.018	0.000	0.000	0.000	0.000	99.734
MS496_08239_BSE2_1	Cu-Fe-sulfide	23.600	4.911	0.000	0.000	73.000	0.000	0.000	0.000	0.038	0.069	0.032	0.008	0.000	0.000	101.658
MS496_08239_BSE2_2	Cu-sulfide	21.605	0.288	0.004	0.013	78.160	0.000	0.000	0.000	0.028	0.030	0.000	0.000	0.000	0.018	100.146
MS496_08239_BSE2_4	Cu-Fe-sulfide	23.581	4.815	0.004	0.000	73.140	0.000	0.000	0.000	0.046	0.069	0.037	0.008	0.018	0.000	101.717
MS496_08239_BSE2_5	Cu-sulfide	21.557	0.167	0.000	0.000	77.986	0.000	0.000	0.000	0.035	0.049	0.000	0.000	0.000	0.017	99.811
MS496_08239_BSE3_2	Cu-sulfide	21.591	0.179	0.004	0.008	78.529	0.000	0.000	0.000	0.034	0.056	0.022	0.000	0.000	0.000	100.423
MS496_08239_BSE4_1	Cu-Fe-sulfide	23.587	4.854	0.000	0.000	73.226	0.000	0.000	0.000	0.041	0.075	0.041	0.010	0.018	0.000	101.853
MS496_08239_BSE4_2	? cpy mixed analysis	31.606	23.898	0.000	0.000	43.556	0.000	0.000	0.000	0.000	0.000	0.000	0.000	0.000	0.000	99.060
MS496_08239_BSE4_3	Cu-sulfide	20.734	0.118	0.003	0.009	79.305	0.000	0.000	0.000	0.000	0.000	0.000	0.000	0.000	0.000	100.168
MS496_08239_BSE4_4	Cu-Fe-sulfide	23.573	4.880	0.000	0.000	73.212	0.000	0.000	0.000	0.038	0.058	0.041	0.012	0.017	0.000	101.832
MS496_08239_BSE4_5	Cu-sulfide	21.917	1.509	0.000	0.009	76.928	0.000	0.000	0.000	0.031	0.027	0.021	0.004	0.000	0.000	100.446
MS496_08241_BSE1a_10	galena	14.688	0.000	0.000	0.000	0.069	0.000	0.021	0.000	0.000	0.031	0.000	0.000	0.000	86.604	101.413
MS496_08241_BSE1a_11	galena	14.722	0.000	0.000	0.000	0.056	0.000	0.019	0.000	0.000	0.000	0.000	0.000	0.000	86.310	101.106
MS496_08241_BSE1a_12	pyrite	53.687	46.223	0.000	0.000	0.216	0.025	0.012	0.010	0.000	0.000	0.000	0.000	0.000	0.000	100.173
MS496_08241_BSE1a_9	galena	14.638	0.000	0.000	0.000	0.074	0.000	0.014	0.000	0.000	0.035	0.000	0.000	0.000	86.274	101.035
MS496_08241_BSE1b_1	tennantite	28.092	0.080	0.005	0.000	44.435	8.659	0.020	0.000	18.003	0.182	0.146	0.000	1.640	0.000	101.263
MS496_08241_BSE1b_2	sphalerite	32.786	0.069	0.000	0.000	1.889	65.240	0.159	0.000	0.036	0.042	0.516	0.000	0.019	0.031	100.787
MS496_08241_BSE1b_3	tennantite	27.520	0.056	0.010	0.007	45.306	9.024	0.000	0.023	13.838	0.000	0.000	0.000	1.474	0.000	97.258
MS496_08241_BSE1b_4	sphalerite	33.219	0.000	0.000	0.000	0.177	66.286	0.176	0.000	0.027	0.017	0.459	0.000	0.000	0.000	100.361
MS496_08241_BSE1b_5	tennantite	27.484	0.067	0.009	0.011	44.938	9.051	0.038	0.014	14.692	0.066	0.000	0.000	1.532	0.000	97.903
MS496_08241_BSE1b_6	sphalerite	33.155	0.000	0.000	0.000	0.171	66.204	0.173	0.000	0.025	0.023	0.573	0.000	0.000	0.000	100.323
MS496_08241_BSE1b_7	tennantite	27.413	0.079	0.006	0.013	45.158	8.999	0.036	0.018	14.369	0.000	0.000	0.000	1.433	0.000	97.524
MS496_08241_BSE1b_8	tennantite	27.409	0.088	0.006	0.011	44.903	8.988	0.032	0.019	15.528	0.125	0.021	0.000	1.574	0.000	98.703
MS496_08241_BSE2a_1	sphalerite	33.050	0.000	0.000	0.000	0.193	66.549	0.184	0.000	0.023	0.020	0.535	0.000	0.000	0.020	100.574
MS496_08241_BSE2a_10	galena	14.528	0.000	0.000	0.000	0.061	0.000	0.014	0.000	0.000	0.000	0.000	0.000	0.000	86.804	101.407
MS496_08241_BSE2a_11	galena	14.597	0.000	0.000	0.000	0.041	0.000	0.017	0.000	0.000	0.000	0.000	0.000	0.000	86.526	101.181
MS496_08241_BSE2a_2	sphalerite	32.938	0.017	0.000	0.000	0.206	66.359	0.178	0.000	0.026	0.018	0.524	0.000	0.000	0.000	100.265
MS496_08241_BSE2a_3	sphalerite	33.052	0.010	0.000	0.000	0.204	66.336	0.180	0.000	0.020	0.017	0.514	0.000	0.000	0.000	100.334
MS496_08241_BSE2a_4	Cu-sulfide	18.732	0.012	0.000	0.007	79.275	0.028	0.000	0.000	0.000	0.000	0.000	0.000	0.000	0.000	98.055
MS496_08241_BSE2a_5	sphalerite	32.988	0.010	0.000	0.000	0.187	66.236	0.181	0.000	0.020	0.000	0.525	0.000	0.000	0.000	100.147
MS496_08241_BSE2a_6	sphalerite	32.982	0.000	0.000	0.000	0.172	66.237	0.179	0.000	0.021	0.000	0.533	0.000	0.000	0.019	100.144
MS496_08241_BSE2a_7	pyrite	53.624	46.329	0.102	0.016	0.000	0.290	0.013	0.000	0.000	0.000	0.024	0.000	0.000	0.000	100.398
MS496_08241_BSE2a_8	galena	14.646	0.000	0.000	0.000	0.055	0.000	0.015	0.000	0.000	0.000	0.000	0.000	0.000	86.106	100.823
MS496_08241_BSE2a_9	galena	14.736	0.000	0.000	0.000	0.130	0.026	0.018	0.000	0.000	0.038	0.000	0.000	0.000	86.229	101.177
MS496_08241_BSE3a_1	galena	14.578	0.000	0.000	0.000	0.021	0.000	0.016	0.000	0.000	0.000	0.000	0.000	0.000	86.623	101.237
MS496_08241_BSE3a_2	galena	14.545	0.000	0.000	0.000	0.065	0.000	0.014	0.000	0.000	0.033	0.000	0.000	0.000	86.596	101.253
MS496_08241_BSE3a_3	galena	14.508	0.000	0.000	0.000	0.014	0.000	0.015	0.000	0.000	0.000	0.000	0.000	0.000	86.508	101.045
MS496_08241_BSE3a_6	Cu-sulfide	21.553	0.012	0.000	0.000	78.038	0.029	0.022	0.000	0.022	0.091	0.032	0.006	0.018	0.024	99.847
MS496_08241_BSE3a_7	sphalerite	33.042	0.000	0.000	0.000	0.174	66.380	0.186	0.000	0.022	0.025	0.496	0.000	0.000	0.000	100.325

MS496_08241_BSE3a_8	Cu-sulfide	21.193	0.000	0.009	0.021	79.954	0.000	0.050	0.000	0.000	0.000	0.000	0.000	0.000	0.000	101.227
MS496_08241_BSE3a_9	sphalerite	33.133	0.000	0.000	0.000	0.179	66.413	0.186	0.000	0.022	0.022	0.540	0.000	0.000	0.000	100.494
MS496_08241_BSE3b_10	tennantite	27.651	0.047	0.005	0.000	44.617	8.868	0.028	0.000	16.921	0.052	0.069	0.000	1.619	0.000	99.878
MS496_08241_BSE3b_11	Cu-sulfide	21.969	0.008	0.000	0.007	77.918	0.056	0.109	0.000	0.000	0.095	0.000	0.000	0.000	0.000	100.162
MS496_08241_BSE4a_1	reniérite	32.466	13.356	0.000	0.000	42.905	2.324	0.208	7.946	2.201	0.024	0.023	0.000	0.043	0.020	101.516
MS496_08241_BSE4a_10	galena	14.540	0.000	0.000	0.000	0.025	0.030	0.014	0.000	0.000	0.000	0.000	0.000	0.000	86.713	101.322
MS496_08241_BSE4a_2	reniérite	32.589	13.357	0.000	0.000	42.775	3.048	0.204	7.908	2.272	0.026	0.020	0.000	0.047	0.016	102.261
MS496_08241_BSE4a_3	? Cu-Pb-S	21.127	1.512	0.000	0.000	62.085	0.390	0.000	0.000	0.000	0.000	0.000	0.000	0.000	16.170	101.284
MS496_08241_BSE4a_4	sphalerite	33.178	0.019	0.000	0.000	0.316	66.025	0.176	0.000	0.024	0.017	0.446	0.000	0.000	0.000	100.201
MS496_08241_BSE4a_5	? Cu-Pb-S	21.104	1.519	0.000	0.000	61.399	0.522	0.000	0.000	0.000	0.041	0.000	0.000	0.000	16.291	100.877
MS496_08241_BSE4a_6	? Cu-Pb-S	21.188	1.450	0.000	0.000	61.702	0.985	0.000	0.000	0.000	0.038	0.000	0.000	0.000	16.273	101.637
MS496_08241_BSE4a_7	sphalerite	33.195	0.017	0.000	0.000	0.251	66.045	0.178	0.000	0.022	0.016	0.461	0.000	0.000	0.000	100.184
MS496_08241_BSE4a_8	sphalerite	33.036	0.023	0.000	0.000	0.260	65.981	0.180	0.000	0.024	0.000	0.399	0.000	0.000	0.000	99.903
MS496_08241_BSE4a_9	galena	14.672	0.000	0.000	0.000	0.079	0.058	0.015	0.000	0.000	0.032	0.000	0.000	0.000	86.836	101.693
MS496_08269_BSE1_2	Cu-sulfide	23.291	0.925	0.000	0.007	76.891	0.000	0.006	0.000	0.026	0.276	0.082	0.013	0.033	0.000	101.550
MS496_08269_BSE1_3	tennantite	28.077	0.081	0.014	0.000	43.841	7.707	0.013	0.000	16.074	0.086	1.662	0.000	3.775	0.000	101.330
MS496_08269_BSE1_6	Cu-sulfide	23.276	0.971	0.000	0.008	76.838	0.000	0.000	0.000	0.026	0.293	0.070	0.013	0.046	0.027	101.569
MS496_08269_BSE2_3	Cu-sulfide	22.812	0.000	0.000	0.000	76.906	0.000	0.000	0.000	0.029	0.354	0.069	0.006	0.034	0.110	100.321
MS496_08277_BSE1_1	pyrite	54.998	45.784	0.014	0.080	0.161	0.350	0.016	0.045	0.000	0.038	0.064	0.000	0.021	0.302	101.872
MS496_08277_BSE1_2	galena	14.775	0.000	0.000	0.000	0.036	0.223	0.019	0.000	0.000	0.026	0.064	0.000	0.018	86.569	101.730
MS496_08277_BSE1_3	reniérite	32.942	13.583	0.000	0.000	42.644	3.056	0.210	8.637	1.764	0.041	0.064	0.000	0.010	0.000	102.951
MS496_08277_BSE1_4	reniérite	32.737	13.620	0.000	0.000	42.682	2.711	0.209	8.412	1.907	0.045	0.057	0.000	0.010	0.000	102.390
MS496_08277_BSE1_5	covellite ?	22.192	0.091	0.000	0.000	73.912	2.117	0.040	0.073	0.033	0.154	0.000	0.000	0.000	0.062	98.675
MS496_08277_BSE1_6	sphalerite	33.283	0.026	0.000	0.000	0.543	65.217	0.571	0.000	0.032	0.034	1.162	0.000	0.010	0.000	100.879
MS496_08277_BSE1_7	tennantite	28.246	0.077	0.000	0.000	43.892	9.028	0.053	0.000	19.253	0.576	0.403	0.000	0.193	0.000	101.720
MS496_08277_BSE2_1	tennantite	28.350	0.202	0.000	0.000	44.161	8.836	0.049	0.000	19.339	0.203	0.402	0.000	0.193	0.000	101.735
MS496_08277_BSE2_2	sphalerite	33.349	0.066	0.000	0.000	0.681	65.235	0.575	0.000	0.025	0.032	1.111	0.005	0.013	0.000	101.093
MS496_08277_BSE2_3	covellite ?	28.268	0.448	0.000	0.000	71.318	0.453	0.220	0.000	0.049	0.356	0.043	0.004	0.013	0.080	101.251
MS496_08277_BSE2_4	sphalerite	33.118	0.197	0.000	0.000	0.637	64.915	0.522	0.000	0.021	0.040	1.090	0.004	0.000	0.000	100.544
MS496_08277_BSE2_5	reniérite	32.758	13.812	0.000	0.000	42.407	2.952	0.000	8.654	1.764	0.047	0.072	0.000	0.012	0.000	102.479
MS496_08277_BSE2_6	pyrite	54.055	46.214	0.000	0.000	0.095	0.399	0.015	0.008	0.000	0.000	0.042	0.000	0.000	0.014	100.842
MS496_08277_BSE3_1	sphalerite	33.380	0.030	0.000	0.000	0.533	65.321	0.498	0.000	0.025	0.028	1.146	0.006	0.000	0.000	100.967
MS496_08277_BSE3_2	tennantite	27.461	0.071	0.005	0.008	44.603	9.062	0.053	0.014	16.228	0.392	0.295	0.000	0.140	0.000	98.332
MS496_08277_BSE3_3	galena	14.759	0.000	0.000	0.000	0.027	0.000	0.017	0.000	0.000	0.037	0.000	0.000	0.000	86.499	101.340
MS496_08277_BSE3_4	pyrite	54.073	46.452	0.000	0.000	0.055	0.252	0.012	0.000	0.000	0.014	0.037	0.000	0.000	0.000	100.896
MS496_08277_BSE3_5	reniérite	32.773	13.219	0.000	0.000	42.426	3.632	0.203	8.092	2.025	0.106	0.059	0.000	0.011	0.000	102.544
MS496_08277_BSE3_8	reniérite	32.555	12.225	0.000	0.000	42.342	2.481	0.206	9.682	1.391	0.043	0.069	0.000	0.000	0.035	101.029
MS496_08280_BSE1_1	pyrite	53.410	45.574	0.008	0.000	0.027	0.000	0.000	0.000	0.000	0.000	0.018	0.000	0.000	0.076	99.113
MS496_08280_BSE1_3	sphalerite	32.738	0.080	0.000	0.000	0.043	63.916	0.029	0.000	0.030	0.000	0.815	0.004	0.000	0.078	97.733
MS496_08280_BSE1_4	galena	14.554	0.000	0.000	0.000	0.000	0.000	0.008	0.000	0.000	0.000	0.000	0.000	0.000	85.954	100.516
MS496_08280_BSE2_1	sphalerite	33.154	0.064	0.000	0.000	0.058	65.831	0.035	0.000	0.027	0.036	0.927	0.000	0.013	0.076	100.221
MS496_08280_BSE2_2	galena	14.606	0.000	0.000	0.000	0.000	0.000	0.000	0.000	0.000	0.032	0.066	0.000	0.024	85.783	100.511
MS496_08280_BSE2_3	pyrite	53.875	46.476	0.078	0.011	0.000	0.000	0.012	0.009	0.000	0.027	0.045	0.000	0.000	0.053	100.586
MS496_08280_BSE2_4	galena	14.430	0.000	0.000	0.000	0.000	0.113	0.000	0.000	0.000	0.033	0.044	0.000	0.000	85.523	100.144
MS496_08280_BSE2_5	sphalerite	33.180	0.069	0.000	0.000	0.034	66.222	0.032	0.000	0.022	0.026	0.885	0.000	0.000	0.063	100.532
MS496_08280_BSE3_1	tennantite	28.162	1.756	0.019	0.000	44.286	6.957	0.007	0.000	16.559	0.000	0.152	0.000	2.101	0.060	100.060

MS496_08280_BSE3_2	sphalerite	33.193	0.082	0.005	0.000	0.084	66.315	0.032	0.000	0.031	0.022	0.931	0.000	0.000	0.093	100.789
MS496_08280_BSE3_3	tennantite	28.194	1.752	0.018	0.000	43.851	6.811	0.009	0.000	16.858	0.025	0.183	0.000	2.306	0.130	100.137
MS496_08280_BSE3_4	galena	14.800	0.000	0.000	0.000	0.000	0.000	0.020	0.000	0.000	0.068	0.045	0.000	0.027	86.026	100.986
MS496_08280_BSE3_5	galena	14.700	0.000	0.000	0.000	0.000	0.000	0.021	0.000	0.000	0.063	0.085	0.000	0.045	86.330	101.243
MS496_08280_BSE3_6	sphalerite	33.256	0.093	0.004	0.000	0.030	66.485	0.035	0.000	0.018	0.028	0.927	0.000	0.015	0.065	100.957
MS496_08298_BSE1_1	Cu-sulfide	21.493	0.009	0.005	0.007	78.969	0.000	0.000	0.000	0.037	0.051	0.031	0.000	0.000	0.000	100.602
MS496_08298_BSE1_2	tennantite	27.899	0.017	0.005	0.000	47.243	6.694	0.019	0.000	19.483	0.066	0.069	0.000	0.173	0.000	101.666
MS496_08298_BSE2_1	tennantite	27.899	0.065	0.005	0.000	44.781	8.766	0.020	0.000	19.294	0.235	0.190	0.000	0.172	0.000	101.428
MS496_08298_BSE2_10	Cu-sulfide	21.621	0.134	0.000	0.000	78.369	0.026	0.000	0.039	0.038	0.053	0.000	0.000	0.000	0.000	100.281
MS496_08298_BSE2_2	sphalerite	32.732	0.029	0.000	0.000	0.443	66.415	0.197	0.000	0.035	0.020	0.614	0.000	0.000	0.000	100.486
MS496_08298_BSE2_3	sphalerite	32.667	0.012	0.000	0.000	1.641	65.724	0.194	0.000	0.031	0.031	0.608	0.000	0.000	0.000	100.908
MS496_08298_BSE2_4	Cu-sulfide	21.264	0.000	0.004	0.000	78.955	0.153	0.000	0.000	0.056	0.039	0.020	0.000	0.000	0.000	100.491
MS496_08298_BSE2_5	pyrite	53.362	46.474	0.005	0.000	0.741	0.016	0.011	0.023	0.000	0.000	0.000	0.000	0.000	0.000	100.632
MS496_08298_BSE2_6	reniérite	32.174	13.256	0.000	0.000	43.478	2.314	0.137	9.208	1.606	0.000	0.023	0.000	0.000	0.000	102.195
MS496_08298_BSE2_7	tennantite	27.892	0.038	0.004	0.000	45.068	8.732	0.024	0.000	19.224	0.154	0.180	0.000	0.173	0.000	101.489
MS496_08298_BSE2_8	reniérite	31.434	11.997	0.000	0.000	42.838	2.698	0.135	8.907	1.761	0.017	0.020	0.000	0.000	0.018	99.824
MS496_08298_BSE2_9	reniérite	31.801	7.339	0.000	0.000	45.829	2.750	0.049	12.713	1.900	0.024	0.116	0.000	0.000	0.000	102.521
MS496_08298_BSE3_10	reniérite	32.007	12.931	0.000	0.000	44.224	2.054	0.149	8.560	1.784	0.016	0.021	0.000	0.000	0.000	101.744
MS496_08298_BSE3_2	reniérite	32.192	13.029	0.000	0.000	43.750	2.125	0.137	9.159	1.672	0.000	0.028	0.000	0.000	0.000	102.092
MS496_08298_BSE3_3	pyrite	53.344	46.132	0.000	0.000	0.606	0.000	0.009	0.000	0.000	0.000	0.018	0.000	0.000	0.000	100.109
MS496_08298_BSE3_4	pyrite	53.392	46.368	0.000	0.000	0.739	0.000	0.009	0.015	0.000	0.000	0.024	0.000	0.000	0.000	100.547
MS496_08298_BSE3_5	reniérite	31.727	8.199	0.000	0.000	46.290	2.278	0.067	11.870	1.729	0.000	0.000	0.000	0.000	0.000	102.159
MS496_08298_BSE3_6	Cu-sulfide	20.541	0.000	0.000	0.011	78.889	0.000	0.000	0.000	0.047	0.000	0.000	0.000	0.000	0.000	99.487
MS496_08298_BSE3_7	tennantite	27.872	0.050	0.004	0.000	44.762	8.603	0.024	0.000	19.105	0.127	0.172	0.000	0.151	0.000	100.869
MS496_08298_BSE3_9	Cu-sulfide	21.200	0.115	0.000	0.000	78.656	0.000	0.000	0.011	0.040	0.056	0.019	0.000	0.000	0.000	100.097
MS496_08298_BSE4_1	reniérite	32.158	13.574	0.000	0.000	43.035	2.107	0.141	9.006	1.786	0.000	0.018	0.000	0.000	0.000	101.825
MS496_08298_BSE4_3	reniérite	32.171	13.422	0.000	0.000	43.140	2.097	0.136	9.016	1.755	0.015	0.024	0.000	0.000	0.000	101.776
MS496_08298_BSE4_4	galena	14.490	0.000	0.000	0.000	0.089	0.000	0.009	0.000	0.000	0.000	0.000	0.000	0.000	85.178	99.766
MS496_08298_BSE4_5	tennantite	27.314	0.087	0.006	0.009	45.007	8.871	0.029	0.010	16.764	0.050	0.147	0.000	0.129	0.000	98.423
MS496_08298_BSE4_6	galena	14.481	0.000	0.000	0.000	0.105	0.000	0.011	0.000	0.000	0.000	0.000	0.000	0.000	85.047	99.644
MS496_08298_BSE4_7	Cu-sulfide	21.353	0.000	0.000	0.007	78.243	0.000	0.000	0.000	0.051	0.020	0.000	0.000	0.000	0.035	99.708
MS496_08298_BSE4_8	tennantite	27.194	0.066	0.006	0.010	45.221	9.032	0.033	0.000	16.116	0.000	0.073	0.000	0.079	0.000	97.829
MS496_08298_BSE4_9	reniérite	32.137	13.290	0.000	0.000	43.018	2.188	0.138	8.918	1.746	0.017	0.018	0.000	0.000	0.000	101.470
MS496_08299_BSE1_1	galena	14.708	0.000	0.000	0.000	0.000	0.000	0.010	0.000	0.000	0.073	0.107	0.009	0.067	86.641	101.614
MS496_08299_BSE1_2	Cu-sulfide	22.731	0.000	0.005	0.009	77.425	0.000	0.000	0.000	0.020	0.068	0.071	0.012	0.031	0.073	100.446
MS496_08299_BSE1_4	pyrite	54.368	46.062	0.015	0.296	0.035	0.000	0.008	0.011	0.000	0.017	0.042	0.000	0.009	0.016	100.880
MS496_08299_BSE1_5	tennantite	27.835	0.144	0.006	0.007	45.762	8.505	0.059	0.014	15.915	0.000	0.231	0.000	0.118	0.000	98.595
MS496_08299_BSE2_1	galena	14.738	0.000	0.000	0.000	0.183	0.000	0.024	0.000	0.000	0.078	0.071	0.009	0.036	86.937	102.076
MS496_08299_BSE2_3	reniérite	32.807	13.615	0.000	0.000	43.888	1.559	0.204	7.989	2.380	0.040	0.066	0.000	0.022	0.000	102.571
MS496_08299_BSE2_4	reniérite	32.823	13.627	0.000	0.000	43.764	1.618	0.201	8.164	2.240	0.046	0.064	0.000	0.019	0.000	102.565
MS496_08299_BSE2_5	pyrite	54.116	46.477	0.065	0.176	0.043	0.000	0.010	0.010	0.000	0.021	0.059	0.000	0.012	0.017	101.006
MS496_08299_BSE3_1	galena	14.795	0.000	0.000	0.000	0.027	0.000	0.022	0.000	0.000	0.046	0.050	0.000	0.018	87.081	102.038
MS496_08299_BSE3_2	pyrite	54.089	46.772	0.031	0.092	0.025	0.000	0.008	0.008	0.000	0.019	0.050	0.000	0.009	0.018	101.122
MS496_08299_BSE3_4	reniérite	32.793	13.728	0.004	0.000	43.810	1.609	0.202	8.077	2.279	0.041	0.064	0.000	0.021	0.021	102.649
MS496_08299_BSE4_2	tennantite	28.359	0.078	0.005	0.000	44.921	8.482	0.044	0.000	19.010	0.122	0.307	0.000	0.176	0.000	101.505
MS496_08299_BSE4_3	Cu-sulfide	21.955	0.007	0.003	0.000	78.401	0.000	0.000	0.000	0.026	0.042	0.024	0.000	0.012	0.000	100.471

Appendix 7-1 List of samples collected from Khusib Springs, KHD** are samples collected from drill cores, and KD**** are samples collected from the mine dumb.

No.	Interval	Reason/Idea
1	KHD06-50,74-50,84	light grey dolomite → petrography
2	KHD06-68,00-68,15	mineralization; Hem after Py?
3	KHD06-70,50-70,65	dark grey dolomite with lamination → petrography
4	KHD06-78,00-78,20	dark grey dolomite with lamination; Lim after Py?
5	KHD06-81,70-81,85	mineralisation; Ccp in dark dolomite?
6	KHD06-83,85-84,00	strange lamination → petrography
7	KHD06-106,00-106,15	mineralization
8	KHD06-110,10-110,25	rip-up clasts → petrography
9	KHD06-124,60-124,75	mineralization; Py lense?
10	KHD06-128,00-128,15	lamination; Py in layers?
11	KHD06-135,26-135,40	mineralization; Ccp disseminated?
12	KHD06-136,35-136,50	mineralization; Ccp disseminated?
13	KHD06-151,50-151,60	dark grey dolomite with lamination; → petrography
14	KHD06-226,00-226,15	strongly brecciated rock; matrix? → petrography
15	KHD06-258,65-258,80	mineralization; Tnt
16	KHD06-309,35-309,50	massive white rock; cal or dol?
17	KHD06-330,00-330,20	strongly brecciated rock; matrix? → petrography
18	KHD06-374,15-374,35	strongly brecciated rock; matrix? → petrography
19	KHD06-389,60-389,74	mineralization; Py+Ccp?
20	KHD06-398,79-398,94	mineralization; Py+Ccp?
21	KHD06-410,59-410,79	mineralization; Py+Ccp?
22	KHD06-431,05-431,20	mineralization; Py+Ccp?
23	KHD06-478,40-478,60	dark dolomite with intense dark layers → petrography
24	KHD06-502,22-502,37	mineralization; Gn
25	KHD06-503,84-504,04	mineralization; Gn
26	KS-DP-1	material old dump; superficial mineralization; massive sulfide
27	KS-DP-2	material old dump; superficial mineralization; massive sulfide
28	KS-DP-3	material old dump; superficial mineralization; massive sulfide
29	KS-DP-4	material old dump; superficial mineralization; massive sulfide
30	KS-DP-5	material old dump; quartzite? → petrography Andreas
31	KS-DP-6	material old dump; quartzite? → petrography Andreas
32	KS-DP-7	material old dump; quarzite? → petrography Andreas

Appendix 7-2 Bulk ore geochemical data of Khusib Springs deposit.

	Li	Na	Mg	Al	K	Ca	Cd	V	Cr	Mn	Fe	Hf	Ni	Er	Be	Ho	Ag	Cs	Co	Eu	Bi	Se	Zn	Ga	As	Rb	Y	Sr
	ppm	%	%	%	%	%	ppm	ppm	ppm	ppm	%	ppm	ppm	ppm	ppm	ppm	ppm	ppm	ppm	ppm	ppm	ppm	ppm	ppm	ppm	ppm	ppm	ppm	ppm
KS	3.3	0.05	6.23	0.54	0.31	5.99	67	7	8	2210	1.76	0.1	3.7	0.1	< 0.1	< 0.1	1090	0.18	31.1	0.025	0.17	55	11600	6.5	63400	10.4	1.4	68.9
KS004	2.2	0.02	0.46	0.4	0.32	41	0.3	7	9	220	0.16	< 0.1	2.6	0.2	< 0.1	< 0.1	1.02	0.27	0.7	0.12	< 0.02	1.2	47.2	0.9	97.8	9.2	2.7	908
KS005	8.2	0.02	8.2	1.38	1.02	13.8	31.6	23	27	3050	2	0.2	9.8	0.4	0.2	0.1	176	0.54	10.3	0.08	0.29	15.2	5450	14.2	20000	32.9	3.8	110
KS010	7	0.01	4.21	1.11	0.83	8.86	81.3	18	14	1280	1.62	0.3	7.6	0.3	0.2	0.1	238	0.42	29.8	0.18	0.57	97.4	14400	5.2	75400	26.2	4.1	72.9
KS013	7.1	0.02	8.02	1.09	0.78	15.7	28.3	20	54	2690	4.39	0.8	13.9	0.6	0.2	0.2	82.9	0.54	7.4	0.16	0.33	18.1	9230	5.4	1930	26.2	5.7	157
KS017	7	0.01	4.21	1.11	0.83	8.86	81.3	18	14	1280	1.62	0.3	7.6	0.3	0.2	0.1	1160	0.42	29.8	0.18	0.57	97.4	27900	5.2	80500	26.2	4.1	72.9
KS019	7.1	0.02	8.02	1.09	0.78	15.7	28.3	20	54	2690	4.39	0.8	13.9	0.6	0.2	0.2	82.9	0.54	7.4	0.16	0.33	18.1	9230	5.4	1930	26.2	5.7	157
KS020	10.6	0.02	6.76	1.75	1.33	15.6	5.9	28	16	1870	0.78	0.6	5	0.7	0.5	0.2	43.1	0.64	2.6	0.18	0.22	5.6	1190	4	3920	41.9	6.8	137
KS021	6.5	0.02	9.51	0.98	0.79	18.5	30.7	17	11	2920	1.7	0.4	5.5	0.4	0.3	0.1	114	0.41	3.4	0.14	0.1	8.3	10300	4.3	2290	24.6	4.3	131
KS022	2.3	0.02	10.4	0.22	0.19	20.7	1.8	14	5	5110	0.08	0.1	1.6	0.7	< 0.1	0.3	7.74	0.16	0.2	0.13	< 0.02	0.2	348	0.9	772	5.4	7.7	153
KS001	5.8	0.05	3.05	0.75	0.56	5.46	141	5	27	956	2.55	0.3	7.7	0.2	0.2	< 0.1	1730	0.33	30.7	0.09	1.4	312	37500	8.8	95100	19.1	2.1	49
KS012	3.5	0.05	2.86	0.42	0.29	4.91	53.1	6	7	1010	9.41	0.3	2.3	0.2	< 0.1	< 0.1	1800	0.18	14.2	0.025	2.02	202	67800	5.5	137000	11.2	1.5	39.6
KS003	3.5	0.01	4.23	0.39	0.3	7.65	188	6	7	1230	2.96	0.3	3.5	0.2	< 0.1	< 0.1	2000	0.19	26.4	0.05	1.84	122	31700	9.6	81100	10.3	2.6	62.7

Appendix 7-2 continues……

Zr	Nb	Mo	In	Sn	Sb	Te	Ba	La	Ce	Pr	Nd	Sm	Gd	Tb	Dy	Cu	Ge	Tm	Yb	Lu	Ta	W	Re	Tl	Pb	Sc	Th	U	Ti	P	S
ppm	ppm	ppm	ppm	ppm	ppm	ppm	ppm	ppm	ppm	ppm	ppm	ppm	ppm	ppm	ppm	ppm	ppm	ppm	ppm	ppm	ppm	ppm	ppm	ppm	ppm	ppm	ppm	ppm	%	%	%
4	< 0.1	3.01	0.1	< 1	8900	< 0.1	25	1.1	2.3	0.2	1.1	0.2	0.2	< 0.1	0.2	166000	30.9	< 0.1	0.1	< 0.1	< 0.1	1.7	< 0.001	0.19	10800	1	0.6	0.9	0.0056	0.104	8.93
2	0.6	0.81	< 0.1	< 1	4.8	< 0.1	28	3.6	7	0.7	2.7	0.5	0.5	< 0.1	0.4	193	< 0.1	< 0.1	0.2	< 0.1	< 0.1	0.4	< 0.001	< 0.05	286	< 1	0.7	1.5	0.0211	0.022	0.11
13	0.1	94.5	< 0.1	< 1	1200	< 0.1	77	1.3	4.5	0.6	2.6	0.7	0.6	< 0.1	0.6	33300	3.2	< 0.1	0.4	< 0.1	< 0.1	9.7	0.008	0.22	1040	2	2	7.2	0.0426	0.178	4
8	0.3	3.86	< 0.1	< 1	5400	0.1	44	6.2	12.3	1.4	5.1	0.9	0.9	0.1	0.6	177000	5.2	< 0.1	0.3	< 0.1	< 0.1	2.6	< 0.001	0.13	19400	2	1.3	1.6	0.036	0.153	11.3
32	2.8	1.43	0.1	2	34.8	< 0.1	77	4.4	10.7	1.2	5.1	1	0.9	0.1	0.8	4100	0.2	< 0.1	0.5	< 0.1	0.2	2.3	0.022	0.17	1480	2	2.5	3	0.0861	0.126	6.9
8	0.3	3.86	< 0.1	< 1	16600	0.1	44	6.2	12.3	1.4	5.1	0.9	0.9	0.1	0.6	203000	5.2	< 0.1	0.3	< 0.1	< 0.1	2.6	< 0.001	0.13	94200	2	1.3	1.6	0.036	0.153	11.3
32	2.8	1.43	0.1	2	6400	< 0.1	77	4.4	10.7	1.2	5.1	1	0.9	0.1	0.8	170000	0.2	< 0.1	0.5	< 0.1	0.2	2.3	0.022	0.17	1480	2	2.5	3	0.0861	0.126	6.9
29	0.2	1.08	< 0.1	< 1	104	< 0.1	94	5.8	13.7	1.6	6.4	1	1.3	0.2	1.1	11100	1	0.1	0.7	0.1	< 0.1	2.4	< 0.001	0.2	1150	4	3	3.3	0.0781	0.089	1
16	1.4	0.63	< 0.1	3	55	< 0.1	78	2.5	6.7	0.8	3.2	0.6	0.7	0.1	0.6	5080	< 0.1	< 0.1	0.4	< 0.1	< 0.1	0.9	< 0.001	0.14	398	2	1.2	1	0.0493	0.07	2.22
6	0.5	0.49	< 0.1	< 1	8.3	< 0.1	16	2.7	7.9	1.1	4.7	1.2	1.3	0.2	1.3	1590	< 0.1	< 0.1	0.5	< 0.1	< 0.1	0.5	< 0.001	< 0.05	13.9	< 1	0.5	0.5	0.0125	0.016	0.12
7	< 0.1	3.86	< 0.1	2	7700	< 0.1	25	1.3	3.9	0.5	2.1	0.5	0.4	< 0.1	0.3	211000	1.2	< 0.1	0.2	< 0.1	< 0.1	1.2	< 0.001	0.14	22000	1	1.1	1	0.023	0.15	16.3
6	0.6	3.4	< 0.1	2	8300	< 0.1	5	0.8	2.1	0.3	1.3	0.2	0.3	< 0.1	0.2	185000	29.4	< 0.1	0.1	< 0.1	< 0.1	28.7	< 0.001	0.14	78100	< 1	0.7	1.2	0.0263	0.083	> 20.0
3	< 0.1	3.87	0.1	1	17400	< 0.1	14	1.4	3.4	0.4	1.8	0.4	0.4	< 0.1	0.4	373000	3.3	< 0.1	0.2	< 0.1	< 0.1	0.9	< 0.001	0.09	22000	< 1	1.2	1	0.0172	0.097	15.6

Appendix 7-3 EPMA results of sulfide mineralisation of the Khusib Springs deposit.

		Weight%												
		S	Mn	Fe	Cu	Zn	Ga	Pb	Ag	Sb	As	In	Ge	Total gerechnet
Pyrite		***53.45***		***46.55***										
KS-DP-26	19 / 1 .	53.58	0.00	45.32	0.80	0.00	0.00	0.29	0.00	0.00	0.00	0.00	0.00	100.00
KS-DP-26	20 / 1 .	53.72	0.00	45.43	0.68	0.00	0.00	0.25	0.00	0.00	0.00	0.00	0.00	100.08
KS-DP-26	31 / 1 .	53.27	0.00	45.25	0.32	0.00	0.00	0.31	0.00	0.00	0.00	0.00	0.00	99.16
KS-DP-26	32 / 1 .	53.21	0.00	45.14	1.03	0.00	0.00	0.00	0.00	0.00	0.00	0.00	0.00	99.38
KS-DP-26	33 / 1 .	53.50	0.00	44.62	0.93	0.00	0.00	0.00	0.00	0.00	0.00	0.00	0.00	99.06
KS-DP-26	53 / 1 .	53.20	0.00	44.63	1.36	0.00	0.00	0.32	0.00	0.00	0.00	0.00	0.00	99.51
KS-DP-26	54 / 1 .	53.51	0.00	45.01	1.05	0.00	0.00	0.30	0.00	0.00	0.00	0.00	0.00	99.87
KS-DP-26	55 / 1 .	53.52	0.00	45.64	0.29	0.00	0.00	0.00	0.00	0.00	0.00	0.00	0.00	99.46
KS-DP-26	56 / 1 .	53.38	0.00	45.72	0.00	0.39	0.00	0.00	0.00	0.00	0.00	0.00	0.00	99.50
KS-DP-26	57 / 1 .	53.35	0.00	45.45	1.00	0.00	0.00	0.00	0.00	0.00	0.00	0.00	0.00	99.79
KS-DP-26	82 / 1 .	53.58	0.00	45.28	0.62	0.00	0.00	0.00	0.00	0.00	0.00	0.00	0.00	99.48
KS-DP-26	83 / 1 .	53.42	0.00	44.91	0.67	0.00	0.00	0.34	0.00	0.00	0.00	0.00	0.00	99.33
KS-DP-26	84 / 1 .	53.16	0.00	45.89	0.50	0.00	0.00	0.33	0.00	0.00	0.00	0.00	0.00	99.88
KS-DP-26	85 / 1 .	53.48	0.00	45.52	0.46	0.00	0.00	0.28	0.00	0.00	0.00	0.00	0.00	99.73
KS-DP-26	86 / 1 .	53.80	0.00	45.85	0.00	0.00	0.00	0.00	0.00	0.00	0.00	0.00	0.00	99.65
KS-DP-26	132 / 1 .	53.28	0.00	45.54	1.03	0.00	0.00	0.00	0.00	0.00	0.00	0.00	0.00	99.84
KS-DP-26	133 / 1 .	53.29	0.00	45.27	0.80	0.00	0.00	0.00	0.00	0.00	0.00	0.00	0.00	99.36
KS-DP-26	134 / 1 .	53.35	0.00	46.14	0.72	0.00	0.00	0.00	0.00	0.00	0.00	0.00	0.00	100.21
KS-DP-26	135 / 1 .	53.53	0.00	45.63	0.35	0.00	0.00	0.39	0.00	0.00	0.00	0.00	0.00	99.90
KS-DP-26	136 / 1 .	53.61	0.00	45.34	0.84	0.00	0.00	0.00	0.00	0.00	0.00	0.00	0.00	99.80
KS-DP-26	137 / 1 .	53.48	0.00	45.16	0.95	0.00	0.00	0.00	0.00	0.00	0.00	0.00	0.00	99.59
KS-DP-26	138 / 1 .	53.62	0.00	45.03	0.69	0.00	0.00	0.00	0.00	0.00	0.00	0.00	0.00	99.34
KS-DP-26	139 / 1 .	53.39	0.00	46.02	0.91	0.00	0.00	0.00	0.00	0.00	0.00	0.00	0.00	100.31
KS-DP-26	140 / 1 .	53.68	0.00	45.19	0.97	0.00	0.00	0.00	0.00	0.00	0.00	0.00	0.00	99.83
KS-DP-26	141 / 1 .	53.33	0.00	45.24	1.10	0.00	0.00	0.28	0.00	0.00	0.00	0.00	0.00	99.95
KS-DP-26	162 / 1 .	53.34	0.00	45.79	0.47	0.00	0.00	0.33	0.00	0.00	0.00	0.00	0.00	99.92
KS-DP-26	163 / 1 .	53.50	0.00	45.05	0.91	0.00	0.00	0.33	0.00	0.00	0.00	0.00	0.00	99.80
KS-DP-26	164 / 1 .	53.60	0.00	45.77	0.00	0.00	0.00	0.31	0.00	0.00	0.00	0.00	0.00	99.67
KS-DP-26	165 / 1 .	53.51	0.00	45.77	0.00	0.00	0.00	0.00	0.00	0.00	0.39	0.00	0.00	99.67
KS-DP-26	166 / 1 .	53.70	0.00	46.17	0.00	0.00	0.00	0.00	0.00	0.00	0.00	0.00	0.00	99.87
KS-DP-26	187 / 1 .	53.92	0.00	46.15	0.39	0.00	0.00	0.30	0.00	0.00	0.00	0.00	0.00	100.76
KS-DP-26	188 / 1 .	53.32	0.00	45.01	0.85	0.00	0.00	0.28	0.00	0.00	0.00	0.00	0.00	99.46
KS-DP-26	189 / 1 .	53.51	0.00	45.30	0.56	0.00	0.00	0.00	0.00	0.00	0.00	0.00	0.00	99.37
KS-DP-26	190 / 1 .	53.78	0.00	46.06	0.72	0.00	0.00	0.26	0.00	0.00	0.00	0.00	0.00	100.82
KS-DP-26	191 / 1 .	53.23	0.00	45.25	0.68	0.00	0.00	0.41	0.00	0.00	0.00	0.00	0.00	99.57
KS-DP-26	207 / 1 .	53.56	0.00	44.91	0.60	0.00	0.00	0.34	0.00	0.00	0.00	0.00	0.00	99.40
KS-DP-26	208 / 1 .	53.57	0.00	45.14	0.71	0.00	0.00	0.00	0.00	0.00	0.00	0.00	0.00	99.41
KS-DP-26	209 / 1 .	53.33	0.00	45.39	0.51	0.00	0.00	0.00	0.00	0.00	0.00	0.00	0.00	99.22
KS-DP-26	210 / 1 .	53.64	0.00	46.24	0.00	0.48	0.00	0.00	0.00	0.00	0.00	0.00	0.00	100.36
KS-DP-26	211 / 1 .	53.33	0.00	45.63	1.13	0.00	0.00	0.00	0.00	0.00	0.00	0.00	0.00	100.09
KS-DP-28	17 / 1 .	53.32	0.00	45.10	1.17	0.00	0.00	0.00	0.00	0.00	0.00	0.00	0.00	99.58

KS-DP-28	18 / 1 .	53.15	0.00	46.77	0.00	0.00	0.00	0.00	0.00	0.00	0.00	0.00	0.00	99.92
KS-DP-28	19 / 1 .	52.96	0.00	45.87	0.00	0.00	0.00	0.34	0.00	0.00	0.00	0.00	0.00	99.16
KS-DP-28	20 / 1 .	53.35	0.00	46.15	0.34	0.00	0.00	0.00	0.00	0.00	0.00	0.00	0.00	99.83
KS-DP-28	21 / 1 .	53.15	0.00	45.59	0.00	0.00	0.00	0.38	0.00	0.00	0.00	0.00	0.00	99.13
KS-DP-28	42 / 1 .	53.30	0.00	45.76	0.00	0.00	0.00	0.00	0.00	0.00	0.00	0.00	0.00	99.06
KS-DP-28	43 / 1 .	53.30	0.00	45.91	0.44	0.00	0.00	0.36	0.00	0.00	0.00	0.00	0.00	100.00
KS-DP-28	44 / 1 .	53.45	0.00	45.36	0.00	0.00	0.00	0.31	0.00	0.00	0.00	0.00	0.00	99.12
KS-DP-28	45 / 1 .	53.17	0.00	45.74	0.00	0.00	0.00	0.31	0.00	0.00	0.00	0.00	0.00	99.23
KS-DP-28	61 / 1 .	53.28	0.00	45.90	0.00	0.00	0.00	0.00	0.00	0.00	0.00	0.00	0.00	99.18
KS-DP-28	62 / 1 .	53.35	0.00	45.74	0.00	0.00	0.00	0.33	0.00	0.00	0.00	0.00	0.00	99.41
KS-DP-28	63 / 1 .	53.40	0.00	45.72	0.00	0.00	0.00	0.00	0.00	0.00	0.00	0.00	0.00	99.12
KS-DP-28	64 / 1 .	53.41	0.00	45.66	0.00	0.00	0.00	0.00	0.00	0.00	0.00	0.00	0.00	99.07
KS-DP-28	65 / 1 .	53.23	0.00	46.26	0.00	0.00	0.00	0.00	0.00	0.00	0.00	0.00	0.00	99.49
Galena		***13.40***						***86.60***						
KS-DP-26	21 / 1 .	13.69	0.00	0.00	0.00	0.00	0.00	85.40	0.00	0.00	0.00	0.00	0.00	99.09
KS-DP-26	22 / 1 .	13.76	0.00	0.00	0.00	0.00	0.00	86.57	0.00	0.00	0.00	0.00	0.00	100.34
KS-DP-26	34 / 1 .	13.78	0.00	0.00	0.00	0.00	0.00	85.49	0.00	0.00	0.00	0.00	0.00	99.27
KS-DP-26	35 / 1 .	13.71	0.00	0.00	0.00	0.00	0.00	86.33	0.00	0.00	0.00	0.00	0.00	100.04
KS-DP-26	36 / 1 .	13.67	0.00	0.00	0.00	0.00	0.00	86.56	0.00	0.00	0.00	0.00	0.00	100.22
KS-DP-26	63 / 1 .	13.72	0.00	0.29	0.52	0.00	0.00	85.25	0.00	0.00	0.00	0.00	0.00	99.78
KS-DP-26	64 / 1 .	13.73	0.00	0.22	0.00	0.00	0.00	85.99	0.00	0.00	0.00	0.00	0.00	99.94
KS-DP-26	65 / 1 .	13.66	0.00	0.39	0.38	0.00	0.00	86.55	0.00	0.00	0.00	0.00	0.00	100.98
KS-DP-26	66 / 1 .	13.74	0.00	0.31	0.48	0.00	0.00	85.51	0.00	0.00	0.00	0.00	0.00	100.04
KS-DP-26	67 / 1 .	13.93	0.00	0.26	1.52	0.00	0.00	85.25	0.00	0.00	0.00	0.00	0.00	100.96
KS-DP-26	92 / 1 .	13.65	0.00	0.00	0.00	0.00	0.00	86.61	0.00	0.00	0.00	0.00	0.00	100.26
KS-DP-26	93 / 1 .	13.46	0.00	0.00	0.00	0.00	0.00	85.71	0.00	0.00	0.00	0.00	0.00	99.17
KS-DP-26	94 / 1 .	13.67	0.00	0.00	0.00	0.00	0.00	86.33	0.00	0.00	0.00	0.00	0.00	100.01
KS-DP-26	95 / 1 .	13.68	0.00	0.00	0.00	0.00	0.00	86.37	0.00	0.00	0.00	0.00	0.00	100.05
KS-DP-26	96 / 1 .	13.73	0.00	0.00	0.00	0.00	0.00	85.42	0.00	0.00	0.00	0.00	0.00	99.15
KS-DP-26	102 / 1 .	13.88	0.00	0.00	0.00	0.69	0.00	85.52	0.00	0.00	0.00	0.00	0.00	100.10
KS-DP-26	103 / 1 .	13.74	0.00	0.00	1.37	0.47	0.00	85.15	0.00	0.00	0.00	0.00	0.00	100.73
KS-DP-26	104 / 1 .	13.66	0.00	0.00	1.47	0.00	0.00	85.80	0.00	0.00	0.00	0.00	0.00	100.94
KS-DP-26	105 / 1 .	13.87	0.00	0.00	1.37	0.00	0.00	85.10	0.00	0.00	0.00	0.00	0.00	100.34
KS-DP-26	106 / 1 .	13.65	0.00	0.00	1.73	0.00	0.00	84.76	0.00	0.00	0.00	0.00	0.00	100.14
KS-DP-26	112 / 1 .	13.79	0.00	0.00	0.00	0.00	0.00	85.61	0.00	0.00	0.00	0.00	0.00	99.40
KS-DP-26	113 / 1 .	13.74	0.00	0.00	0.00	0.00	0.00	85.48	0.00	0.00	0.00	0.00	0.00	99.22
KS-DP-26	114 / 1 .	13.78	0.00	0.00	0.37	0.53	0.00	85.99	0.00	0.00	0.00	0.00	0.00	100.67
KS-DP-26	115 / 1 .	13.81	0.00	0.00	0.00	0.00	0.00	85.38	0.00	0.00	0.00	0.00	0.00	99.19
KS-DP-26	116 / 1 .	13.80	0.00	0.00	0.72	0.00	0.00	85.95	0.00	0.00	0.00	0.00	0.00	100.47
KS-DP-26	147 / 1 .	13.51	0.00	0.00	0.00	0.00	0.00	86.66	0.00	0.00	0.00	0.00	0.00	100.16
KS-DP-26	148 / 1 .	13.59	0.00	0.00	0.00	0.00	0.00	86.50	0.00	0.00	0.00	0.00	0.00	100.09
KS-DP-26	149 / 1 .	13.52	0.00	0.00	0.00	0.00	0.00	85.83	0.00	0.00	0.00	0.00	0.00	99.35
KS-DP-26	150 / 1 .	13.75	0.00	0.00	0.00	0.00	0.00	86.25	0.00	0.00	0.00	0.00	0.00	99.99
KS-DP-26	151 / 1 .	13.62	0.00	0.00	0.00	0.00	0.00	85.94	0.00	0.00	0.00	0.00	0.00	99.55
KS-DP-26	172 / 1 .	13.35	0.00	0.00	0.00	0.00	0.00	86.75	0.00	0.00	0.00	0.00	0.00	100.10

KS-DP-26	173 / 1 .	13.55	0.00	0.00	0.00	0.00	0.00	86.37	0.00	0.00	0.00	0.00	0.00	99.92
KS-DP-26	174 / 1 .	13.64	0.00	0.00	0.00	0.00	0.00	85.88	0.00	0.00	0.00	0.00	0.00	99.52
KS-DP-26	175 / 1 .	13.70	0.00	0.00	0.00	0.00	0.00	86.81	0.00	0.00	0.00	0.00	0.00	100.52
KS-DP-26	176 / 1 .	13.62	0.00	0.00	0.00	0.00	0.00	86.33	0.00	0.00	0.00	0.00	0.00	99.94
KS-DP-26	197 / 1 .	13.58	0.00	0.38	0.00	0.00	0.00	85.70	0.00	0.00	0.00	0.00	0.00	99.66
KS-DP-26	198 / 1 .	13.59	0.00	0.50	0.00	0.00	0.00	85.89	0.00	0.00	0.00	0.00	0.00	99.98
KS-DP-26	199 / 1 .	13.58	0.00	0.51	0.00	0.00	0.00	85.92	0.00	0.00	0.00	0.00	0.00	100.01
KS-DP-26	200 / 1 .	13.58	0.00	0.47	0.37	0.00	0.00	86.58	0.00	0.00	0.00	0.00	0.00	101.00
KS-DP-26	201 / 1 .	13.43	0.00	0.58	0.00	0.00	0.00	85.28	0.00	0.00	0.00	0.00	0.00	99.29
KS-DP-26	212 / 1 .	13.56	0.00	0.00	0.00	0.00	0.00	86.42	0.00	0.00	0.00	0.00	0.00	99.99
KS-DP-26	213 / 1 .	13.67	0.00	0.00	0.00	0.00	0.00	85.92	0.00	0.00	0.00	0.00	0.00	99.59
KS-DP-26	214 / 1 .	13.67	0.00	0.00	0.00	0.00	0.00	86.04	0.00	0.00	0.00	0.00	0.00	99.72
KS-DP-26	215 / 1 .	13.56	0.00	0.00	0.00	0.00	0.00	86.40	0.00	0.00	0.00	0.00	0.00	99.96
KS-DP-26	216 / 1 .	13.65	0.00	0.00	0.00	0.00	0.00	86.06	0.00	0.00	0.00	0.00	0.00	99.70
KS-DP-28	22 / 1 .	13.54	0.00	0.00	0.00	0.00	0.00	85.56	0.00	0.00	0.00	0.00	0.00	99.11
KS-DP-28	23 / 1 .	13.49	0.00	0.00	0.00	0.00	0.00	86.64	0.00	0.00	0.00	0.00	0.00	100.13
KS-DP-28	24 / 1 .	13.56	0.00	0.00	0.00	0.00	0.00	86.51	0.00	0.00	0.00	0.00	0.00	100.07
KS-DP-28	25 / 1 .	13.58	0.00	0.00	0.00	0.00	0.00	85.77	0.00	0.00	0.00	0.00	0.00	99.35
KS-DP-28	26 / 1 .	13.52	0.00	0.00	0.00	0.00	0.00	86.21	0.00	0.00	0.00	0.00	0.00	99.74
KS-DP-28	46 / 1 .	13.68	0.00	0.00	0.00	0.00	0.00	86.37	0.00	0.00	0.00	0.00	0.00	100.05
KS-DP-28	47 / 1 .	13.66	0.00	0.00	0.00	0.00	0.00	86.51	0.00	0.00	0.00	0.00	0.00	100.17
KS-DP-28	48 / 1 .	13.63	0.00	0.00	0.00	0.00	0.00	85.81	0.00	0.00	0.00	0.00	0.00	99.43
KS-DP-28	49 / 1 .	13.65	0.00	0.00	0.00	0.00	0.00	86.39	0.00	0.00	0.00	0.00	0.00	100.04
KS-DP-28	50 / 1 .	13.44	0.00	0.00	0.00	0.00	0.00	86.82	0.00	0.00	0.00	0.00	0.00	100.26
KS-DP-28	51 / 1 .	13.50	0.00	0.00	0.00	0.00	0.00	85.64	0.00	0.00	0.00	0.00	0.00	99.14
KS-DP-28	66 / 1 .	13.73	0.00	0.00	0.00	0.00	0.00	85.62	0.00	0.00	0.00	0.00	0.00	99.35
KS-DP-28	67 / 1 .	13.59	0.00	0.00	0.00	0.00	0.00	85.46	0.00	0.00	0.00	0.00	0.00	99.06
KS-DP-28	68 / 1 .	13.52	0.00	0.00	0.00	0.00	0.00	85.48	0.00	0.00	0.00	0.00	0.00	99.00
KS-DP-28	69 / 1 .	13.67	0.00	0.00	0.00	0.00	0.00	86.15	0.00	0.00	0.00	0.00	0.00	99.82
KS-DP-28	70 / 1 .	13.51	0.00	0.00	0.00	0.00	0.00	86.52	0.00	0.00	0.00	0.00	0.00	100.04
KS-DP-28	76 / 1 .	13.58	0.00	0.00	0.00	0.00	0.00	85.45	0.00	0.00	0.00	0.00	0.00	99.02
KS-DP-28	77 / 1 .	13.64	0.00	0.00	0.00	0.00	0.00	86.42	0.00	0.00	0.00	0.00	0.00	100.06
KS-DP-28	78 / 1 .	13.62	0.00	0.00	0.00	0.00	0.00	85.63	0.00	0.00	0.00	0.00	0.00	99.26
KS-DP-28	79 / 1 .	13.57	0.00	0.00	0.00	0.00	0.00	86.47	0.00	0.00	0.00	0.00	0.00	100.04
KS-DP-28	80 / 1 .	13.64	0.00	0.00	0.00	0.00	0.00	86.01	0.00	0.00	0.00	0.00	0.00	99.65
KS-DP-28	111 / 1 .	13.53	0.00	0.00	0.00	0.00	0.00	85.96	0.00	0.00	0.00	0.00	0.00	99.49
KS-DP-28	112 / 1 .	13.57	0.00	0.00	0.00	0.00	0.00	86.40	0.00	0.00	0.00	0.00	0.00	99.97
KS-DP-28	113 / 1 .	13.34	0.00	0.00	0.00	0.00	0.00	86.18	0.00	0.00	0.00	0.00	0.00	99.52
KS-DP-28	114 / 1 .	13.46	0.00	0.00	0.00	0.00	0.00	86.13	0.00	0.00	0.00	0.00	0.00	99.59
KS-DP-28	115 / 1 .	13.57	0.00	0.00	0.00	0.00	0.00	85.59	0.00	0.00	0.00	0.00	0.00	99.17
Sphalerite		***33.06***		***2.88***		***64.06***								
KS-DP-26	97 / 1 .	32.84	0.00	0.20	0.00	66.76	0.00	0.00	0.00	0.00	0.00	0.00	0.00	99.80
KS-DP-26	98 / 1 .	33.03	0.00	0.00	0.38	65.84	0.00	0.00	0.00	0.00	0.00	0.00	0.00	99.25
KS-DP-26	99 / 1 .	32.91	0.00	0.41	0.51	66.66	0.00	0.00	0.00	0.00	0.00	0.00	0.00	100.49
KS-DP-26	100 / 1 .	33.19	0.00	0.42	0.46	65.99	0.00	0.00	0.00	0.00	0.00	0.00	0.00	100.07

KS-DP-26	101 / 1 .	32.68	0.00	0.38	0.50	66.45	0.00	0.00	0.00	0.00	0.00	0.00	0.00	100.02
KS-DP-26	117 / 1 .	32.91	0.00	0.78	0.33	66.43	0.00	0.00	0.00	0.00	0.00	0.00	0.00	100.46
KS-DP-26	118 / 1 .	32.87	0.00	0.87	0.47	65.69	0.00	0.00	0.00	0.00	0.00	0.00	0.00	99.90
KS-DP-26	119 / 1 .	32.85	0.00	0.35	0.90	66.43	0.00	0.00	0.00	0.00	0.00	0.00	0.00	100.54
KS-DP-26	120 / 1 .	32.92	0.00	0.35	0.45	66.02	0.00	0.00	0.00	0.00	0.00	0.00	0.00	99.74
KS-DP-26	121 / 1 .	32.80	0.00	0.28	1.06	66.31	0.00	0.00	0.00	0.00	0.00	0.00	0.00	100.45
KS-DP-26	152 / 1 .	33.07	0.00	0.31	0.00	67.08	0.00	0.00	0.00	0.00	0.00	0.00	0.00	100.45
KS-DP-26	153 / 1 .	32.68	0.00	0.22	0.00	66.77	0.00	0.00	0.00	0.00	0.00	0.00	0.00	99.67
KS-DP-26	154 / 1 .	33.00	0.00	0.00	0.00	66.60	0.00	0.00	0.00	0.00	0.00	0.00	0.00	99.60
KS-DP-26	155 / 1 .	33.07	0.00	0.21	0.00	66.03	0.00	0.00	0.00	0.00	0.00	0.00	0.00	99.30
KS-DP-26	156 / 1 .	32.93	0.00	0.19	0.00	66.78	0.00	0.00	0.00	0.00	0.00	0.00	0.00	99.90
KS-DP-26	177 / 1 .	32.77	0.00	0.25	0.00	67.66	0.00	0.00	0.00	0.00	0.00	0.00	0.00	100.68
KS-DP-26	178 / 1 .	32.78	0.00	0.34	0.00	67.04	0.00	0.00	0.00	0.00	0.00	0.00	0.00	100.15
KS-DP-26	179 / 1 .	32.97	0.00	0.27	0.00	66.20	0.00	0.00	0.00	0.00	0.00	0.00	0.00	99.43
KS-DP-26	180 / 1 .	33.03	0.00	0.28	0.00	67.52	0.00	0.00	0.00	0.00	0.00	0.00	0.00	100.82
KS-DP-26	181 / 1 .	32.83	0.00	0.27	0.00	67.08	0.00	0.00	0.00	0.00	0.00	0.00	0.00	100.17
KS-DP-28	27 / 1 .	32.67	0.00	0.00	0.00	66.40	0.00	0.00	0.00	0.00	0.00	0.00	0.00	99.07
KS-DP-28	28 / 1 .	32.83	0.00	0.00	0.35	67.63	0.00	0.00	0.00	0.00	0.00	0.00	0.00	100.80
KS-DP-28	29 / 1 .	32.59	0.00	0.00	0.47	67.28	0.00	0.00	0.00	0.00	0.00	0.00	0.00	100.34
KS-DP-28	30 / 1 .	32.72	0.00	0.00	0.62	66.13	0.00	0.00	0.00	0.00	0.00	0.00	0.00	99.47
KS-DP-28	31 / 1 .	32.73	0.00	0.00	0.59	65.93	0.00	0.31	0.00	0.00	0.00	0.00	0.00	99.55
KS-DP-28	57 / 1 .	32.59	0.00	0.00	0.00	67.41	0.00	0.38	0.00	0.00	0.00	0.00	0.00	100.37
KS-DP-28	58 / 1 .	32.77	0.00	0.00	0.00	67.38	0.00	0.00	0.15	0.00	0.00	0.00	0.00	100.30
KS-DP-28	59 / 1 .	32.60	0.00	0.00	0.00	68.05	0.00	0.00	0.00	0.00	0.00	0.00	0.00	100.65
KS-DP-28	60 / 1 .	32.68	0.00	0.00	0.00	66.86	0.00	0.00	0.00	0.00	0.00	0.00	0.00	99.54
KS-DP-28	91 / 1 .	32.46	0.00	0.19	0.86	66.49	0.00	0.00	0.14	0.00	0.00	0.00	0.25	100.39
KS-DP-28	92 / 1 .	32.81	0.00	0.00	0.65	66.36	0.00	0.00	0.00	0.00	0.00	0.00	0.00	99.82
KS-DP-28	93 / 1 .	32.91	0.00	0.00	0.72	66.12	0.00	0.00	0.00	0.00	0.00	0.00	0.00	99.75
KS-DP-28	94 / 1 .	32.85	0.00	0.00	1.19	65.23	0.00	0.00	0.14	0.00	0.00	0.00	0.00	99.41
KS-DP-28	95 / 1 .	32.59	0.00	0.00	0.91	65.89	0.00	0.00	0.00	0.00	0.00	0.00	0.00	99.38
KS-DP-28	121 / 1 .	32.90	0.00	0.14	0.00	66.01	0.00	0.00	0.00	0.00	0.00	0.00	0.00	99.04
KS-DP-28	122 / 1 .	32.57	0.00	0.00	0.00	67.16	0.00	0.00	0.00	0.00	0.00	0.00	0.00	99.73
KS-DP-28	123 / 1 .	32.71	0.00	0.00	0.00	66.97	0.00	0.00	0.00	0.00	0.00	0.00	0.00	99.68
KS-DP-28	124 / 1 .	32.64	0.00	0.00	0.00	67.27	0.00	0.00	0.00	0.00	0.00	0.00	0.00	99.91
KS-DP-28	125 / 1 .	32.63	0.00	0.00	0.52	66.93	0.00	0.00	0.00	0.00	0.00	0.00	0.00	100.08
Chalcopyrite		***34.94***		***30.43***	***34.63***									
KS-DP-26	42 / 1 .	34.21	0.00	30.54	33.14	0.00	0.00	1.38	0.94	0.06	0.38	0.00	0.00	100.65
KS-DP-26	43 / 1 .	30.13	0.00	22.41	32.62	2.24	0.00	5.49	0.38	0.25	6.26	0.00	0.00	99.79
KS-DP-26	44 / 1 .	33.29	0.00	26.70	35.67	0.00	0.00	4.26	0.34	0.00	0.00	0.00	0.00	100.25
KS-DP-26	46 / 1 .	32.86	0.00	25.00	36.26	0.00	0.00	5.23	0.51	0.00	0.00	0.00	0.00	99.85
KS-DP-26	47 / 1 .	32.64	0.00	25.33	33.66	0.00	0.00	7.67	0.22	0.08	0.00	0.00	0.00	99.60
KS-DP-26	75 / 1 .	32.71	0.00	29.43	37.47	0.00	0.00	0.32	0.43	0.00	0.00	0.00	0.00	100.36
KS-DP-26	227 / 1 .	34.05	0.00	30.72	33.03	0.00	0.00	0.83	0.66	0.19	0.40	0.00	0.00	99.87
KS-DP-26	229 / 1 .	34.57	0.00	30.12	31.70	0.00	0.00	1.36	1.30	0.32	0.52	0.00	0.00	99.89
KS-DP-26	231 / 1 .	34.58	0.00	29.70	34.38	0.00	0.00	0.35	0.49	0.00	0.36	0.00	0.00	99.86

KS-DP-28	32 / 1 .	34.95	0.00	30.79	34.36	0.00	0.00	0.00	0.00	0.00	0.00	0.00	0.00	100.10
KS-DP-28	33 / 1 .	34.79	0.00	30.56	34.72	0.00	0.00	0.00	0.13	0.00	0.00	0.00	0.00	100.19
KS-DP-28	34 / 1 .	34.79	0.00	31.07	34.77	0.00	0.00	0.00	0.00	0.00	0.00	0.00	0.00	100.63
KS-DP-28	35 / 1 .	34.72	0.00	30.86	34.74	0.00	0.00	0.00	0.00	0.00	0.00	0.00	0.00	100.32
KS-DP-28	36 / 1 .	34.81	0.00	30.31	34.19	0.00	0.00	0.00	0.17	0.00	0.00	0.00	0.00	99.48
KS-DP-28	86 / 1 .	34.97	0.00	30.77	33.59	0.00	0.00	0.00	0.13	0.00	0.00	0.00	0.00	99.45
KS-DP-28	87 / 1 .	34.52	0.00	30.57	34.20	0.00	0.00	0.28	0.15	0.00	0.00	0.00	0.00	99.71
KS-DP-28	88 / 1 .	34.74	0.00	30.53	34.47	0.00	0.00	0.00	0.00	0.00	0.00	0.00	0.00	99.73
KS-DP-28	89 / 1 .	34.67	0.00	30.50	33.67	0.00	0.00	0.00	0.13	0.00	0.08	0.00	0.00	99.04
KS-DP-28	90 / 1 .	34.80	0.00	29.71	34.29	0.00	0.00	0.43	0.21	0.00	0.00	0.00	0.00	99.44
KS-DP-28	102 / 1 .	34.77	0.00	29.91	34.38	0.00	0.00	0.00	0.17	0.00	0.20	0.00	0.00	99.44
KS-DP-28	103 / 1 .	34.81	0.00	30.40	33.91	0.00	0.00	0.00	0.22	0.00	0.00	0.00	0.00	99.34
KS-DP-28	104 / 1 .	34.81	0.00	29.12	34.86	0.00	0.00	0.00	0.25	0.00	0.10	0.00	0.00	99.14
KS-DP-28	105 / 1 .	34.85	0.00	30.66	33.69	0.00	0.00	0.00	0.14	0.00	0.11	0.00	0.00	99.45
KS-DP-28	126 / 1 .	34.84	0.00	30.46	33.70	0.00	0.00	0.00	0.21	0.00	0.00	0.00	0.00	99.21
KS-DP-28	127 / 1 .	34.85	0.00	30.56	34.10	0.00	0.00	0.31	0.00	0.00	0.00	0.00	0.00	99.82
KS-DP-28	128 / 1 .	34.73	0.00	30.37	33.57	0.00	0.00	0.31	0.18	0.00	0.00	0.00	0.00	99.16
KS-DP-28	129 / 1 .	34.90	0.00	30.86	33.84	0.00	0.00	0.00	0.16	0.00	0.00	0.00	0.00	99.77
KS-DP-28	130 / 1 .	34.86	0.00	30.61	33.87	0.00	0.00	0.00	0.25	0.00	0.00	0.00	0.00	99.60
KS-DP-28	131 / 1 .	34.80	0.00	30.35	33.96	0.00	0.00	0.00	0.41	0.00	0.00	0.00	0.00	99.52
KS-DP-28	132 / 1 .	34.89	0.00	30.72	33.71	0.00	0.00	0.00	0.20	0.00	0.09	0.00	0.00	99.61
KS-DP-28	133 / 1 .	34.60	0.00	29.84	34.54	0.00	0.00	0.36	0.22	0.00	0.00	0.00	0.00	99.55
KS-DP-28	134 / 1 .	34.90	0.00	30.70	33.78	0.00	0.00	0.00	0.00	0.00	0.00	0.00	0.00	99.38
KS-DP-28	135 / 1 .	34.74	0.00	30.90	33.47	0.00	0.00	0.00	0.15	0.00	0.00	0.00	0.00	99.27
Digenite		***21.90***			***78.10***									
KS-DP-26	122 / 1 .	21.67	0.00	0.40	76.71	0.43	0.00	0.31	0.30	0.00	0.00	0.00	0.00	99.82
KS-DP-26	29 / 1 .	21.87	0.00	1.65	76.80	0.00	0.00	0.27	0.39	0.00	0.00	0.00	0.00	100.99
KS-DP-26	30 / 1 .	21.95	0.00	1.78	76.38	0.00	0.00	0.00	0.46	0.00	0.00	0.00	0.00	100.56
KS-DP-26	68 / 1 .	21.78	0.00	1.34	77.32	0.00	0.00	0.00	0.55	0.00	0.00	0.00	0.00	100.98
KS-DP-26	69 / 1 .	21.53	0.00	1.19	76.74	0.00	0.00	0.00	0.66	0.00	0.00	0.00	0.00	100.13
KS-DP-26	70 / 1 .	21.92	0.00	1.43	76.73	0.00	0.00	0.00	0.40	0.00	0.00	0.00	0.00	100.49
KS-DP-26	71 / 1 .	23.75	0.00	1.35	74.45	0.00	0.00	0.00	0.34	0.31	0.00	0.00	0.00	100.20
KS-DP-26	123 / 1 .	21.87	0.00	0.45	77.59	0.00	0.00	0.00	0.40	0.00	0.00	0.00	0.00	100.30
KS-DP-26	124 / 1 .	21.92	0.00	0.45	78.00	0.00	0.00	0.00	0.32	0.00	0.00	0.00	0.00	100.70
KS-DP-26	125 / 1 .	21.53	0.00	0.44	77.10	0.00	0.00	0.00	0.37	0.00	0.00	0.00	0.00	99.45
KS-DP-26	157 / 1 .	21.96	0.00	0.00	76.43	1.56	0.00	0.00	0.00	0.00	0.00	0.00	0.00	99.96
KS-DP-26	158 / 1 .	22.16	0.00	0.16	75.37	1.83	0.00	0.00	0.17	0.00	0.00	0.00	0.00	99.67
KS-DP-26	159 / 1 .	22.03	0.00	0.00	76.51	1.42	0.00	0.00	0.00	0.00	0.96	0.00	0.00	100.91
KS-DP-26	160 / 1 .	21.85	0.00	0.16	75.90	1.46	0.00	0.00	0.00	0.00	0.94	0.00	0.00	100.31
KS-DP-26	161 / 1 .	21.73	0.00	0.00	76.25	1.76	0.00	0.00	0.14	0.00	0.00	0.00	0.00	99.88
Tennantite		***28.33***		***3.80***	***47.51***						***20.37***			
KS-DP-26	23 / 1 .	28.21	0.00	2.38	44.06	5.71	0.00	0.35	0.32	1.67	17.67	0.00	0.00	100.38
KS-DP-26	24 / 1 .	28.07	0.00	2.35	44.36	5.40	0.00	0.00	0.23	1.68	17.78	0.00	0.00	99.86
KS-DP-26	37 / 1 .	27.90	0.00	2.33	43.66	5.95	0.00	0.00	0.22	1.53	17.70	0.00	0.00	99.29

KS-DP-26	38 / 1 .	28.02	0.00	2.34	44.71	5.77	0.00	0.35	0.28	1.56	17.92	0.00	0.00	100.96
KS-DP-26	39 / 1 .	28.01	0.00	2.26	44.09	5.62	0.00	0.00	0.33	1.61	17.77	0.00	0.00	99.67
KS-DP-26	48 / 1 .	28.28	0.00	2.14	45.57	5.33	0.00	0.00	0.14	1.75	17.48	0.00	0.00	100.69
KS-DP-26	49 / 1 .	28.26	0.00	2.34	45.28	5.41	0.00	0.00	0.19	1.69	17.33	0.00	0.00	100.50
KS-DP-26	50 / 1 .	28.29	0.00	2.38	44.97	5.65	0.00	0.00	0.00	1.72	17.47	0.00	0.00	100.47
KS-DP-26	51 / 1 .	28.15	0.00	1.74	45.28	5.32	0.00	0.00	0.23	1.68	17.29	0.00	0.00	99.69
KS-DP-26	52 / 1 .	28.10	0.00	2.41	44.99	5.32	0.00	0.00	0.00	1.69	17.59	0.00	0.00	100.10
KS-DP-26	58 / 1 .	27.51	0.00	3.30	43.24	5.35	0.00	0.00	1.69	1.54	18.26	0.00	0.00	100.88
KS-DP-26	59 / 1 .	27.71	0.00	2.97	43.27	5.94	0.00	0.00	0.44	1.48	18.24	0.00	0.00	100.06
KS-DP-26	60 / 1 .	27.77	0.00	2.70	42.66	5.90	0.00	0.00	1.33	1.55	18.97	0.00	0.00	100.87
KS-DP-26	61 / 1 .	27.28	0.00	0.88	43.54	7.51	0.00	0.52	0.24	3.09	17.34	0.00	0.00	100.39
KS-DP-26	62 / 1 .	27.65	0.00	2.88	43.77	5.94	0.00	0.00	0.46	1.48	18.10	0.00	0.00	100.27
KS-DP-26	87 / 1 .	28.00	0.00	2.87	43.86	5.79	0.00	0.00	0.17	1.50	18.68	0.00	0.00	100.87
KS-DP-26	88 / 1 .	28.07	0.00	2.84	43.88	5.82	0.00	0.00	0.20	1.46	18.70	0.00	0.00	100.97
KS-DP-26	89 / 1 .	27.92	0.00	2.76	43.89	5.91	0.00	0.00	0.14	1.38	18.67	0.00	0.00	100.65
KS-DP-26	90 / 1 .	28.09	0.00	2.86	43.10	6.01	0.00	0.00	0.19	1.34	18.66	0.00	0.00	100.24
KS-DP-26	91 / 1 .	27.98	0.00	2.99	44.05	5.73	0.00	0.00	0.00	1.36	18.62	0.00	0.00	100.73
KS-DP-26	107 / 1 .	28.11	0.00	2.67	44.53	5.87	0.00	0.32	0.20	1.42	17.28	0.00	0.00	100.39
KS-DP-26	108 / 1 .	27.99	0.00	2.44	44.29	6.03	0.00	0.00	0.35	1.44	16.85	0.00	0.00	99.39
KS-DP-26	109 / 1 .	27.83	0.00	1.94	43.79	7.48	0.00	0.00	0.15	1.43	16.89	0.00	0.00	99.52
KS-DP-26	110 / 1 .	27.99	0.00	2.85	43.62	5.38	0.00	0.00	0.13	1.48	18.76	0.00	0.00	100.21
KS-DP-26	111 / 1 .	27.99	0.00	2.90	43.50	5.79	0.00	0.00	0.21	1.37	18.59	0.00	0.00	100.34
KS-DP-26	142 / 1 .	27.86	0.00	2.99	43.08	6.14	0.00	0.00	0.20	1.37	19.29	0.00	0.00	100.93
KS-DP-26	143 / 1 .	28.15	0.00	2.96	43.50	6.24	0.00	0.00	0.20	1.34	17.39	0.00	0.00	99.79
KS-DP-26	144 / 1 .	28.00	0.00	2.66	43.54	6.09	0.00	0.00	0.22	1.41	17.39	0.00	0.00	99.30
KS-DP-26	145 / 1 .	27.79	0.00	2.69	43.27	5.68	0.00	0.00	0.25	1.42	19.33	0.00	0.00	100.43
KS-DP-26	146 / 1 .	28.11	0.00	2.82	43.38	5.99	0.00	0.00	0.13	1.36	17.32	0.00	0.00	99.10
KS-DP-26	167 / 1 .	27.81	0.00	2.64	44.29	6.30	0.00	0.00	0.00	1.34	18.41	0.00	0.00	100.78
KS-DP-26	168 / 1 .	27.94	0.00	2.37	44.41	5.95	0.00	0.00	0.13	1.34	18.49	0.00	0.00	100.62
KS-DP-26	169 / 1 .	27.85	0.00	2.60	43.91	5.70	0.00	0.00	0.00	1.33	18.07	0.00	0.00	99.46
KS-DP-26	170 / 1 .	27.83	0.00	2.32	44.41	5.57	0.00	0.00	0.00	1.35	18.27	0.00	0.00	99.75
KS-DP-26	171 / 1 .	28.04	0.00	2.55	44.00	6.08	0.00	0.00	0.12	1.38	18.11	0.00	0.00	100.26
KS-DP-26	192 / 1 .	27.90	0.00	2.77	43.90	5.84	0.00	0.00	0.00	1.28	18.67	0.00	0.00	100.35
KS-DP-26	193 / 1 .	27.79	0.00	2.76	44.41	5.63	0.00	0.00	0.22	1.34	18.71	0.00	0.00	100.85
KS-DP-26	194 / 1 .	27.69	0.00	2.62	44.25	5.73	0.00	0.00	0.00	1.25	18.78	0.00	0.00	100.32
KS-DP-26	195 / 1 .	27.72	0.00	2.69	44.48	5.78	0.00	0.00	0.13	1.26	18.78	0.00	0.00	100.84
KS-DP-26	196 / 1 .	27.97	0.00	2.64	45.00	5.62	0.00	0.00	0.17	1.28	16.65	0.00	0.00	99.33
KS-DP-26	202 / 1 .	27.95	0.00	2.64	44.11	6.21	0.00	0.00	0.00	1.26	18.51	0.00	0.00	100.68
KS-DP-26	203 / 1 .	27.63	0.00	2.68	44.83	5.80	0.00	0.00	0.15	1.28	16.80	0.00	0.00	99.17
KS-DP-26	204 / 1 .	27.73	0.00	2.80	44.39	5.60	0.00	0.00	0.13	1.27	18.51	0.00	0.00	100.41
KS-DP-26	205 / 1 .	27.60	0.00	3.20	43.85	5.94	0.00	0.00	0.16	1.28	18.73	0.00	0.00	100.75
KS-DP-26	206 / 1 .	27.84	0.00	3.12	43.36	5.81	0.00	0.00	0.18	1.33	18.66	0.00	0.00	100.28
KS-DP-26	217 / 1 .	27.66	0.00	2.65	43.27	5.83	0.00	0.00	0.67	1.44	19.17	0.00	0.00	100.69
KS-DP-26	218 / 1 .	27.86	0.00	2.64	43.55	5.68	0.00	0.26	0.68	1.31	17.37	0.00	0.00	99.35
KS-DP-26	219 / 1 .	27.67	0.00	2.82	43.43	5.43	0.00	0.00	0.34	1.25	19.45	0.00	0.00	100.38
KS-DP-26	220 / 1 .	28.08	0.00	2.61	43.17	5.93	0.00	0.00	0.68	1.20	19.31	0.00	0.00	100.96

KS-DP-26	221 / 1 .	27.84	0.00	2.61	42.68	5.77	0.00	0.00	0.46	1.17	19.49	0.00	0.00	100.02
KS-DP-26	222 / 1 .	28.00	0.00	2.43	43.74	5.86	0.00	0.00	0.57	1.41	18.86	0.00	0.00	100.87
KS-DP-26	223 / 1 .	27.93	0.00	2.42	43.04	5.74	0.00	0.00	0.48	1.44	18.77	0.00	0.00	99.83
KS-DP-26	224 / 1 .	27.99	0.00	2.28	43.70	6.03	0.00	0.00	0.82	1.49	17.00	0.00	0.00	99.31
KS-DP-26	225 / 1 .	28.08	0.00	2.50	43.01	5.70	0.00	0.00	0.53	1.50	18.71	0.00	0.00	100.02
KS-DP-26	226 / 1 .	27.94	0.00	2.44	43.90	6.01	0.00	0.00	0.76	1.49	17.07	0.00	0.00	99.62
KS-DP-28	37 / 1 .	27.74	0.00	1.59	43.37	7.31	0.00	0.32	0.44	2.00	17.02	0.00	0.00	99.78
KS-DP-28	38 / 1 .	27.60	0.00	1.70	43.35	7.08	0.00	0.00	0.61	1.97	16.88	0.00	0.00	99.19
KS-DP-28	39 / 1 .	27.70	0.00	1.52	43.15	7.02	0.00	0.00	0.46	2.01	18.72	0.00	0.00	100.58
KS-DP-28	40 / 1 .	27.83	0.00	1.73	42.50	7.29	0.00	0.00	0.52	2.03	18.67	0.00	0.00	100.57
KS-DP-28	41 / 1 .	27.61	0.00	1.55	43.13	6.88	0.00	0.00	0.51	2.04	18.82	0.00	0.00	100.54
KS-DP-28	52 / 1 .	27.55	0.00	1.55	42.87	6.87	0.00	0.00	1.27	1.33	19.13	0.00	0.00	100.57
KS-DP-28	53 / 1 .	27.44	0.00	1.45	42.10	7.15	0.00	0.00	1.25	1.35	19.05	0.00	0.00	99.78
KS-DP-28	54 / 1 .	27.33	0.00	1.40	41.85	7.21	0.00	0.00	2.73	1.36	18.97	0.00	0.00	100.85
KS-DP-28	55 / 1 .	27.31	0.00	1.52	41.43	7.15	0.00	0.00	1.76	1.36	18.99	0.00	0.00	99.52
KS-DP-28	56 / 1 .	27.38	0.00	1.51	41.09	7.15	0.00	0.00	2.64	1.32	18.96	0.00	0.00	100.05
KS-DP-28	71 / 1 .	27.87	0.00	1.48	42.96	7.04	0.00	0.27	0.43	1.55	19.24	0.00	0.00	100.84
KS-DP-28	72 / 1 .	27.86	0.00	1.56	42.92	6.98	0.00	0.00	0.55	1.51	19.07	0.00	0.00	100.45
KS-DP-28	73 / 1 .	27.92	0.00	1.59	43.44	7.13	0.00	0.00	0.35	1.57	17.24	0.00	0.00	99.25
KS-DP-28	74 / 1 .	27.70	0.00	1.57	43.07	7.36	0.00	0.00	0.39	1.56	19.25	0.00	0.00	100.90
KS-DP-28	75 / 1 .	27.56	0.00	1.48	43.55	7.68	0.00	0.00	0.46	1.54	17.42	0.00	0.00	99.68
KS-DP-28	81 / 1 .	27.43	0.00	1.54	41.84	6.85	0.00	0.27	1.04	4.05	17.25	0.00	0.00	100.26
KS-DP-28	82 / 1 .	27.37	0.00	1.57	42.16	7.51	0.00	0.00	0.96	4.21	17.13	0.00	0.00	100.91
KS-DP-28	83 / 1 .	27.55	0.00	1.56	42.30	6.91	0.00	0.00	0.96	4.41	17.13	0.00	0.00	100.81
KS-DP-28	84 / 1 .	27.59	0.00	1.47	41.66	6.99	0.00	0.00	1.23	3.89	17.35	0.00	0.00	100.17
KS-DP-28	85 / 1 .	27.54	0.00	1.62	40.79	6.98	0.00	0.00	1.73	3.75	17.50	0.00	0.00	99.91
KS-DP-28	96 / 1 .	31.81	0.00	0.18	48.00	0.00	0.00	0.00	0.45	1.93	17.40	0.00	0.00	99.77
KS-DP-28	97 / 1 .	31.79	0.00	0.21	47.75	0.00	0.00	0.00	0.52	1.82	17.15	0.00	0.00	99.24
KS-DP-28	98 / 1 .	31.84	0.00	0.20	48.21	0.00	0.00	0.00	0.42	2.13	17.37	0.00	0.00	100.18
KS-DP-28	99 / 1 .	31.74	0.00	0.23	48.53	0.00	0.00	0.00	0.53	1.39	17.31	0.00	0.00	99.71
KS-DP-28	100 / 1 .	31.90	0.00	0.00	47.65	0.00	0.00	0.00	0.47	1.64	17.67	0.00	0.00	99.34
KS-DP-28	106 / 1 .	27.33	0.00	1.61	41.50	7.04	0.00	0.00	1.88	2.49	18.30	0.00	0.00	100.15
KS-DP-28	107 / 1 .	27.29	0.00	1.60	40.73	6.85	0.00	0.00	1.82	2.59	18.13	0.00	0.00	99.02
KS-DP-28	108 / 1 .	27.23	0.00	1.52	40.96	7.12	0.00	0.00	1.86	2.73	18.06	0.00	0.00	99.48
KS-DP-28	109 / 1 .	27.34	0.00	1.54	40.67	7.16	0.00	0.00	1.66	2.75	18.15	0.00	0.00	99.26
KS-DP-28	110 / 1 .	27.38	0.00	1.64	40.87	7.25	0.00	0.00	2.49	2.67	18.24	0.00	0.00	100.55
Argentiferous Tennantite (Argento-Tennantite???)		***28.33***		***3.80***	***47.51***						***20.37***			
KS-DP-28	117 / 1 .	27.10	0.00	1.54	37.68	5.72	0.00	0.00	8.76	1.59	17.90	0.00	0.00	100.28
KS-DP-28	118 / 1 .	27.30	0.00	1.45	37.76	6.44	0.00	0.00	7.58	1.71	18.40	0.00	0.00	100.64
KS-DP-28	119 / 1 .	27.27	0.00	1.57	37.16	6.37	0.00	0.00	7.43	1.73	18.43	0.00	0.00	99.96
KS-DP-28	116 / 1 .	26.55	0.00	1.31	32.59	6.83	0.00	0.00	13.77	1.71	17.74	0.00	0.00	100.50
KS-DP-28	120 / 1 .	26.65	0.00	1.27	33.28	6.62	0.00	0.00	13.19	1.73	17.87	0.00	0.00	100.59
Weathering product of galena???														
KS-DP-26	232 / 1 .	7.75	0.00	0.00	0.44	0.00	0.00	67.23	0.00	0.00	0.00	0.00	0.00	75.42

KS-DP-26	233 / 1 .	7.77	0.00	0.00	0.51	0.00	0.00	68.51	0.00	0.00	0.00	0.00	0.00	76.80
KS-DP-26	234 / 1 .	7.83	0.00	0.00	0.39	0.00	0.00	67.24	0.00	0.00	0.00	0.00	0.00	75.45
KS-DP-26	235 / 1 .	7.80	0.00	0.00	0.00	0.00	0.00	67.00	0.00	0.00	0.00	0.00	0.00	74.79
KS-DP-26	236 / 1 .	7.69	0.00	0.00	0.43	0.00	0.00	65.86	0.57	0.00	0.00	0.00	0.00	74.54